Observations of Middle Atmosphere Dynamics over Antarctica

A thesis
submitted in partial fulfilment
of the requirements for the Degree
of
Doctor of Philosophy in Physics
in the
University of Canterbury

by

Andreas J. G. Baumgaertner

University of Canterbury
2007

Abstract

This thesis is concerned with the dynamics of the middle atmosphere over the southern-most continent on our planet, Antarctica. Building on previous observational and theoretical efforts to understand the dynamics of this region of the atmosphere, the work encompasses instrument improvements as well as data analysis studies of gravity waves in the lower and middle stratosphere, tides in the upper mesosphere and lower thermosphere, and short-period planetary waves in the stratosphere and mesosphere.

An upgrade of the Medium-Frequency Spaced Antenna (MFSA) radar at Scott Base, Antarctica, was carried out in 2004/5 in order to ensure continued operation and enhance its capabilities to measure gravity waves. As a result, the quality of the wind measurements was greatly enhanced and the amount of data collected is now greater by a factor of approximately 15 compared with before the upgrade.

Analysis of over two decades of wind velocity data from Scott Base yields a reliable climatology of the dynamics of the upper mesosphere and lower thermosphere in this area, namely the tidal oscillations and the background winds. In addition, interannual variability is assessed and periodicities of approximately 11 years and strong positive trends in tidal amplitudes are reported. Mechanisms that could explain the observed behaviour are proposed. The data are then combined with wind measurements from Halley, the longitudinal conjugate site, in order to study the zonal character of the semi-diurnal tide. Zonal wavenumber 1 and 2 waves are both found and mechanisms that could explain the generation of a wavenumber 1 component are suggested. Two further sets of MFSA radar wind measurements are used to investigate the behaviour of planetary waves with periods of between two and four days in the Antarctic middle atmosphere. Satellite temperature measurements further help to create a more complete picture of these waves. Baroclinic and barotropic instabilities, which result from shears of the zonal wind, appear to be responsible for much of the observed wave activity. In addition, a quasi-to day wave event in mid-May 2005 with unusually large amplitudes is examined and suggested to be linked to a solar proton event.

Gravity wave activity over Antarctica is studied using temperature profiles obtained through the satellite radio occultation technique. Although the measurements are restricted to below 35 km altitude, high-resolution temperature profiles allow conclusions to be drawn about the seasonal, geographical, and height distribution of gravity wave activity. Mountain waves are found to be important over the Antarctic Peninsula and the Transantarctic mountains where they contribute more than 20% of the observed wave activity in the lower stratosphere. In addition, the analysis indicates the importance of critical-level filtering and Doppler-shifting.

Acknowledgements

Many people have contributed to this work, and even more have supported me during the time of my PhD. I owe sincere gratitude to Adrian McDonald who encouraged me to commence a PhD in atmospheric dynamics under his supervision. I have never regretted my positive decision and thank him for the continued support and interesting and enjoyable discussions on the ice and in Christchurch. Many thanks go to Grahame Fraser, who built the MFSA radar on which much of this thesis is based, and who was always there for discussions. I am very thankful to my parents, Ursula and Hans-Dieter, and my sister, Heike, who supported my decision to stay in New Zealand from the very beginning. Many emails, phone calls and sometimes even a video conference didn't make it feel far away from home. Thanks for the countless number of parcels containing chocolate and other goodies. Special thanks go to all my many office mates and students and staff in the atmospheric group, Kate Monahan, Petra Huck, John Grant, Jack Baggaley, Graeme Plank, Steve George, and especially to Beth Geraghty. Many friends outside Physics helped to keep me sane - my flatmates Dave, Volker, Helen, Sylvia, Andrew, and Ian; Rosa, Juliane and all my friends in the tramping club, university choir and the dance club. Sorry I can't list you all. Many thanks go to Martin Jarvis who invited me to work in Cambridge as part of my thesis. I very much enjoyed my visit, thanks to all British Antarctic Survey staff who made me feel very welcome.

The support from Graeme McDonald, Ross Ritchie and Geoff Grahame in the department's technical workshop and the work by the Scott Base technical staff are very much appreciated. Logistic support for the Scott Base radar was provided by Antarctica New Zealand. I am grateful to the British Antarctic Survey for providing Rothera MFSA and Halley IDI data. I thank the GFZ Potsdam and the ISDC for providing the CHAMP data. The NCEP/NCAR reanalysis data were kindly provided by the NOAA-CIRES Climate Diagnostics Center, Boulder, Colorado, USA. The Met Office stratospheric assimilated data were made available by the British Atmospheric Data Centre. The EOS MLS data were contributed by the Jet Propulsion Laboratory/NASA via their website. I thank D. Murphy for kindly providing the Davis MFSA radar data. GOES proton flux measurements were taken from the website of the Space Environment Center at NOAA.

Myself and the co-authors of the published chapters wish to thank the reviewers of the respective journals for their constructive criticism. Financial support from the University of Canterbury in the form of a doctoral "Canterbury Scholarship" is gratefully acknowledged.

Preface

The Earth's atmosphere is a layer of gas surrounding our planet and it is essential to life. Compared with the size of the Earth it is a very thin layer and as such very vulnerable. An understanding of the dynamics, physics and chemistry of the atmosphere is of great importance for humanity in order to be able to lead a sustainable existence, as exemplified by the so-called ozone hole. Although the atmosphere is a complex and nonlinear system, surprisingly many different approximations yield valuable insights. This also applies to the vertical temperature structure of the atmosphere which experiences several reversals of its gradient, as seen in Figure 1. This has led to a traditional division of the atmosphere into different spheres, the troposphere, stratosphere, mesosphere and thermosphere. This thesis is concerned mainly with the stratosphere, mesosphere, and the part of the thermosphere up to the homopause, below which the atmosphere remains well mixed. Traditionally, this region is called the middle atmosphere. More specifically, the focus of this thesis is on various types of atmospheric waves that can be observed in the middle atmosphere and have a great impact on the global circulation. Many types of waves carry energy from their source regions to higher altitudes where the waves break and change the mean flow. The implications for the global temperature distribution and chemistry are vast but are not subject to investigation here.

This thesis studies the occurrence and forcing mechanisms of waves and how these change over time. Antarctica is an important region for this type of study for several reasons. Firstly, certain types of waves have important consequences for the ozone hole (Newman and Nash, 2005; Palm et al., 2005). Secondly, greenhouse gases have been suggested to cause a large cooling in the mesosphere over Antarctica (Thomas, 1996). Finally, the Antarctic middle atmosphere has in the past received less attention than lower latitudes due to its inaccessibility for ground-based measurements but also for satellites which often had orbital inclinations that did not allow measurements at high latitudes. However, much progress has been made in the last decade and many data sets are now available and form the basis of this thesis.

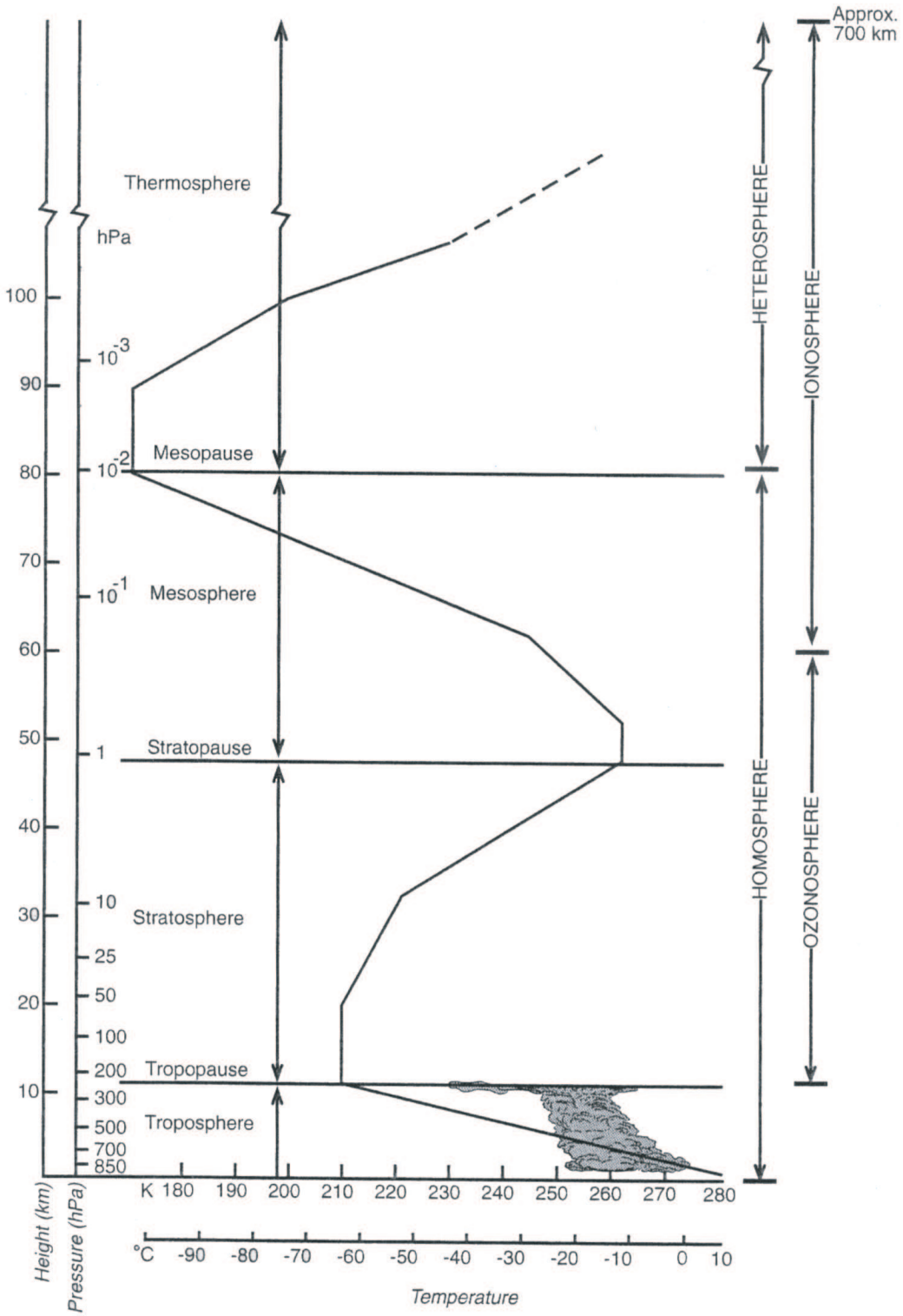

Figure 1: Vertical structure of the atmosphere. From Sturman and Tapper (1996).

Contents

[1]Note that a more general solution to this problem is presented in Appendix B.

List of Figures

List of Tables

Chapter 1

Introduction

Many aspects of the dynamics of the middle atmosphere over Antarctica region have been described previously. However, many important aspects remain to be studied. The main objective of this thesis is to present climatologies of different types of atmospheric waves in this region. The temporal and geographical variability, and the mechanisms behind these, are the primary focus of much of the work as these are in many cases either completely unknown or not understood yet. Temporal variability of wave activity on timescales ranging from several days to two decades will be described and possible reasons for the variabilities will be discussed. Also, geographical variability of small-scale waves and the longitudinal structures of planetary-scale waves will be addressed. This is still an enormous task, and it is only possible to focus on some aspects. The choice of questions to be addressed was ultimately based on their importance and the data sets available. Starting point for the development of scientific questions were data sets that have recently become available as well as data that have previously not been examined. This led to a variety of aspects which will be briefly introduced here. The decadal variability of tides and the prevailing winds in the mesosphere and lower thermosphere is largely unknown. Almost all existing studies focus on the northern hemisphere. However, the Scott Base medium-frequency spaced antenna (MFSA) radar has been measuring winds over Antarctica since 1982 and is thus ideally suited to address this. In order to understand the variability of tidal motions it is necessary to know the wavenumber spectrum and the associated forcing mechanisms for each component. For Antarctic latitudes there exist only few studies on this issue and none have been able to present solid conclusions on these questions. A combination of the Halley and Scott Base radars makes it possible to study this in detail. Here we focus on only two wavenumber components of the semi-diurnal tide. In the stratosphere, gravity wave activity is a ubiquitous feature over Antarctica and can for the first time be studied with respect to geographic variability thanks to a new technique termed radio occultation. The work in this thesis is based on measurements by an instrument onboard the CHAMP (CHallenging Minisatellite Payload) satellite which was the first instrument to provide such data for Antarctica. Combining several radar wind measurements with satellite temperature measurements from the MLS

(Microwave limb sounder) instrument made it possible to address the question of the occurrence and variability of short-period planetary waves especially in the winter mesosphere over Antarctica. They are characterised for the first time and suggestions for their origins are discussed. The fact that there are very few instruments that can sample the mesosphere and lower thermosphere at a sufficient resolution to study gravity waves in this region led to the upgrade of the Scott Base MFSA radar. This was possible due to the advance in computer and data acquisition hardware.

1.1 Atmospheric Dynamics Overview

The basics of atmospheric dynamics necessary for the discussion of the results of this thesis are briefly introduced here. Starting point are the equations describing the basis of atmospheric motion and the derivations that lead to the perturbation equations for atmospheric tides, planetary waves, and gravity waves. Some basic properties resulting from the waves' mathematical descriptions will be shown. In addition, wave excitation mechanisms will be briefly touched on. References to more detailed discussions will be given where appropriate. More specific literature that is relevant to individual chapters of this thesis will be reviewed in the introductory sections to those chapters.

1.1.1 The Basic Equations

The physical laws of conservation of momentum, mass, and energy lead to the fundamental fluid equations. In spherical coordinates several approximations can be made to simplify these equations. The Coriolis force associated with the horizontal component of the Earth's rotation is neglected, and the distance from a point in the atmosphere to the centre of the Earth is replaced by a mean radius a. The resulting system of equations are called the primitive equations.

There are several possibilities for the choice of the vertical coordinate and it depends on the aim of the study which system is the most appropriate. For the purposes here, the primitive equations are introduced in the log-pressure and the cartesian system. Note that when using log-pressure coordinates, in the mesosphere substantial deviations from the geometrical height can occur. In log-pressure coordinates on a sphere the zonal and meridional momentum equations, the mass continuity equation, the thermodynamic energy equation, and the equation for hydrostatic balance which approximates the vertical momentum equation can be written as (Holton, 1975):

$$\frac{\partial u}{\partial t} + \frac{u}{a\cos\phi}\frac{\partial u}{\partial \lambda} + \frac{v}{a\cos\phi}\frac{\partial}{\partial \phi}(u\cos\phi) + w\frac{\partial u}{\partial z} - fv + \frac{1}{a\cos\phi}\frac{\partial \Phi}{\partial \lambda} = X \quad (1.1)$$

$$\frac{\partial v}{\partial t} + \frac{u}{a\cos\phi}\frac{\partial v}{\partial \lambda} + \frac{v}{a}\frac{\partial v}{\partial \phi} + w\frac{\partial v}{\partial z} + \frac{u^2\tan\phi}{a} + fu + \frac{1}{a}\frac{\partial \Phi}{\partial \phi} = Y \quad (1.2)$$

$$\frac{1}{a\cos\phi}\frac{\partial u}{\partial \lambda} + \frac{1}{a\cos\phi}\frac{\partial}{\partial \phi}(v\cos\phi) + \frac{\partial w}{\partial z} - \frac{w}{H} = 0 \quad (1.3)$$

$$\frac{\partial T}{\partial t} + \frac{u}{a\cos\phi}\frac{\partial T}{\partial \lambda} + \frac{v}{a}\frac{\partial T}{\partial \phi} + w\left(\frac{\partial T}{\partial z} + \frac{\kappa T}{H}\right) = \frac{J}{c_p} \quad (1.4)$$

$$\frac{\partial \Phi}{\partial z} = \frac{RT}{H} \quad (1.5)$$

where

t	time
ϕ	latitude
λ	longitude
z	log-pressure height ($= -H\ln(p/p_0)$)
u	eastward velocity
v	northward velocity
w	upward velocity ($= dz/dt$)
H	scale height ($\equiv RT/g$ where T is a constant mean temperature)
f	Coriolis force ($= 2\Omega\sin\phi$)
Ω	angular velocity of Earth
Φ	geopotential
T	temperature
c_p	specific heat at constant pressure
κ	gas constant R divided by c_p
R	gas constant for dry air
a	radius of Earth
J	heating rate per unit mass
X, Y	horizontal components of unspecified nonconservative forcings

In cartesian coordinates, with height as a vertical coordinate, and small incremental distances $dx = a\cos\phi d\lambda$ in the eastward direction and $dy = ad\phi$ in the northward direction, the momentum equations become (Andrews, 2000):

$$\frac{du}{dt} - \left(2\Omega + \frac{u}{a\cos\phi}\right)(v\sin\phi - w\cos\phi) + \frac{1}{\rho}\frac{\partial p}{\partial x} = X \quad (1.6)$$

$$\frac{dv}{dt} + \frac{wv}{a} + \left(2\Omega + \frac{u}{a\cos\phi}\right)u\sin\phi + \frac{1}{\rho}\frac{\partial p}{\partial y} = Y \quad (1.7)$$

$$\frac{dw}{dt} - \frac{u^2+v^2}{a} - 2\Omega u\cos\phi + \frac{1}{\rho}\frac{\partial p}{\partial z} + g = Z \quad (1.8)$$

where d/dt is the total derivative, the rate of change of a variable following the

motion ($= \frac{\partial}{\partial t} + u\frac{\partial}{\partial x} + v\frac{\partial}{\partial y} + w\frac{\partial}{\partial z}$) and Z is the vertical component of unspecified nonconservative forcings.

Using the approximations

$$\frac{|u|}{a\cos\phi} \ll 2\Omega$$
$$|w\cos\phi| \ll |v\sin\phi|$$
$$|wv|/r \ll 2\Omega|u\sin\phi|$$

equations 1.6 to 1.8 simplify to:

$$\frac{du}{dt} - fv + \frac{1}{\rho}\frac{\partial p}{\partial x} = X \tag{1.9}$$
$$\frac{dv}{dt} + fu + \frac{1}{\rho}\frac{\partial p}{\partial y} = Y \tag{1.10}$$
$$\frac{dw}{dt} + \frac{1}{\rho}\frac{\partial p}{\partial z} + g = 0 \tag{1.11}$$

In the Cartesian coordinate system the continuity equation and the thermodynamic energy equation can be written as:

$$\frac{1}{\rho}\frac{d\rho}{dt} + \frac{\partial u}{\partial x} + \frac{\partial v}{\partial y} + \frac{\partial w}{\partial z} = 0 \tag{1.12}$$
$$\frac{d\theta}{dt} = J \tag{1.13}$$

where $\theta = T(p_0/p)^\kappa$ is potential temperature.

Further simplification can be achieved using scale analysis (e.g. Andrews, 2000). Then equations 1.9–1.11 become:

$$fv = \frac{1}{\rho}\frac{\partial p}{\partial x} \tag{1.14}$$
$$-fu = \frac{1}{\rho}\frac{\partial p}{\partial y} \tag{1.15}$$
$$\frac{\partial p}{\partial z} = -g\rho \tag{1.16}$$

In this form the equations are called the geostrophic (equation 1.14 and 1.15) and hydrostatic (equation 1.16) approximations. The thermal windshear equations can be derived using the ideal gas law ($p = RT\rho$) and the geostrophic approximation (equation 1.14 and 1.15):

$$f\frac{\partial v}{\partial z} = \frac{g}{T}\frac{\partial T}{\partial x} \tag{1.17}$$
$$f\frac{\partial u}{\partial z} = -\frac{g}{T}\frac{\partial T}{\partial y} \tag{1.18}$$

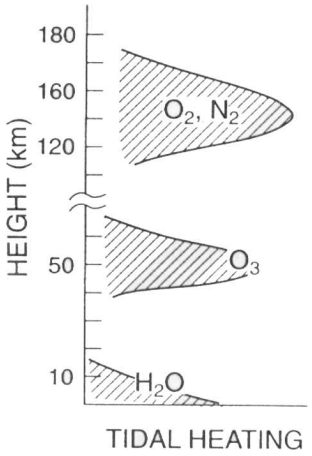

Figure 1.1: Illustration of the vertical variation of tidal heating. Taken from Forbes (1995).

1.1.2 Atmospheric Tides and Planetary Waves

Planetary waves and tides can cause very large perturbations of atmospheric parameters such as the wind velocity. A common feature of planetary waves and tides are their large horizontal scales, so for these types of waves, effects of the rotating spherical Earth become important. This leads to a common mathematical description. However, the physical forcing mechanisms are very different. Primary energy sources, most importantly solar heating, lead to the existence of solar thermal tides. Secondary sources are a result of the interaction of the primary sources with continents, the ocean, etc. and are responsible for the excitation of planetary waves.

Planetary waves, also called Rossby waves, shape in part the general circulation and play a well recognised role in chemical transport processes. They are responsible for sudden stratospheric warmings and are important for the breakdown of the vortex during the final warming. In the Antarctic this has significant consequences for ozone depletion.

Tides generally dominate the wind field above the stratopause where they have effects on the dynamics and chemistry. Solar tides are ultimately excited by the diurnal cycle in the absorption of solar radiation. In particular, the absorption of infrared radiation by water vapour in the troposphere, the absorption of UV radiation by ozone in the stratosphere and mesosphere, and the absorption of radiation in the Schumann-Runge bands and Schumann-Runge continuum by molecular oxygen and nitrogen in the lower thermosphere contribute to the forcing. This is illustrated schematically in Figure 1.1. Lunar tides result from the differential gravitational forces exerted by the moon on the earth's atmosphere. Their amplitudes are much smaller than those of solar tides but finite.

The following discussion is based on Holton (1975), Chapman and Lindzen (1970), Forbes (1995), and Volland (1988) and their work should be consulted for details.

For the study of planetary-scale waves it is necessary to consider the basic equations in spherical coordinates (equations 1.1–1.5). All atmospheric variables are expanded into a zonal mean and perturbations, for example for the eastward velocity: $u = \bar{u} + u'$. The resulting equations are then linearised. Several assumptions are made to simplify the equations without loosing necessary properties. Firstly, the background atmosphere is treated as being horizontally stratified. Secondly, an isothermal atmosphere is assumed. This procedure yields the following set of perturbation equations:

$$\frac{\partial u'}{\partial t} - fv' + \frac{1}{a\cos\phi}\frac{\partial \Phi'}{\partial \lambda} = 0 \tag{1.19}$$

$$\frac{\partial v'}{\partial t} + fu' + \frac{1}{a}\frac{\partial \Phi'}{\partial \phi} = 0 \tag{1.20}$$

$$\frac{1}{a\cos\phi}\left[\frac{\partial u'}{\partial \lambda} + \frac{\partial\left(v'\cos\phi\right)}{\partial\phi}\right] + \frac{1}{\rho_0}\frac{\partial}{\partial z}(\rho_0 w') = 0 \tag{1.21}$$

$$\frac{\partial}{\partial t \partial z}\Phi' + N^2 w' = \frac{\kappa J'}{H} \tag{1.22}$$

where

u'	perturbation eastward velocity
v'	perturbation northward velocity
w'	perturbation upward velocity
Φ'	perturbation geopotential
J'	perturbation heating rate per unit mass
ρ_0	basic state density ($\propto e^{-z/H}$)
N	buoyancy frequency

The buoyancy frequency N can be defined as

$$N^2 = \frac{g}{T}\left(\frac{dT}{dz} + \frac{g}{c_p}\right).$$

$N^2 > 0$ indicates a statically stable region of the atmosphere where parcels can oscillate at the frequency N. If $N^2 < 0$ the region is statically unstable. Equations 1.19 and 1.20 are the horizontal momentum equations, equation 1.21 is the continuity equation, and equation 1.22 is the thermodynamic energy equation. Equations 1.21 and 1.22 can be combined to eliminate w':

$$\frac{\partial}{\partial t}\left[\frac{1}{\rho_0}\frac{\partial}{\partial z}\left(\frac{\rho_0}{N^2}\right)\right] - \frac{1}{a\cos\phi}\left[\frac{\partial u'}{\partial \lambda} + \frac{\partial}{\partial\phi}\left(v'\cos\phi\right)\right] = \frac{1}{\rho_0}\frac{\partial}{\partial z}\left(\frac{\kappa}{H}\frac{\rho_0 J}{N^2}\right) \tag{1.23}$$

We assume the perturbations to be east- or westward propagating waves of zonal wavenumber s and frequency σ and to be separable in the vertical and

latitudinal dependencies as follows:

$$\{u', v', w', \Phi'\} = \left\{\hat{u}, \hat{v}, \hat{w}, \hat{\Phi}\right\} \exp[i(s\lambda - \sigma t)] \tag{1.24}$$

The wave amplitudes $\hat{u}$, $\hat{v}$, $\hat{w}$, and $\hat{\Phi}$ are assumed to be separable in the vertical and latitudinal dependencies. If a complete orthogonal set Y_n is introduced as basis functions for the wave amplitudes, a solution for equations 1.19–1.22 that describes the horizontal dependence can be found:

$$\frac{d}{d\mu}\left[\frac{1-\mu^2}{\sigma^2-\mu^2}\frac{dY}{d\mu}\right] - \frac{1}{\sigma^2-\mu^2}\left[-\frac{s}{f}\frac{\sigma^2+\mu^2}{\sigma^2-\mu^2} + \frac{s^2}{1-\mu^2}\right]Y + \epsilon Y = 0 \tag{1.25}$$

where $\mu = \sin\phi$ and $\epsilon = (2\Omega a)^2/gh$. Equation 1.25 is generally called Laplace's tidal equation (Laplace, 1799, 1825).

Equation 1.25 can be written in a form that allows easy identification of its structure:

$$F_{s,\sigma}\left(Y_n^{s,\sigma}\right) = \epsilon_n^{s,\sigma} Y_n^{s,\sigma}. \tag{1.26}$$

The ϵ_n are the eigenvalues of the problem, the Y_n are the eigenfunctions and are called Hough functions. S. S. Hough pioneered the numerical computation of the eigenfunctions (Hough, 1897, 1898), and Michael Longuet-Higgins was the first to formally solve Laplace's equation Longuet-Higgins (1968). Each eigenvalue belongs to an eigenfunction: together they constitute a "mode", which is usually written in the form Y_n^s or (s, n). s is the zonal wavenumber, n is called the meridional index and provides information on the number of latitudinal nodes and symmetry.

The solutions to equation 1.25 show that ϵ_n^s and σ are related parametrically for any given s (Volland, 1988). The relationships for $s = 1$ and various n are shown in Figure 1.2. It is evident that this allows a classification of modes. For both eastward and westward propagating waves, two families of curves are found, called "class I" solutions, also termed "gravity modes", and "class II" solutions, termed "Rossby", "rotational", or "planetary wave" modes. Note however that mixed modes that belong to both classes can appear. It can be shown that for negative or small ϵ_n the vertical structures are "trapped" or "evanescent" (confined to the region of excitation), and for sufficiently large ϵ waves are vertically propagating. Figure 1.2 also allows identification of periods for resonant responses of the atmosphere, called normal modes or free solutions. For an isothermal atmosphere at 256 K and H=7.5 km the normal modes are found at ϵ_n=8.4. The resulting periods are marked by dots in Figure 1.2.

After the calculation of the eigenvalues ϵ_n^s and eigenfunctions $Y_n^{s,\sigma}$ it is possible to derive the velocity expansion functions. As an example, this is shown for the diurnal tide in Figure 1.3.

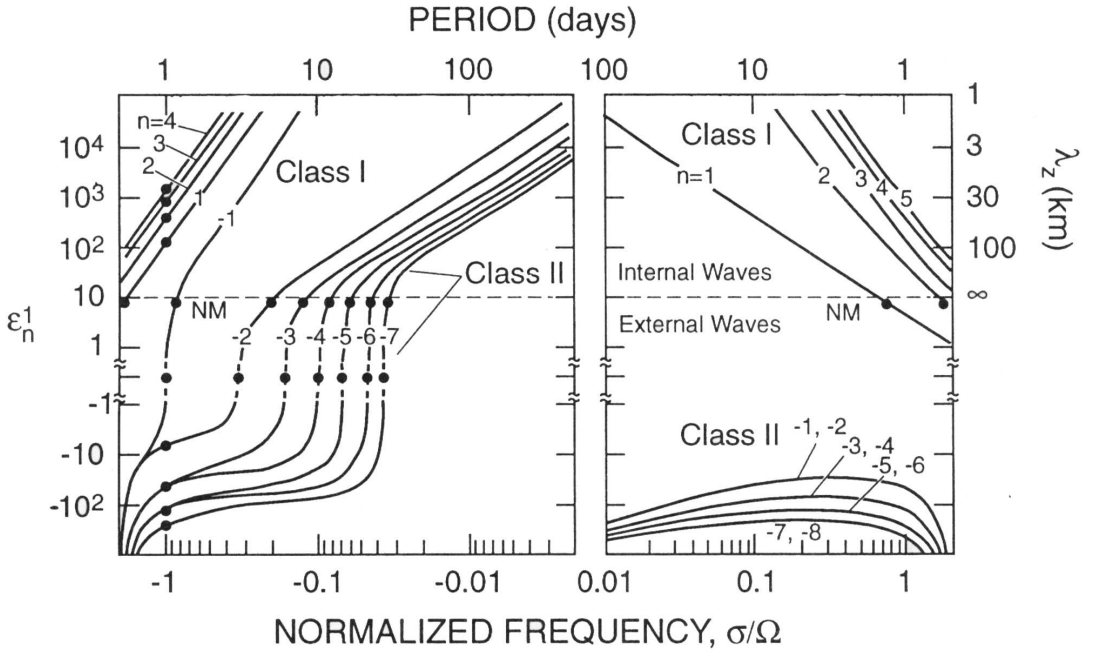

Figure 1.2: Eigenvalues ϵ_n^s for $s = 1$. Waves with positive (negative) frequencies propagate to the east (west). NM: normal modes. Adapted from Forbes (1995) and Volland (1988).

Important constraints on planetary waves can be obtained using a different set of approximations to the primitive equations. The starting point is equations 1.9–1.11. They can be approximated by the so-called Boussinesq equations where density variations are ignored except when they are coupled to gravity. In the next step the Boussinesq equations are approximated by restricting the flow to a quasi-geostrophic flow. The resulting equations can be combined to yield the quasi-geostrophic vorticity equation:

$$D_g q = 0 \tag{1.27}$$

where D_g is the time derivative following the geostrophic flow (u_g, v_g):

$$D_g = \frac{\partial}{\partial t} + u_g \frac{\partial}{\partial x} + v_g \frac{\partial}{\partial y}.$$

q is quasi-geostrophic potential vorticity and is defined as:

$$q = f_0 + \beta y + \frac{\partial^2 \psi}{\partial x^2} + \frac{\partial^2 \psi}{\partial y^2} + \frac{\partial}{\partial z}\left(\frac{f_0^2}{N^2}\frac{\partial \psi}{\partial z}\right) \tag{1.28}$$

for the geostrophic streamfunction $\psi \equiv \frac{p}{f_0 \rho_0}$. Equation 1.28 uses the β-plane approximation (Andrews, 2000), $f(y) \approx f_0 + \beta y$. Assuming a uniform zonal

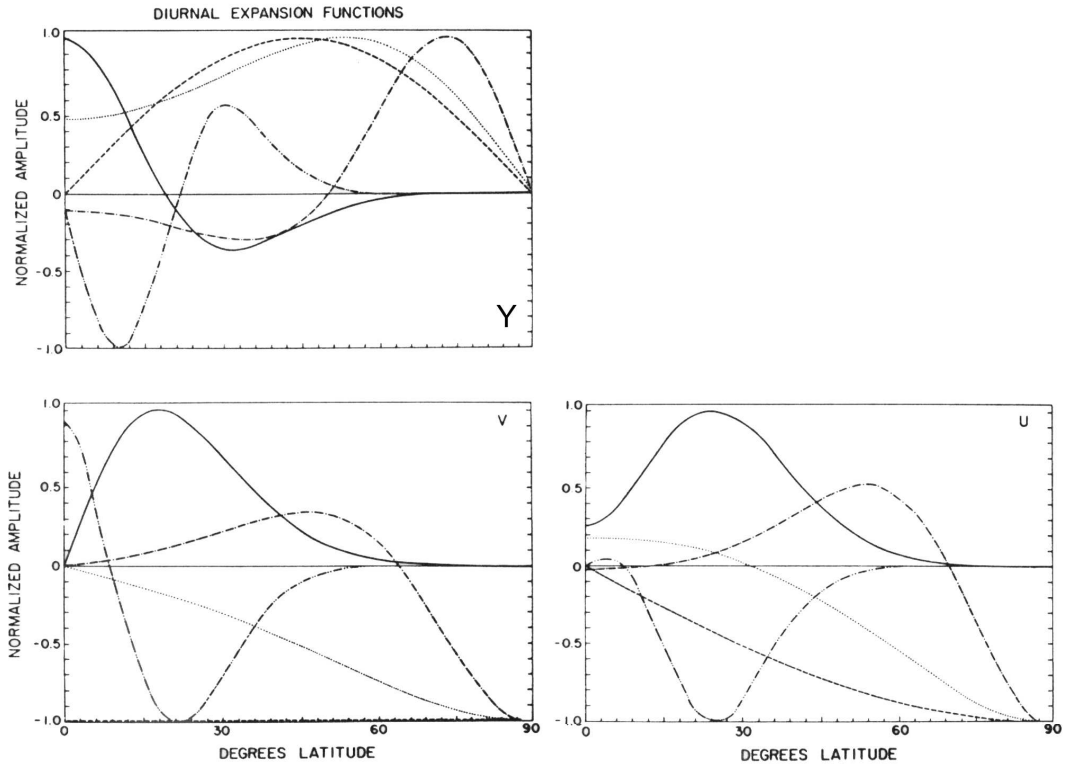

Figure 1.3: Normalised expansion functions for the solar diurnal tide. Top: Hough function, bottom left: eastward wind expansion, bottom right: northward wind expansion. Solid line: (1,1), dashed: (1,-1), dashed-double dot: (1,2), dashed: (1,-2), dashed-dot: (1,-4). Adapted from Forbes (1982a).

background flow $(U, 0, 0)$ with small-amplitude disturbances yields the following geostrophic streamfunction:

$$\psi = -Uy + \psi'. \tag{1.29}$$

The quasi-geostrophic potential vorticity equation 1.27 becomes

$$\left(\frac{\partial}{\partial t} + U\frac{\partial}{\partial x}\right)\left(\nabla^2\psi + \frac{f_0^2}{N^2}\frac{\partial^2\psi}{\partial z^2}\right) + \beta\frac{\partial\psi}{\partial x} = 0. \tag{1.30}$$

The solutions are assumed to be of the form

$$\psi = Re(\psi_0 \exp[i(\omega t + kx + ly + mz)]) \tag{1.31}$$

where ψ_0 is amplitude, ω is angular frequency, and k, l, m are the zonal, meridional, and vertical wavenumbers, respectively. This can be used in combination with the quasi-geostrophic potential vorticity equation (equation 1.27) to yield the dispersion relation:

$$m^2 = \frac{N}{f_0}\left(\frac{\beta}{U - (\omega/k)} - (k^2 + l^2)\right). \tag{1.32}$$

Valuable insight can be gained from considering implications of equation 1.32. Because $\beta > 0$ the zonal phase speed of the waves

$$c = \frac{\omega}{k} = U - \frac{\beta}{k^2 + l^2 + f_0^2 m^2/N^2}$$

always satisfies

$$U - c > 0. \tag{1.33}$$

This means that waves always propagate westward with respect to the background flow. Vertical propagation can only occur if m is real and non-zero, so this requires $m^2 > 0$. From the dispersion relation we can then infer

$$U - c = \frac{\beta}{k^2 + l^2 + f_0^2 m^2/N^2} < U_c \equiv \frac{\beta}{k^2 + l^2} \tag{1.34}$$

For stationary ($c = 0$) waves, forced for example by topography, this implies $0 < U < U_c$ (note that U_c depends on the vertical wavelength). This is called the Charney-Drazin criterion (Charney and Drazin, 1961) and implies that no vertical propagation is allowed if the background wind has a very large eastward component. These properties of planetary waves will be referred to in several chapters of this thesis.

Atmospheric tides have been subject to intensive research for several decades, and only a few references to publications with further information on modelling and observations can be given here (Forbes and Garrett, 1978, 1979; Forbes, 1982a,b, 1984, 1991; Hagan et al., 1995; Haurwitz and Cowley, 1973; Kato et al.,

1982; Lindzen, 1979; Manson et al., 1989, 1990, 1991, 1999, 2002; McLandress, 2002a,b; Morel et al., 2004; Pancheva et al., 2002; Portnyagin et al., 1993a; Smith and Ortland, 2001; Vial, 1989; Vial and Forbes, 1989).

Similarly, Rossby waves have been studied extensively. Additionally to the general references above, the reader is referred to Charney and Drazin (1961); Dickinson (1968); Garcia et al. (2005); Haurwitz (1940); Madden (1979); Rossby (1939); Salby (1981b,c, 1984); Walterscheid (1980). More specific references for aspects of tides and planetary that are of importance for work in this thesis will be given in the relevant chapters.

1.1.3 Gravity Waves

Gravity waves are a ubiquitous phenomenon in the middle atmosphere and have many important effects on atmospheric mean states, dynamics and chemistry (Fritts and Alexander, 2003). By transporting energy and momentum from their source regions in the troposphere into the middle atmosphere, gravity waves play an important role in driving the general circulation. The form of the perturbation equations useful for many types of gravity wave studies can be derived from the basic equation in Cartesian coordinates, equations 1.9–1.12 (Fritts and Alexander, 2003). The background wind $(\bar{u}, \bar{v}, 0)$, potential temperature $\bar{\theta}$, pressure $\bar{p}$, and density $\bar{\rho}$ are taken to vary only with altitude, the forcings X,Y,J are taken to be 0. The linearised perturbation equations then become:

$$\frac{Du'}{Dt} + w'\frac{\partial \bar{u}}{\partial z} - fv' + \frac{\partial}{\partial x}\frac{p'}{\bar{\rho}} = 0 \tag{1.35}$$

$$\frac{Dv'}{Dt} + w'\frac{\partial \bar{v}}{\partial z} + fv' + \frac{\partial}{\partial y}\frac{p'}{\bar{\rho}} = 0 \tag{1.36}$$

$$\frac{Dw'}{Dt} + \frac{\partial}{\partial z}\frac{p'}{\bar{\rho}} - \frac{1}{H} + g\frac{p'}{\bar{\rho}} = 0 \tag{1.37}$$

$$\frac{D}{Dt}\frac{\rho'}{\bar{\rho}} + \frac{\partial u'}{\partial x} + \frac{\partial v'}{\partial y} + \frac{\partial w'}{\partial z} - \frac{w'}{H} = 0 \tag{1.38}$$

$$\frac{D}{Dt}\frac{\theta'}{\bar{\theta}} + w'\frac{N^2}{g} = 0 \tag{1.39}$$

$$\frac{\theta'}{\bar{\theta}} = \frac{1}{c_s^2}\frac{p'}{\bar{\rho}} - \frac{p'}{\bar{\rho}} \tag{1.40}$$

where c_s is the speed of sound given by $c_s^2 = c_p/c_v R\bar{T}$ and $\frac{D}{Dt} = \frac{\partial}{\partial t} + \bar{u}\frac{\partial}{\partial x} + \bar{v}\frac{\partial}{\partial y}$ is the linearised time derivative.

The background horizontal wind vertical shear terms (second term in equations 1.35 and 1.36) are neglected and the solutions are assumed to be of the

form

$$\left(u', v', w', \frac{\theta'}{\bar{\theta}}, \frac{p'}{\bar{\rho}}, \frac{\rho'}{\bar{\rho}}\right) = (\tilde{u}, \tilde{v}, \tilde{w}, \tilde{\theta}, \tilde{p}, \tilde{\rho}) \exp\left[i(kx + ly + mz - \omega t) + \frac{z}{2H}\right] \tag{1.41}$$

k,l,m are wave number components and ω is the frequency of the monochromatic wave with respect to the ground. Substituting equation 1.41 into equations 1.35–1.40, solving the resultant equations for w', setting all imaginary terms to zero and letting the speed of sound $c_s \to \infty$ yields

$$\hat{\omega}^2 = \frac{N^2(k^2 + l^2) + f^2(m^2 + 1/4H^2)}{k^2 + l^2 + m^2 + 1/4H^2} \tag{1.42}$$

which can be solved for the vertical wavenumber m:

$$m^2 = \frac{(k^2 + l^2)(N^2 - \hat{\omega}^2)}{\hat{\omega}^2 - f^2} - \frac{1}{4H^2} \tag{1.43}$$

where $\hat{\omega} = \omega - k\bar{u} - l\bar{v}$ is the wave intrinsic frequency, the frequency relative to the mean motion $(\bar{u}, \bar{v})$. Equation 1.43 is the gravity wave dispersion relation for the vertical wavenumber and relates the intrinsic wave frequency to the spatial structure of the wave as well as properties of the background atmosphere, the scale height and the buoyancy frequency.

From equation 1.42 the group velocity $(c_x^{\text{group}}, c_y^{\text{group}}, c_z^{\text{group}}) = \left(\frac{\partial\omega}{\partial k}, \frac{\partial\omega}{\partial l}, \frac{\partial\omega}{\partial m}\right)$ and the intrinsic phase velocity $(\hat{c}_x^{\text{phase}}, \hat{c}_y^{\text{phase}}, \hat{c}_z^{\text{phase}}) = \left(\frac{\hat{\omega}}{k}, \frac{\hat{\omega}}{l}, \frac{\hat{\omega}}{m}\right)$ can be calculated. From the latter the direction of phase propagation can be inferred.

The dispersion relation leads to an important constraint for vertically propagating waves, which have real (k, l, m): $N > \hat{\omega} > |f|$. In general, this entire frequency range has to be considered, but much insight can be gained from studying three smaller frequency ranges, namely high-frequency waves with $\hat{\omega} >> f$, medium-frequency waves with $N >> \hat{\omega} >> f$, and low-frequency waves with $\hat{\omega} \sim f$.

For medium-frequency waves the dispersion relation simplifies to

$$\hat{\omega} = N\left|\frac{\sqrt{k^2 + l^2}}{m}\right| \tag{1.44}$$

which leads to

$$|m| = \frac{N}{|\hat{c}_h^{\text{phase}}|} \tag{1.45}$$

where $\hat{c}_h^{\text{phase}}$ is the horizontal phase velocity. m goes to infinity and therefore the vertical wavelength to zero for $\hat{c}_h^{\text{phase}} = c_h^{\text{phase}} - \bar{u}_h$, and therefore the altitude where the horizontal phase speed reaches the background horizontal wind speed is called a critical level. This is illustrated schematically in Figure 1.4. At the

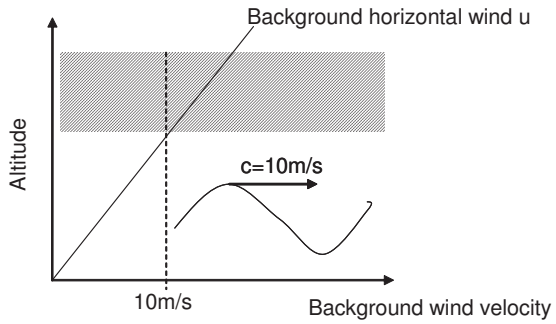

Figure 1.4: Schematic illustration of a critical level for gravity waves. A wave with a horizontal phase speed of 10 m/s propagates vertically in a background wind field with a vertical gradient (straight solid line). When it approaches the level where the background wind speed equals its phase speed it will be dissipated or reflected and it will not be able to reach the hashed region above this level.

critical level the wave can be dissipated or reflected. This will be important for discussions of gravity waves in chapter 6.

The sources for gravity waves are numerous and many have only begun to be understood recently (Fritts and Alexander, 2003). Major sources include topography, convection, and wind shear. Possibly of importance are also geostrophic adjustment processes and wave-wave interactions. Important for the discussion of the results of chapter 6 are especially mountain waves which have horizontal wavelengths of tens to hundreds of kilometres and approximately zero horizontal phase speeds.

References to gravity wave publications of relevance to this thesis will be given where appropriate. More general descriptions, additional to references already given, include Allen and Vincent (1995); Fritts (1984, 1995a); Hines (1960); McLandress (1998); McLandress et al. (2000); Nappo (2002); Ratnam et al. (2004a); de la Torre et al. (2004).

1.2 Thesis Outline

This thesis covers work which has already been published by the author in peer reviewed journals, as well as unpublished studies. In order to make the published work clearly identifiable, each publication forms a separate chapter and the results and discussion sections are reproduced here without any major modifications.

This chapter has presented an introduction to the field of atmospheric dynamics and provided the theoretical background necessary to discuss the results from the current work. Chapter 2 describes the main instruments and data sets

employed in this thesis. Chapter 3 describes the upgrade of the MFSA radar at Scott Base. This study has been submitted and accepted as a contribution to the proceedings of the Electronics New Zealand Conference (ENZCon) 2006. Chapter 4 discusses the climatologies and interannual variability of background winds and tides observed with the Scott Base MFSA radar. This study has been published in the Journal of Atmospheric and Solar-Terrestrial Physics (Baumgaertner et al., 2005).

The Scott Base radar is situated at a similar latitude to the imaging Doppler interferometer at Halley which also provides wind measurements. These data sets were combined in order to better understand the behaviour of the semi-diurnal tide in this latitude region. The results are discussed in chapter 5 and have been published in the Journal of Atmospheric and Solar-Terrestrial Physics (Baumgaertner et al., 2006). A study of gravity waves in the stratosphere over Antarctica using satellite radio occultation measurements of temperature is presented in chapter 6. This work has been accepted for publication by the Journal of Geophysical Research – Atmospheres. Short-period planetary waves have been studied using satellite limb-sounding data as well as MFSA radar data from Scott Base, Davis, and Rothera. This work is discussed in chapter 7 and has not been published so far. Chapter 8 summarises the studies of different types of waves over Antarctica and presents conclusions from this work. Possibilities for further work are outlined.

Chapter 2

Instruments and Data Sets

2.1 MFSA Radars

Medium-frequency spaced antenna (MFSA) radars are primarily used to measure horizontal wind velocities in the mesosphere and lower thermosphere and play an important part in shaping our understanding of the global circulation of the atmosphere. These radars have made significant contributions to the discovery and the understanding of different types of atmospheric waves, namely tides, planetary waves, and gravity waves.

The underlying ideas which MFSA radars are based on were developed over 70 years ago (Briggs, 1993). Ratcliffe and Pawsey (1933) and Pawsey (1935) investigated the fading of echoes reflected from the ionosphere. They observed total reflections from the E-layer and recorded the reflected power received by two antennae with a variable distance between them. Their work, carried out at the Cavendish Laboratory in Cambridge, showed that the recorded amplitude patterns were correlated between the two antennae but showed time displacements, which Pawsey interpreted as wind which advects the scatterers. Briggs et al. (1950) were the first to utilise correlation functions to calculate the horizontal wind components from measurements with a triangular antenna array. The calculation was called "similar fades" but is based on some assumptions that are not valid and a more elaborate technique was needed. Phillips and Spencer (1955) further developed the technique in order to allow for elongated patterns. This technique is now commonly called Full Correlation Analysis (FCA). The observations made until then relied on total reflections, so measurements of the wind were only possible for the height where total reflection occurs. This was overcome by Fraser (1965) by using more sensitive equipment which was able to record partial reflections.

A variety of other methods for the calculation of the wind velocities have been developed, however, they are not widely used. They are similar in that they use the same initial information, the time series of amplitude and phase of signals from several receivers. However, they use different mathematical tools,

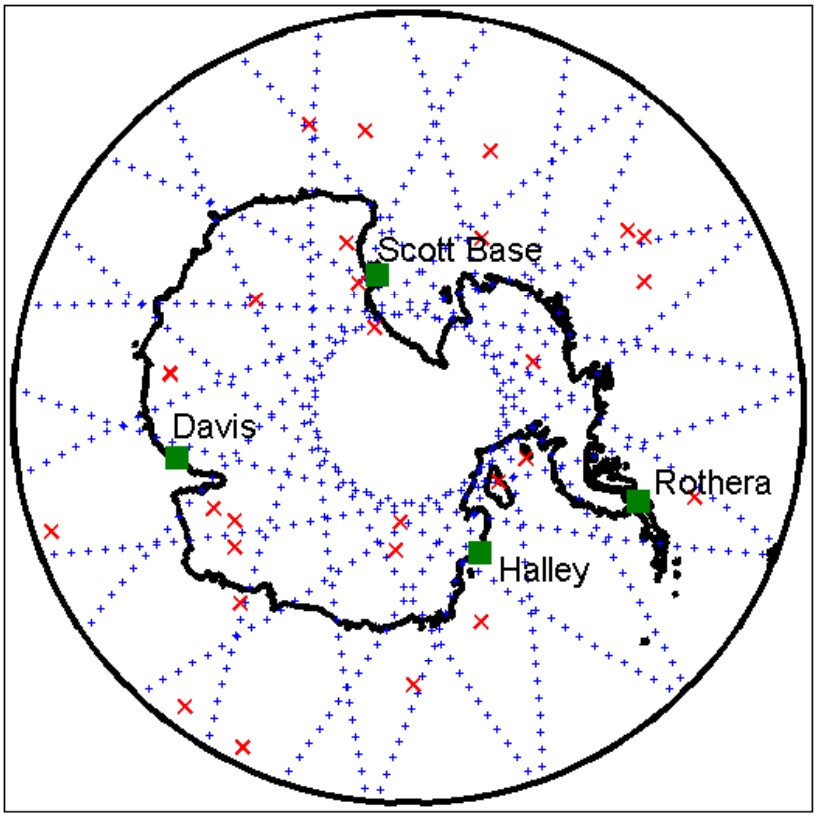

Figure 2.1: Map of Antarctica showing the location of medium-frequency radars (green squares) and locations of satellite measurements on 25 May 2005 (blue '+': limb-sounding EOS MLS, red crosses: radio-occultation measurements by CHAMP).

different equations for relating these parameters to characteristics of the scattering medium, and different assumptions for deriving the operational equations. "Spatial correlation analysis" (SCA) techniques, discussed e.g. in Holdsworth (1999b), use four antennae, hence with most MFSA radars, which have only three antennae, these techniques cannot be implemented without hardware upgrades. Another technique frequently called "full spectral analysis" is available for use with only three antennae. It is described in e.g. Briggs and Vincent (1992) and was shown to be mathematically equivalent to FCA. However, under certain circumstances the full spectral analysis has some advantages. For example, it allows removal of interference at specific known frequencies, such as sea echoes (Briggs, 1993). Another correlation function based technique which assumes models of the scattering medium is known as the Holloway and Doviak (HAD) technique and is described by Holloway et al. (1997). However, it has been shown that it is very similar to modern versions of FCA (Hocking, 1997). A relatively new technique called "UCAR-STARS" uses structure functions to calculate horizontal wind velocities amongst other parameters. A description of UCAR-STARS is given by Praskovsky et al. (2004).

2.1.1 Technique

The operation principles of modern MFSA radars have not changed since the development of FCA. A short (of the order of microseconds) electromagnetic pulse at medium frequencies (between 300 kHz and 3 MHz) is generated by a transmitter. Antennae send it vertically into the atmosphere, and the signal is reflected by irregularities in the refractive index of the atmosphere, which are due to variations in the density of free electrons in the ionosphere. The structures of varying electron density move with the neutral atmosphere, so by analysing the movement of the Fresnel diffraction patterns on the ground, the horizontal wind velocities in the reflecting volume can be calculated. However, it is important to extend these ideas to allow patterns that are not isometric and that change as they move. This will be discussed in more detail in this section.

Wave Propagation and Reflection

Electromagnetic waves can be reflected by certain properties of the atmospheric refractive index. In general, the refractive index depends on dry air pressure, water vapour pressure, temperature and the density of free electrons (Kingsley and Quegan, 1999):

$$n = 1 + \frac{3.75 * 10^{-1} e}{T^2} + \frac{7.76 * 10^{-5} P}{T} - 40.3 \frac{N_e}{f_0^2} \tag{2.1}$$

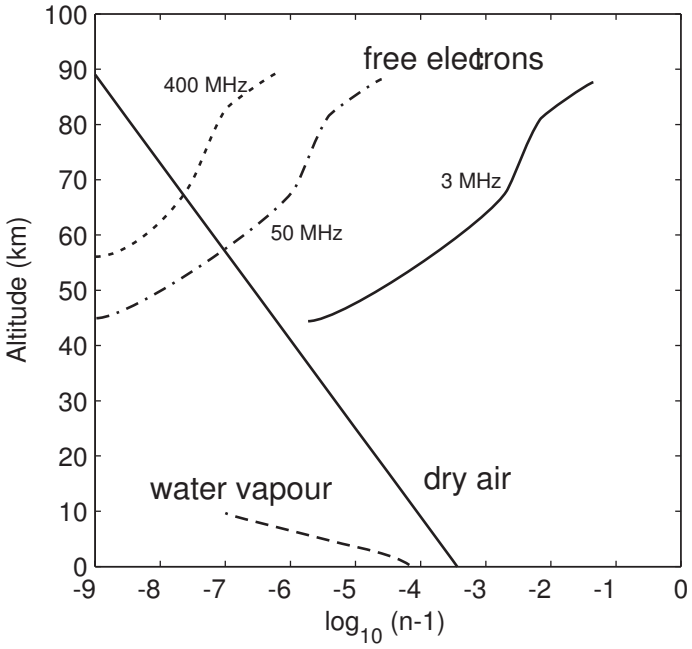

Figure 2.2: Typical height profiles of contributions to the refractive index, after Fraser (1994).

where

e	partial pressure of water (in hPa)
P	total atmospheric pressure (in hPa)
T	temperature (in K)
N_e	number density of electrons
f_0	radar frequency

A height profile of the contributions to the refractive index at various frequencies is depicted in Figure 2.2. Using 2-6 MHz, significant increases in refractive index, which are due to free electrons, occur at altitudes greater than 40 km. At altitudes greater than about 100 km n is very small and total reflection occurs. Above 100 km free electrons do not move with the neutral atmosphere anymore. Hence, at medium frequencies, dynamical parameters can only be measured between 40 and 100 km. Reliable observations of dynamics can be made in the altitude range of 65 to 95 km (Fraser, 1994).

Partial reflections from coherent discontinuities in the refractive index occur if dn/dz is large and are also called specular or Fresnel reflections. For a model ionosphere consisting of plane stratified layers with step-like boundaries it can be shown that below 100 km the amplitude reflection coefficient R is approximately

given by

$$R = |\frac{n_2 - n_1}{n_2 + n_1}| \tag{2.2}$$

Equation 2.2 is a Fresnel equation for the case of normally incident waves (Budden, 1961). The radar equation can then be used to approximate the received power P_r:

$$P_r = \frac{P_t A_e^2}{4\lambda^2 r^2} R^2 \tag{2.3}$$

where P_t is the transmitted power, A_e is the effective aperture, λ is the employed wavelength and r is the range to the scatterer.

Full Correlation Analysis

In the following a brief derivation of the "Full Correlation Analysis" (FCA) method of analysing reflected signals to determine wind velocities from spaced antennae is presented. The discussion is based on Briggs (1984), which provides full details about the analysis.

FCA uses auto- and cross-correlation functions to calculate wind velocities. Several assumptions about the pattern observed are necessary to make FCA feasible. In order to derive the equations for FCA, we will start with unrealistically strong assumptions, gradually developing ideas how to get to a set of less stringent assumptions.

In the following discussion, we assume a set of antennae which record the returned signal f. The antennae are separated by ξ and η in the x and y directions, respectively. The two-dimensional correlation coefficient between values of $f(x, y)$ and $f(x + \xi, y + \eta)$ is generally defined as

$$\rho(\xi, \eta) = \frac{< f(x, y) \cdot f(x + \xi, y + \eta) >}{< [f(x, y)]^2 >} \tag{2.4}$$

where $<>$ denotes averaging over x and y. For simplicity, for f a mean value of zero is assumed, but in practice $f(x, y)$ would have to be substituted by $f(x, y) - < f(x, y) >$. The averaging $<>$ would be very difficult to carry out spatially because measurements would need to be made at all positions (x, y) while keeping the distance (ξ, η) between the aerials, but because the patterns move and randomly change their shapes, the averaging can be approximated with temporal averaging which will be denoted as $<>_t$. Considering patterns that change or move we need to introduce time as an additional dimension, which leads to a spatial- and temporal correlation function:

$$\rho(\xi, \eta, \tau) = \frac{< f(x, y, t) \cdot f(x + \xi, y + \eta, t + \tau) >_t}{< [f(x, y, t)]^2 >_t} \tag{2.5}$$

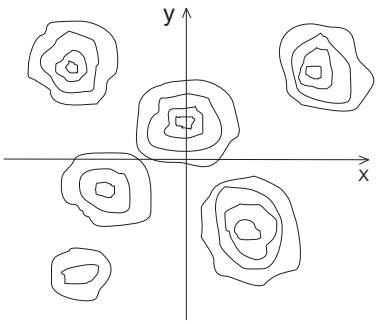

Figure 2.3: A stationary and isometric pattern.

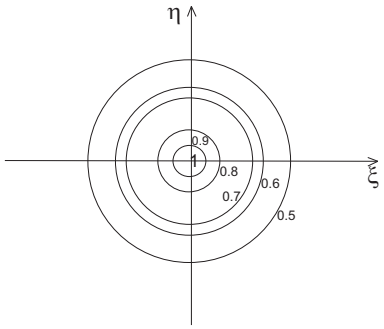

Figure 2.4: Correlation diagram corresponding to the pattern in Figure 2.3.

In order to evaluate $\rho(\xi, \eta)$, measurements would have to be made at all positions (ξ, η). This can only be avoided if assumptions are made about the observed pattern.

The functional form of the correlation functions

To begin with we assume a pattern that is stationary, non-changing and isometric (not elongated in any preferred direction), as depicted in Figure 2.3. Now the correlation $\rho(\xi, \eta)$ will only depend on the distance between two sensors and not direction, hence, lines of constant correlation will form circles as shown in Figure 2.4. Mathematically ρ can therefore be described as a function of the distance $\sqrt{\xi^2 + \eta^2}$ from the origin:

$$\rho(\xi, \eta) = \rho\left(\sqrt{\xi^2 + \eta^2}\right) \tag{2.6}$$

This means, in order to determine ρ, we would only need sensors along one axis.

Now we assume an anisometric pattern, but restrict it to elliptic shapes as depicted in Figure 2.5. Therefore, lines of constant correlation will be ellipses as shown in Figure 2.6. Now the function $\rho(\xi, \eta)$ will be of the form

$$\rho(\xi, \eta) = \rho(A\xi^2 + B\eta^2 + 2H\xi\eta) \tag{2.7}$$

which contains the algebraic constraints for an ellipse with parameters A, B, and H.

This analysis can be extended to a randomly changing pattern, so a third dimension, which represents time, has to be introduced when depicting the pattern and its movement. An example is depicted in Figure 2.7. Two patterns are shown at two times (solid line), and the random movement of the contour line of the lowest signal is shown as a dotted line for both patterns. Only random changes of

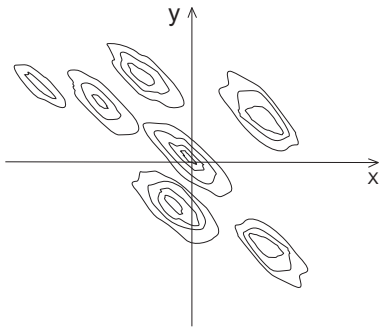

Figure 2.5: A stationary and non-isometric pattern.

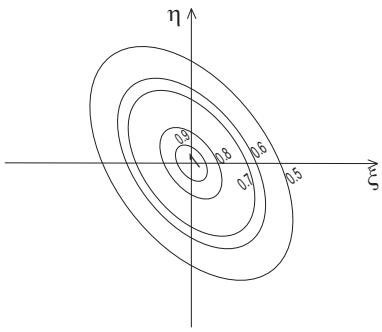

Figure 2.6: Correlation diagram corresponding to the pattern in Figure 2.5.

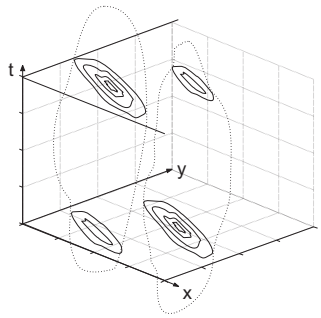

Figure 2.7: A changing pattern that exhibits no systematic movement.

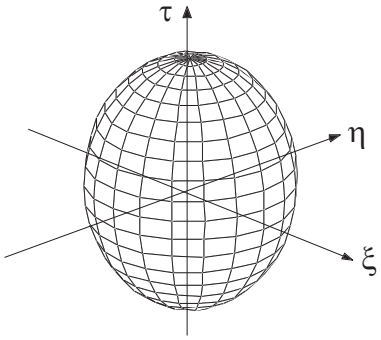

Figure 2.8: Correlation diagram corresponding to the pattern in Figure 2.7.

the pattern are allowed, so there is no systematic movement in any direction. In (ξ, η, τ) space we obtain surfaces of constant correlation. Disallowing systematic movement means that the surfaces are symmetric around the τ-axis. The situation is again simplified by assuming the same functional form for the temporal part of the correlation function as for the spatial parts, namely an ellipse. Thus, the surfaces of constant correlation will adopt the shape of concentric ellipsoids. The ellipsoid for one correlation value is depicted in Figure 2.8. One axis of the ellipsoid will be the τ-axis, and the correlation function will have the form

$$\rho(\xi, \eta, \tau) = \rho(A\xi^2 + B\eta^2 + K\tau^2 + 2H\xi\eta) \tag{2.8}$$

where A, B, H, and K are the parameters for the algebraic description of an ellipsoid centred on the origin.

Finally we introduce systematic movement of the pattern. The situation is depicted in Figure 2.9. The pattern in the (x, y) plane moves systematically as t advances. This is reflected in the systematic tilt of the correlation ellipsoid shown in Figure 2.10.

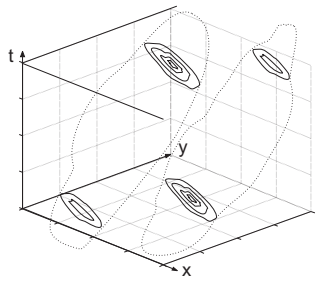

Figure 2.9: A randomly changing and moving pattern.

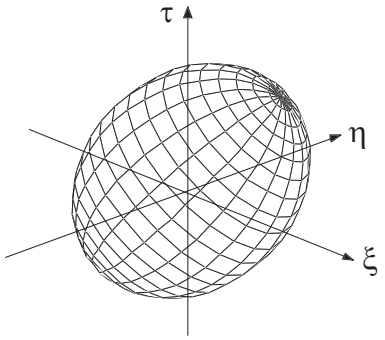

Figure 2.10: Correlation diagram corresponding to the pattern in Figure 2.9.

In a coordinate system that is moving with the pattern, the correlation function would have the form

$$\rho(\xi', \eta', \tau) = \rho(A\xi'^2 + B\eta'^2 + K\tau^2 + 2H\xi'\eta') \tag{2.9}$$

using primed variables in the moving coordinate system. The coordinate system that is moving with the pattern, and the stationary coordinate system are related by

$$x = x' + V_x t \tag{2.10}$$
$$y = y' + V_y t \tag{2.11}$$

where V_x and V_y are the components of V. It follows that

$$\begin{aligned} \rho(\xi, \eta, \tau) &= \rho[A(\xi - V_x\tau)^2 + B(\eta - V_y)^2 + K\tau^2 \\ &\qquad +2H(\xi - V_x\tau)(\eta - V_y\tau)] \qquad (2.12) \\ &= \rho(A\xi^2 + B\eta^2 + C\tau^2 + 2F\xi\tau + 2G\eta\tau + 2H\xi\eta) \qquad (2.13) \end{aligned}$$

where

$$F = -(AV_x + HV_y) \tag{2.14}$$
$$G = -(BV_y + HV_x) \tag{2.15}$$

Determination of the pattern velocity

If there are three or more sensors we look at pairs i, j which are separated by ξ_{ij} and η_{ij} in the x and y direction, respectively. For time shifts of τ_{ij} the form of the correlation function will be

$$\rho(\xi_{ij}, \eta_{ij}, \tau_{ij}) = \rho(A\xi_{ij}^2 + B\eta_{ij}^2 + C\tau_{ij}^2 + 2F\xi_{ij}\tau_{ij} + 2G\eta_{ij}\tau_{ij} + 2H\xi_{ij}\eta_{ij}) \tag{2.16}$$

The function will have a value of maximum correlation at time τ'_{ij} which can be determined by evaluating equation 2.5 with the obtained data. On the other hand, we know that for the maximum of the correlation function

$$\frac{\partial \rho}{\partial \tau_{ij}} = 0 \tag{2.17}$$

holds true. Using equation 2.16 this can be evaluated to be:

$$\tau'_{ij} = -\frac{F}{C}\xi_{ij} - \frac{G}{C}\eta_{ij}. \tag{2.18}$$

Using two sets of sensors yields two sets of equations of the form of equation 2.18 with two sets of values for τ'_{ij}, ξ_{ij}, and η_{ij}. From this set of linear equations the ratios F/C and G/C can be obtained. Now only the ratios $\frac{A}{C}$, $\frac{B}{C}$ and $\frac{H}{C}$ remain to be determined. For a given pair i,j of sensors the value of the cross-correlation function at zero time shift is $\rho(\xi_{ij}, \eta_{ij}, 0)$. From the data we can find the time shift τ_{ij} so that the autocorrelation function $\rho(0, 0, \tau_{ij})$ assumes the same value, thus

$$\rho(0, 0, \tau_{ij}) = \rho(\xi_{ij}, \eta_{ij}, 0). \tag{2.19}$$

Because we know the functional form of the correlation function (equation 2.16), equation 2.19 implies

$$\rho(C\tau_{ij}^2) = \rho(A\xi_{ij}^2 + B\eta_{ij}^2 + 2H\xi_{ij}\eta_{ij}) \tag{2.20}$$

which gives

$$\tau_{ij}^2 = \frac{A}{C}\xi_{ij}^2 + \frac{B}{C}\eta_{ij}^2 + \frac{2H}{C}\xi_{ij}\eta_{ij} \tag{2.21}$$

Thus, in order to obtain the ratios $\frac{A}{C}$, $\frac{B}{C}$ and $\frac{H}{C}$ we need at least three sets of measurements for τ'_{ij}, ξ_{ij}, η_{ij}. If the two equations 2.14 and 2.15 are divided by C, the calculation of the velocity of the pattern V is then possible.

Several authors have carried out a number of different tests in order to determine if the data is likely to be reliable. Inaccuracies can result from a weak signal or atmospheric conditions that do not satisfy the assumptions of the Full Correlation Analysis. This work has resulted in a list of criteria, that build a basis for the decision if a measurement and the calculated velocity should be regarded as reliable or has to be rejected. Most importantly, the signal-to-noise ratio has to be sufficiently large, and the mean auto-correlation function has to fall sufficiently fast. A comprehensive list of the rejection criteria is given by Briggs (1984), and Hocking et al. (1989) discusses rejection criteria with application to the Buckland Park array in Adelaide, Australia.

2.1.2 Accuracy

Random statistical errors have not been found to degrade MFSA measurements significantly. Using measurements from two simultaneous independent MFSA

experiments at Buckland Park, differences of approximately 10% of the magnitude of the wind velocity were found by May (1988). Systematic errors have been studied extensively as they were found to have an effect under certain conditions. However, many early objections to the technique have since been dismissed. A theory by Hines and Rao (1968) and Hines et al. (1993) suggested that MFSA measures the phase speed of gravity wave perturbations, but Hocking et al. (1989), Kudeki et al. (1993), and Sürücü et al. (1995) found the theory to be either invalid or to have a negligible effect on velocities averaged over sufficiently long time scales (approx. 30 minutes). The true velocity has sometimes been found to be a function of the spacing of the three receiving antennas, the so-called "triangle size effect". The reasons for this error seem to be manifold. The attenuation of the cross-correlation functions in the FCA analysis, receiver characteristic differences, antenna coupling, non-application of noise correction to correlation functions, and coarse digitization have been put forward to explain the triangle size effect (Holdsworth, 1999a). They all suggest that considerable care has to be taken when implementing the FCA and creating and maintaining the radar hardware.

For the evaluation of the MFSA technique, measurements have been compared with other instruments. For mesospheric measurements, comparisons with meteor radars (e.g. Hocking and Thayaparan, 1997; Thayaparan and Hocking, 2002) and high-resolution Doppler imaging (HRDI) satellite wind velocities (e.g. Burrage et al., 1996) have been carried out. FCA velocities were generally found to be in good agreement with other techniques, but sometimes FCA was reported to underestimate true wind velocities, especially in the meridional direction (Thayaparan and Hocking, 2002). Because meteor radar wind measurements agree well with satellite measurements (Lieberman et al., 1998) and theoretical explanations they are often considered to yield true wind velocities, despite strong diurnal cycles of meteor count rates and thus of data quality.

The accuracy of the FCA method can more easily be discussed when employed for VHF radar measurements of the lower atmosphere between 2 and 20 km. In this region, radiosonde and radar Doppler beam steering measurements are available for comparison with FCA results and Vincent et al. (1987) found very good agreement.

2.1.3 MFSA radars at Scott Base, Rothera, and Davis

The Department of Physics and Astronomy at the University of Canterbury operates an MFSA radar at Scott Base (78°S, 167°E), the New Zealand base in Antarctica. It was installed in 1982, based on concepts developed with an MFSA radar at its field station at Birdlings Flat (44°S, 173°E). The transmitter has a frequency of 2.9 MHz, a peak power of 100 kW, a pulse width of 30 μs (corresponding to a pulse length of 4.5 km in vacuum), and a variable pulse repetition frequency (currently up to 30 Hz). The three receiving aerials are

located at the electromagnetically quiet site on Arrival Heights, 3.3 km from Scott Base. They are arranged in an equilateral triangle with sides of approximately 127 m (1.23 wavelengths). Each aerial is a full-wave triangular loop three metres above the ground. For the first three years, the radar's data acquisition consisted of a hard-wired data system and only one measurement per hour was made and written to an incremental magnetic tape. More frequent measurements could be taken with the first computer-based data acquisition system which was installed together with a new transmitter in 1987. New personal computers (PC) followed in the summers of 1991/2, 1992/3, and 1994/5. There was no PC upgrade until the most recent one in 2004. Other advances in the radar's history were the use of clock synchronisation with the Global Positioning System in 1996 and the installation of coherent receivers, developed by the Department of Physics and Astronomy, in the summer of 2001/2.

A map of the physical layout of the receiving aerials including elevation contours and buildings is depicted in Figure 2.11. Figure 2.12 shows the rack which houses the receivers along with auxiliary instruments that can be used for fault diagnosis, namely an oscilloscope (middle) and an audio amplifier with speaker (bottom).

More details on the initial setup of the radar can be found in Fraser (1984). The radar is central to chapters 3, 4, and 5 where further information about its characteristics and history are presented.

Data from the MFSA radars at Davis (69°S, 78°E) and Rothera (68°S, 68°W), operated by the Australian Antarctic Division and the British Antarctic Survey, respectively, are only employed for the study of planetary waves in chapter 7. At Davis, a frequency of 1.94 MHz is used and the Rothera radar has a frequency of 1.98 MHz. Further details about these radars can be found in Greet et al. (2000) for Davis and in Hibbins et al. (2005) for Rothera.

The locations of all three MFSA radars are indicated in Figure 2.1 by green squares. The geographical area covered by each of the squares is roughly the horizontal region of the reflecting volumes for these radars.

2.2 Imaging Doppler Interferometers

Imaging Doppler interferometry (IDI) is a medium-frequency radar technique that can provide estimates of the neutral wind velocity in the mesosphere and lower thermosphere and represents an alternative to the MFSA radar technique. Doppler interferometry, also called time-domain Fourier interferometry, for use in the ionosphere was first suggested by Pfister (1971). The first implementation is described in Farley et al. (1981), but Adams et al. (1985) were the first to demonstrate that the technique can be employed for mesospheric measurements using

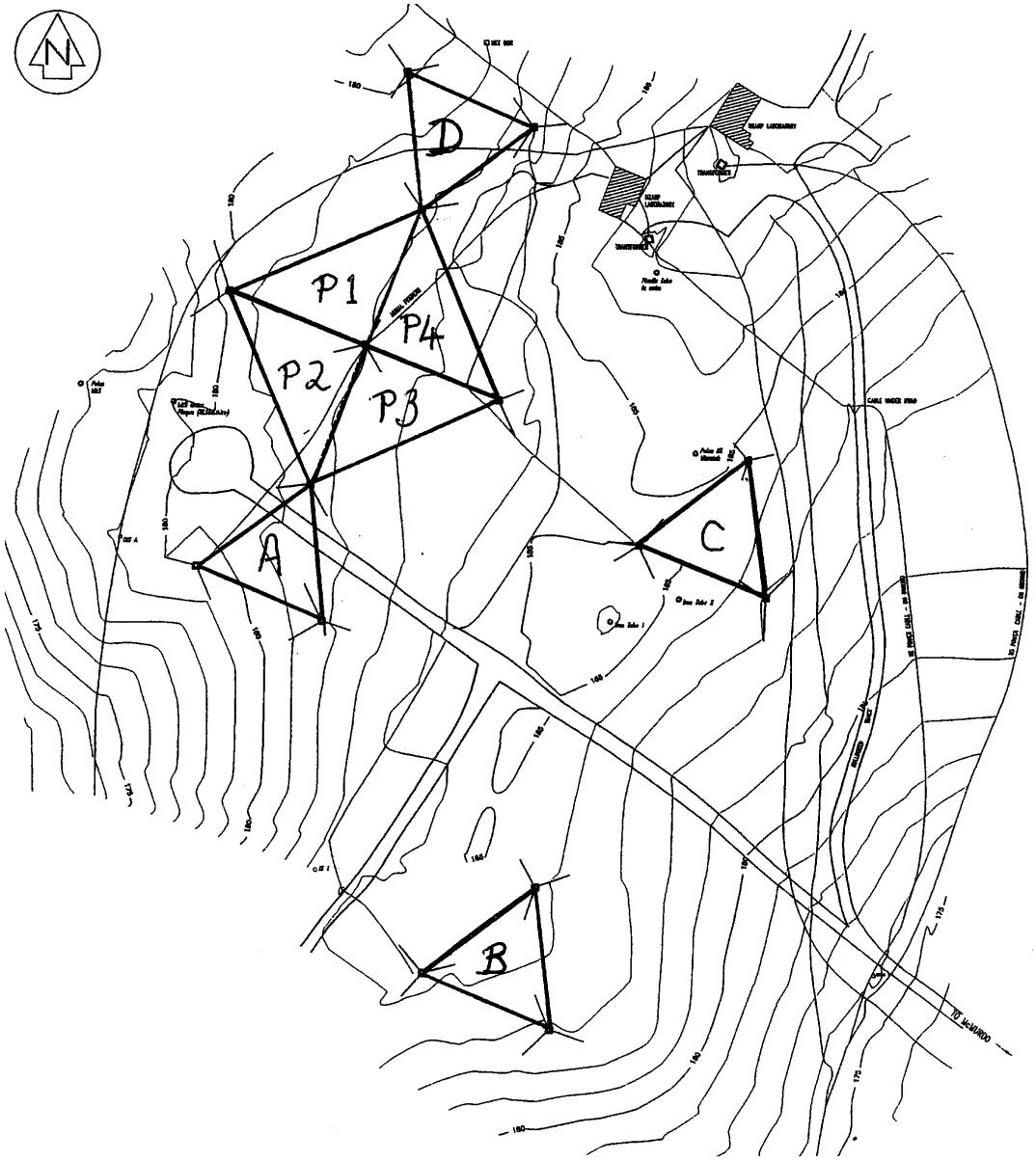

Figure 2.11: Layout of the receiving aerials of the MFSA radar at Arrival Heights. The currently employed aerials are labelled A, B, and C. Underlying map courtesy of Land information New Zealand.

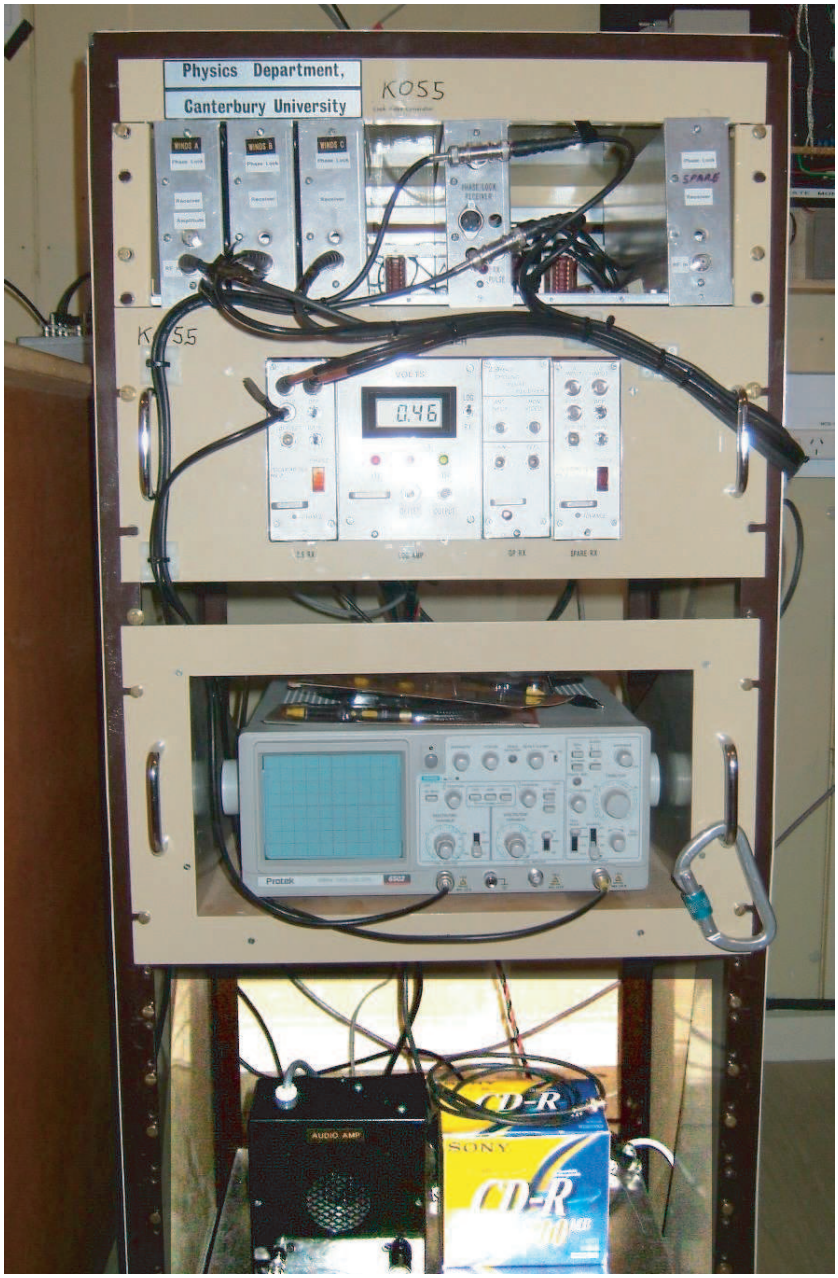

Figure 2.12: The rack in the Arrival Heights Laboratory containing the receivers (top), an oscilloscope (middle) and a speaker with an integrated audio amplifier (bottom).

partial reflections. The IDI technique treats signal returns from the mesosphere as reflections from individual scattering points. Because scatterers are too close to each other they cannot be resolved using beam-forming radars. However, the Doppler shifts of the scatterers can be found in Fourier space and allow the radial velocity of each scatterer to be determined. Interferometry with several spaced antennas can be used to identify the 3D locations of the scatterers. Combining the information about location and radial velocity allows the wind vectors to be calculated. The technique is described for example by Brosnahan and Adams (1993). Data from the IDI at Halley (75.8°S, 26.4°W) is used in combination with the Scott Base MFSA radar in chapter 5 for an investigation into the zonal structure of the semi-diurnal tide. The instrument is an upgraded dynasonde described in detail by Jones et al. (1997). The geographical position of the Halley IDI is also indicated in Figure 2.1.

2.3 Radio Occultation Measurements of Dry Temperature

The radio occultation (RO) of global positioning system (GPS) satellites is a relatively new and inexpensive technique for atmospheric measurements. The radio signal transmitted by GPS satellites is subject to refraction when it travels through the Earth's atmosphere. High-resolution profiles of atmospheric refractivity can be determined from precise measurements of the signal using a GPS receiver either on the Earth's surface or in low Earth orbit (LEO). From the refractivity measurements profiles of dry temperature can be inferred. When receivers onboard satellites in LEO are utilised the technique is referred to as radio occultation and global coverage can be achieved. Application of the RO technique to atmospheric measurements was already suggested in the 1960s (Fishbach, 1965) and was successfully employed on NASA missions (e.g. the Mariner, Pioneer, and Voyager series) to other planets in the solar system. Because a single transmitter and receiver would only generate a small number of profiles, it was not seen as a justifiable undertaking for measurements of Earth's atmosphere until the launch of GPS navigational satellites. The first mission for the RO remote sounding of Earth's atmosphere using GPS was the GPS-MET experiment on the Microlab 1 satellite which was put into orbit in April 1995. The success of the mission quickly lead to the inclusion of GPS receivers on other LEO missions such as Oersted, SUNSAT, CHAMP, SAC-C, MetOp-A, and the multi-satellite constellation FORMOSAT-3/COSMIC.

2.3.1 Technique

The RO technique employs receivers on low earth orbiting satellites to measure properties of signals transmitted by GPS satellites which have been affected

by atmospheric refractivity (Figure 2.13a). An occultation occurs whenever a GPS satellite rises or sets from the point of view of the receiver. The basic viewing geometry is depicted in Figure 2.13b. As seen in Figure 2.13b, RO is a limb-scanning technique and the relative motion between the satellites during an occultation leads to a vertical scan. The vertical gradient of the refractive index refracts the radio signal transmitted by the GPS satellite according to Snell's law. This leads to a bending of the ray of angle α. Hereby the contribution to the bending is largest at the tangent point of the planet because of the large vertical density gradient which leads to a similar gradient in the refractive index. By measuring the phase delay of the GPS signal at the receiver, the bending angle can be calculated. The refractive index can then be inferred, and then atmospheric parameters, most importantly temperature and electron density, can be calculated (see equation 2.1).

The following discussion of the RO technique is based on Hajj et al. (2002) and Kursinski et al. (1997). This is only intended to give the basic principles of RO and many important details, for example relativistic effects, have been omitted. GPS satellites transmit signals at two L-band frequencies (f_1=1575.42 MHz and f_2=1227.60 MHz) which are both amplitude modulated. The receiver measures the phase of both signals which can be written as:

$$L_k = -\frac{c}{f_k}\phi_k = \rho + \gamma_k + C^{\mathrm{tx}} + C^{\mathrm{rx}} + \upsilon_k \tag{2.22}$$

$$\gamma_k = \eta_k + d\frac{TEC_k}{f_k^2} \tag{2.23}$$

where

k	1 or 2 for f_1 and f_2, respectively
L_k	phase in distance
f_k	signal frequency
ϕ_k	measured phase
c	speed of light in vacuum
ρ	range between transmitter and receiver
d	a constant
TEC_k	integrated electron density along the signal path
C^{tx} and C^{rx}	transmitter and receiver clock error
υ_k	measurement noise

In order to find the atmospheric delay γ_k, the clock errors C^{tx} and C^{rx} need to be modelled as described in Hajj et al. (2002). Traditionally this is done using a technique termed double differencing where an additional non-occulting satellite must be visible by the receiver in LEO and a ground-based receiver must see both GPS satellites in a non-occulting view. Single differencing, which only uses an additional non-occulting satellite, is possible if the GPS Selective Availability mode is turned off. Zero differencing can be employed if the receiver clock is sufficiently accurate to allow it to be modelled completely.

(a)

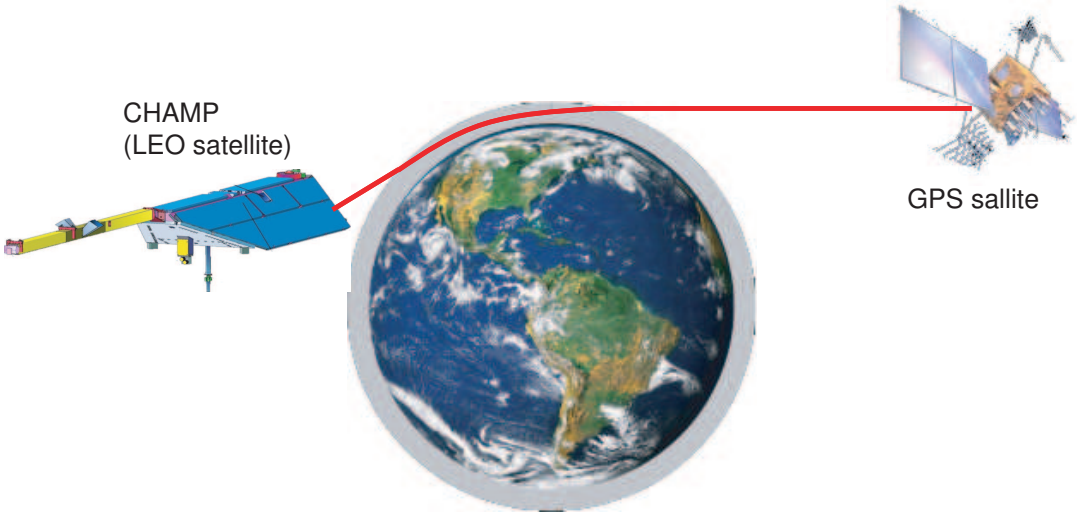

(b)

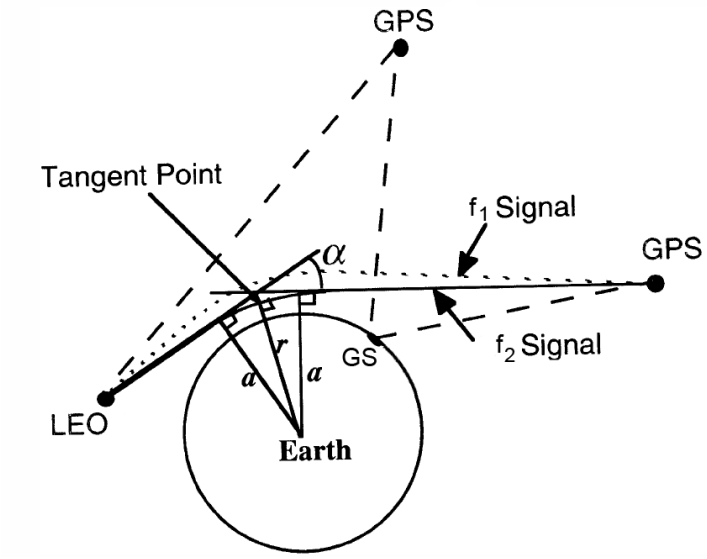

Figure 2.13: (a) Artist's impression of the GPS RO technique. The GPS satellite (top right) transmits signals (red line) which are bent by the Earth's atmosphere and reach a receiver (left) in a limb-sounding occultation. (b) Viewing geometry of RO for double differencing and definition of the asymptotic miss distance a.

The additional phase delay can also be understood as an additional Doppler shift. The receiving and transmitting satellite are moving with different velocity vectors, which leads to an expected Doppler shift in the absence of an atmosphere. The atmosphere bends the signal so it travels a different path which leads to a different Doppler shift, the measured Doppler shift. The Doppler shift is measured by forming the time derivative of the phase measurement. The atmospheric Doppler shift Δf_k, which is the difference between the expected and measured Doppler shift, can be expressed as

$$\frac{d\gamma_k}{dt} = \lambda_k \Delta f_k = [\mathbf{v}_{\text{tx}} \cdot \hat{\mathbf{k}}_{\text{tx}} - \mathbf{v}_{\text{rx}} \cdot \hat{\mathbf{k}}_{\text{rx}} - (\mathbf{v}_{\text{tx}} - \mathbf{v}_{\text{rx}})\hat{\mathbf{k}}] \tag{2.24}$$

where

λ_k	radio signal wavelength
$\mathbf{v}_{\text{tx}}$	transmitter velocity vector
$\mathbf{v}_{\text{rx}}$	receiver velocity vector
$\hat{\mathbf{k}}_{\text{tx}}$	direction of the transmitted signal (unit vector)
$\hat{\mathbf{k}}_{\text{rx}}$	direction of the received signal (unit vector)
$\hat{\mathbf{k}}$	unit vector with the direction from the transmitted to the receiver

The number of unknowns can be reduced by assuming spherical symmetry and equation 2.24 can be written as

$$\frac{d\gamma_k}{dt} = (v_{\text{tx}} \cos(\phi_{\text{tx}} - \delta_{\text{tx}}) - v_{\text{rx}} \cos(\phi_{\text{rx}} - \delta_{\text{rx}})) - (v_{\text{tx}} \cos\phi_{\text{tx}} - v_{\text{rx}} \cos\phi_{\text{rx}}). \tag{2.25}$$

The angles are defined in Figure 2.14 and the unknowns are now only δ_{tx} and δ_{rx}. Snell's law under spherical symmetry is known as Bouguer's rule (Born and Wolf, 1980) and can be written as

$$n_{\text{tx}} r_{\text{tx}} \sin(\theta_{\text{tx}} + \delta_{\text{tx}}) = n_{\text{rx}} r_{\text{rx}} \sin(\theta_{\text{rx}} + \delta_{\text{rx}}) = \text{constant} = a \tag{2.26}$$

for the geometry in Figure 2.14. It can be assumed that $n_{\text{tx}} = n_{\text{rx}} = 1$ and then equations 2.25 and 2.26 can be solved for δ_{tx} and δ_{rx}. The total atmospheric bending angle α is simply the sum of δ_{tx} and δ_{rx}. The asymptotic miss distance a can then be calculated from equation 2.26.

In order to derive properties of the neutral atmosphere alone it is necessary to remove effects due to the ionosphere. The bending angle is frequency dependent, so the usage of two frequencies by the transmitter and receiver yields two different bending angles. The ionospheric effects can be removed by combining the two bending angles:

$$\alpha(a_0) = \frac{f_1^2}{f_1^2 - f_2^2}\alpha_1(a_0) - \frac{f_2^2}{f_1^2 - f_2^2}\alpha_2(a_0) \tag{2.27}$$

where both profiles α_1 and α_2 have been interpolated onto the same vertical grid a_0.

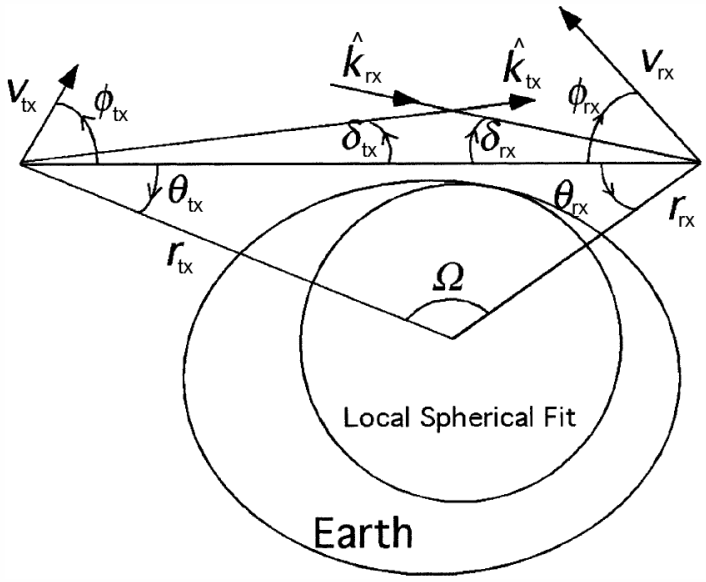

Figure 2.14: Geometry of the radio occultation technique, after Hajj et al. (2002).

The total bending of the signal induced by the atmosphere depends on the atmospheric refractive index n. Assuming spherical symmetry, the formula of Bouguer can be used to evaluate the integral

$$\alpha(a) = 2 \int_a^\infty \mathrm{d}\alpha \tag{2.28}$$

to

$$\alpha(a) = -2a \int_a^\infty \frac{1}{\sqrt{a'^2 - a^2}} \frac{\mathrm{d} \ln n}{\mathrm{d}a'} \mathrm{d}a'. \tag{2.29}$$

Equation 2.29 has to be solved for n which requires the integral to be inverted. This is performed using an Abel integral transform and yields

$$n(a) = exp \left[\frac{1}{\pi} \int_a^\infty \frac{\alpha(a')}{\sqrt{a'^2 - a^2}} \mathrm{d}a' \right]. \tag{2.30}$$

Finally, the equation for the refractive index, already given in equation 2.1 in section 2.1, is combined with the ideal gas law and the equation for hydrostatic equilibrium to derive atmospheric variables. In the simplest case, profiles of pressure and dry temperature are obtained by assuming the water vapour pressure e to be zero.

From Fresnel diffraction theory it can be shown that the basic processing technique described here leads to a true vertical resolution of approximately

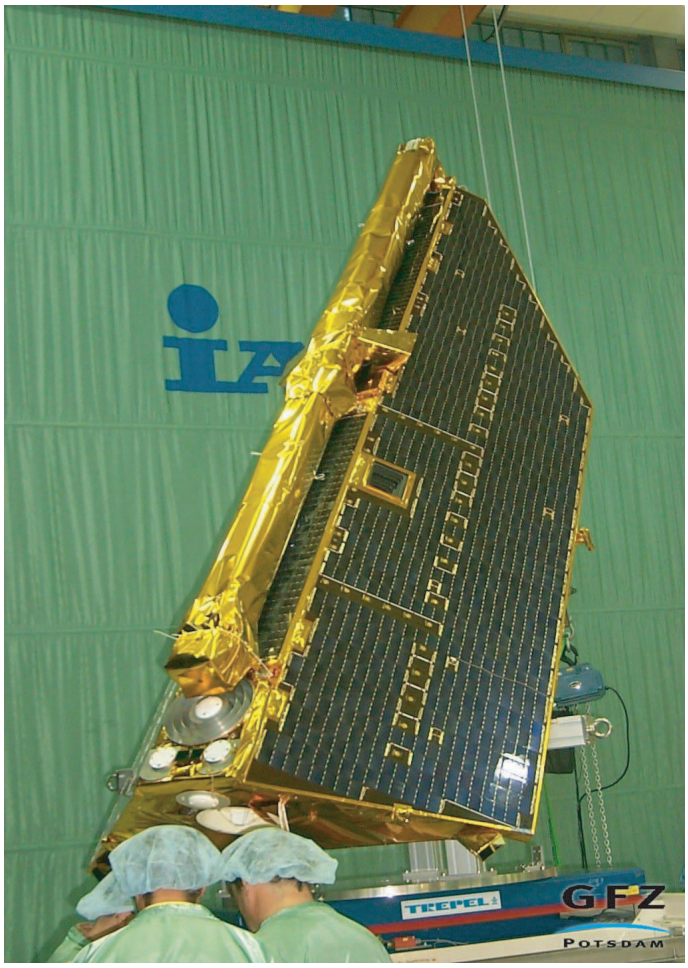

Figure 2.15: Photograph of the CHAMP satellite before launch, the GPS antenna array can be seen at the bottom. Photo courtesy of GFZ.

1.4 km in the stratosphere. The horizontal resolution of an occultation is 200–400 km along the line of sight (LOS) and of the order of 1 km across the LOS.

There have been several different suggestions to replace the basic processing technique but they are not widely used yet. Those concepts include the use of amplitude data and radioholographic methods but will not be discussed here.

2.3.2 The RO experiment aboard CHAMP

This thesis only considers data from the RO experiment on the CHAMP (CHAllenging Minisatellite Payload) satellite. CHAMP was launched on 15 July 2000, a photo of the satellite before launch is shown in Figure 2.15.

CHAMP has an inclination of 87° and orbited initially at approximately

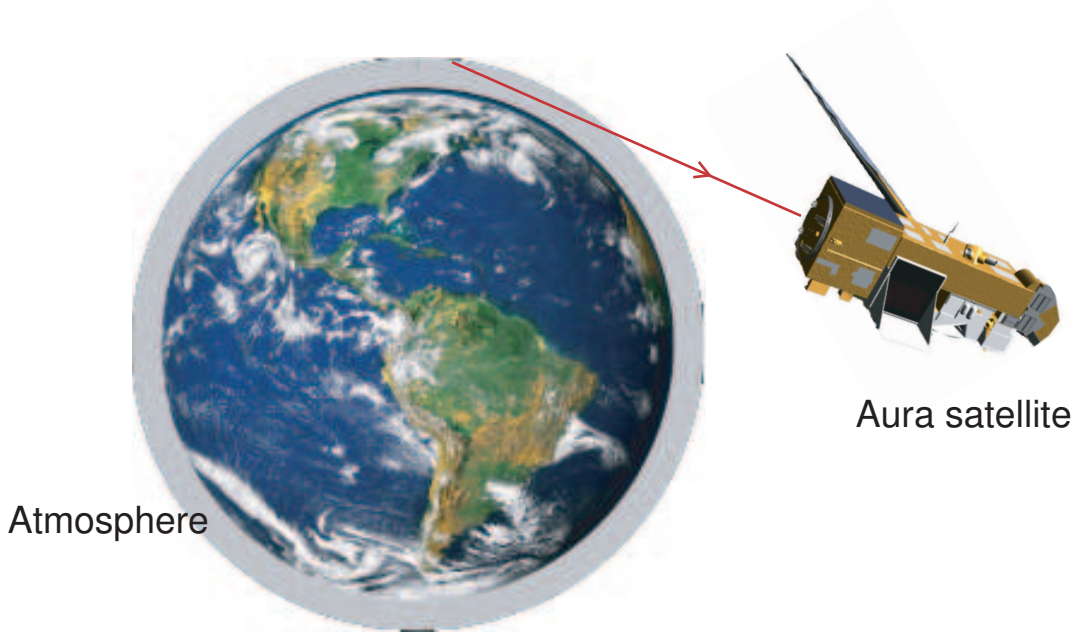

Figure 2.16: Illustration of limb viewing geometry employed by EOS MLS.

450 km altitude. The high inclination leads to a greater density of profiles at high latitudes. The instrument yields approximately 150–200 profiles of dry temperature each day. The geographical positions of the measurements on 25 May 2005 are marked as red crosses in Figure 2.1. More details and references regarding the RO experiment on CHAMP can be found in chapter 6.

2.4 Microwave Limb Sounding Satellite Observations of the Atmosphere

Microwave limb sounding is a remote sounding technique which uses thermal emissions with wavelengths in the millimetre and sub-millimetre region to infer atmospheric parameters. The geometry of limb viewing is illustrated in Figure 2.16. The instrument field of view is scanned with every sounding to obtain a complete vertical profile. Measurements can be made day and night with a high vertical resolution.

Profiles of atmospheric variables such as temperature, pressure, and the mixing ratio of various chemical species can be calculated from the calibrated radiances using retrieval theory (e.g. Rodgers, 2000; Livesey et al., 2006). Usually the standard "optimal estimation" approach is employed. Retrieval theory aims to determine the state of an atmospheric variable by calculating the best match using the observed radiances. A cost function describing the goodness of the fit

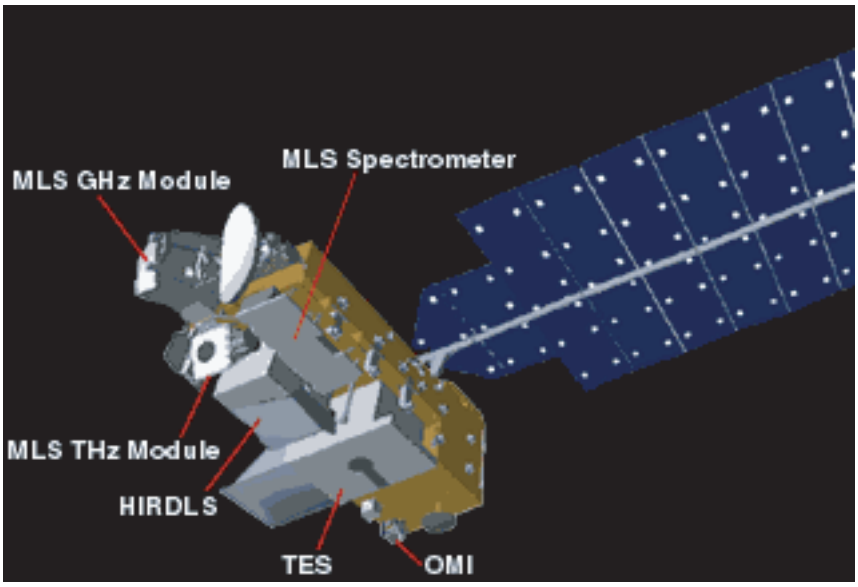

Figure 2.17: The Aura spacecraft (artist's impression) showing the different instruments.

to the observed radiances is optimised using nonlinear weighted least squares. In addition, *a priori* constraints are generally needed.

2.4.1 EOS MLS aboard the Aura satellite

The Earth Observing System Microwave Limb Sounder (EOS MLS) is one of four instruments on NASA's Aura satellite (Figure 2.17). Aura was launched on 15 July 2004 into an orbit with an inclination of 98° (a retrograde orbit) to 705 km altitude and flies in formation with the "A-Train", a collection of several other Earth observation satellites. The satellite orbits the Earth every 100 minutes and performs 240 scans per orbit. EOS MLS measurements cover 82°N to 82°S every orbit and yield concentrations of various constituents as well as temperature. The instrument is an advanced follow-on to the first MLS on the Upper Atmosphere Research Satellite (UARS) launched in September 1991 and decommissioned in December 2005.

EOS MLS covers five spectral regions in two broad categories, gigahertz and terahertz. Five heterodyne radiometers each cover a dedicated spectral region and have associated primary measurements but all yield additional measurements. A switch network distributes the signals to a total of 40 spectrometers of four different types with different bandwidths and spectral resolutions. Measurements are processed using retrieval algorithms based on optimal estimation theory as described above. An overview of the MLS instrument is given by Waters et al. (2006), the MLS retrieval algorithm is described in Livesey et al. (2006) and the

details of the forward model can be found in Read et al. (2006) and Schwartz et al. (2006).

In this thesis, the temperature, ozone and hydroxyl products are employed. Temperatures between 316 and 0.001 hPa are obtained from radiance measurements of O_2 at 118 GHz. Ozone (O_3) volume mixing ratios are measured at 240 GHz and the hydroxyl radical (OH) is measured at 2.5 THz.

The vertical resolution of the temperature product decreases throughout the stratosphere and mesosphere, starting at 4 km and decreasing to 9 km at 0.1 hPa. The first published validation study by Froidevaux et al. (2006) states precisions of 0.5 K to 2 K and reports a warm bias of between 1 and 2 K when compared with other satellite and balloon measurements in the stratosphere. The vertical resolution of O_3 is given to be 6 km in the mesosphere and the useful range of measurements is stated to be 215–0.46 hPa, but there is "clearly good O_3 sensitivity into the upper mesosphere" (Livesey et al., 2005). Therefore, data is presented up to 0.046 hPa. However, it has to be noted that a problem with the retrieval sometimes yields negative volume mixing ratios above 0.46 hPa. As we are only interested in changes of the concentration and not the absolute value, the data was used in the provided form for the present analysis. The precision of single ozone profiles up to the lower mesosphere is stated to lie between 0.2 and 0.4 ppmv or between 2% and 15% (Froidevaux et al., 2006). A comparison with *in situ* measurements during balloon flights showed quite good agreement. A tendency to slightly higher MLS ozone values in the lower stratosphere and slightly lower values in the upper stratosphere was found in comparisons with ozone data from other satellites.

In the case of OH the upper boundary for very good quality measurements is stated to be 0.22 hPa, but the top recommended level is 0.001 hPa. Above 0.1 hPa the vertical resolution is 5–6 km (Livesey et al., 2005). Pickett et al. (2006) assessed MLS OH accuracies by comparing the data to measurements from balloon-borne instruments and to the output of a constrained photochemical model. On average, the balloon measurements of OH agreed with MLS within 17% over 25-40 km and the measurements agree with the model within 12%. Above 40 km OH was only validated in the form of OH columns where differences of up to 12% were reported.

The geographical positions of profiles measured on 25 May 2005 are included in the map in Figure 2.1. They are indicated by blue '+' markers.

2.5 Reanalysis and Assimilation Data Sets

Global data sets for basic atmospheric variables can be computed using combinations of available observational data and atmospheric models with a technique

called assimilation. The model is fitted to observed data, so the model ensures that the analysed fields are physically self-consistent. Modern assimilations use a technique called variational analysis to find the model representation which is most consistent with the observations. Variational analysis involves minimisation of a cost function similar to retrieval theory, see e.g. Lorenc et al. (2000). The assimilation technique allows data of many different types, for example satellite soundings, radiosondes and aircraft data, to be included in the analysis. While the model is being integrated forward in time, the model state is nudged towards observed values and the observation weights take into account the expected accuracy of each observation type.

2.5.1 The NCEP/NCAR Reanalysis

The NCEP/NCAR reanalysis is based on the NCEP global spectral model operational in 1995. The model has a 3-dimensional variational analysis scheme cast in spectral space and includes 28 vertical levels from the ground to 3 hPa. A large range of physical processes is represented in the form of parameterisations. The assimilated observations are upper air rawinsonde observations of temperature, horizontal wind, and specific humidity, operational vertical temperature soundings from NOAA polar orbiters, cloud tracked winds from geostationary satellites, aircraft observations of wind and temperature, land surface reports of surface pressure, and oceanic reports of surface pressure, temperature, horizontal wind, and specific humidity. The final NCEP/NCAR reanalysis product has a horizontal resolution of 2.5° latitude by 2.5° longitude and covers the whole globe. In the vertical, 17 pressure levels from 1000 to 10 hPa are available. The data is available as 6-hourly or daily means. More details about the project can be found in Kalnay et al. (1996).

2.5.2 The UK Met Office Stratospheric Assimilated Data

The forecast model at the heart of the UK Met Office (UKMO) assimilation is the Met. Office Unified Model. For the stratospheric analysis, the model is run with a vertical coverage from the Earth's surface to above the stratopause. The model is a global primitive equation model, with a split-explicit time integration scheme. Similar to the NCEP/NCAR reanalysis, it employs a 3-dimensional variational data assimilation system since November 2000. In October 2003 the model was changed to a non-hydrostatic model which uses a semi-Lagrangian dynamical core which allowed a greater vertical extent. The model also incorporates a comprehensive range of physical parametrisation schemes.

The assimilated data is essentially the same set of meteorological observations as are used for operational weather forecasting. For the stratosphere, the most important observations are data from the NOAA polar orbiters and radiosonde

soundings. The final output fields are daily means of the vertically interpolated fields from the model data. Until 27 October, 42 model levels were interpolated to 22 pressure levels from 1000 hPa to 0.316 hPa (approximately 55 km). From 28 October 2003, 50 model levels were available and the output was extended by 3 levels to 0.1 hPa. In the horizontal the data fields are on the grid used by the numerical model which has a resolution of 2.5° latitude by 3.75° longitude. The model uses a staggered grid so that wind fields are stored on different points from the other fields. The provided fields are the three components of the wind, geopotential height and temperature.

The Met. Office states temperature RMS errors of 1.0 K at up to 10 hPa increasing to 2.0 K at 1 hPa. The horizontal wind components have errors of 6.0 m/s at 100 hPa, 8 m/s at 10 hPa, and 12 m/s at 1 hPa. Geopotential height errors increase from 20 m at 100 hPa to 100 m at 1 hPa. More details on the middle atmosphere data quality can be found in Swinbank et al. (1998). A description of the variational data assimilation used in the Unified model is presented in Lorenc et al. (2000).

Chapter 3

High Resolution Wind Measurements in the Upper Mesosphere and Lower Thermosphere with the Scott Base Medium-Frequency Radar[1]

Medium-frequency spaced antenna (MFSA) radars in conjunction with other ground-based and satellite techniques significantly contribute to our understanding of the wave driven dynamics of the middle atmosphere. Current areas of research include for example interannual variations, wave breaking, and nonlinear interactions of waves with each other and the background wind. At present, there are about 15 operational MFSA radars in the world. The Department of Physics and Astronomy at the University of Canterbury operates a MFSA radar at Scott Base (78°S, 167°E), Antarctica. The radar technique and the specifics of the instrument at Scott Base have been described in chapter 2. In general, the number of instruments that observe the middle atmosphere is far greater in the northern hemisphere than in the southern hemisphere which attributes great importance to the Scott Base radar. The instrument was upgraded significantly as part of the work for this thesis in order ensure the continued operation of the radar and to enhance its capabilities. The radar has been measuring wind velocities since 1982 and the data set is therefore invaluable for studies of interannual variations which will be discussed in chapter 4. This means that continued operation is highly desirable for future research, but this is only possible if obsolete parts of the system are upgraded frequently. At the same time, the performance of the radar can be improved to pursue new research aspects. In the case of the upgrade performed as part of this thesis, it was aimed at enabling the instrument to observe a greater part of the gravity wave spectrum. Ultimately, this will allow us to enhance our understanding of gravity wave properties which is one of the goals of this thesis. The necessary instrument improvements were achieved by increasing the time resolution, by reducing the amount of dead time of the data collection,

[1]This chapter has in a similar form been submitted and accepted as a contribution to the proceedings of the Electronics New Zealand Conference (ENZCon) 2006 and was co-authored by A. J. McDonald and G. J. Fraser at the University of Canterbury.

and by enhancing the accuracy of individual wind velocity measurements. As expected, the upgrade has led to significant improvements in the derived wind data quality and quantity.

This chapter presents details of the upgrade of the control and data acquisition system that was carried out in December 2004. Section 3.1 gives a description of the new hardware and software installed since December 2004, followed by a discussion of the advantages of the new system in section 3.2 which includes a comparison of the data before and after the upgrade. Appendix A of this thesis presents a technical documentation of the radar control and data collection software that was designed as part of this work.

3.1 The New Control and Data Acquisition System

While for many decades MFSA radars were in-house developments of universities and research institutes, they are now also commercially available. Currently MFSA radars are produced by ATRAD (Atmospheric Radar Systems), Genesis Software Pty Ltd, and MARDOC (Modular Antenna Radar Designs Of Canada). However, all radars operated by the University of Canterbury have been designed, built, and maintained by research and technical staff at the Department of Physics and Astronomy. The MFSA radar at Scott Base, which was installed in late 1982, has been upgraded every few years (see chapter 4). Advances in computer technology and faster data acquisition cards have always been the main drivers of improvements of MFSA radars, this also applies to the most recent upgrade of the Scott Base radar in December 2004. The central piece of this upgrade are the data acquisition card, a DATEL PCI416-L, and a personal computer using an Intel Pentium 4 processor. The DATEL card offers higher precision (12 bits) than the previous systems (up to 8 bits) and allows simultaneous sampling on up to 16 channels at a maximum sampling rate of 190 ksamples/s. The card can be configured to generate trigger pulses with no limitations on the repetition frequency. Limiting factors for the pulse repetition frequency are the transmitter design, the speed of the data processing, and the physical problem of multiple-time-around echoes. The software that controls the transmitter and the data acquisition system is an in-house development and incorporates an adapted form of the FCA algorithm described in chapter 2. It is written in Visual C++ 6.0 and runs under a Windows XP environment. The FCA algorithm is based on previous FORTRAN versions. A major advantage of the new system is its multi-threading capability which means that measurements continue to be made while the wind velocities are calculated from 1 minute blocks of data. This was not possible with the previous data acquisition system. Hard disks are now large enough to store at least 6 months worth of raw MFSA radar data which amounts to approximately 200 gigabytes. Therefore the current Scott Base system saves the in-phase (I) and quadrature (Q) raw data derived from the three phase sensitive detectors in

addition to the calculated wind velocities. It is hoped that the I and Q data can be used later for refinement of the processing algorithm and initial results will be presented in the next section.

Figure 3.1 depicts a schematic overview of the upgraded radar. The transmitter (TX) and the transmitting antenna are located next to the buildings of Scott Base. The receiving antennae, the receivers (RX) and the computer are at the Arrival Heights laboratory, approximately 5 km away from Scott Base. A timing diagram of the operation is shown in Figure 3.2. The DATEL card currently creates a trigger pulse every 50 ms (20 Hz) which is a major advancement over pulse repetition frequencies of 8 Hz and less that were used in the past and has led to large data quality improvements. Each pulse is amplified by a line-driver and sent to Scott Base (see Figure 3.1). Optocouplers solve problems associated with a 70 V ground difference of the power supply mains between Arrival Heights and Scott Base. This pulse then leads the transmitter to generate a pulse at 2.9 MHz with a pulse length of 30 μs using vacuum tubes. The signal has a peak power of 100 kW and is fed into the transmitting aerial. The largest signal received by the antennas at Arrival Heights has travelled the direct path and is called the ground pulse (see Figure 3.2 bottom). The ground pulse acts as a phase reference for the coherent receivers which are then able to extract I and Q information from the ionospheric reflections of the signal. The signals from all receivers are fed into the DATEL data acquisition card (see Figure 3.1) which provides the analogue-to-digital conversion and transfers the data from the card's FIFO (first-in-first-out) memory to the PC's kernel memory via direct memory access (DMA). Each pulse is sampled at 150 kHz (see Figure 3.2) to provide a height resolution of 1 km. The sampling of each pulse is carried out for approximately 1 ms so that signals from up to the lower thermosphere can be received. Note that group retardation due to increased electron density above approximately 95 km creates differences between virtual and real heights, which means that data above this level is not generally utilised.

Figure 3.3a depicts the sampled output from one channel of one receiver for the duration of the echo of a single pulse (approximately 1 ms). The amplitude of the signal as recorded by one antenna is reconstructed by calculating $\sqrt{I^2 + Q^2}$ and is depicted in Figure 3.3b. The ground pulse at the start of the sampling sequence can be identified easily. Below approximately 70 km the reflections of the signal are very weak because electron density variations are small in that region. However, strong reflections from electron density variations can be seen above that altitude. Note that between 10 and 55 km no signal is saved in order to conserve disk space. When 1200 pulses have been recorded, the FCA algorithm processes this data to calculate wind velocities while the next block of pulses is being collected (Figure 3.2a).

A flowchart for the control of the data acquisition card and the data processing is shown in Figure 3.4. Two DMA buffers are used in order to allow simultaneous

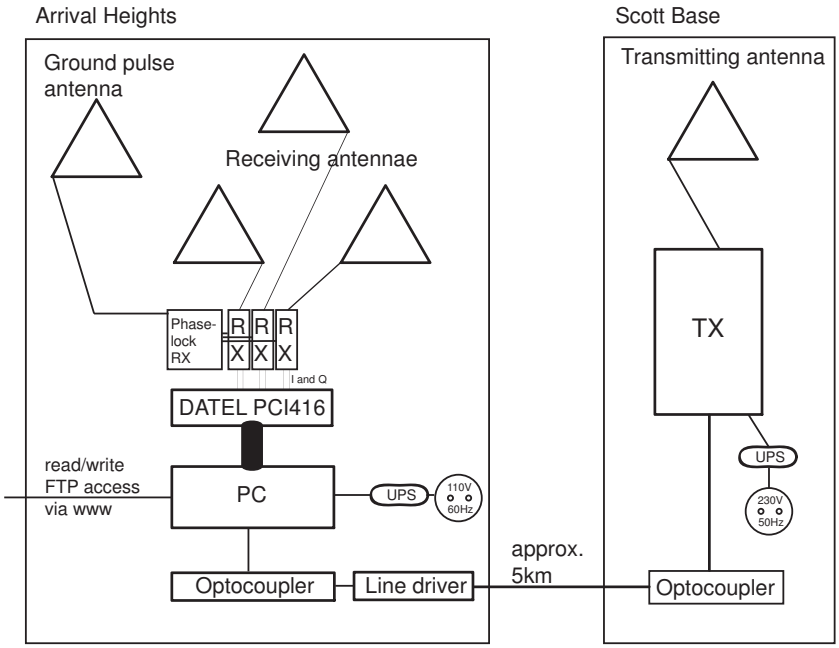

Figure 3.1: Schematic of the MFSA radar at Scott Base, Antarctica.

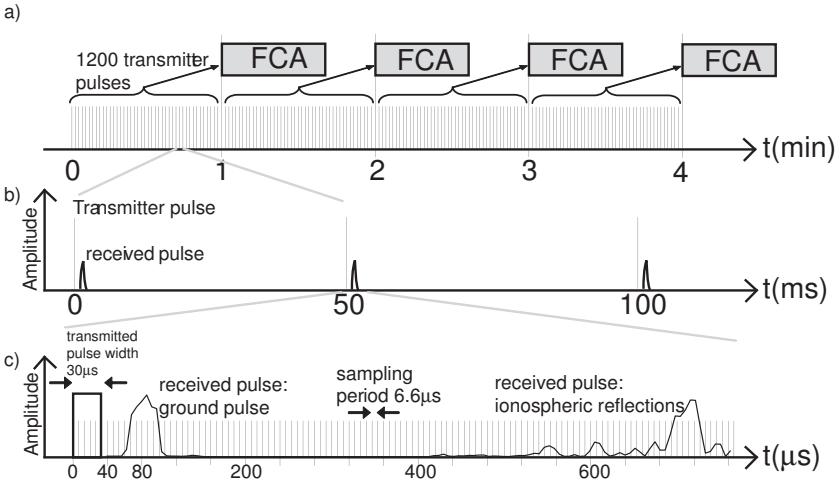

Figure 3.2: Timing diagram of the current operation of the Scott Base radar.

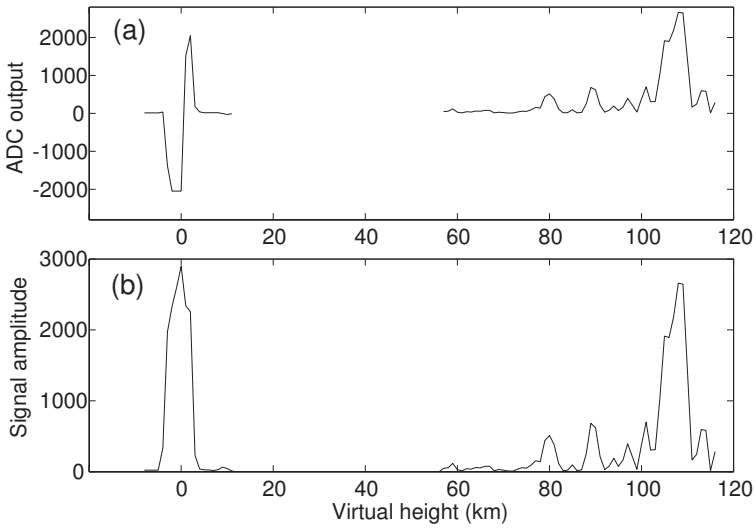

Figure 3.3: (a) Raw receiver output from channel 3. (b) Reconstructed signal from antenna 2 (channel 3 and 4) at 28/12/2004 23.02:46 NZST.

data acquisition and processing. While new data is written to buffer number 1 the data from buffer number 2 can be accessed and processed. When buffer number 1 is full, new data is written to buffer number 2 and the recently acquired data from buffer number 1 is processed. This technique allows for continuous data acquisition. The MFSA software collects data for 1 minute before swapping buffers and then copies the data into memory space that is directly accessible to the software. From there it is saved to hard disk in the NetCDF format (Rew and Davis, 1990) and copied into a data structure that is suitable for processing by the FCA algorithm. The FCA is then performed and the results are displayed on the screen and saved to the hard disk in text files. The processing takes less than 1 minute and the software then waits until the next buffer is ready for processing. Figure 3.5 provides a screen-shot of the running control- and acquisition software. The top panel displays the I and Q data and can be used to identify if all aerials and receivers are working properly. The bottom half of the window displays results from the FCA algorithm. The main control of the radar (Start/Stop/Change parameters) can be found on the right hand side of the screen.

The PC at Arrival Heights is connected to the world-wide-web via the satellite connection of Scott Base and runs an FTP (File Transfer Protocol) server. This allows us to fetch the data frequently and to deploy new versions of the processing software. A server at the University of Canterbury downloads a new data file every hour and prepares the data for display on the website

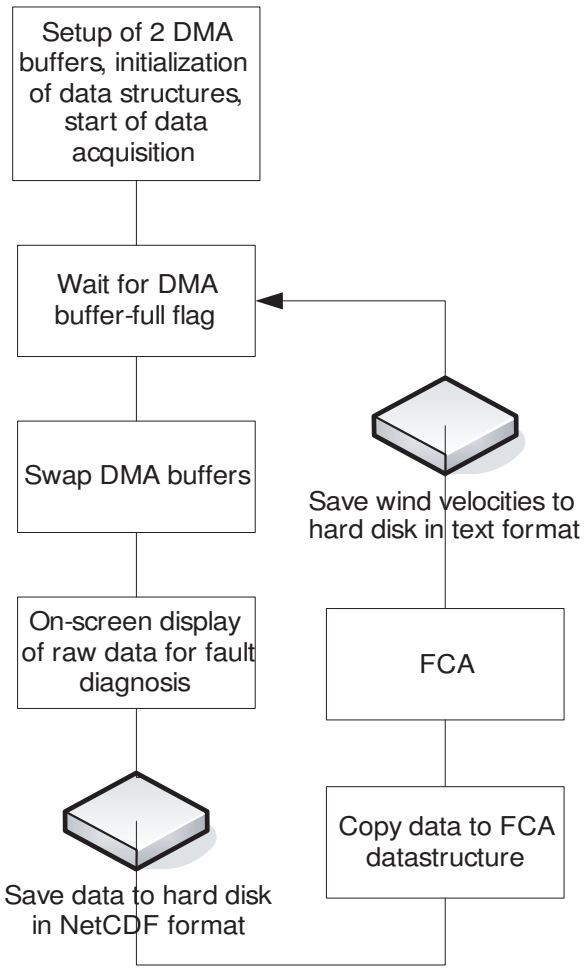

Figure 3.4: Flowchart of the MFSA software.

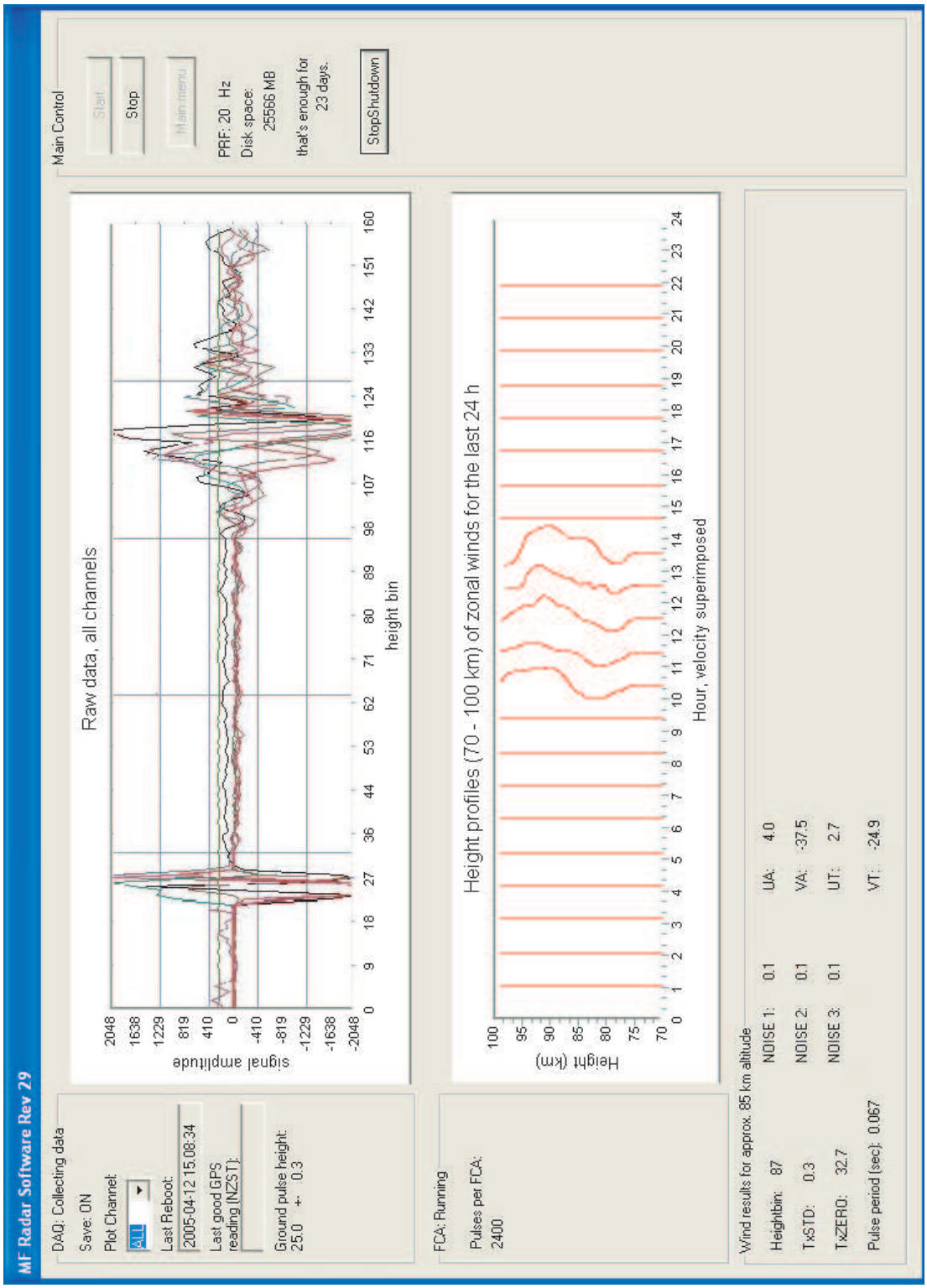

Figure 3.5: Screenshot of the radar software.

http://www2.phys.canterbury.ac.nz/∼physatmo. The software update process is initiated by setting a stop-flag in a file which is checked by the software every five minutes. If the flag is true, the software shuts down and the executable file can be overwritten with a new version. A reboot flag in a file is then set causing an additional tool on the Arrival Heights computer to initiate a reboot. On startup the new software version is loaded and starts the transmitter and the data acquisition.

3.2 Results and Discussion

The data quality of the Scott Base MFSA radar has continuously improved over the last 24 years. However, when comparing the most recent data with data from different periods since 1982 it becomes evident that the upgrade described here was one of the biggest single improvements in the radar's history. Figure 3.6a depicts raw velocity data from one day in 2004 before the upgrade. Every circle represents one measurement in the east-west direction, the shading indicates the measured velocity. Positive values denote eastward velocities, negative values denote westward velocities. Occasionally the FCA algorithm can produce unrealistic velocities which need to be removed before the data is processed further. Note that no outliers have been removed in Figure 3.6. The depicted day is representative of times when the radar was performing well. Several oblique stripes of large westward (dark grey/black) and eastward (light grey/white) velocities can be identified, which are due to the atmospheric semi-diurnal tide generated by solar heating of ozone and water vapour in the lower atmosphere. Figure 3.6b shows 24 hours of data from two years later when all the described modifications were in place. It can be seen that the number of data points has greatly increased from approximately 1400 measurements to over 20,000 or by a factor of about 15. This factor is representative of the average increase in data quantity if two periods where the radar was not experiencing technical problems are compared.

As mentioned above, the system now has the capability to save the raw I and Q data for processing at a later stage. This can be used to test different parameters for the FCA algorithm or compare different analysis techniques. An initial study identified that modification of the FCA block length and a quality control threshold could improve the system's performance. One wind measurement is obtained from every FCA block, and a FCA block length of five minutes had been used since 1987. However, our analysis in late 2005 showed that shorter blocks would increase the quality of each measurement. One minute was found to optimise the performance and therefore data collected in 2005 was re-processed offline to yield one minute resolution winds. In addition, it was found that a quality control threshold which rejects measurements where lag 2 of the auto-correlation function falls below a certain value had been chosen too conservatively in the past and was reduced significantly. This modification increased the quantity of wind

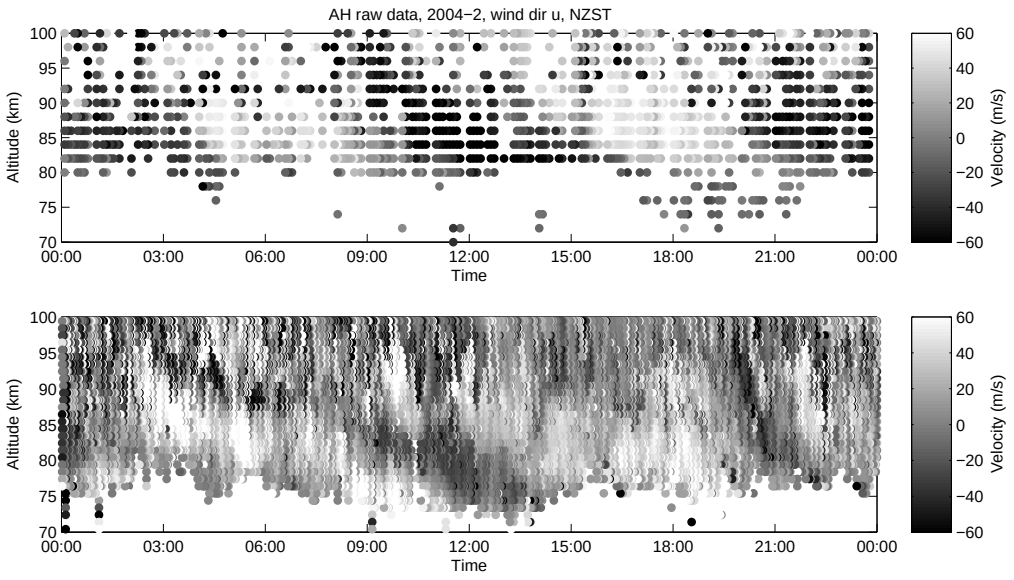

Figure 3.6: Zonal component of raw velocity data for 19 February 2004 before the upgrade in 2004 (a) and 2 September 2006 after the upgrade (b).

measurements especially at altitudes below 80 km.

The specifications of the new Scott Base radar system are similar to state-of-the-art commercial systems, with the exception of saving and reanalysing large amounts of raw I and Q data which is not employed by other MFSA radar systems to the author's knowledge. The new generation MFSA radars by ATRAD use 12 bit data acquisition cards, whereas Genesis offers 16 bit. The new systems also offer coherent receivers and some degree of remote control. A comparison of the Scott Base radar's data quality and quantity with other radars is subject to future work, although care has to be taken as geophysical effects have a large impact on data quality and quantity.

3.3 Conclusions

A new generation MFSA radar is now in operation at Scott Base, Antarctica, after major upgrades in December 2004, followed by some further improvements. The main features of the new system are its high precision (12 bit), its increased pulse repetition frequency (20 Hz), continuous data acquisition, and raw data storage. This was made possible by the installation of a new data acquisition card, a DATEL PCI416L, a new PC and multi-threading software. In addition, faults can be detected more easily because the measurements can be accessed from New Zealand using FTP. Using the same connection, operational parameters or the entire software package can be upgraded remotely if necessary. The new

possibility to save raw I and Q data has been exploited and parameters of the FCA algorithm were significantly improved. When comparing the old raw data with the new data it becomes evident that the quality and quantity have improved drastically; the number of velocity measurements has increased by a factor of 15.

These improvements open up many new possibilities for future studies with this radar, for example the study of high-frequency gravity waves. The data would be especially suited for the study of interactions between planetary waves, tides and gravity waves, using advanced techniques such as Empirical Mode Decomposition (McDonald et al., 2007). Wave interactions are an area of ongoing research with many open questions (Fritts and Alexander, 2003, and references therein). Originally, it was planned to pursue work on wave interactions for this thesis, but because of time constraints this was unfortunately not possible. In addition, gravity wave sources and propagation throughout the middle atmosphere was planned to be examined by using gravity wave information from the stratosphere and mesosphere. Because of the importance of momentum transport by gravity waves for the general circulation, an understanding as well as quantitative information on gravity wave propagation is needed for example for general circulation models (Fritts and Alexander, 2003). For this, mesospheric gravity wave data from the new Scott Base MFSA radar can be combined with stratospheric data sets. Radio occultation experiments are a relatively new and exciting technique that deliver temperature profiles up to at least 35 km altitude and can be used to obtain gravity wave information. A climatology of gravity wave activity, sources, and mean-flow interactions will be presented in chapter 6. However, the comparison of the stratospheric and mesospheric data sets to deduce wave propagation properties throughout the middle atmosphere has to be left for future work because of the limited amount of time available. Note that work with a similar objective is now underway at the British Antarctic Survey (R. E. Hibbins, personal communication); their analysis focuses on radiosonde and MFSA radar data at a single site (Rothera).

Due to problems with the line driver during the winter of 2005 there is no data available for several months. In winter 2006 a broken aerial meant that no data was collected in June and July. However, parts of the new data set are included in chapter 7 for the study of planetary waves.

Chapter 4

Long-term Observations of Mean Winds and Tides in the Upper Mesosphere and Lower Thermosphere above Scott Base, Antarctica[1]

The medium-frequency spaced antenna (MFSA) radar at Scott Base (78°S, 167°E) has been measuring winds in the upper mesosphere and lower thermosphere region since December 1982. It is ideally suited to further our understanding of the wave-driven dynamics in this area of the atmosphere. Previous work related to this instrument focused on only small portions of the larger data set. The present study examines seasonal as well as interannual changes of monthly mean wind velocities and tidal amplitudes from 1982 to 2004. Changes in the full data set with respect to phenomena associated with multi-year periods, namely the quasi-biennial oscillation (QBO) and the solar cycle, and long-term trends are discussed. Processes that could lead to explanations for the observed seasonal and interannual variations are discussed.

4.1 Introduction

Radar wind observations of the mesosphere and lower thermosphere (MLT) have been made since the late 1950s. Long-term studies have the aim to provide a sound climatology and information about interannual variability. Climatologies are now available from many stations, giving a reasonably consistent picture of the prevailing winds (hereafter termed mean wind, zonal wind, or meridional wind) and tides in the MLT region. However, reliable data that spans at least two solar cycles and could be used for examination of the effect of multi-year periodicities and climate trend studies is rare. Table 4.1 presents an overview of MLT wind observations worldwide. It only includes instruments which have been

[1]This chapter has in a similar form been published in the Journal of Atmospheric and Solar-Terrestrial Physics (Baumgaertner et al., 2005). It was co-authored by A. J. McDonald, G. J. Fraser and G. E. Plank at the University of Canterbury.

Table 4.1: Overview of sites of long-term observations of winds in the mesosphere and lower thermosphere worldwide. Instruments: ionospheric drift measurements (D1: total reflection, PR: partial reflection), ionised meteor trails (D2).

Station, Instrument	Location	Period	References
Heiss Island, D2	81°N, 58°E	1965-1985	Portnyagin et al. (1993b), Portnyagin et al. (1993a)
Obninsk, D2	55°N, 38°E	1964-1995	Portnyagin and Solovjova (2000)
Kühlungsborn, D1	54°N, 12°E	1964-1994	Bremer et al. (1997)
Kühlungsborn, D2	54°N, 12°E	1976-1994	Bremer et al. (1997)
Saskatoon, PR	52°N, 107°W	1979-1988	Namboothiri et al. (1993)
UK, D2	52°N, 2°W	1988-2000	Middleton et al. (2002)
Collm, D1	51°N, 13°E	1964-1994	Bremer et al. (1997)
Atlanta, D2	34°N, 84°W	1975-1986	Bremer et al. (1997)
Adelaide, PR	35°S, 138°E	1984-1995	Vincent et al. (1998)
Christchurch, PR	44°S, 173°E	1978-1986	Fraser (1990)
		1987-2003	unpublished
Molodezhnaya, D2	68°S, 45°E	1967-1986	Portnyagin et al. (1993b), Portnyagin et al. (1993a)
Scott Base, PR	78°S, 167°E	1982-1984	Fraser (1989)
		1985-2004	present study

operating over a period spanning at least one solar cycle. A number of authors have analyzed MLT wind measurements for signatures of multi-year oscillations, the most common long-term periodicities being the eleven year solar cycle and the quasi-biennial oscillation (QBO). In addition, it has been suggested that the mesosphere, in particular the polar mesosphere, should be a sensitive indicator for long-term global changes in the atmosphere (Thomas, 1996). Thus, efforts are made to identify trends in long-term data sets. The purpose of this chapter is to first present an updated climatology of the Scott Base MFSA radar mean wind and tidal amplitude data. The second purpose of this chapter is to examine the seasonal interannual variability in the data set for multi-year periodicities and trends.

The most common multi-year periodicity examined in the MLT winds is the 11 year solar cycle. Most studies focusing on the relationship between the solar cycle and MLT winds have found a negative correlation between solar activity and tidal amplitudes. However, the relationship between the prevailing wind and solar activity is less clear. The earliest publication to discuss the influence of solar activity on MLT region winds was by Sprenger and Schminder (1969) who examined LF radar data from 1957 to 1968. They found that the mean zonal and meridional winds in winter in Central Europe are positively correlated with solar activity. A negative correlation with solar activity was found for the semi-diurnal tide. These results were confirmed by Dartt et al. (1983) who used observations from additional sites.

Using LF and meteor radars in Kühlungsborn and Collm for a longer period Greisiger et al. (1987), found positive and negative correlations between zonal winds and solar activity depending on the period employed. However, the semi-diurnal tide still displayed a negative correlation with solar flux density data. Later analysis by Jacobi et al. (1997b) using the same data sets found no dependency of mean winds or tides on the solar cycle. Their study indicated that the correlation depended on the period used and they proposed longer period oscillations to explain this behaviour. Bremer et al. (1997) found weak negative dependence of zonal wind and semi-diurnal tidal amplitudes for several northern hemisphere sites.

A number of other studies using shorter periods (less than two solar cycles) have also examined the effect of solar activity on MLT winds. With data from the MFSA radar at Saskatoon from 1974 to 1991, Namboothiri et al. (1993) and Namboothiri et al. (1994) found a positive correlation between the solar cycle and zonal winds, and a negative correlation for the semi-diurnal tidal amplitude. However, the significance levels indicated in both studies were small. Using meteor radar observations from 1988 to 2000 over England, Middleton et al. (2002) could infer a correlation between mean winds and solar activity, but it depended on the season. Fahrutdinova et al. (1997) also reported a strong correlation between the annual amplitude of the prevailing zonal wind and solar activity for nine years worth of mid-latitude data. Thus, a relatively large number of studies based on the analysis of data from northern hemisphere sites have shown a relationship between solar activity and MLT winds or tidal amplitudes.

Southern hemisphere observations at 44°S, described by Fraser (1990), showed no solar cycle dependency of the mean zonal wind but possibly a decreasing semi-diurnal tidal amplitude with decreasing solar activity. The significance of this trend was relatively low given the limited amount of data used in the study. An earlier study by Fraser et al. (1989) involving observations from four radars at northern and southern mid-latitudes concluded that a positive correlation for the semi-diurnal tidal amplitude existed during southern hemisphere summers. However, the observational evidence for the relationship between the solar cycle and MLT winds is much weaker in the southern hemisphere than the northern hemisphere.

Evidence of the effect of other multi-year periodicities on MLT dynamics has also been found. The quasi-biennial oscillation (QBO) dominates the variability of the equatorial stratosphere and is easily seen as downward propagating easterly and westerly wind regimes in the stratosphere, with a variable period of approximately 28 months. The QBO is a fascinating example of a coherent, oscillating mean flow that is driven by propagating waves with periods unrelated to that of the resulting oscillation. Vincent et al. (1998) displayed evidence of strong interannual variability in the diurnal tide at three tropical stations, with the effect being strongest at Adelaide at the March equinox. Comparisons with

the phase of the QBO show that the amplitudes are larger (weaker) than the 12 year average when the winds are predominantly eastward (westward). Gurubaran and Rajaram (1999) also presented results which clearly indicate pronounced interannual variability in the tidal activity over Tirunelveli (9°N) which are linked to the stratospheric QBO. Their study indicates that the principal factors in producing the QBO modulation appear to be the variabilities associated with tidal forcing and the interaction with the stratospheric winds, with gravity wave–tidal interactions also being expected to contribute. It should be noted that while these studies have indicated the impact of the QBO on the tropical tidal amplitudes, work by Jarvis (1996) also indicates that a similar impact can be observed in the Antarctic lower thermosphere.

A summary of trends for mean winds and tides can be found in Bremer et al. (1997). They conclude that zonal mean winds experience a trend towards smaller velocities. Some sites also show evidence of a positive trend in meridional mean winds. With respect to tidal amplitudes a significant negative trend was observed by all instruments. It should be noted that most of the instruments did not employ height finding. Jacobi et al. (1997b) reports oscillations at very long time scales (approximately 20 years) from LF wind measurements in Germany, covering a time span of 25 years. These oscillations were especially found in summer zonal winds, but also for the amplitudes of the semi-diurnal tide and obviously make it difficult for short data sets to be of use in identifying trends. Similar results for the semi-diurnal tide were obtained by D'Yachenko et al. (1986) from meteor wind observations.

Portnyagin et al. (1993b) and Portnyagin et al. (1993a) discuss trends found in the mean wind and tides over Molodezhnaya (68°S) with a meteor radar. The results from both studies are included in Bremer et al. (1997), but due to the fact that they discuss the only other long data set from Antarctica, their results are mentioned here in more detail. The authors observed a decrease in amplitude of eastward winds at 95 km altitude for the period 1968 to 1977. They suggested that this trend could be due to a number of processes including ozone forcing, a latitudinal shift of the mesospheric jet, or a change in in-situ heating of solar or geomagnetic origin. For Arctic data, no similar effect was found. In addition, a decrease in the amplitude of the semi-diurnal tide by 0.3 - 0.5 $\mathrm{ms}^{-1}\mathrm{yr}^{-1}$ was found, depending on the time of year. A decrease in ozone forcing due to anthropogenic ozone depletion is proposed as a possibility that might explain the amplitude decrease. However, this result is made more difficult to interpret by the fact that the annual mean amplitude of the semi-diurnal tide did not show a trend.

In mean wind observations over Japan, Central Europe and Canada, spanning about 15 years, Gavrilov et al. (2002) found interannual changes that varied substantially between stations. Both the interannual changes and the dependence on location were attributed to variations in the strengths of internal gravity wave sources and the propagation conditions for them. These changes, in turn, were

attributed to solar activity, the Pinatubo eruption, and El Nino events. Portnyagin et al. (2006) pointed out that, while the interannual variations at stations of similar longitude could be different, the long-term variability is very similar.

In summary, only at very few sites statistically significant trends or multi-year modulations have been found. No consistent and global consensus on the nature of interannual variations of prevailing winds and tidal amplitudes has emerged yet. This could be due to real differences in dynamics between the measurement sites, for example because of locally varying gravity wave fields, or instrumental differences such as the problems that arise when comparing measurements that do not employ height-finding with measurements that do.

4.2 The Data Set

The MFSA radar technique and specific details about the radar system at Scott Base have been described in chapter 2. This section focuses on instrumental changes during the period 1982–2004. When studying interannual variability it becomes important to consider all instrumental changes and to assess whether they have the potential to be partially responsible for any observed variability. Note that data after the upgrade described in chapter 3 is not included here as this study was completed before the upgrade.

Figure 4.1 depicts the amount of data collected during each month as well as major system changes over the operational period discussed in this chapter. Data between 1982 and 1986 was obtained once per hour using a hard-wired system with a pulse repetition frequency (PRF) of 4 Hz. Since 1987 online analysis was carried out and data was obtained approximately every 5 minutes using a PRF of 8 Hz. It should be noted that when the first PC was installed in early 1992, the software that was in place until early 1995 used the operating system for time measurements. This was found not to be a reliable technique since the clock was either slow or fast, resulting in time stamps that were wrong by anything between minutes and even several days. This has an effect on amplitudes and phases of oscillations present in the data for this time period. Hence tidal parameters obtained during this period will not be used in this study. In early 1995 new software used the CMOS clock, which solved the latter problem.

The data from 1982 to 2004 that is available today uses eight different data formats, depending on space available for data storage, but they all contain similar information. For example, apparent wind speed, true wind speeds, height, date and time, as well as parameters of the FCA are always available. In addition, it should be noted that the radar during the whole observational period is essentially the same in terms of performance and layout. The form of the data processing used on the data to produce the velocities has also remained essentially unchanged throughout the radar's lifetime and thus the trends and patterns observed are

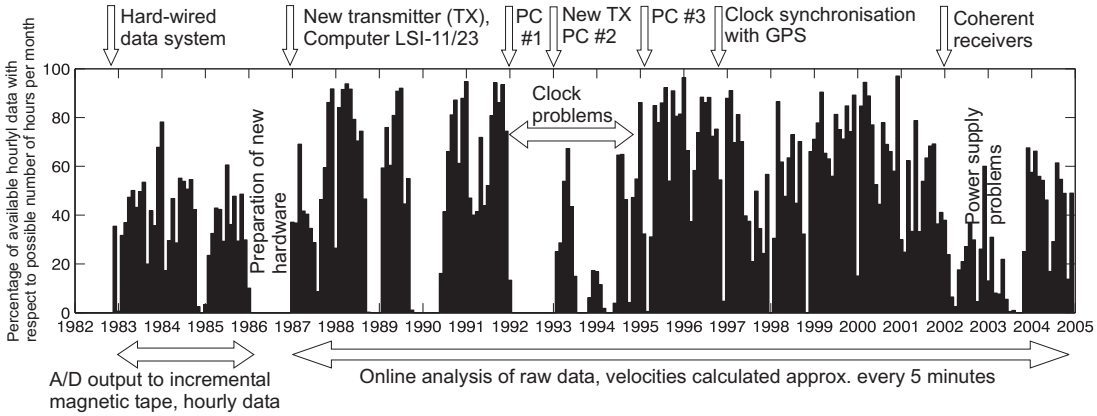

Figure 4.1: Available measurements overview including major radar equipment and software changes.

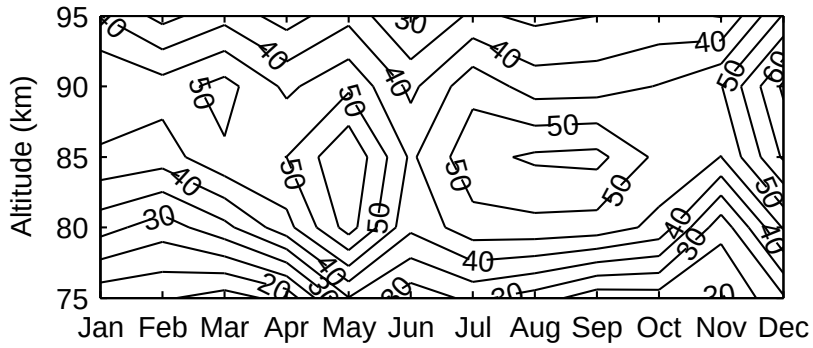

Figure 4.2: Percentage of available hours with respect to month and height bin, averaged over all years.

unlikely to be associated with instrumental effects. This has been verified by examining the timing of instrumental changes relative to variations in the winds.

An all-year-average for the percentage of available hours calculated for each month and for each height bin is depicted in Figure 4.2. Examination of Figure 4.2 suggests that most measurements are obtained from between 80 and 90 km altitude, the maximum number of hours is available in December at 90 km. It has to be noted, however, that this pattern is probably not produced by geophysical processes alone. The instrument was formerly maintained in November or December and hence would perform best just after this period.

4.3 Data Processing

The raw zonal and meridional velocity data used in this chapter is processed to produce hourly averages of the zonal and meridional wind in 5 km altitude bins. Between 1982 and 1986 only one measurement per hour was made and no outliers are removed. For the data since 1987, which has a higher time resolution, two acceptance criteria are applied. In every two hour window at least 5 velocity measurements are required. The average and standard deviation of the data in the two hour window are then used to examine the quality of individual velocity values by rejecting velocities 2 standard deviations away from the mean. This process acts to improve the continuity of the data set and remove any outliers that have not been previously removed by the acceptance criteria used in the FCA. In the final step the velocities are averaged over time-altitude windows using data between 30 minutes before and after each hour and ± 2.5 km around the considered altitude bin.

The outlier removal and averaging process for the data since 1987 creates a bias between the two data sets. The described process of removing outliers and averaging the measurements over one hour could not be applied to the data before 1987 because there is only a single measurement per hour. This leads to a higher variance of the data before 1987 when compared with the data after 1987. Over a month, the standard deviation of the early hourly data is larger by a factor of about 1.5 compared with the averaged hourly data from 1987 onwards. This will not affect the mean winds, but tidal amplitudes will be biased. In order to create comparable data sets, for the 1987+ data all but the first measurement of each hour would have to be discarded. We chose to accept the bias between the data sets for the presented time series and for deriving all-year means. For the derivation of trends we ignored the data between 1982 and 1986 inclusive.

Periodograms for the entire months time series revealed the presence of a 12 and a 24 hour oscillation in both the zonal and meridional flow and at all heights and all times of the year (not shown). To determine the magnitude of the mean wind and the amplitude and phase of the 12 and 24 hour waves, the following processing scheme is utilised. All the individual hourly averages at each altitude over an entire calendar month are used to form a composite day. It should be noted that using 10 days to form a composite day is also possible, but using a longer period reduces the impact of planetary wave variations. Therefore the variability and the trends become clearer. The composite day is then defined to be useful for further analysis if at least 19 of the hourly bins out of the possible 24 are filled.

To determine the magnitude of the mean wind and the amplitude and phase of the 12 and 24 hour wave a nonlinear least squares algorithm was used. The fitting could be done using a simple least squares fitting algorithm, however, it was found that the nonlinear least squares algorithm had the added benefit of being able

to define physically meaningful upper and lower limits for amplitudes and phases which were useful in reducing the effect of any remaining outliers at this point. The means, amplitudes and phases resulting from this process form the basis for this study. Oscillations with other frequencies, originating from planetary waves and gravity waves for example, as well as geophysical and instrumental noise, cancel out or leave signatures in the residual and these are not discussed in the present chapter.

4.4 Climatology

In order to visualise seasonal behaviour, all quantities were averaged over the entire available period, but for each month and height bin separately. The results are displayed as contour plots in Figure 4.3. Zonal winds (Figure 4.3a) are westward during the summer months, with velocities up to -20 ms^{-1}. The weaker eastward winds during winter are likely to be the top of the polar night jet. Velocities are decreasing from 10 ms^{-1} at 75 km to almost 0 ms^{-1} at 95 km. The transition between east- and westward winds occurs at all altitudes in September. At 90 to 95 km zonal winds reverse in January, while at lower altitudes the reversal does not take place until March.

Comparison of the mean zonal winds observed by the Scott Base MFSA radar with previous climatologies using a subset of the data suggests good agreement (see Fraser (1989)). Comparison of the current climatology with data from the CIRA86 climatology (Rees et al., 1990) shows a number of significant differences. Examination of the zonal winds in the CIRA86 climatology in winter show eastward winds that are much stronger than those observed by the Scott Base MFSA radar. The zonal winds in the summer are significantly weaker in the CIRA86 climatology than those in the MFSA radar data.

Examination of the mean meridional flow (Figure 4.3b) indicates that this is generally much weaker than the zonal wind pattern as should be expected. Inspection indicates that no strong seasonal pattern can be observed in the meridional velocity in the long-term average unlike the strong pattern observed in the zonal velocity. The only suggestion of a seasonal pattern is the change of wind direction which occurs at the autumn equinox (March) and to a lesser extent at the spring equinox (September) with southward velocities around the equinoxes. Velocities range from northward 5 ms^{-1} in April (75 km), May (75 km), December (85 km) and January (85 km) to southward 5 ms^{-1} in August (90 km).

Time series displaying the interannual variability of the zonal and meridional wind at 85 km between 1982 and 2004 are shown in Figure 4.4a and Figure 4.4b, respectively. The time series include several gaps caused by instrumental problems. Examination reveals that the interannual variation at this altitude can be large with monthly mean zonal velocities for December varying between -10 and

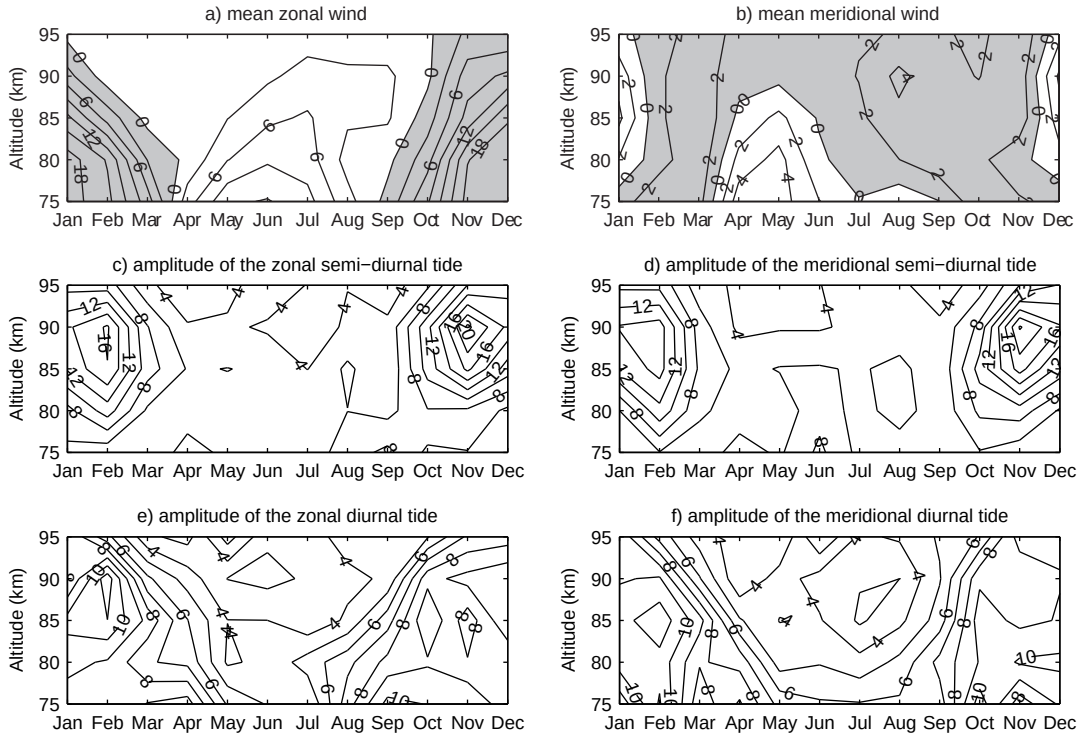

Figure 4.3: All-year-averages of mean winds and tidal amplitudes. For the mean zonal (meridional) wind positive is eastward (northward). Negative areas are grey.

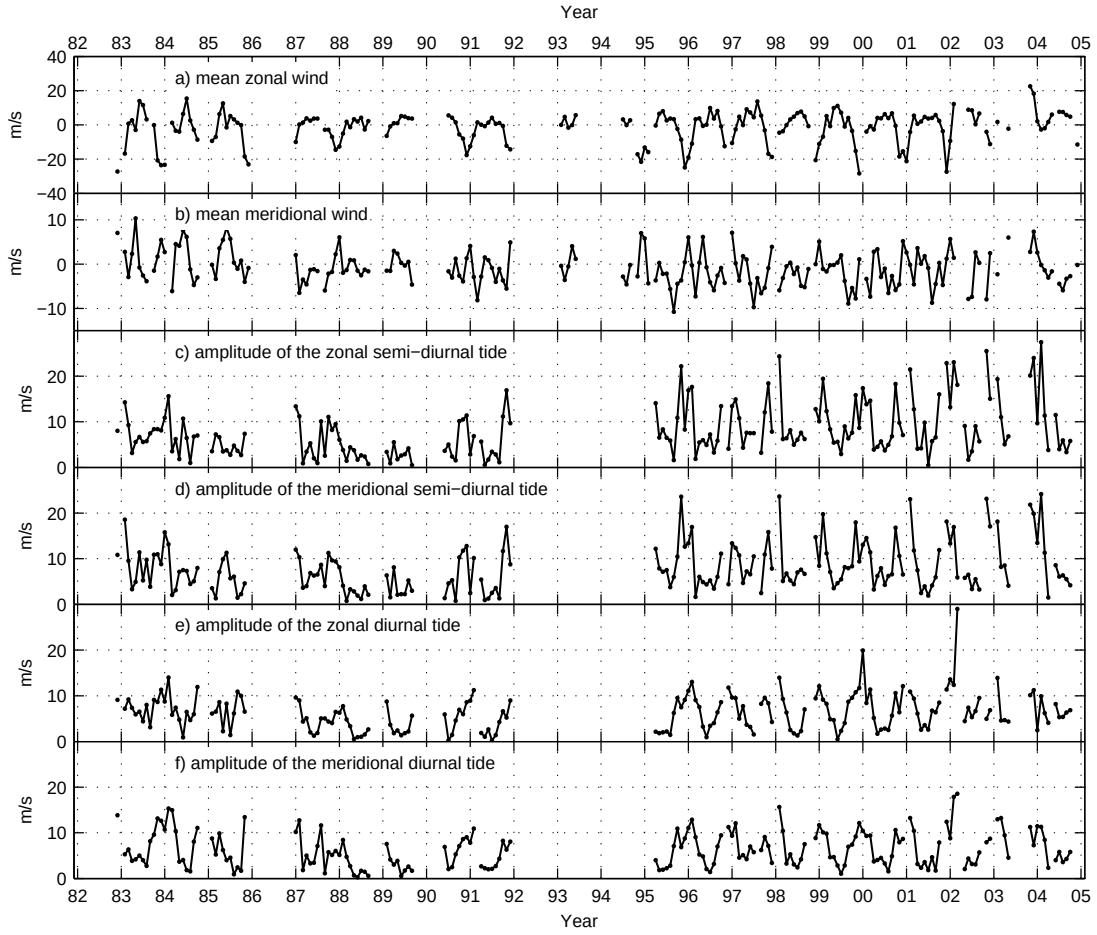

Figure 4.4: Time series of mean wind and tidal amplitude monthly means at 85 km altitude. The time axis ticks which label the year mark January.

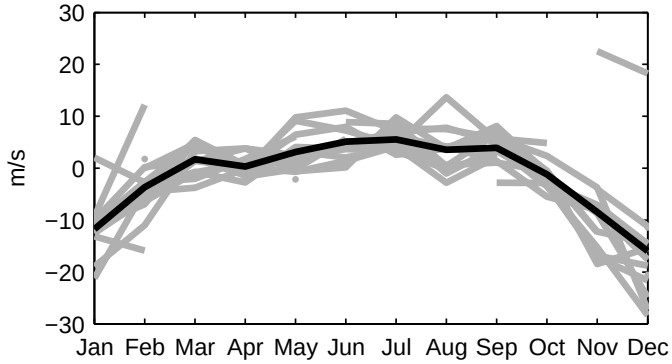

Figure 4.5: Time series of zonal wind monthly means at 85 km altitude. The thick black line represents the average value for each month over the entire time series. The grey lines represent variations for individual years.

-30 ms^{-1} at this altitude for example. Figure 4.5 displays the superimposed zonal wind monthly means at 85 km together with the average intra-annual variation of the mean wind. Examination clearly indicates large interannual variability and when the individual years are compared with each other it becomes clear that the mean for the winds is representative of the true mean. However, the mean value of the tidal amplitudes (not shown) is clearly affected by long-term variations and trends and therefore this mean varies greatly dependent of the period of data utilised. Therefore, the interannual variation found in the tidal amplitudes suggests that the utility of a tidal climatology employing a small data set can be misleading because trends or oscillations contribute significantly. A large data set will probably not considerably improve a mean wind climatology as there appears to be no strong trend or periodicity.

Figure 4.3c–f displays the all-year-averages of the tidal amplitudes. The zonal semi-diurnal tide (Figure 4.3c) experiences maxima in February and November at around 90 km with the amplitude of the zonal component reaching 20 ms^{-1} in November. The meridional component (Figure 4.3d) displays a similar seasonal behaviour, but the amplitudes are generally slightly smaller. Inspection of Figure 4.3c and Figure 4.3d also displays an increase in the amplitude of the semi-diurnal tide with height between 75 km and 90 km as expected. However, this amplitude increase is significantly less than the expected increase associated with the change in density. A decrease of tidal amplitude with height is observed above 90 km. The diurnal tide consistently maximises in February and November (Figure 4.3e and Figure 4.3f), however, the magnitude of the diurnal tide is generally much smaller than that of the semi-diurnal tide. For example, the average amplitude of the diurnal tide does not exceed 12 ms^{-1}. The winter amplitudes of both tides are small and range from 3 to 10 ms^{-1}.

Time series displaying the interannual variability of the diurnal and semi-

diurnal tidal amplitudes at 85 km between 1982 and 2004 are shown in Figure 4.4c–f. Examination of these time series shows several gaps caused by instrumental problems. In particular note the data gap between 1992–1995 which is caused by the timing problems discussed previously. A high degree of interannual variability is evident for the tidal amplitudes. The amplitude of the zonal semi-diurnal tide (Figure 4.4c) shows a positive trend for the period 1989 to 2004 especially for the summer months.

4.5 Interannual Variability

In an attempt to understand the interannual variability in the mean winds and tidal amplitudes, displayed in Figure 4.4, the monthly mean values of the mean zonal wind and the amplitude of the zonal component of the semi-diurnal tide have been plotted against solar activity and separated into different phases of the QBO in Figure 4.6. It should be noted that the data was separated into periods of eastward and westward flow over the equator because recent work by Labitzke (2005) and earlier work signified the importance of separating data by phase of QBO to allow the impact of solar activity variations to be observed. Note that the phase of the QBO was determined using empirical orthogonal functions on stratospheric zonal winds (Baldwin and Dunkerton, 1998) taken from the NCEP/NCAR reanalysis data (see chapter 2) at various heights over Singapore. For Figure 4.6 the phase is equivalent to the phase of the QBO at 10 hPa. Other heights corresponding to phase shifts between 0 and π were tested but did not yield significantly different results. Examination of Figure 4.6 indicates that the mean zonal wind shows no relationship to the solar activity for either phase of the QBO. Comparison of Figure 4.6a with Figure 4.6b also indicates that the QBO does not seem to affect either the mean value or the size of the variation of the mean zonal wind. Similar analysis for the meridional winds suggests that neither solar activity nor the QBO seems to explain the interannual variability for this parameter. This analysis was repeated using data from only one season at a time. None of the seasons yielded significant correlations in any category.

Inspection of Figure 4.6c and Figure 4.6d shows a weak negative relationship between the amplitude of the zonal component of the semi-diurnal tide and solar activity. This relationship seems to be slightly stronger during the westward phase of the QBO, but this change between phases of the QBO is not statistically significant. Comparison of Figure 4.6c with Figure 4.6d indicates, similarly to the case for mean winds, that the QBO does not seem to affect either the mean value or the size of the variation of the tidal amplitude. Analogous analysis for the meridional component of the semi-diurnal tide and the components for the diurnal tide show similar negative relationships between solar activity and the amplitudes observed. However, it should be noted that this effect is clearer in the semi-diurnal tidal amplitudes than the diurnal amplitudes. In addition, the

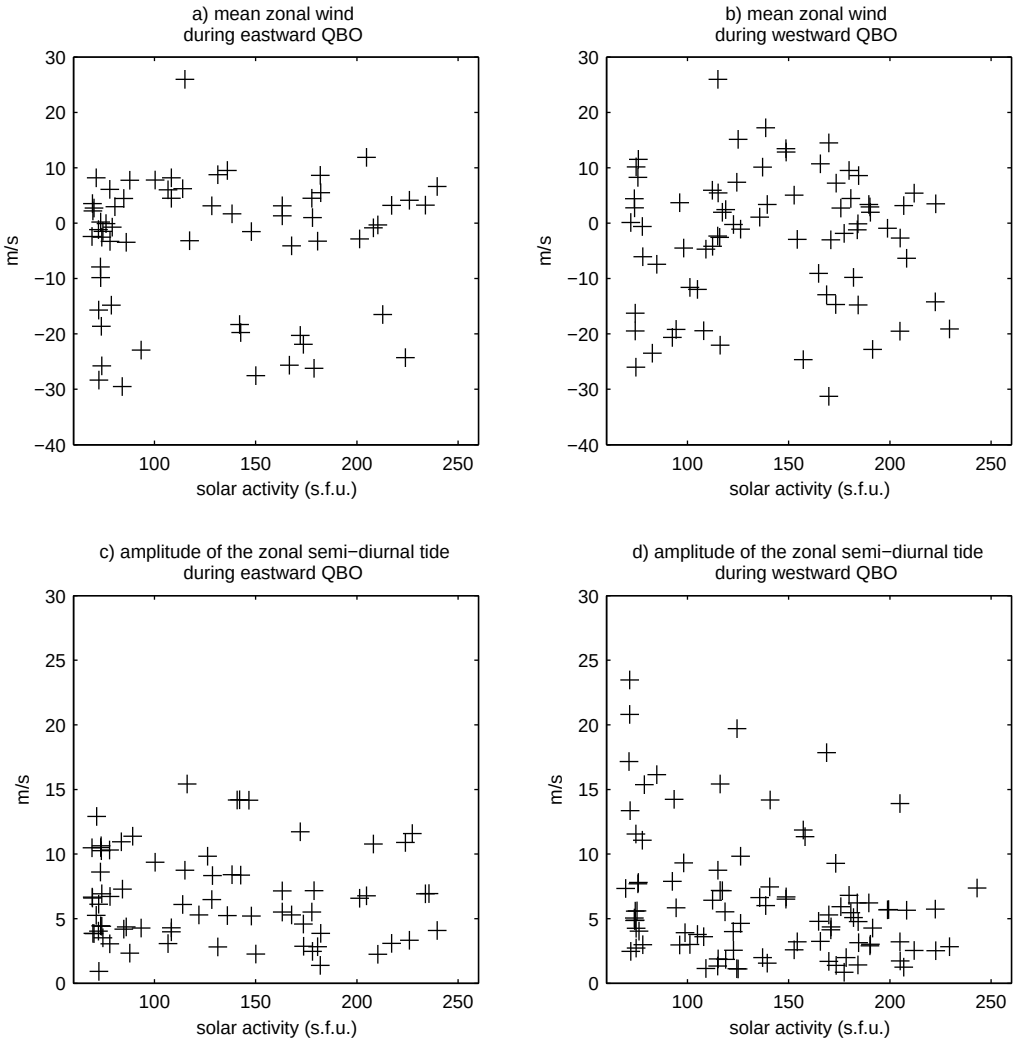

Figure 4.6: Mean zonal winds at 80 km (a and b) and amplitudes of the zonal component of the semi-diurnal tides at 80 km (c and d) and their dependence on solar activity (F10.7) measured in solar flux units (s.f.u.) during the eastward (a and c) and westward (b and d) phase of the QBO at approximately 10 hPa.

QBO does not seem to impact any of the tidal amplitudes. Analysis of the data separately for each season did not change these results.

In order to allow for varying effects of solar activity or the QBO phase on different heights and at different times of the year, and also with the aim of quantifying the significance of the results, analysis of variance (ANOVA) tests (Johnston, 1978) were carried out. When data is grouped into different categories, the ANOVA method allows the variance between the groups to be compared with the variance within the groups. The ANOVA technique can therefore be used to determine whether greater variations are related to specific circumstances. Again following the conclusions of Labitzke (2005) discussed above, the monthly data was grouped according to the level of solar activity and phase of the QBO. The absolute phase of the QBO was again varied between 0 and π. A first run employed five groups: low/high solar activity, west/eastward QBO phase and medium solar activity in conjunction with no QBO. Although significant (to the 99% level) month / altitude bins were found, no consistent pattern was observed for particular seasons or altitudes. It should be noted that some of the groups contained small numbers of observations and hence the validity of the test result is debatable. To remove this bias, a second series was run without the QBO subset, but still yielded no consistent results.

In order to further check the variables for a relationship to the QBO, a 27 month oscillation was also fitted to each set of three years of low pass filtered monthly means. The resultant amplitude of the least squares fit to any of the variables were smaller than 0.5 ms^{-1} and hence unlikely to be significant.

Multiple regression was applied to all height bins and months of the year separately using combinations of solar activity, QBO direction and strength, and time as variables. The mean winds showed small positive and negative correlations with solar activity and time, however, they strongly varied with height and month.

In an effort to examine the importance of other long-term variabilities in the data, Lomb-Scargle periodograms were calculated from the time series of monthly mean zonal and meridional winds at a variety of altitude ranges. Figure 4.7 depicts the periodogram for the zonal mean wind at 85 and 90 km. No significant frequencies could be detected in the time series of the monthly mean winds. To remove the effect of the large interannual variations, the time series was filtered with a low pass filter (Hamming window with cutoff period 12 months) and passed to the periodogram. However, while this removed some artefacts, no significant variations associated with known long-term periodicities (i.e. the solar cycle and QBO) were observed as previously confirmed by examination of Figure 4.6.

In contrast, similar analysis of both the semi-diurnal and diurnal tidal amplitudes showed significant power at a period of 11 years which would be expected based on a relationship between solar activity and tidal amplitudes. Figure 4.8

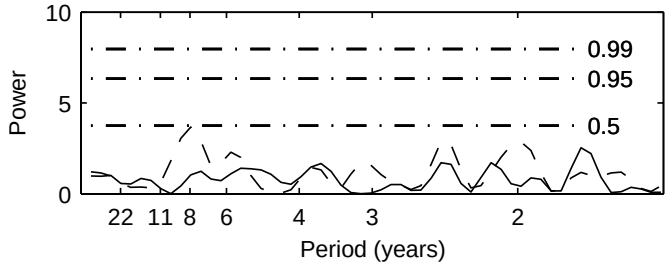

Figure 4.7: Lomb-Scargle periodogram of unfiltered monthly means of the zonal mean wind at 85 (solid line) and 90 km (dashed line). Significance levels are indicated by the dash-dotted lines.

displays Lomb-Scargle periodograms of the amplitude of the zonal (Figure 4.8a) and meridional (Figure 4.8b) semi-diurnal tide at 75 and 80 km. Inspection shows significant peaks at approximately 10–11 years in both components and at both heights. The peaks are close to the expected 11 year solar cycle periodicity, the significance of the peak decreases with increasing height, such that the effect of the solar cycle is greater at 75 km than at 95 km.

Close examination of the zonal component of the semi-diurnal tidal amplitudes at 75 km (Figure 4.8a) displays a second peak more significant than the 95% level close to a 2.3 year period. This is near the expected period of the QBO, however, this period is not significant at any of the other altitudes (for 80 km see Figure 4.8a, other altitudes not shown). While the meridional semi-diurnal tidal amplitude also exhibits a significant peak in the periodogram at roughly 11 years, it does not display a corresponding periodicity near the QBO period. Therefore, the periodicity near 2.3 years in the semi-diurnal tide at 75 km is believed not to be connected to the QBO. Similarly the significant peak near 6 years in the zonal semi-diurnal tide at 80 km cannot be seen in any of the other periodograms of tidal amplitudes and is regarded as an artefact.

The relationship of the zonal and meridional components of the tidal amplitudes to the solar cycle is shown in Figure 4.9 for the semi-diurnal tide and in Figure 4.10 for the diurnal tide. It should be noted that the three year running mean of the amplitude of the tide (dots) and solar flux density measured at 10.7 cm (solid line) on a reverse axis (right vertical axis) are displayed. Both the zonal (Figure 4.9a) and meridional (Figure 4.9b) components of the tide show a similar periodicity to the solar flux density approximately 180° out of phase. If only data from 1987 onwards is used, the relationship is still significant in all cases. This clearly indicates a negative correlation between tidal amplitudes and solar activity. An evaluation of all height bins suggests that the relationship is stronger for the meridional component of the tide. Examination of the diurnal tidal amplitudes (Figure 4.10a and Figure 4.10b) displays a comparable, but less

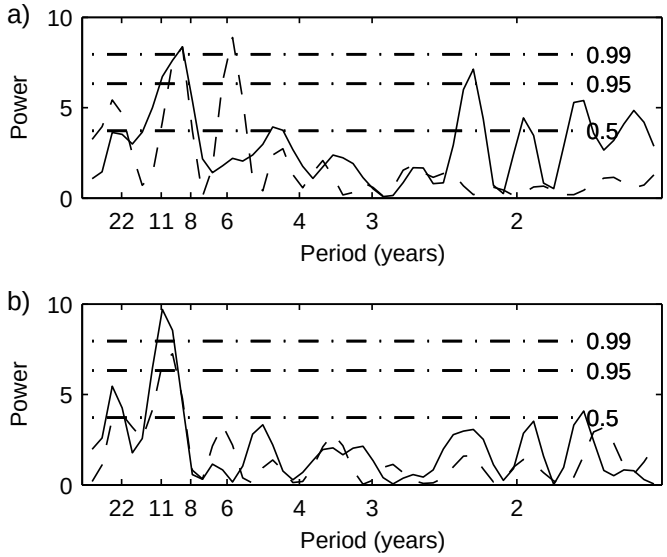

Figure 4.8: Lomb-Scargle periodograms of unfiltered monthly means of the amplitude of the zonal (a) and meridional (b) semi-diurnal tide at 75 (solid lines) and 80 km (dashed lines). Significance levels (in percent) are indicated by the dash-dotted line.

clear relationship than the semi-diurnal tide. It seems likely that this may be associated with the generally smaller amplitudes of this tide which are likely to be impacted more by geophysical and instrumental noise.

In Figure 4.9 and Figure 4.10 the amplitudes before 1987 appear considerably larger than the amplitudes from 1987 onwards. This is due to the data processing noted in section 4.3. Ignoring the data before 1987, the amplitudes also show a positive trend superimposed on the 11 year oscillation which was already noted by examination of Figure 4.3c in section 4.4. To determine the trend of both the 12 and the 24 h wave, a nonlinear least squares algorithm was used to fit the solar cycle variation and a linear trend to the tidal amplitude data. Before this analysis a three year running mean was applied to the tidal amplitude data. It should be noted that to reduce the effects of data gaps, an algorithm which replaced data gaps with the climatological mean was utilised. The relatively small interannual variation in tidal amplitudes made this a logical method of interpolation which did not produce discontinuities. The results for all the heights examined are listed in Table 4.2. Examination of these trends suggests that the trend is clearest at 80 to 90 km and is also strongest in the zonal and meridional components of the semi-diurnal tide. The fact that the variation is observed most clearly between 80 and 90 km may indicate that the data density may have some impact on this result.

Multiple regression as mentioned above in connection with mean winds was

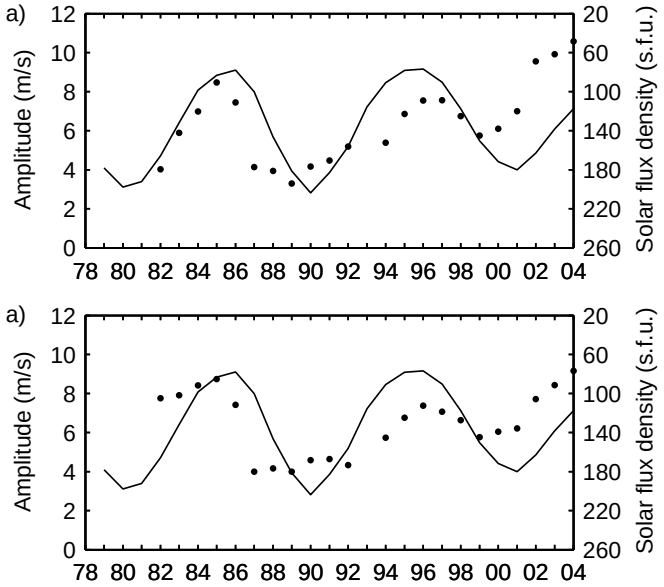

Figure 4.9: Three year running mean (dots) of zonal (a) and meridional (b) amplitude of the semi-diurnal tide measured at 80 km, and solar flux density (solid line).

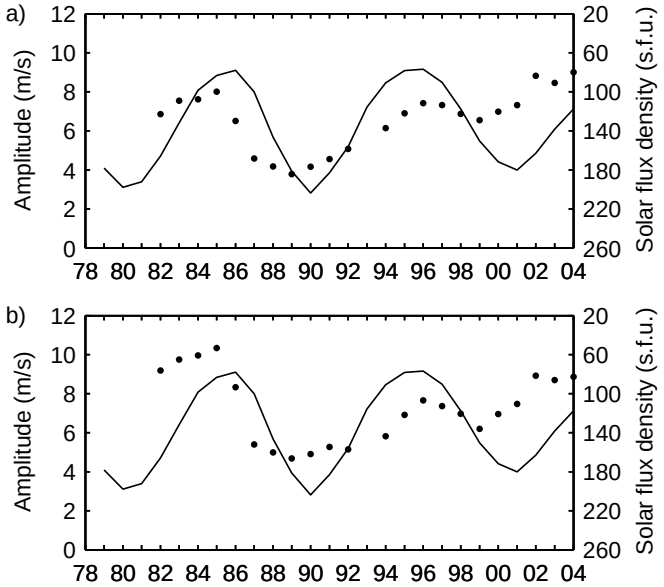

Figure 4.10: Same as Figure 4.9 but for the diurnal tide.

Table 4.2: Trends in tidal amplitude since 1987, in ms^{-1} per decade.

Wave	75 km	80 km	85 km	90 km	95 km
zonal 12 h	1.8	2.3	4.5	3.1	1.6
merid. 12 h	0.3	1.7	3.7	3.1	0.9
zonal 24 h	2.1	2.6	3.1	2.1	1.0
merid. 24 h	0.6	1.9	2.2	1.4	1.1

also applied to the tidal amplitude data. For most height bins this technique also showed the 11 year cycle in the amplitudes of the semi-diurnal and diurnal tide as well as the positive trend since 1987.

4.6 Discussion

A climatology of Scott Base mean winds from two years of observations has been discussed earlier (Fraser, 1989). The mean winds presented here have the same seasonal structure and the absolute values agree well. The seasonal structure of the mean zonal and meridional wind is also similar to observations at the Antarctic stations of Mawson (67°S) and Molodezhnaya (68°S) as published in Portnyagin et al. (1993b). The semi-diurnal tide at Mawson and Molodezhnaya discussed in Portnyagin et al. (1993a) shows comparable spring and autumn amplitude maxima. However, both studies also found a high degree of inter-annual variability in the mean wind and tides, respectively, again highlighting the importance of a long data set such as that of the Scott Base radar.

The geographical location of the Scott Base radar is an important factor in explaining the observed seasonal variation of the mean winds and tides. The seasonal pattern of the mean zonal winds can be related to the polar night and the associated stratospheric jet. However, the origins of seasonal variations of tidal amplitudes are not yet well understood. The phase speed of a wavenumber 2 semi-diurnal tide at 78°S is approximately 90 ms^{-1} and stratospheric velocities are usually below such velocities. Therefore, it is not expected that the zonal mean wind or planetary waves have a significant effect on the vertical propagation of the tide. The high latitude of Scott Base is likely to be of importance for the observed semi-diurnal tide because it was found to consist of at least zonal wavenumber 1 and 2 components, as discussed by Hernandez et al. (1993) and Riggin et al. (1999). Unfortunately it is impossible to distinguish between the different components using data from only one location, therefore we can only tentatively discuss what implications these findings have for Scott Base observations. In chapter 5 the Scott Base data will be combined with data from Halley, approximately the longitudinal conjugate point, to examine the wavenumber components and their origins in more detail. Angelats i Coll and Forbes

(2002) have shown that nonlinear interaction between a wavenumber 1 planetary wave and a semi-diurnal tide with wavenumber 2 can create a semi-diurnal tide with wavenumber 1. The possibility that the tide observed at Scott Base has a large wavenumber 1 component generated by planetary waves was examined by comparing the seasonal pattern of planetary wave amplitudes (Figure 4.11) with amplitudes of the semi-diurnal tide (Figure 4.12). It becomes evident that the amplitude maxima of the semi-diurnal tide in spring, summer and autumn as observed in the climatology in section 4.4 result from several relatively short peaks. Note that the tidal amplitudes were calculated by fitting the tides and a mean to ten days of data. This window was shifted by one day to get values for each day of the year. The higher resolution amplitudes do not significantly affect the observations thus far indicated. Figure 4.11 shows the 10 hPa wavenumber 1 planetary wave amplitudes during 2000 at 78°N (Figure 4.11a) and 78°S (Figure 4.11b). The amplitudes were calculated from geopotential height data using the NCEP/NCAR reanalysis. The height of 10 hPa was chosen as it is often used for planetary wave analyses. The choice of latitudes was based on the fact that they correspond closely to the latitude of Scott Base. When comparing Figure 4.11 with Figure 4.12 it can be seen that the seasonal variation of the tide as well as individual peaks on shorter timescales appear to follow planetary wave activity. Similar results were obtained for other years (not shown). This suggests that the tide at Scott Base has a strong wavenumber 1 component that is generated by nonlinear interaction with planetary waves in the northern and southern hemispheres.

The seasonal pattern of the diurnal tide (Figure 4.3e and 4.3f) is similar to that of the semi-diurnal tide, although the polar mesospheric diurnal tide is likely to be a trapped or evanescent component excited in-situ. The source of its seasonal and inter-annual variability may therefore be un-related to that of the semidiurnal tide. This implies that there could be different factors that contribute to the seasonal variation of the tides. Without the ability to resolve the wavenumber of the observed semi-diurnal tide the conclusions drawn about the origin of its variability have to remain tentative. As mentioned above, this will be examined in more detail in chapter 5.

Another phenomenon that could be related to the seasonal pattern of the semi-diurnal tide is found in the stratospheric mean winds. Figure 4.13 and Figure 4.15 display time-height contour plots of the zonal winds at lower altitudes above Scott Base for 2000 and 1996, respectively. The mean winds were calculated from UKMO assimilated data (see chapter 2). Note that for this analysis UKMO data was preferred to NCEP/NCAR data because of the greater vertical extent of the UKMO assimilation. However, NCEP/NCAR data was used previously because of its greater temporal range. It appears that the amplitude peaks as seen in Figure 4.12 and Figure 4.14 occur during times of very small zonal wind velocities above about 30 km altitude. Strong coupling between the zonal wind and tides has been suggested for example by McLandress (2002b). This phe-

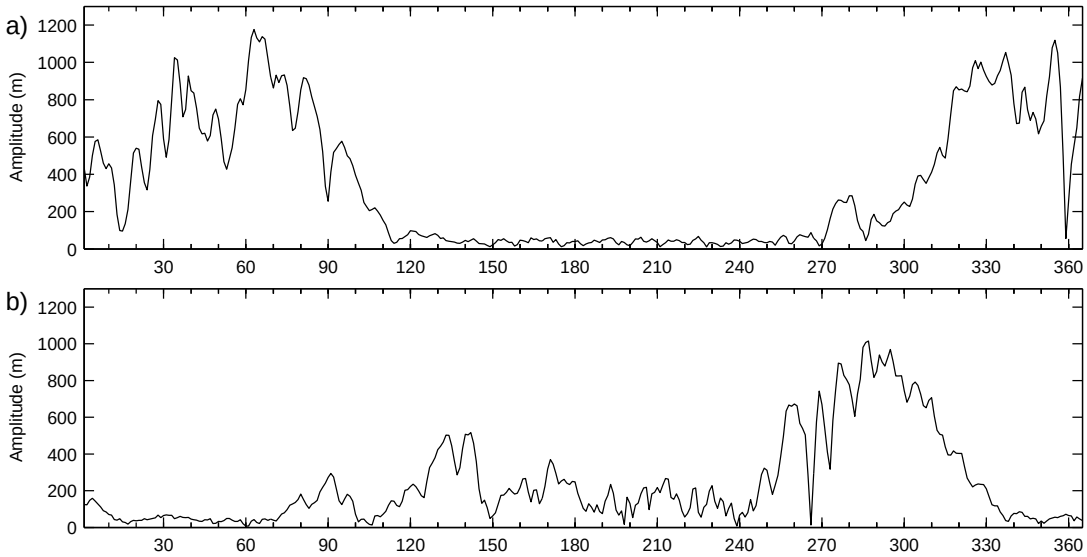

Figure 4.11: Daily planetary wave amplitudes at 78°N (a) and 78°S (b) during the year 2000, calculated from geopotential height data from the NCEP/NCAR reanalysis.

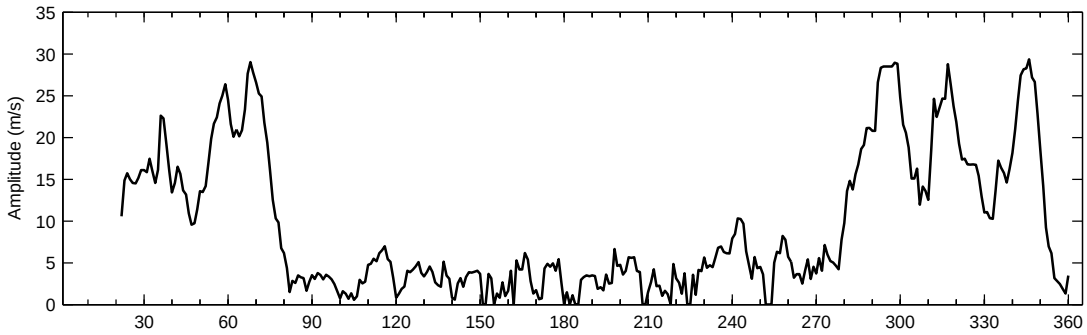

Figure 4.12: Day-to-day variability of the amplitude of the semi-diurnal tide at 80 km in 2000.

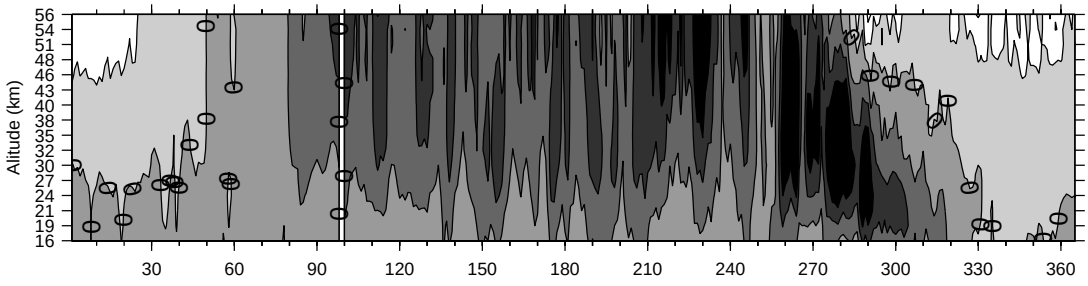

Figure 4.13: Mean zonal winds over Scott Base during 2000, calculated from UKMO assimilated data. The zero wind line is indicated, contour intervals are 20 m/s. Dark shadings indicate eastward directed winds, light shadings westward winds.

nomenon is most clearly observed by comparison of these two years. In 1996 the eastward vortex winds commence around day 65 (March 5), and the amplitude of the semi-diurnal tide decreases just before this time and stays small throughout the duration of the Antarctic vortex period. In 2000 the onset of the vortex occurs about 15 days later, at day 80 (March 20), and the final decrease in tidal amplitude is not observed until around day 80. The physical mechanism behind this observed phenomenon remains unclear. One possibility is the interaction between the gravity wave field and the tides because of the changes in the gravity wave field observed due to critical layer filtering (see chapter 1). However, the result of such interactions is not completely resolved at present. Damping and amplification of the tide through this process has been described in the literature, for a summary see Fritts (1995b). Gravity wave activity is higher in winter when the zonal winds are westward and no critical layer filtering occurs (examined in detail in chapter 6). The tides are small during that time, suggesting that if gravity wave / tidal interaction is responsible for the seasonal pattern of the tide then gravity wave activity damps tidal amplitudes. However, the period of small tidal amplitudes in the middle of summer cannot be explained by this mechanism because the changes in the gravity wave field should not be large at that time. Another possibility is that the correlation observed between the mean winds and tidal amplitudes is purely associated with the effect of planetary wave activity on the mean wind with some time lag.

We believe that Molodezhnaya, Christchurch and Adelaide are the only other stations in the southern hemisphere with data sets covering more than one solar cycle. For the period between 1982 and 2004 there are no other published long-term MLT wind observations from the Antarctica. Thus, the solar cycle relationship and trends observed in the Scott Base data have to be compared with observations mainly from the northern hemisphere.

Several authors have found QBO effects on tides or mean winds in the MLT region, especially at low or mid-latitudes. For Antarctic latitudes, Jarvis (1996) found QBO signatures in the semi-diurnal tide in geomagnetic field data from Faraday station (65°S). However, in the present study no QBO effect on mean winds or tides was found. For the semi-diurnal tide, a possible explanation for this apparent contradiction could be the component of the observed 12 hour wave. Hagan et al. (1992) showed that primarily the zonal wavenumber 2 component of the 12 hour wave is affected by the QBO, but the strength of the wavenumber 2 component decreases towards the pole, where only a wavenumber 1 component is found. Riggin et al. (1999) have experimentally shown the presence of both wavenumber 1 and 2 tides at the latitude of Scott Base. It is likely that the Scott Base semi-diurnal tide is not affected by the QBO if the wavenumber 2 component is not the dominant component during the high amplitude months in summer. Due to its lower latitude, Faraday station measurements could be more sensitive to QBO effects through the wavenumber 2 component. This possibility is the subject of future work.

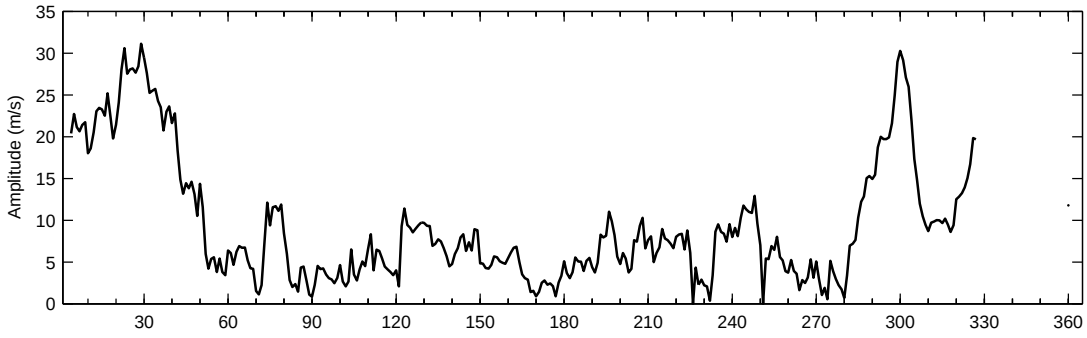

Figure 4.14: Same as Figure 4.12 but for 1996.

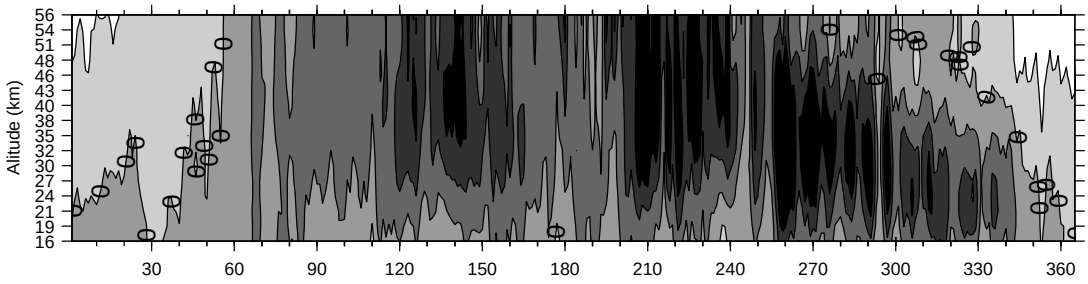

Figure 4.15: Same as Figure 4.13 but for 1996.

The discussion of results from other studies mentioned in section 4.1 has been summarised in Lastovicka (2005) which reviewed MLT variability. Their study concluded that neither a consistent worldwide relationship between mesospheric winds and solar activity nor trends had been found so far. However, their study indicates a fairly consistent anti-correlation between tidal amplitudes and solar activity in the Northern Hemisphere. The present study indicates little or no statistically significant relationship between the mean winds and solar activity, but an observable negative relationship between tidal amplitudes and solar activity. The mechanism for the solar control of the tides is not fully understood yet, but several processes have been proposed. These include a change in tidal forcing with varying solar activity, changes in the propagation conditions as well as changes of the gradient of atmospheric density and therefore changes in the observed altitude for techniques without height finding (Bremer et al., 1997).

An increase in amplitude of the 12 and 24 hour oscillation since 1987 is observed in the current study. It was investigated if the increase in measurement accuracy and a decrease in data gaps could yield this phenomenon. For this purpose, Monte Carlo simulations of variations in the quality of the data and changes in the occurrence of data gaps were performed. Composite days with a prevailing wind and sinusoidal oscillations with periods of 12 and 24 hours were constructed. White Gaussian noise was added so that the resulting time

series had a signal-to-noise ratio of 6 dB for example. Finally, data gaps were introduced ranging from 0 to 100%. Mean amplitudes of the oscillations were calculated from 1000 realizations per percentage level. At 6 dB noise, amplitude deviations of less than 8% occurred when less than 80% of the data were missing. The results indicate that if more than 80% or at least 19 out of 24 hours in a composite day are present then instrumental effects are unimportant. This threshold has been adapted for the current study (see above) and therefore the veracity of the observations is supported.

We discuss several phenomena that could be related to the observed tidal amplitude dependence on solar activity and the positive amplitude trend.

As indicated above and supported by the conclusions of chapter 5, nonlinear interaction with planetary waves might play a significant role in the behaviour of the semi-diurnal tide. Therefore the observed positive trend in tidal amplitudes and their relationship to the solar cycle could be related to changes in planetary wave activity. Figure 4.16 shows the planetary wavenumber 1 amplitudes (line) together with the amplitudes of the semi-diurnal tide (dots). The tidal amplitudes are taken from the 80 km height bin. The planetary wave amplitudes were calculated from NCEP/NCAR data, which spans the entire period of the Scott Base observations, in a similar way to that described in the discussion of seasonal variations. However, the amplitudes from 78°S and 78°N were averaged and monthly means were formed. Finally, similarly to Figure 4.9, both data sets were smoothed with a three year running mean. The planetary wave amplitudes show similar patterns when compared to the tide. An 11 year cycle as well as a trend can be identified. Interannual variations of wavenumber 1 planetary waves in the vicinity of the poles have been identified and discussed by Salby and Callaghan (2004). The authors attributed variations related to the solar cycle to latitudinal shifts of the critical region, or surf zone, which in turn is associated with low latitude winds. However, this approach does not immediately explain the similar behaviour of the diurnal tide, although interactions between the diurnal tide and planetary waves could also account for this observation. Further work on this subject is needed.

The second phenomenon to be discussed is associated with the onset and breakup dates of the polar vortex. Stratospheric dynamics seem to play an important role for the tides as seen in the discussion of the seasonal variations. The strength of the Antarctic vortex was found to be negatively correlated with solar activity during the westerly QBO phase (Labitzke, 2004). Therefore it is possible that during high solar activity the weaker vortex commences later in the year and breakup occurs earlier. According to the observations presented above, this could affect the timing of the large amplitude peaks and therefore have an impact on their strength. Similarly, the positive trend in the tidal amplitudes could then possibly be explained by the observed and modelled strengthening of the polar vortex due to ozone depletion (e.g. Watanabe et al., 2002). However,

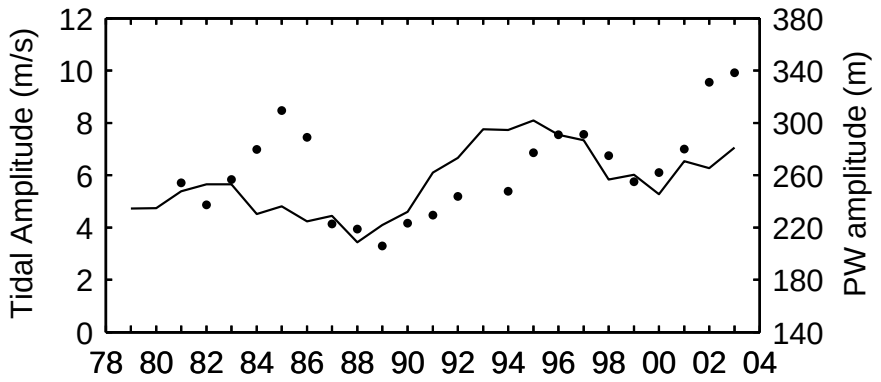

Figure 4.16: Three year running mean of tidal amplitudes at 80 km (dots) and planetary wave 1 amplitudes (line) at 2 hPa (approximately 43 km), average of 78°S and 78°N, calculated from geopotential height data from the NCEP/NCAR reanalysis.

this hypothesis needs much further work and will be the subject of future studies.

Another possible mechanism that could contribute to the observed tidal interannual variability is based on pressure and density gradient changes. Observations summarised in Lastovicka (2005) and models (Khosravi et al., 2002) show that the middle atmosphere should experience a warming (cooling) with increasing (decreasing) solar activity because of more (less) absorption of solar radiation by atmospheric gases. A warming (cooling) would then result in pressure and density increase (decrease) at a given altitude. The amplitude of the tide is likely to be connected to pressure height, so measurements made at a fixed altitude could observe amplitude variations with changing solar activity. Tidal amplitudes generally increase with height, especially when they are strongest in February and November (see Figure 4.3), therefore a relative decrease (increase) in tidal amplitude would be measured during years of high (low) solar activity.

In this scenario the tidal amplitude trends could be explained by the increase of CO_2 in the atmosphere. Modelling studies (Khosravi et al., 2002; Gruzdev and Brasseur, 2005) and experiments (Emmert et al., 2004) suggest middle and upper atmosphere cooling caused by increased amounts of CO_2. A general mesospheric cooling was also reported in a review of measurements and model simulations by Beig et al. (2003). Similar to a decrease in solar activity, this cooling could cause a pressure and density decrease at fixed altitudes and the tidal amplitude observed there would increase. The fact that this trend has not been observed at other stations could be related to the dominant solar activity dependence but also to the geographical location. It has been shown by models (Khosravi et al., 2002) that mesospheric cooling is more pronounced at the poles and could therefore be clearer in the Scott Base measurements than in data sets from lower latitudes.

For this trend to be detected height finding by the measuring instrument would be important, therefore data sets from instruments without height finding as for example discussed in Bremer et al. (1997) might be less affected by the mesospheric shrinking.

Akmaev (2002) has calculated the global mean vertical displacement of pressure levels due to the increase in CO_2 of 15% over the last 40 years. According to this study at a height of 90 km the displacement would be approximately one kilometre. The resulting increase in tidal amplitudes can be estimated if the height profiles of the tides are known. These were calculated from the Scott Base data presented above. A 250 m displacement at 90 km would result in an amplitude increase of up to 1.5 ms^{-1}. Even if the pressure level displacement in the vicinity of the pole was underestimated this mechanism can only partially contribute to the observed amplitude increase. It should also be noted that not all models and observations support the theory of mesospheric cooling, see for example Lübken (2000). The hypothesis of pressure level displacement is supported by the fact that the diurnal and the semi-diurnal tide display the same behaviour (section 4.5). However, in the mean winds no oscillations related to the solar cycle or trends were found, which would also be expected in this scenario. Therefore this theory in its present form is also unsatisfactory.

4.7 Conclusions

Comparison with previous studies show the consistency of mean winds and tidal amplitudes over Scott Base. However, the large interannual variability observed in some parameters suggests the importance of long records in identifying precise climatological values. Observations of mean winds over the entire data period relative to long-term oscillations, such as the solar cycle and QBO, show no clear correspondence and no consistent statistically significant patterns can be observed as a function of time of year or altitude. However, the amplitude of both zonal and meridional components of the semi-diurnal and the diurnal tide display a clear relationship to the solar cycle as well as a trend using a range of analysis methods.

It was shown that the seasonal behaviour of the semi-diurnal tide bears a striking resemblance to the behaviour of planetary wave activity at high latitudes in the northern and southern hemispheres. A large wavenumber 1 tide generated through nonlinear interaction between a wavenumber 2 tide and wavenumber 1 planetary wave could be responsible for this finding. This will be examined further in chapter 5. Large peaks in the semi-diurnal amplitude, for example around day 60 in 2000 (see Figure4.12), could also be related to the timing of zero winds in the stratosphere. Amplitude damping by enhanced gravity wave activity in winter is a possible explanation for the observed correlations. Characteristics of

stratospheric gravity wave activity will be presented in chapter 6, but further examination with respect to interactions with tides will remain subject to further work.

Nonlinear least squares fitting allows the trend in the tidal amplitudes to be examined. Inspection suggests that the tidal amplitudes are increasing when the data from 1987 to 2004 is utilised. Tidal amplitude data before 1987 cannot be used for this analysis because of differing measuring/processing schemes. The positive trend in the tidal amplitudes was found in the zonal and meridional diurnal and semi-diurnal tides at all heights.

Several phenomena that could contribute to the observed relationship between tidal amplitudes and solar activity as well as the positive amplitude trends were discussed. The long-term changes in planetary wave amplitudes are similar to those observed in the semi-diurnal tide. Therefore it is possible that planetary waves contribute not only to the seasonal but also to the interannual variation of the tide. The apparent long-term behaviour of the tides might also be controlled by the observed short peaks in early and late summer. These peaks appear to correlate with the changeover between the winter and summer circulation in the stratosphere. Long-term changes in polar vortex location, strength and duration could affect the timing and strength of the amplitude peaks. A third possible mechanism explaining the relationship of the tides to the solar cycle and the observed trends is based on vertical displacement of pressure levels induced by solar activity changes and greenhouse cooling. Estimations of the magnitude of amplitude changes through vertical displacement indicated that this effect can only account for a small part of the observed trend.

Our results with respect to the positive tidal amplitude trend analysis contradict some earlier publications discussed in section 4.1, although most of them discuss northern hemisphere observations and many did not employ height finding. This study confirms the conclusion of Lastovicka (2005) in the sense that that neither a consistent worldwide relationship between mesospheric winds and solar activity or trends have been found so far. The wind variability with respect to time and geographic location are not fully understood at present and reliable long-term observations from several stations seem necessary.

Chapter 5

Observations of the Wavenumber 1 and 2 Components of the Semi-Diurnal Tide over Antarctica[1]

The semi-diurnal tide dominates the winds in the mesosphere and lower thermosphere (MLT) at mid- and high latitudes. In chapter 4 this has been clearly confirmed for high southern latitudes. At mid-latitudes, the main component is the wavenumber 2 (s=2) semi-diurnal tide (Jacobi et al., 1999; Burrage et al., 1995), also referred to as a migrating tide because for an observer on the Earth's surface the two maxima rotate along a latitude circle synchronous with the sun. This wave is the primary response of the atmosphere at the 12 hour period to the periodic variation of absorption of solar radiation. However, it can be shown theoretically that at the poles only a s=1 component can be supported in the wind field (Forbes et al., 1999), which is classified as a nonmigrating tide. Nonmigrating semi-diurnal tides also oscillate with a period of 12 hours but can be standing or propagate eastward or westward with respect to the sun. Evidence for the existence of nonmigrating tides over Antarctica has been provided by Hernandez et al. (1993), Forbes et al. (1995), and Angelats i Coll and Forbes (2002).

This chapter combines four years of radar wind data from Halley and Scott Base in an attempt to resolve the zonal structure of the semi-diurnal tide over Antarctica and to determine the dominant component as a function of time. This will also allow conclusions to be drawn about the forcing mechanisms of the wavenumber 1 component and can therefore potentially contribute to our understanding of the seasonal and interannual variation of tidal amplitudes discussed in chapter 4.

[1]This chapter has in a similar form been published in the Journal of Atmospheric and Solar-Terrestrial Physics (Baumgaertner et al., 2006). It was co-authored by M. J. Jarvis (British Antarctic Survey, Cambridge, UK), A. J. McDonald and G. J. Fraser (University of Canterbury).

5.1 Introduction

It is not possible for single ground-based instruments alone to determine the zonal structure of the tide, apart from instruments located at a pole that can observe in several directions. Single ground-based measurements can only give a picture of wave amplitude and phase and their variability at individual locations. At latitudes where two tidal components are suspected, some conclusions can be drawn about one of the components if the amplitude and phase of the other component are assumed to be constant. Satellites offer good geographical coverage but have a poor time resolution at local time (LT) and therefore it is difficult to measure the amplitude and phase of tides on less than seasonal time scales accurately. There have been several studies which have attempted to overcome these difficulties by combining either several radars that are located in a narrow latitude belt (Jacobi et al., 1999) or combining radar and satellite measurements (Cierpik et al., 2003). In addition, mechanistic models have been developed with the aim to resolve the spatial structure of the 12 hour wave, as discussed in Angelats i Coll and Forbes (2002).

Portnyagin et al. (1998) used a meteor radar at the South Pole to examine the seasonal variation of the 12 hour wave. Their observations confirm the wavenumber 1 structure during summer months, during winter the 12 hour oscillation was too weak to allow determination of the dominant wavenumber. As generation mechanisms the authors suggest in-situ generation, nonlinear interaction between the migrating tide and a stationary planetary wave with zonal wavenumber 1, and thermal excitation in the troposphere. They also compared their measurements with tidal amplitudes from Scott Base (78°S), Molodezhnaya (68°S) and Mawson (67°S) and conclude that at 78°S the semi-diurnal tide with s=1 is still dominant but at lower latitudes a mixture of the s=1 and s=2 waves is likely. Observations from the South Pole have shown a strong wavenumber 1 semi-diurnal tide in summer months (Portnyagin et al., 1998; Hernandez et al., 1993; Forbes et al., 1995). Davis (69°S), Syowa (69°S) and Rothera (68°S) measurements were used in Murphy et al. (2003) and revealed a nonmigrating component in the 12 hour wave which the authors were able to relate to the zonal s=1 wave.

Angelats i Coll and Forbes (2002) combined a model with data from the Upper Atmosphere Research Satellite (UARS) and were able to show that nonlinear interaction between the wavenumber 2 migrating tide and a wavenumber 1 planetary wave generated 12 hour waves with wavenumbers 1 and 3. At high latitudes in the Southern Hemisphere the model resolved a large s=1 tide but the s=3 tide was negligible. The UARS data presented for comparison did not show this difference as clearly, although in summer months the s=1 tide dominated the s=3 tide. However, it has to be taken into account that the UARS coverage of high latitudes is very limited. Employing UARS, radar and model data Cierpik et al. (2003) found significant amplitude contributions by wavenumber 1 to 3 compo-

nents in the studied latitude region 50–55°N. Yamashita et al. (2002) showed that in the Middle Atmosphere Circulation Model at Kyushu University (MACMKU) stationary planetary waves with zonal wavenumber 1 generate a wavenumber 1 semi-diurnal tide. Mayr et al. (2005a,b) discuss the role of planetary waves and gravity waves in the generation of nonmigrating tides. They propose a mechanism which requires both types of waves for the generation of nonmigrating tides.

Using radar wind measurements from only one station at 69°S, Murphy (2002) explained amplitude and time of maximum variations of the semi-diurnal tide by interactions between the wavenumber 1 and 2 component. However, amplitude and phase of one of the components were assumed to be invariant. He was also able to explain phase variations with height using his model.

Riggin et al. (1999) used the dynasonde at Halley (76°S) and a medium-frequency spaced antenna (MFSA) radar at McMurdo (78°S) to determine the phase difference of the 12 hour wave between the two stations. They found good agreement between the zonal and the meridional phase differences. Generally however the phase difference was very variable and only allowed very poor approximations for the zonal wavenumber. In winter the phase difference was approximately 0° hence suggesting dominance of the wavenumber 2 component, in summer 1998 a phase difference with a mean of around 180° suggests the presence of a wavenumber 1 component, but the authors did not investigate its origin or forcing mechanisms. In the present study we employ four years of wind data obtained by the Halley dynasonde and the Scott Base MFSA radar which is very close to the location of the McMurdo system. We specifically calculate the amplitudes of the wavenumber 1 and 2 components as a function of time and analyse the relationship to planetary waves which are a possible forcing mechanism.

In section 5.2 we introduce the two radar systems and implications of their geographical locations. This section also outlines the data analysis procedure. This is followed by a description of the observations of the 12 hour wave at each station in section 5.3. In section 5.4 the phases of the 12 hour waves at Halley and Scott Base are compared and initial conclusions on the components of the semi-diurnal tide are drawn. More detailed information about amplitudes and phases of the two tidal components is presented in section 5.5. Section 5.6 introduces a method to calculate the longitude at which the maxima of the two tidal components coincide. The discussion section focusses on the possible generation mechanisms of the wavenumber 1 component.

5.2 Instruments and Data Analysis

The Scott Base MFSA radar and the IDI at Halley have been described in chapter 2. Instrument biases have to be considered when comparing measurements

from different instruments. As a result of comparisons between meteor and MFSA radars, it has been suggested that MFSA radar winds are too small (Thayaparan and Hocking, 2002). Although there are no indications for a bias in dynasonde wind measurements (Jones et al., 2003), a bias between the MFSA radar and the dynasonde remains a possibility. The effects of a hypothetical velocity measurement bias of 30% on the two tidal components were investigated by introducing this bias for every measurement of the MFSA radar. This showed that amplitudes of the different tidal components, which will be presented in section 5.5, varied up to 25% but the amplitude ratio changed by less than 10%. The effect on tidal phases would be negligible. Therefore we conclude that instrument biases are unlikely to affect the overall results of the present study.

The latitudinal difference between Scott Base and Halley is 2.0° (approximately 200 km), which is small compared with the large-scale dynamics in the middle atmosphere. Therefore in this study the two instruments are assumed to be located at the same latitude. The difference in longitude of the instruments is 166.9°, so the instruments are approximately on opposite sides of the geographic South Pole. The ideal longitudinal difference for the determination of the zonal structure of the semi-diurnal tide would be 180°, so the deviation from this perfect case is 13.1°. If the stations were exactly 180° apart, the phase difference of the zonal wavenumber 1 component would be 6 hours and there would be no phase difference for the wavenumber 2 component (two maxima). The 13.1° deviation causes phase deviations of $12h/360° \cdot 13.1° = 0.44h$ for a zonal wavenumber 1 structure (therefore the total phase difference is $6.44h$) and $12h/180° \cdot 13.1° = 0.87h$ for a zonal wavenumber 2 structure.

The raw wind velocities from both instruments were divided in 5 bins centred around 75, 80, 85, 90 and 95 km. Each hour of measurements centred around the hour was averaged while rejecting measurements that were more than 2 standard deviations away from the median for the considered hour. The Scott Base radar only operated between the full hour and 48 minutes past the hour, the remaining 12 minutes were used for other experiments. This biases the hourly binning. In order to correct for this, hourly averaging would have to be done from 32 minutes before until 28 minutes after the hour. This was considered to be an insignificant correction when compared with the period of the semi-diurnal tide and therefore no correction was applied in the current study. From 10 days of data a composite day was formed using the median. The median rather than the mean was chosen because the presence of outliers significantly affected the mean. A period of 10 days was chosen to minimise the effects of the 2, 5 and 10 day waves. A linear least squares fit was then performed. We fitted a mean, a 12 hour and a 24 hour sine wave to the data which are the dominant features as observed in periodograms. The 10 day window and the described analysis were applied to every day of the year centred around midnight local time of day 5. For both instruments uncertainties on the measurements are not available, therefore when forming the composite day for the linear fit the standard deviations over

the hourly measurements were calculated, and these were used for the calculation of confidence levels for the amplitudes and phases using standard techniques.

5.3 The 12 Hour Wave at Scott Base and Halley

For the present study it was necessary to derive tidal parameters with a high time resolution of 10 days because the amplitude ratio of the two considered components of the tide appears to vary greatly over the period of one month. Figure 5.1a and 5.1b display the amplitudes of the zonal 12 hour wave at Scott Base during the year 1999 at 85 and 90 km, respectively. In addition, the standard deviations are shown every 20 days for clarity. It is evident that at both altitudes the amplitude peaks for only short periods during early and late summer where it reaches maximum values of over 35 ms^{-1} at 90 km. Comparing the amplitude at the two altitudes bins reveals a high degree of correlation. At altitudes of 75, 80 and 95 km (not shown) the amplitude is generally weaker than at 85 km, but the position of the peaks is very similar when compared to the 85 and 90 km data. In winter the wave amplitude rarely exceeds 10 ms^{-1} at all altitudes (approximately from day 70 (11/03/1999) to day 220 (08/08/1999)). The standard deviations vary between 3 and 6 ms^{-1}, therefore winter tidal amplitudes are sometimes below the noise level. The results from the analysis of other years (not shown) yielded very similar results. The amplitude of the zonal 12 hour wave at Halley during 1999 is similarly displayed for 85 and 90 km in Figure 5.2. The amplitude peaks in early and late summer seen at Scott Base are also present at both altitudes at Halley. The position of the peaks is sometimes very similar between the two stations. In disagreement with the data from Scott Base the amplitudes at 85 km are slightly greater than those at 90 km, especially during the times of peak amplitudes. In accordance with the Scott Base data amplitudes decrease below and above the 85 to 90 km altitude range. The amplitudes observed at Halley are generally smaller than at Scott Base; they very rarely exceed 15 ms^{-1} during times of high wave activity. In winter the amplitude is often below 5 ms^{-1}. Standard deviations range from 3 to 9 ms^{-1}. The standard deviation for the 12 hour wave amplitudes averaged over 1998 to 2001 is 4.6 ms^{-1} for both Scott Base and Halley. This coincidence suggests that the variability arises from a common geophysical source rather than the more unlikely possibility that the two different instruments have exactly the same instrumental noise.

5.4 Phase Comparison

The phase differences of the 12 hour wave between Scott Base and Halley for 1998 to 2001 are displayed in Figure 5.3 for the zonal phases and in Figure 5.4 for the meridional phases. The phase difference is plotted three times for clarity

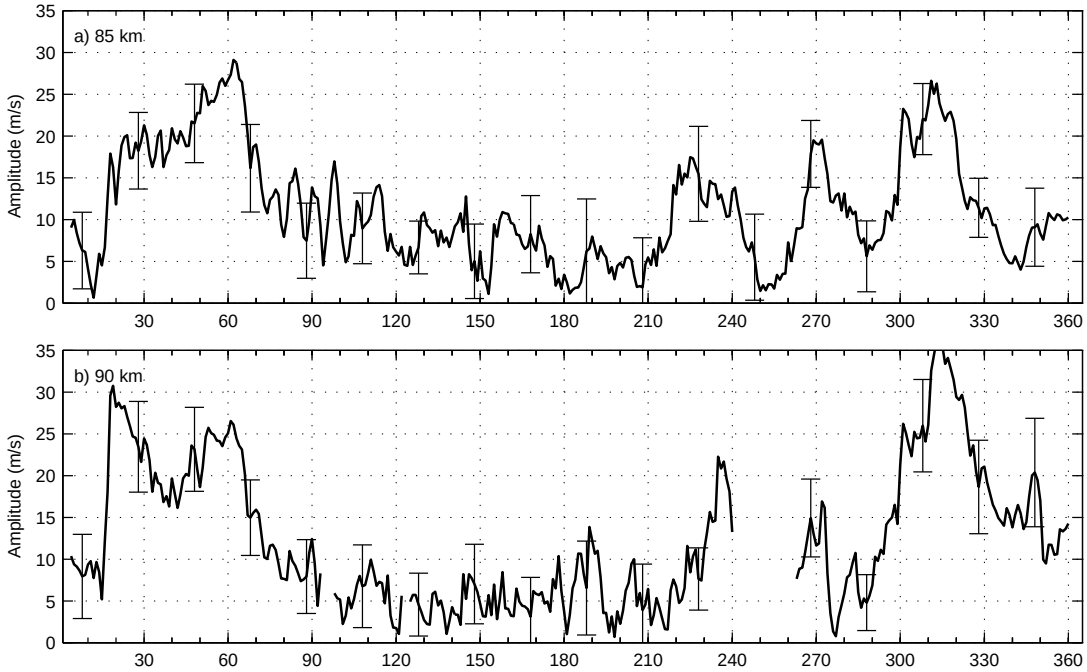

Figure 5.1: Zonal amplitude of the 12 hour wave at Scott Base during 1999 at 85 km (a) and 90 km (b) at a resolution of one day (sliding 10 day window).

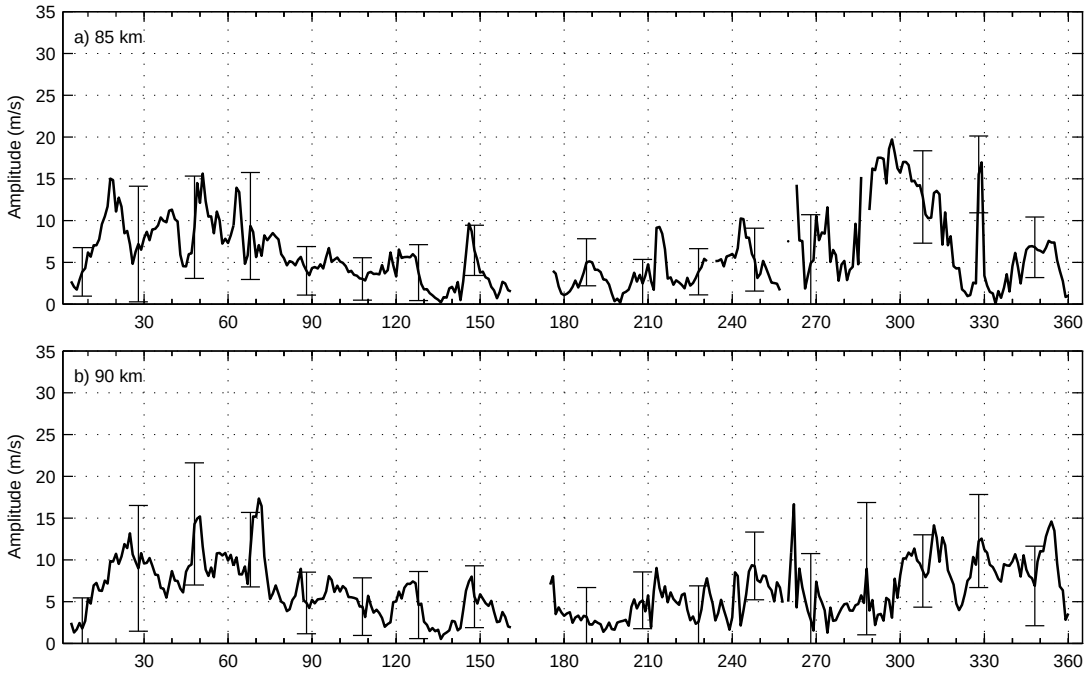

Figure 5.2: Same as Figure 5.1 but for Halley.

because it is often observed to pass through several cycles in one year. In addition, the standard deviation is indicated for every 20th measurement for clarity. As mentioned above, the phase differences expected would be 0.87 h for a sole zonal wavenumber 2 structure and 6.44 h for a sole wavenumber 1 structure. These theoretical values are indicated with grey lines in all figures. Other odd (even) tidal components would imply similar phase differences of approximately 6 hours (0 hours) making it impossible to distinguish between contributions from a wavenumber 1 and a wavenumber 3 component for example.

Examination of Figure 5.3 and Figure 5.4 shows that the phase difference is consistent from day to day during the months November to March (days 305 to 90) when the amplitude of the 12 hour wave is large. In winter the phase differences are more variable and the standard deviation is larger which is a result of the reduced phase accuracy of the tidal fit when the wave amplitudes are small.

Comparison of the time series of the zonal and meridional phase differences displayed in Figure 5.3 and Figure 5.4 usually shows good agreement. There appears to be little seasonal structure apart from the amount of variation between summer and winter. In 1998 until day 60 (01/03/1998) the phase difference is nearly 6 hours indicating a strong wavenumber 1. Throughout the winter of 1998 there is a tendency towards a phase difference of about 1 hour, but the variability is large. After a data gap in early summer the phase difference is very stable at about 6 hours for the rest of the year. Early in the year 1999 (Figure 5.3b and 5.4b) the phase difference appears again to be locked to about 6 hours, suggesting continued dominance of components with an odd wavenumber. Abrupt changes occur around day 90 (31/03/1999), and in the following winter months the phase difference is highly variable. At around day 300 (27/10/1999) it becomes stable and slowly drifts towards zero phase difference. In 2000 (Figure 5.3c and 5.4c) the variability early in the year is larger than in 1998 and 1999 (in 2001 there is no data available for this period). Similarly to late 1999, between day 300 and 345 it appears to drift towards zero phase difference. In 2001 (Figure 5.3d and 5.4d) the usual variability in winter is observed and the phase becomes more stable at around day 275 (02/10/1999). A very sudden change is observed around day 330 (26/11/2001) in both the zonal and meridional phase differences, the phase difference changes from approximately 8 hours to 1 hour. This is the largest sudden change observed in the available data set and will be discussed later with reference to solar proton events.

As already noted by Murphy (2002), the phase difference between the observed semi-diurnal tide at Halley and Scott Base (Figure 5.3 and Figure 5.4) can arise through two different scenarios, namely varying amplitude ratios between different tidal components and varying time-of-maximum difference. In order to illustrate this fact we reduce the problem to the superposition of two 12 hour waves. In the spatial dimension the waves have wavenumbers of 1 and 2, respectively. We first examine the case in which the amplitude ratio of the two waves

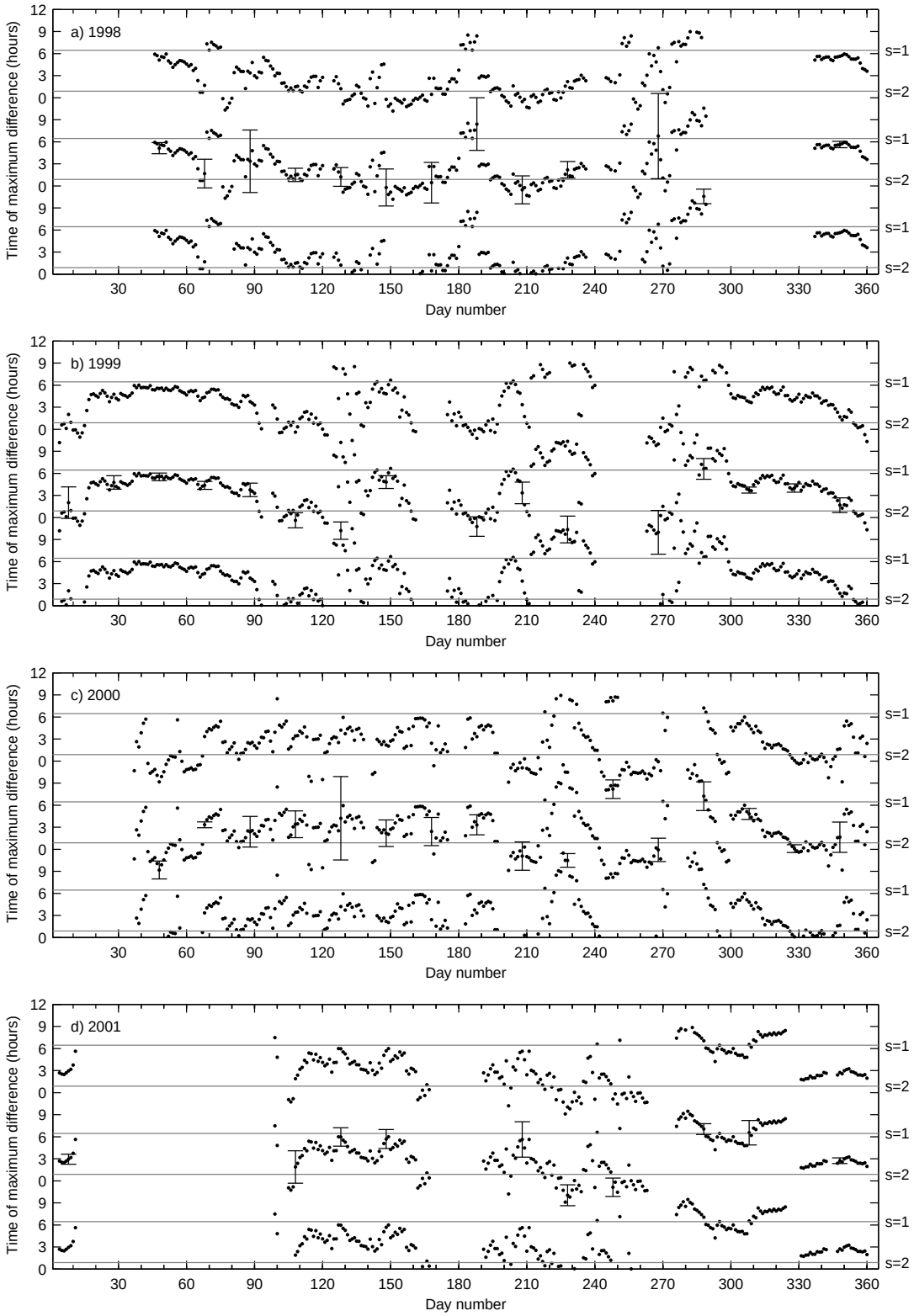

Figure 5.3: Phase differences between Halley and Scott Base for the zonal semi-diurnal tide for 1998–2001. The data are plotted three times, separated by 12 hours, in order to remove the need for phase wrapping.

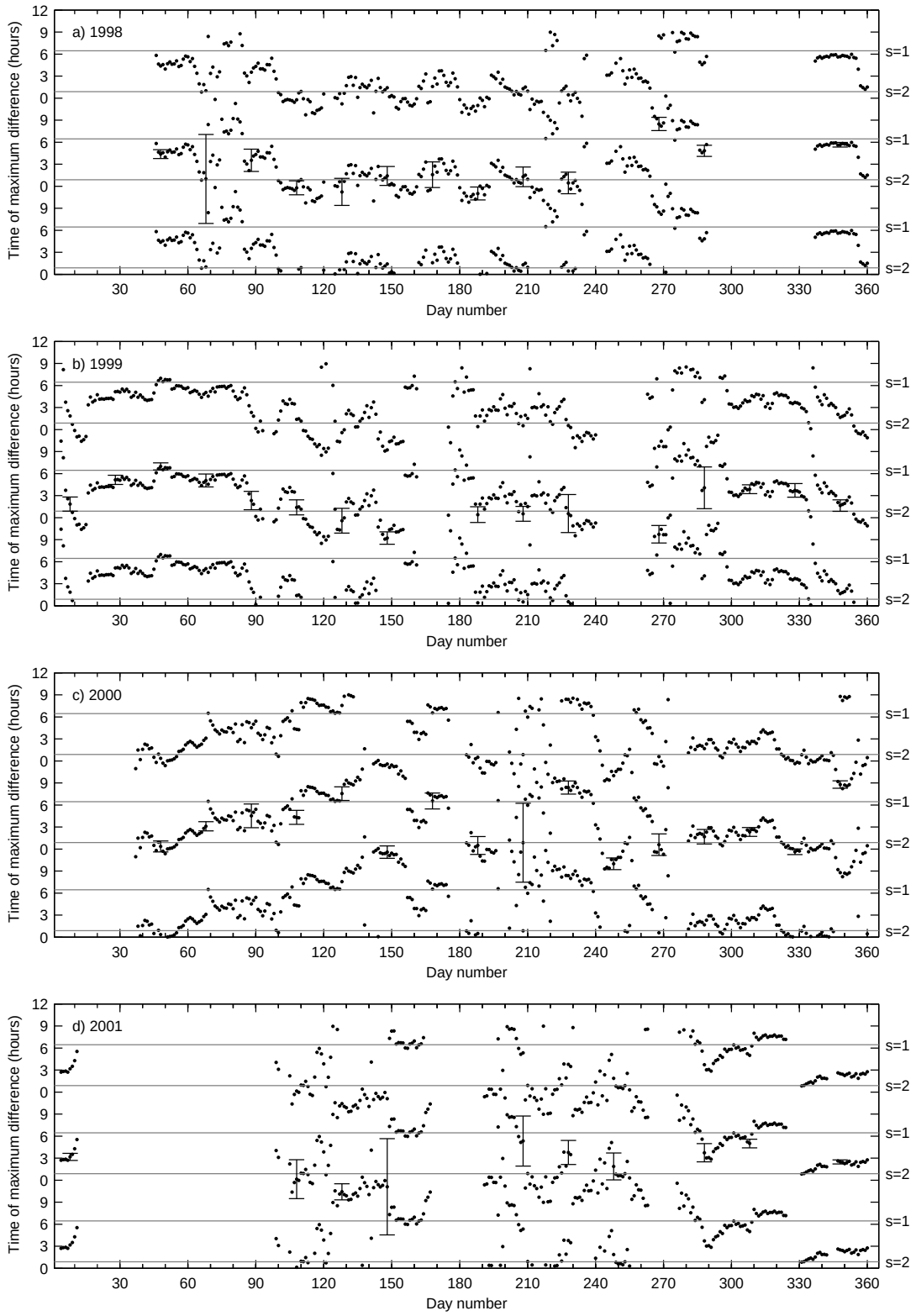

Figure 5.4: Same as Figure 5.3 but for the meridional phases.

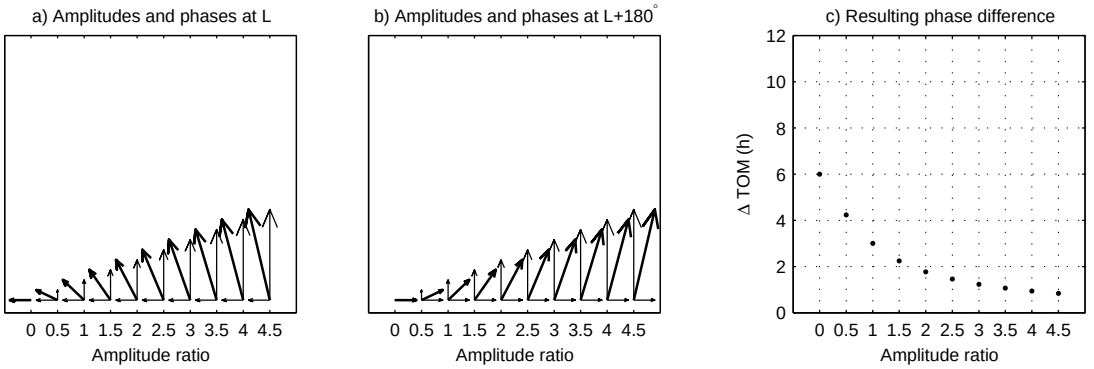

Figure 5.5: Phasor diagrams visualising the effect of varying amplitude ratios of sine waves with wavenumber 1 (time of maximum 9 UTC) and 2 (time of maximum 0 UTC) . (a) and (b) depict phasor diagrams at two locations which are separated in longitude by 180°. (c) shows the resulting phase difference.

varies. Figure 5.5a and 5.5b show the phasor representation of the two waves and their superposition for two stations separated by 180° in longitude. The time of maximum does not vary, the wavenumber 1 and 2 waves have their maxima at 9 UTC and 0 UTC, respectively. Phasor diagrams for amplitude ratios ranging from 0 to 4.5 are depicted. The resulting phase difference (Figure 5.5c) ranges from 0.9 to 6 hours. Figure 5.6 displays the opposite case of sole variation of time-of-maximum (TOM) difference, or phase difference, between the two waves. As expected the phase difference (Figure 5.6c) is either 3 or 9 hours. It becomes clear that if both amplitude ratio and time-of-maximum difference vary, the resulting phase difference can become rather complex, as observed in Figure 5.3 and Figure 5.4. Therefore it is often impossible from the phase difference alone to understand the relative contributions of the two tidal components.

5.5 Amplitude and Phase of the Wavenumber 1 and 2 Components[2]

In order to further examine the semi-diurnal tide a simple technique to separate the first two components has been developed. The technique uses the amplitudes and phases of the 12 hour wave as observed at the two stations. It is possible to account for the deviation from 180° longitude separation but we will introduce the technique with the simpler case of 180° longitude separation. In the phasor diagram in Figure 5.7a assume $\overrightarrow{S_1}$ to be the vector of the wavenumber 1 component.

[2]Note that a more general solution to this problem is presented in Appendix B.

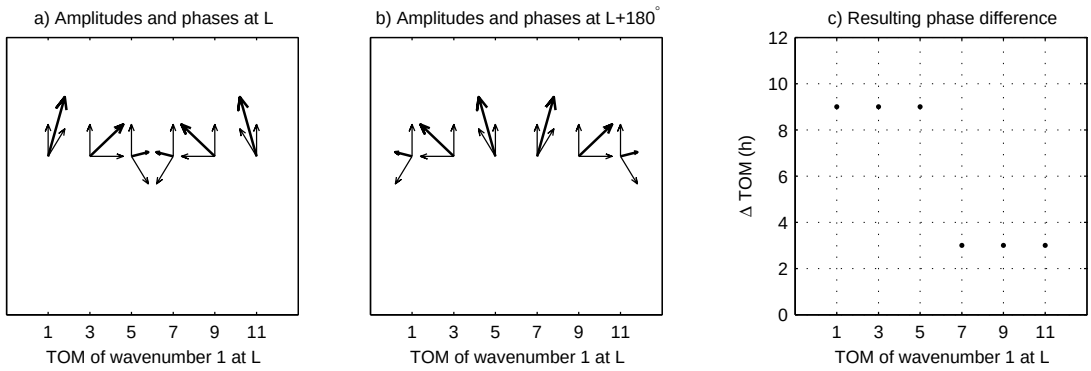

Figure 5.6: Phasor diagrams of two sine waves with varying times of maximum (TOM) of the wavenumber 1 wave. For the wavenumber 2 wave TOM = 0 UTC and the amplitude ratio is 1. (a) and (b) depict phasor diagrams at two locations which are separated in longitude by 180°. (c) shows the resulting phase difference.

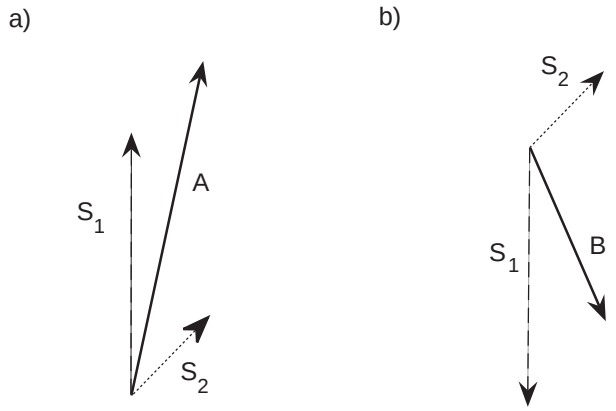

Figure 5.7: Phasor diagrams for the wavenumber 1 (S1) and 2 (S2) semi-diurnal tides at longitudes L_A (a) and L_B (b).

Its length represents the amplitude and the angle away from 0 UTC its time of maximum at longitude L_A. $\overrightarrow{S_2}$ is the vector of the wavenumber 2 component and is to be understood similarly. If only a wavenumber 1 and 2 component are present, the observed 12 hour wave at this longitude will be the vector sum of $\overrightarrow{S_1}$ and $\overrightarrow{S_2}$ and can be written as:

$$\overrightarrow{A} = \overrightarrow{S_1} + \overrightarrow{S_2} \tag{5.1}$$

A similar diagram can now be created for longitude $L_B = L_A + 180°$ (Figure 5.7b). In UTC the wavenumber 1 component will have its time of maximum six hours later, so its vector representation will be $-\overrightarrow{S_1}$, and the wavenumber 2 component will have its maximum at the same time as the other station. We add the vectors of $-\overrightarrow{S_1}$ and $\overrightarrow{S_2}$ to get the amplitude and phase $\overrightarrow{B}$ of the 12 hour wave at this longitude:

$$\overrightarrow{B} = -\overrightarrow{S_1} + \overrightarrow{S_2} \tag{5.2}$$

From the radar measurements we can determine $\overrightarrow{A}$ and $\overrightarrow{B}$, therefore we express the vectors representing the wavenumber 1 and 2 component as:

$$\overrightarrow{S_1} = \frac{1}{2}(\overrightarrow{A} - \overrightarrow{B}) \tag{5.3}$$

$$\overrightarrow{S_2} = \frac{1}{2}(\overrightarrow{A} + \overrightarrow{B}) \tag{5.4}$$

which yields the amplitude and phase of the two components. If other components are present, $\overrightarrow{S_1}$ will be the vector sum of all odd components and $\overrightarrow{S_2}$ the vector sum of the even components. In the case where only a wavenumber 1 and a wavenumber 2 component are present we can expand this method to account for the deviation of $\gamma = 13.1°$ from 180° longitude separation. We express the vector $\overrightarrow{A}$ in polar coordinates as:

$$\overrightarrow{A} = r_1 \begin{pmatrix} cos\theta_1 \\ sin\theta_1 \end{pmatrix} + r_2 \begin{pmatrix} cos\theta_2 \\ sin\theta_2 \end{pmatrix} \tag{5.5}$$

where r_1 and r_2 are the amplitudes of the wavenumber 1 and 2 components and θ_1 and θ_2 are the respective phases.

Let C be the vector of the 12 hour wave at the location $L_C = L_B + \gamma$. At C the phase of the wavenumber 1 component will be $\theta_1 + \frac{\gamma}{2} + \pi$ and the phase of the wavenumber 2 component will be $\theta_2 + \gamma$. Now we can express C in polar coordinates using the vectors for $\overrightarrow{S_1}$ and $\overrightarrow{S_2}$ at L_C as:

$$\overrightarrow{C} = r_1 \begin{pmatrix} cos(\theta_1 + \frac{\gamma}{2} + \pi) \\ sin(\theta_1 + \frac{\gamma}{2} + \pi) \end{pmatrix} + r_2 \begin{pmatrix} cos(\theta_2 + \gamma) \\ sin(\theta_2 + \gamma) \end{pmatrix} \tag{5.6}$$

$$= -r_1 \begin{pmatrix} cos(\theta_1 + \frac{\gamma}{2}) \\ sin(\theta_1 + \frac{\gamma}{2}) \end{pmatrix} + r_2 \begin{pmatrix} cos(\theta_2 + \gamma) \\ sin(\theta_2 + \gamma) \end{pmatrix} \tag{5.7}$$

Using trigonometric identities and combining Equations 5.5 and 5.6 yields the vectors $\overrightarrow{S_1}$ and $\overrightarrow{S_2}$:

$$\overrightarrow{S_2} = \begin{pmatrix} \frac{l_1}{l_1^2+l_2^2}\left(\frac{-l_2(m_2-c_y)}{l_1}+c_x-m_1\right) \\ \frac{-l_2}{l_1^2+l_2^2}\left(\frac{-l_2(m_2-c_y)}{l_1}+c_x-m_1\right)-\frac{m_2-c_y}{l_1} \end{pmatrix} \quad (5.8)$$

$$\overrightarrow{S_1} = \overrightarrow{A}-\overrightarrow{S_2} \quad (5.9)$$

where

$$l_1 = cos\gamma + cos\frac{\gamma}{2} \quad (5.10)$$

$$l_2 = sin\gamma + sin\frac{\gamma}{2} \quad (5.11)$$

$$m_1 = -a_x cos\frac{\gamma}{2} + a_y sin\frac{\gamma}{2} \quad (5.12)$$

$$m_2 = -a_x sin\frac{\gamma}{2} - a_y cos\frac{\gamma}{2} \quad (5.13)$$

Zonal (meridional) amplitudes calculated with this technique are displayed in Figure 5.8 (Figure 5.9), for the years 1998 through 2001. For all years the zonal and meridional amplitudes show very similar characteristics, therefore our confidence in the results is high although they may still be biased by the presence of other components.

In 1998 between day 45 (14/02/1998), when data is available from both radars, and day 65 (06/03/1998) both tidal components are strong, the wavenumber 1 amplitude is about 5 ms^{-1} larger than the wavenumber 2. Then both amplitudes drop sharply and stay below 10 ms^{-1} for the entire winter period. Usually the wavenumber 2 appears to be slightly stronger than the wavenumber 1 during this time. Another data gap in summer obscures the onset of larger amplitudes. When both radars are operational again at day 335 (01/12/1998) a very strong wavenumber 1 tide is found reaching nearly 30 ms^{-1} in the meridional direction. The wavenumber 2 tide is small in comparison, it does not exceed 15 ms^{-1}.

In 1999 (Figure 5.8b and 5.9b) the wavenumber 2 component is dominant for about 14 days. Then the wavenumber 1 amplitude increases by more than 15 ms^{-1} within 2 days. Its amplitude remains large while the amplitude of the wavenumber 2 component is roughly half that of the wavenumber 1. After day 60 (01/03/1999) both amplitudes decrease in a similar manner to that observed in 1998 and stay small until about day 290 (17/10/1999) interrupted only by about 10 days where both zonal tides reach amplitudes larger than 10 ms^{-1} between day 230 (18/08/1999) and 240 (28/08/1999). The amplitude of both components grows from day 290 (27/10/1999) onwards. Wavenumber 1 dominates between day 300 (27/10/1999) and 340 (06/12/1999), after that and for the rest of the year wavenumber 2 is dominant.

There is no data during January 2000 (Figure 5.8c and 5.9c). Amplitudes of both components rise around day 50 (19/02/2000), the wavenumber 2 amplitude is about 5 ms^{-1} larger until both amplitudes decrease between day 70 (10/03/2000) and 80 (20/03/2000). The zonal amplitudes of both components stay below 5 ms^{-1} until day 240 (27/08/2000). The amplitudes of the meridional tides exceed this value between day 100 (09/04/2000) and 150 (29/05/2000). After day 240 (27/08/2000) the tides increase in amplitude culminating at day 295 (21/10/2000). For the rest of the year the wavenumber 2 mostly dominates over the slightly weaker wavenumber 1. Both amplitudes decrease sharply until they are negligibly small between day 346 (11/12/2000) and 355 (20/12/2000).

Data for 2001 is available for day 100 (10/04/2001) onwards (Figure 5.8c and 5.9d). On several occasions the amplitudes spike until a very quite period begins around day 190 (09/07/2001). In the meridional direction especially the wavenumber 2 tide increases at day 230 (18/08/2001) for about 10 days. From day 290 (17/10/2001) until 310 (06/11/2001) the wavenumber 1 clearly dominates in both directions. Both amplitudes increase simultaneously during day 310, but wavenumber 1 is still the dominating component. After a short gap in the data the situation is reversed on day 330 (26/11/2001). Both amplitudes then decrease slowly until the end of the year.

Note that periods where one component was clearly dominating over the other can be related to Figure 5.3 and 5.4. In late 1998 for example a strong wavenumber 1 tide was found. Examination of this period in Figure 5.3a and 5.4a indicates a phase difference of nearly 6 hours suggesting the consistence of the presented results.

While only results from the 90 km altitude bin are shown here, we have also analysed the data from 85 km. While the absolute amplitudes are different the amplitude ratio of the two wave components is similar throughout the four years of data.

5.6 Longitude of Coincidence of the Wavenumber 1 and 2 Tides

The wavenumber 2 wave has the same angular velocity as the sun and its phase is therefore locked to the motion of the sun. The wavenumber 1 wave however rotates at half that angular velocity. This raises the question of its phase with respect to the sun and to the wavenumber 2 component. As mentioned in the introduction it is likely that the wavenumber 2 tide plays an important role in the generation of the wavenumber 1 component. Therefore the longitude where the maxima of the two components coincide should be a meaningful measure for the investigation of other contributors in the generation process. This longitude was calculated for each 10 day window. Knowing the time of maximum of both

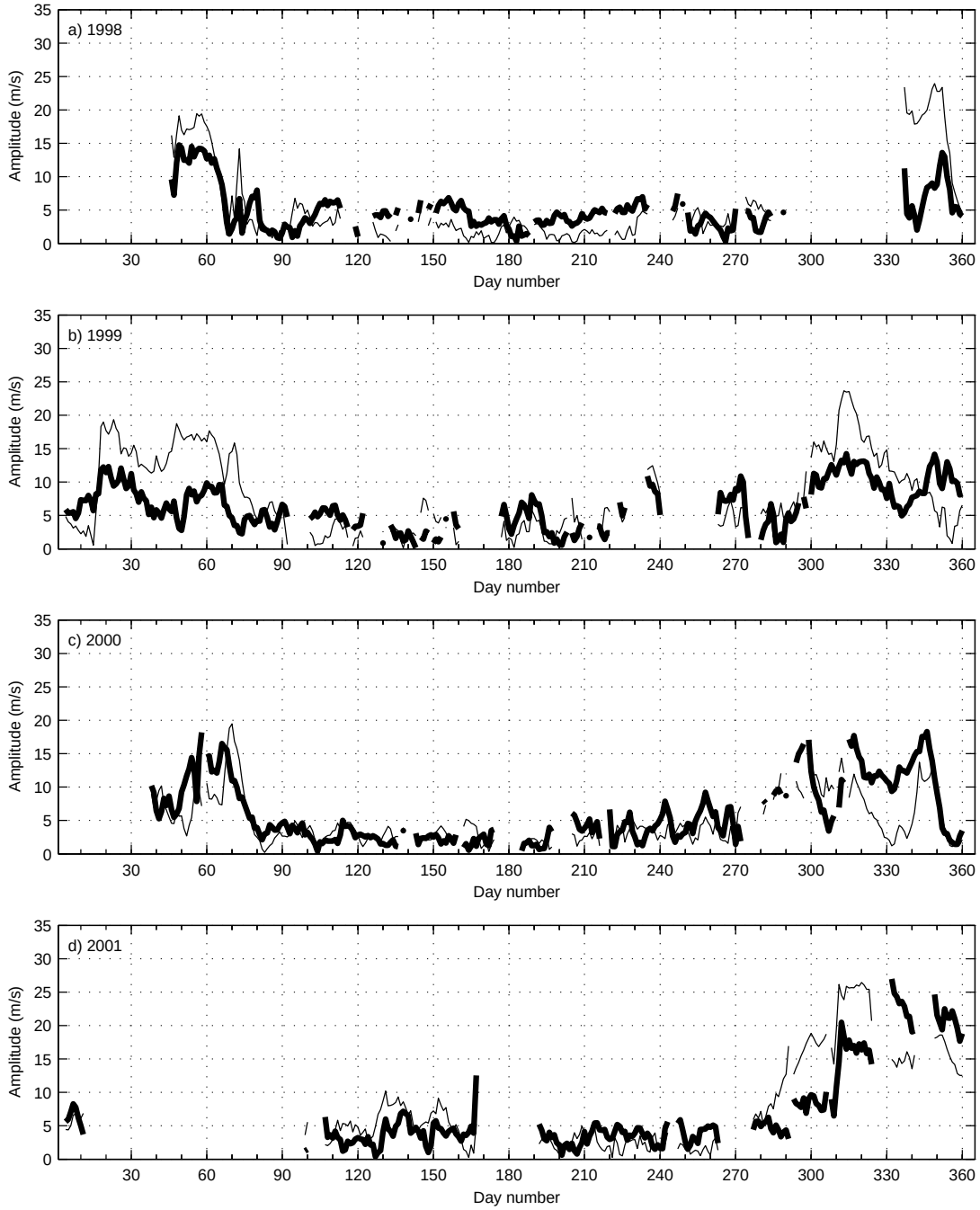

Figure 5.8: Amplitudes of the zonal wavenumber 1 (thin line) and 2 (bold line) components for 1998–2001.

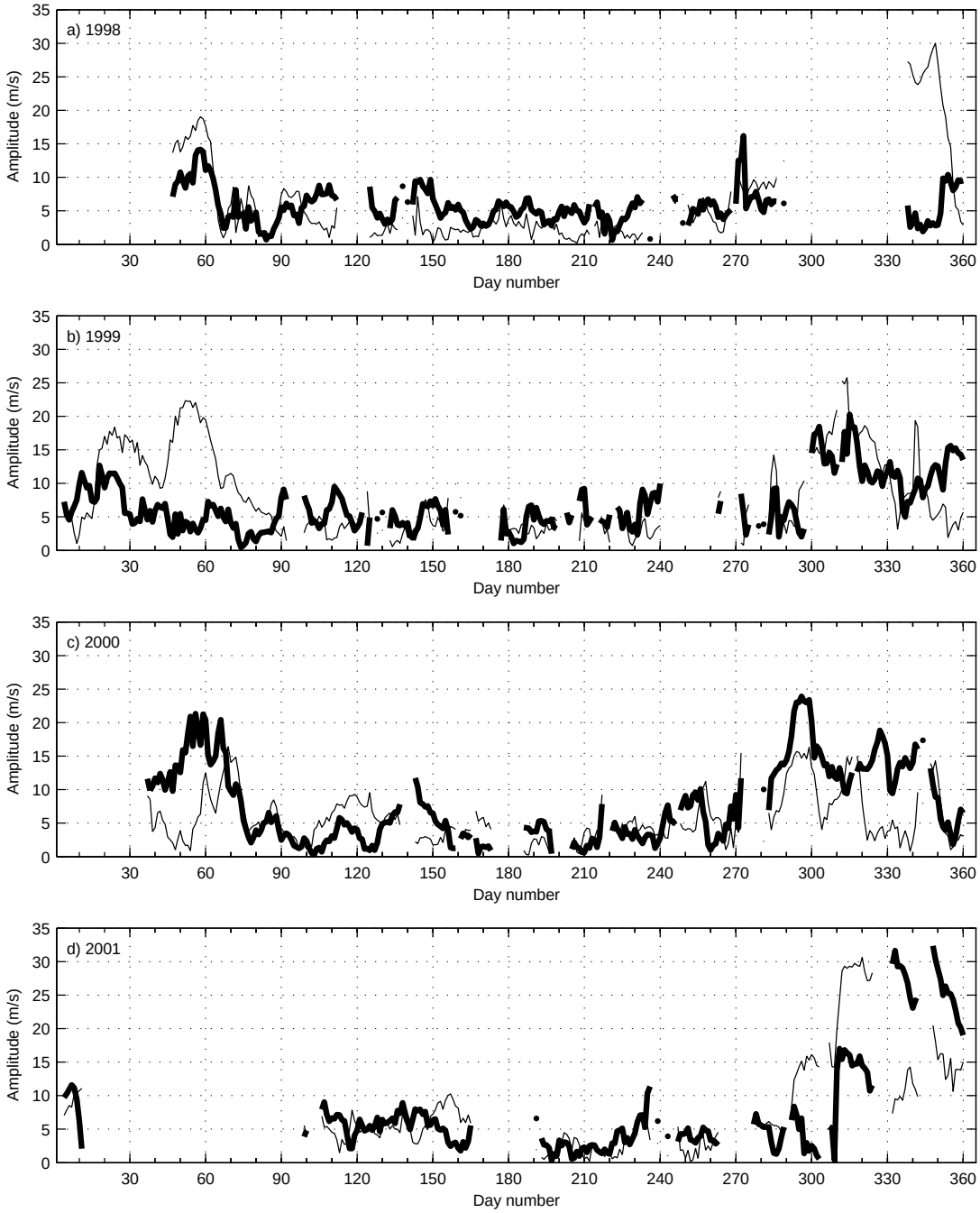

Figure 5.9: Same as Figure 5.8 but for the meridional amplitudes.

components at one location makes it possible to determine the longitude where the maxima of the two waves coincide. In order to derive this quantity we start by expressing the longitude of the maximum of each wave as a function of time:

$$L_1(t) = L_{station} + \frac{t - t_1}{12h} \cdot 360^\circ \tag{5.14}$$

$$L_2(t) = L_{station} + \frac{t - t_2}{12h} \cdot 180^\circ \tag{5.15}$$

where L_1 is the longitude of the wavenumber 1 maximum (west of Greenwich), L_2 is the longitude of the wavenumber 2 maximum (west of Greenwich), $L_{station}$ is the longitude of the station for which phases were calculated (Halley), t_1 is the time of maximum of wavenumber 1 at longitude $L_{station}$, t_2 is the time of maximum of wavenumber 2 at longitude $L_{station}$, t is the time elapsed in hours.

We now determine the time t_c at $L_{station}$ when the maxima of both components coincide:

$$L_1(t_c) = L_2(t_c) \tag{5.16}$$

$$\Rightarrow \quad L_{station} + \frac{t_c - t_1}{12} \cdot 360^\circ = L_{station} + \frac{t_c - t_2}{12} \cdot 180^\circ \tag{5.17}$$

$$\Rightarrow \quad 2(t_c - t_1) = t_c - t_2 \tag{5.18}$$

$$\Rightarrow \quad t_c = 2t_1 - t_2 \tag{5.19}$$

Substitution of this result into Equation 5.14 or 5.15 yields the longitude L_c (west of Greenwich) where the two maxima coincide:

$$L_c = L_{station} + \frac{t_1 - t_2}{12h} \cdot 360^\circ \tag{5.20}$$

It should be noted that the position of maxima coincidence observed at 90 km altitude is not necessarily the same at the altitude where the wavenumber 1 was generated. This is only the case if the vertical wavelength of the two components is equal. If the vertical wavelengths are not the same but the ratio of the two vertical wavelengths is not changing in time, then the longitudinal offset between the maxima coincidence at the source region and the observing region will be constant.

As an example the resulting longitudes for a selected period in 2000 are depicted in Figure 5.10. The period displayed was chosen so that both the wavenumber 1 and 2 component have sufficient amplitudes to determine the position of coincidence of the maxima accurately. The longitude of maxima coincidence in the zonal (meridional) component is shown in the outer (inner) ring. During this period maxima coincide in a longitudinal sector with a width of approximately 100° centred around Scott Base. This means that it is likely that the vertical wavelength ratio is approximately constant during this period and

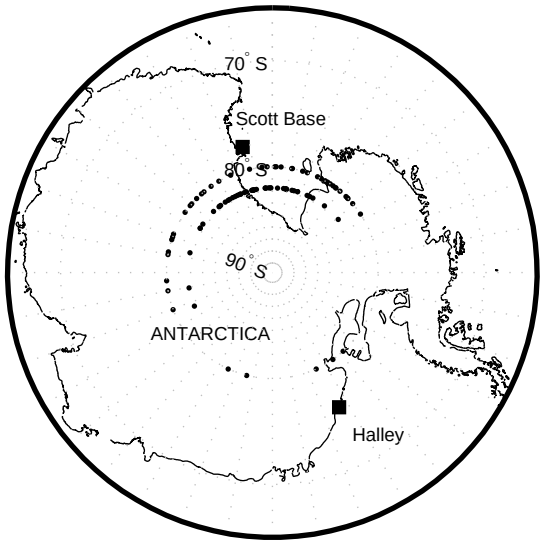

Figure 5.10: Longitude where the wavenumber 1 and 2 component maxima coincide between 26/10/2000 and 15/12/2000. The outer ring shows the results from the zonal tide, the inner ring from the meridional tide.

that the zonal structure of the source mechanism for the wavenumber 1 component is approximately stationary. However, no conclusions about the longitude of maxima coincidence at the source region can be made. Additional results will be presented in the discussion section.

5.7 Discussion

The presented work is based on the assumption that the dominant components of the semi-diurnal tide at the latitude of Scott Base and Halley are wavenumber 1 and wavenumber 2. As mentioned in the introduction, several observational studies and models indicate that this holds true, but the presence of tides with other wavenumbers, especially wavenumber 0 and a wavenumber 3, cannot be ruled out. In general, the two time-series presented in section 5.5 will represent the vector sum of all even wavenumbers (..., -2, 0, +2, ...) and odd wavenumbers (..., -3, -1, +1, +3, ...) respectively. For the case of each vector sum being dominated by one wavenumber, as assumed here, the effect on the resulting time-series will be small. However, if there are two or more components with amplitudes of the same magnitude then the resulting amplitudes as shown above will be meaningless. Only satellites, models or very extensive ground-based networks have the potential to resolve all dominant components. Angelats i Coll and Forbes (2002) studied s=1 and s=3 nonmigrating tides using UARS data and a model. For 78°S the model results showed that the wavenumber 1 dominates

over the wavenumber 3 and therefore confirms our assumption with regard to odd wavenumbers. UARS results were not available for this latitude, but for the highest UARS latitude (70°S) during summer months the s=1 tide was also larger than the s=3 tide. More studies are clearly needed in order to clarify and verify the relative importance of other components of the semi-diurnal tide.

The phase differences between the Halley and Scott Base 12 hour wave discussed in section 5.4 agree reasonably well with the data presented in Riggin et al. (1999) who used the Halley IDI as well as an MFSA radar at McMurdo. A direct comparison of the obtained phase differences is possible for 1998, which is the only overlapping year between the studies. A phase difference of 6 hours in February, November and December which is a prominent feature in the data presented here can also be found in the study by Riggin et al. (1999). This pattern is very similar from year to year, therefore the results presented here indicate little interannual variation of the phase differences. Portnyagin et al. (1998) presented amplitude measurements of the wavenumber 1 component from the South Pole and found amplitudes of up to 25 ms^{-1} in November, December and late January during measurement campaigns lasting from October to February in 1995/1996 and 1996/1997. These values compare well with our results although from other years (see Figure 5.8 and Figure 5.9).

It has been suggested that planetary waves play an important role in the generation of nonmigrating tides. Angelats i Coll and Forbes (2002) have shown that nonlinear interaction between the wavenumber 2 semi-diurnal tide and a stationary planetary wave with s=1 (PW1) creates 12 hour waves with wavenumbers 1 and 3. For 78°S in chapter 4 it was suggested that planetary waves in both the Southern Hemisphere (SH) and Northern Hemisphere (NH) partly account for the seasonal variability of the semi-diurnal tide via the generation of a wavenumber 1 tide. In the present study we investigate this further. In order for planetary waves and the s=2 semi-diurnal tide to be responsible for the s=1 component of the tide, a correlation between the s=1 tidal amplitude and PW1 activity as well as s=2 amplitudes would be expected. For the analysis of correlation coefficients the year 1999 was chosen because the radar data records have very few gaps. The expectation that nonlinear interaction between the planetary waves and tides will occur in regions where both waves are large has been examined. This relationship has been examined as a function of latitude and altitude by identifying the region of interaction by correlating the time series of the wavenumber 1 tide and PW1 amplitudes. PW1 parameters were calculated using geopotential height data from the UKMO assimilated data (see chapter 2). A Fourier transformation was employed to yield amplitudes and phases for the PW1 at all altitudes and latitudes of the UKMO grid and for every day. Note that we did not restrict the analysis to stationary planetary waves, but the results showed that the wavenumber 1 wave was nearly stationary (see below). Then Spearman correlation coefficients and the corresponding significance levels were computed between the time series of the s=1 tide and the time series of the

planetary wave amplitudes. This yielded correlation coefficients for all UKMO grid altitudes and latitudes. The results vary depending on the period used, this complication arising because planetary wave activity is large from approximately September to October in the SH and from November to March in the NH. On the other hand the tide has large amplitudes during both periods, so no latitude region can explain the time series of the tide during a whole year. Therefore, two periods for the calculation of the correlation coefficients were chosen so that in the first period only the NH (SH) planetary waves had large amplitudes. The results for 1999 are displayed in the form of contour plots in Figure 5.11. Figure 5.11a shows the correlation coefficients for the SH summer period (1/1/1999 – 1/3/1999 and 21/11/1999 – 31/12/1999) and Figure 5.11b for the SH winter period (07/04/1999 – 07/09/1999). Only regions with correlation coefficients greater than 0.3 are shown. Significance levels reach 95% in the region of largest correlation in the NH but only 80% in the SH. Note that if the daily tidal amplitude points are assumed to be independent those values increase significantly. When time lags were introduced, the correlation coefficients decreased. The largest correlation coefficients are found around 55°N at 0.3 hPa and in the region 40–55°S at 5–20 hPa. The significance level discrepancy could be a result of the fact that both the s=1 tide and the planetary wave have smaller amplitudes during the SH winter period, this could also explain the finding that the region of interaction in the SH is less clearly defined, especially with respect to altitude. The correlation coefficient for the 1999 time series of s=1 and s=2 tidal amplitudes is 0.62 and significant above the 95% level. The amplitude of the s=2 tide as observed here is most likely different from its amplitude in the region of interaction with the PW1. Therefore the observed value indicates that the s=2 tide could be involved in the generation process of the s=1 component.

The PW1 maximises at latitudes between approximately 50° and 80° (SH and NH) in the UKMO assimilated data (not shown), and the s=2 tide has its maximum amplitude between 40° and 60° in both hemispheres (Angelats i Coll and Forbes, 2002). During times where NH planetary wave activity appears to be responsible for the s=1 tide, an s=2 tide is also necessary in the NH. Jacobi et al. (1999) investigates the semi-diurnal tide at 52–56°N. Their Figure 7 shows that most sites have significant amplitudes in the crucial months of January, February and December. Therefore the interaction latitude regions inferred from Figure 5.11 are consistent with the assumption that the interaction of the two waves is likely to occur in latitude regions where both waves have large amplitudes.

For further analysis the two regions with largest correlation coefficients were chosen from Figure 5.11, namely 57°N / 0.3 hPa and 47°S / 10 hPa. In a next step the planetary wave with the highest amplitude (either from the NH or the SH) was selected for each day, yielding a single time series for planetary wave activity which will be used for discussion in the remainder of this chapter. Figure 5.12 displays the amplitudes of the zonal wavenumber 1 (thin line) and 2 (bold line) components

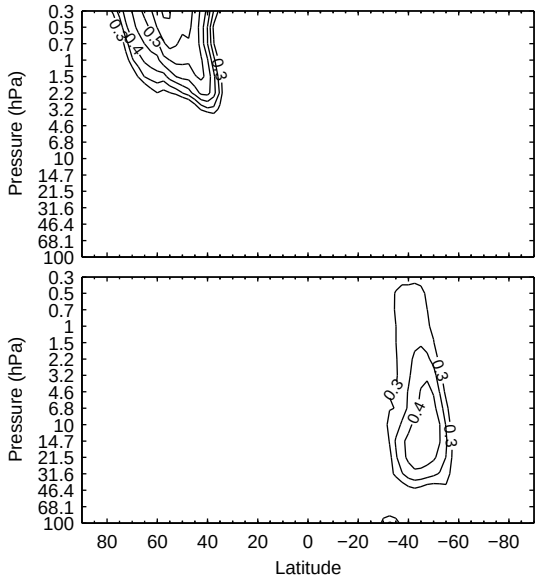

Figure 5.11: Correlation coefficients between the amplitude of the wavenumber 1 tide and planetary wave amplitudes as a function of height and latitude, determined from geopotential height in the UKMO assimilated data for times of mainly NH PW1 activity (01/01/1999–01/03/1999, 21/11/1999–31/12/1999) (a) and SH PW1 activity (07/04/1999–07/09/1999) (b). Contour intervals are 0.05 starting at 0.3.

of the semi-diurnal tide together with the amplitudes of the PW1 (dotted line) for the years 1998 to 2001. The seasonal variations of the planetary wave activity and the wavenumber 1 tide show a clear relationship as expected from the findings above. In addition, in many cases there appears to be a correlation on time scales of tens of days, for example the peak in planetary wave activity from day 65 to 80 (05/03/2000 – 20/03/2000) is also found in the amplitude of the s=1 tide. In some instances the wavenumber 1 tide can exist without a strong planetary wave. For example the sharp rise of tidal wavenumber 1 amplitude between day 10 and 20 in January 1999 (Figure 5.12a) occurs before the rise of planetary wave activity. This indicates that additional factors control the behaviour of the s=1 tide.

In section 5.6 it was shown that the longitude at which the wavenumber 1 and 2 maxima coincide varies little. As the suspected generation mechanism of the wavenumber 1 tide is an interaction between the wavenumber 2 tide and a PW1, it was investigated if there is a relationship between the longitude where the planetary wave has its maximum and the longitude where the wavenumber 1 and 2 maxima coincide. We investigate this hypothesis by means of Hovmoller diagrams which are time-longitude contour plots and display the amplitude of a wave as a function of longitude and time. Figure 5.13a, c, e and g depict Hovmoller diagrams of the s=1 tide for the years 1998–2001. Similarly Figure 5.13b, d, f and h show the planetary wavenumber 1. In all diagrams the colour indicates the normalised amplitude of the waves. The amplitudes are the same as in Figure 5.12 and the maxima coincidence longitude for the tide was calculated as introduced in section 5.6. In 1998 (Figure 5.13a and Figure 5.13b) there are two observed periods of strong tidal wavenumber 1 activity. For the first period the maxima coincidence longitude is approximately 170°E while the planetary wave has its maximum at longitudes around 135°E. Late in the year the second period of wavenumber 1 tide varies around 130–170°E. The planetary wave's maximum is found between 110 to 140°E. During 1999 (Figure 5.13c and Figure 5.13d) similar approximate agreement is found during two periods of large wavenumber 1 tides. Both appear to be centred around 180°E but deviations can be as large as 70°. The maxima of the planetary waves are centred around 180°E with deviations smaller than 45° during both periods. In the following year (Figure 5.13e and Figure 5.13f) the period around day 70 is noteworthy. The longitude of tidal maxima coincidence drifts from 225°E to 180°E, a similar drift is also observed for the planetary wave from 110°E to 65°E. Comparable drifts are also observed later in the year, for example between day 290 and 320 (16/10/2000 – 15/11/2000). In 2001 good correspondence of amplitude and longitude is found between day 280 (07/10/2001) and 305 (01/11/2001). After this period the behaviour of the s=1 tide differs significantly from the behaviour of the planetary wave (see also Figure 5.8d) and will be discussed separately below.

We can conclude that there often appears to be a relationship between the amplitudes of the wavenumber 1 component of the semi-diurnal tide and amplitudes

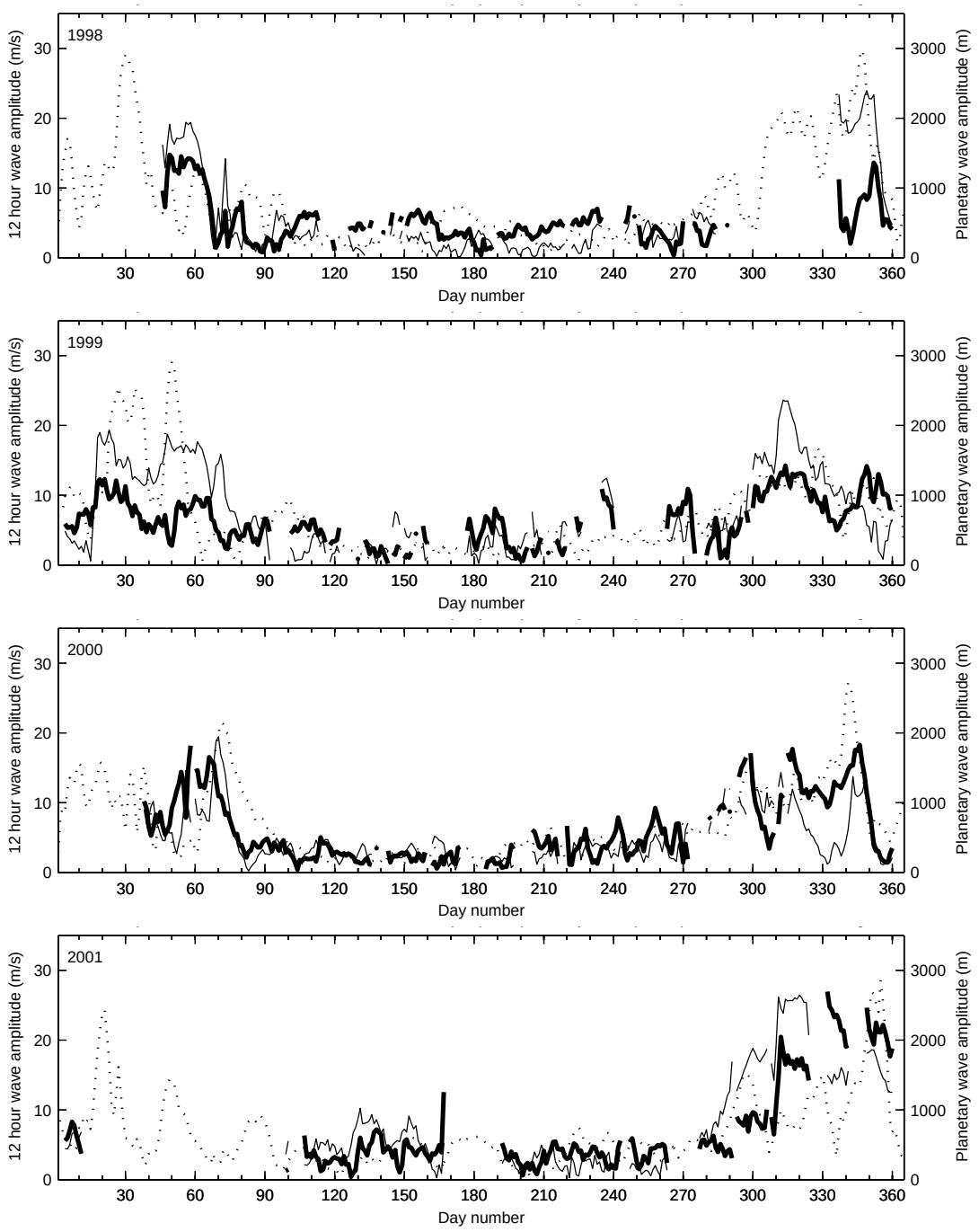

Figure 5.12: Amplitudes of the zonal semi-diurnal wavenumber 1 component (thin line), the semi-diurnal wavenumber 2 component (bold line) and the planetary wave with wavenumber 1 (dotted line) for 1998–2001. Planetary wave amplitudes were calculated from the UKMO assimilation geopotential height data at a combination of SH and NH regions. For details see text.

of the PW1 as well as between the longitude of maxima coincidence of the two tidal components and the planetary wave maximum. The maxima of the waves generally appear in the same longitude region, and often show similar variations in time. This indicates that the vertical wavelengths of the two tides must be similar and stable during many periods. As noted earlier, different vertical wavelengths would create an offset between the longitude where the planetary wave has its maximum and the longitude at which the maxima of the tides coincide. If the ratio of the wavelengths varies the longitude where the maxima of the tides coincide will drift and decorrelate with the planetary wave.

Note that Figure 5.10 and Figure 5.13 show that the maxima of the wavenumber 1 and 2 component appear to coincide closer to Scott Base (166.7°E) than to Halley (333.6°E). Therefore in the vicinity of Halley the wavenumber 1 will have a minimum and the wavenumber 2 a second maximum. The 12 hour wave amplitude differences between Scott Base and Halley, with larger values at Scott Base (see Figure 5.1 and Figure 5.2), can then be understood as approximate constructive interference of the two components at Scott Base and destructive interference at Halley.

Planetary wave interactions with tides appear to play an important role in the generation of the s=1 semi-diurnal tide but do not explain every period of s=1 tide activity (for example in January 1999, Figure 5.12b) and every feature in the behaviour of the longitude of tidal maxima coincidence (for example in November 2001, Figure 5.13g and h). Riggin et al. (1999) and others have suggested that zonally asymmetric heating via particle precipitation in the auroral oval could be amongst alternative generation mechanisms. The auroral oval is approximately centred around the magnetic south pole (currently at 64.6°S and 138.5°E), therefore heating in this area would approximately create a wavenumber 1 temperature structure with respect to the geographic pole. Through interaction with the s=2 tide this could potentially generate a s=1 tide. We have used proton flux data provided by GOES satellites (NOAA, 2005) as a proxy for heating through particle precipitation in the auroral oval. Initial investigations indicate that there is some correlation between high solar proton flux rates after solar proton events and amplitudes of the components of the semi-diurnal tide. Correlation coefficients and significance levels are not meaningful at this stage of the analysis because even if a real relationship exists we have no understanding of the mechanisms and circumstances of this interaction and therefore cannot choose the appropriate variables or times to make a comparison. To indicate that this may be an interesting area of further work, two example periods are discussed briefly. In November 2001 the flux of protons with energy greater then 10 MeV rose to $6.2 \cdot 10^8$ protons/(cm^2·day·sr) on day 310 (06/11/2001) during a strong solar flare which lasted for several days (data obtained by the GOES-8 instrument and provided by the NOAA Space Environment Center). Especially the 12 hour s=1 component experienced a dramatic amplitude increase on that day (see Figure 5.8d and Figure 5.9d) which is sustained for the entire period of

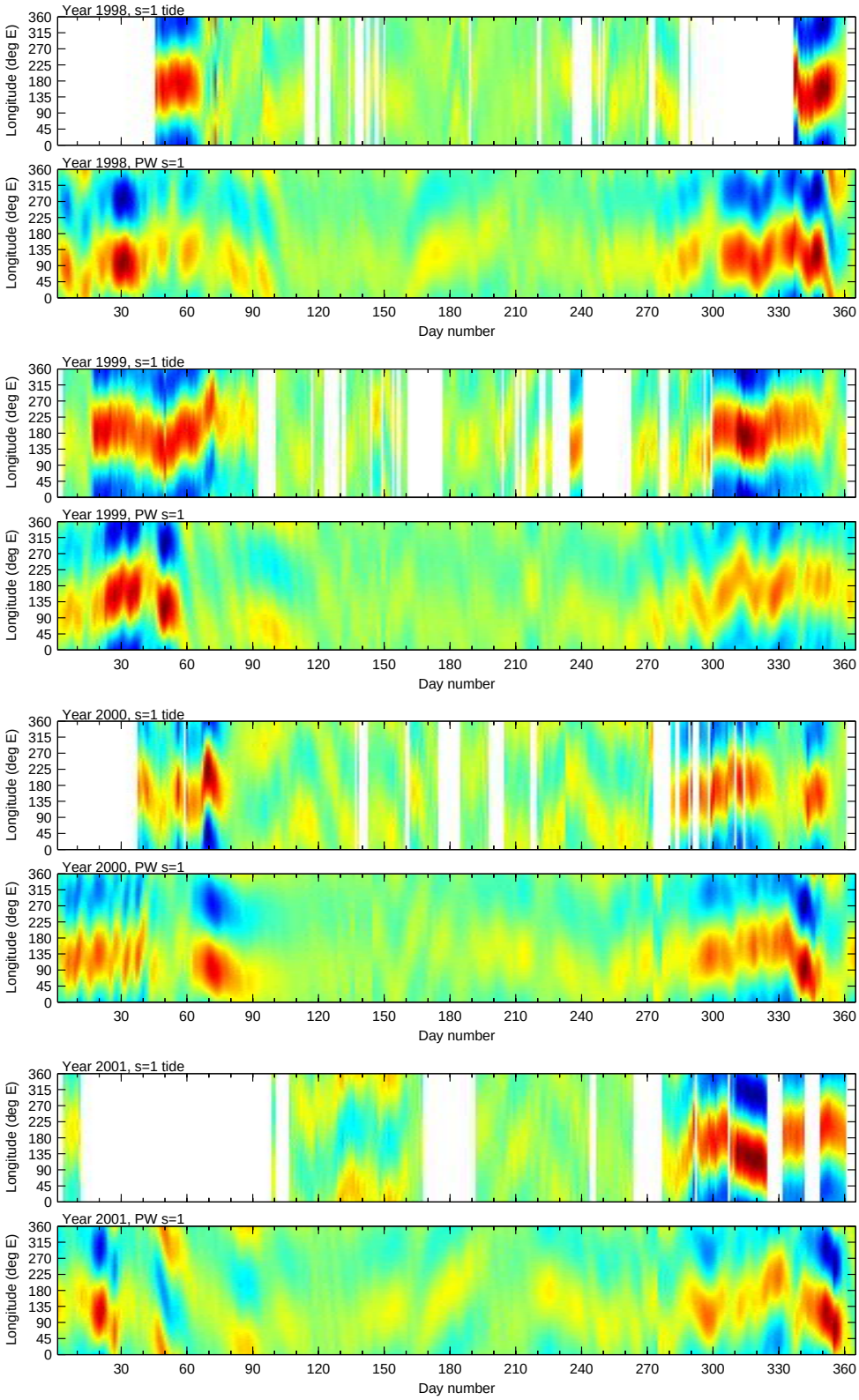

Figure 5.13: Hovmoller diagrams for the wavenumber 1 tide (a,c,e,g) and the wavenumber 1 planetary wave (b,d,f,h). See text for details.

the enhanced proton flux rate. Note that the PW1 amplitude does not change significantly during this period. Another example of large s=1 tidal amplitudes coinciding with a solar flare but not with large PW1 activity occurs in January 1999. The amplitude increase observed occurs just after the onset of the solar flare. However, these findings are highly speculative and much further investigation is necessary.

5.8 Conclusions

It has been shown that the zonal structure of the semi-diurnal tide at the latitudes of Scott Base and Halley can be described consistently using a combination of wavenumber 1 and 2 waves. Wind velocity data from a medium frequency radar at Scott Base and the imaging Doppler interferometer at Halley allowed the separation of the wave components under certain assumptions. In summer the wavenumber 1 component is often dominant; through most of the winter months both components have similarly small amplitudes. Tidal wave wavenumber 1 amplitudes in the southern and northern hemispheres was confirmed as having a strong relationship with planetary wavenumber 1 activity. Therefore generation of the wavenumber 1 tide through interaction between the wavenumber 2 tide and planetary waves seems likely. The regions where this interaction is most likely to occur were identified to be the upper stratosphere at mid- to high-latitudes. We were further able to show that when the s=1 tide was large the longitude where maxima of the s=1 and s=2 tide coincide is related to the maximum of the planetary wave. In addition, asymmetric heating through proton flux into the auroral oval was indicated to be a possible mechanism for the generation of the wavenumber 1 tide and in one particular case was shown to be important. However, the latter hypothesis needs much further investigation.

Chapter 6

A Gravity Wave Climatology for Antarctica Compiled from CHAMP/GPS Radio Occultations[1]

Gravity waves are a ubiquitous phenomenon in the middle atmosphere and have many important effects on atmospheric mean states, dynamics and chemistry. This chapter presents the seasonal, geographical, and altitudinal dependence of gravity wave activity in the lower stratosphere over Antarctica. The analysis allows conclusions to be drawn about wave sources and propagation. The work serves as a basis for further study on propagation of gravity waves through the upper stratosphere and mesosphere, and for studies of interactions with other types of waves such as planetary waves and tides.

For the analysis presented in this chapter, gravity wave activity is estimated by calculating potential energy, E_p, from radio occultation profiles obtained by the CHAMP/GPS (CHAllenging Minisatellite Payload/Global Positioning System) experiment. Significant seasonal variation of wave activity is observed. Smaller wave activity in summer is attributed to waves with small phase velocities experiencing critical level filtering. At other times of the year, when wave activity is large, less filtering occurs and the strong background wind is likely to cause Doppler shifting of waves to longer vertical wavelengths, which can reach larger amplitudes before saturating. Relationships between gravity wave activity and geographic location indicate that topography is a strong source for wave activity especially over the Antarctic Peninsula. However, wind rotation in this area was found to reduce the wave energy in summer at certain altitudes. A strong enhancement of wave energy is observed at the edge of the polar vortex. Again, reduced critical level filtering and Doppler shifting in the area of the jet are likely to be major causes for this finding. Possible limitations to this study due to observational filtering are discussed.

[1]This chapter has in a similar form been accepted for publication by the Journal of Geophysical Research (Baumgaertner and McDonald, 2007) and was co-authored by A. J. McDonald.

6.1 Introduction

A general introduction on gravity waves and their mathematical description has been given in chapter 1. Here, an overview of wave properties and measurement techniques important for the study of gravity waves over Antarctica is presented.

In the Arctic and Antarctic gravity waves have been found to have an influence on the formation of polar stratospheric clouds (PSC) (Cariolle et al., 1989; Carslaw et al., 1998; Wu and Jiang, 2002; Shibata et al., 2003; Palm et al., 2005) which in turn play an important role in ozone depletion. In particular, mountain waves have been reported to be of relevance for PSC formation (Cariolle et al., 1989; Höpfner et al., 2006). In addition, the mesopause is the region of the atmosphere furthest away from radiative equilibrium at the poles and thus gravity waves must have a large impact there. It has been shown that gravity wave breaking has important consequences for the polar winter stratosphere down to altitudes below 30 km because of downward control (Haynes et al., 1991; Garcia and Boville, 1994).

Gravity waves are evident as fluctuations in many atmospheric parameters, such as wind velocity and temperature, on time scales of minutes to several hours, and on horizontal scales ranging from approximately 100 m to 1000 km. There are many different observational techniques that can measure gravity wave activity. However, it is difficult to obtain a complete picture of the gravity wave field because each technique has limitations with regards to the resolved vertical wavenumbers, horizontal wavenumbers and frequencies. Doppler shifting and refraction in combination with the observational filter (Alexander, 1998) also make interpretation difficult, therefore it is difficult to assess the variability of wave sources, filtering, and wave saturation without accounting for these observational influences.

The radio occultation (RO) technique (Kursinski et al., 1997) provides a well quality controlled atmospheric data set with global coverage and high vertical resolution in the troposphere and stratosphere. Profiles of dry temperature obtained in this way complement balloon soundings, lidar and satellite measurements. Studies in remote areas like Antarctica especially benefit from this technique. Details of the experiment and the analysis technique have been described in chapter 2. Tsuda et al. (2000) was among the first to study gravity wave potential energy calculated from temperature profiles obtained by GPS/MET, the first RO experiment for Earth. They found that the temperature profiles and wave energy compared well with other measurements and theoretical considerations and presented a nearly global gravity wave climatology. Note that the GPS/MET experiment yields very few soundings over the polar regions due to the low inclination of the satellite, so no data were presented for Antarctica. Tsuda et al. (2000) indicated that the largest wave activity was found over the equator which was assumed to be related to convection. At midlatitudes greater

wave activity was observed over the continents than over the Pacific ocean. This was tentatively treated as possible evidence for the presence of orographic gravity waves over the continents. Using three months of data from CHAMP and SAC-C, de la Torre et al. (2004) studied the geographical distribution of gravity wave potential energy. Activity associated with low-latitude convection was reported as well as enhancements of potential energy over the continents in the northern hemisphere and over the southern hemisphere Andes Range. de la Torre and Alexander (2005) investigated the peak energy over the Andes in more detail and found that it is not necessarily related to orography. Observational filtering was found to reduce the likelihood of observations of mountain waves with the RO technique, and other wave sources, especially geostrophic adjustment processes caused by the presence of a permanent jet below the tropopause, were found to be more likely to create the observed wave activity over the Andes. Ratnam et al. (2004a) used CHAMP data for a global analysis of gravity wave activity and also found large wave potential energy over the equator below 25 km. In addition, large wave energy was found at midlatitudes in winter. Their study also indicated large E_p values over Antarctica during spring 2002, which were described in more detail in Ratnam et al. (2004b) and found to be related to the stratospheric warming that occurred during that period.

It is possible to infer gravity wave activity from a range of satellite measurements as mentioned previously. Radiance fluctuations measured by the Upper Atmosphere Research Satellite Microwave Limb Sounder (UARS MLS) were used by Wu and Waters (1996) and McLandress et al. (2000) for this purpose. McLandress et al. (2000) reported that the instrument was able to resolve longitudinal differences in wave activity, and correlations between wave activity and deep convection and topography in South America were demonstrated. Similarly, a strong enhancement of wave energy over the Drake Passage was examined in more detail by Wu and Jiang (2002) and shown to peak in August and September every year. The authors were not able to clearly identify the reason for the large wave activity measured over this area.

There are several studies which specifically address gravity wave activity in the polar regions using ground-based instruments. Using radiosonde data from Eureka (80°N), Whiteway and Duck (1996) found that gravity wave activity was only enhanced if no critical level filtering occurred. Whiteway and Duck (1996) also emphasised the intermittency of the wave activity as they found several isolated periods of large wave energy rather than a smooth seasonal cycle. Their study also displayed a high correlation between wave energy and the background horizontal wind at 1 km altitude. These results indicate that the major gravity wave source at Eureka is topography. Lidar measurements from the same location, presented in Whiteway et al. (1997), showed that the strongest wave activity occurred when Eureka was at the edge of the polar vortex, which was attributed to reduced filtering of orographic waves during those times. This was especially evident at longer vertical wavelengths because of Doppler shifting. Similarly,

Duck and Whiteway (2000) presented data from four Arctic radiosonde stations and showed that gravity wave energy decreased dramatically after the vortex breakdown. Again, this was attributed to the reduction of critical level filtering of topographic waves.

Yoshiki and Sato (2000) analysed 10 years of radiosonde data from the Arctic (12 stations) and Antarctica (21 stations). In the Arctic at all altitudes maximum wave energy was found in winter. In the Antarctic at 25–30 km the maximum also occurred during winter, but between 15 and 25 km the maximum appeared in spring and was described as a downward progression of an area of high stability and high wave energy. Topography was found to be important in the Arctic but not in the Antarctic, where filtering of mountain waves was found to occur at approximately 5 km. Syowa (69°S) radiosonde data were presented separately in Yoshiki et al. (2004). Similar to the results at Eureka (Whiteway et al., 1997), enhancements at the edge of the southern polar vortex were found. However, in the study of Yoshiki et al. (2004) this observation was attributed to gravity waves generated at the edge of the vortex.

The important role orographically generated gravity waves play is widely recognised. Case studies over mountainous terrain (Bacmeister et al., 1990), where data were collected by aircraft, as well as studies of a more statistical nature (Nastrom and Fritts, 1992; de la Torre et al., 2004; Wu and Jiang, 2002) have shown that airflow over orographic features contributes significantly to the overall gravity wave activity. Most of these studies also found that critical levels can inhibit vertical propagation of orographic gravity waves very effectively.

In the present chapter we first give a brief description of the data set in section 6.2, followed by a statistical analysis of gravity wave potential energy in section 6.3. Section 6.4 presents results regarding various aspects of wave activity over Antarctica, and section 6.5 discusses those findings. Conclusions and future work are outlined in section 6.6.

6.2 The Data Set

This study employs data from the radio occultation (RO) experiment on the CHAMP satellite. In this experiment, GPS radio signal bending due to atmospheric refractivity is used to determine profiles of atmospheric parameters as described in chapter 2. Level 3 version 005 data were used in this study. Only data from the region 60°S to 90°S are presented here, which restricts the number of available profiles to approximately 25 per day. The geographical distribution of the profiles is relatively even in this area if data are employed at a resolution of approximately 500 by 500 km and one month. However, during several months every year the maximum resolution for an even distribution is approximately 1000 by 1000 km. Another exception is the area south of 85°S where in some months

the number of profiles is very small. From Fresnel diffraction theory it can be shown that the profiles have a true vertical resolution of approximately 1.4 km in the stratosphere. However, the data is provided by the GFZ at a vertical resolution of 200 m. The horizontal resolution of an occultation is 200–400 km along the line of sight (LOS) and of the order of 1 km across the LOS.

For the present study, the gravity wave activity measure used is gravity wave potential energy. In general, gravity wave energy is the sum of potential and kinetic wave energy, but linear gravity wave theory predicts that on average the ratio of potential to kinetic Energy, E_p/E_k, is constant (Nastrom et al., 2000; Ratnam et al., 2004a). Therefore we can assume the total gravity wave energy to be proportional to potential energy, which can be calculated from temperature profiles alone. The calculation of potential energy from temperature profiles is described in detail by Tsuda et al. (2000). Briefly, the entire temperature profile from the ground to 35 km is high-pass filtered with a Hamming window using a cutoff wavelength of 10 km yielding temperature perturbations T'. T'^2 was integrated using a sliding window with a width of 2 km and a step size of 200 m equivalent to the vertical resolution of the profile. The mean temperature $\bar{T}$ and the temperature gradient were calculated using a sliding window with a width of 600 m and from this the Brunt-Väisälä frequency N was computed. Finally, potential energy E_p was estimated as:

$$E_p = \frac{1}{2}\frac{g^2}{N^2}\overline{\left(\frac{T'}{\overline{T}}\right)^2} \tag{6.1}$$

As an example, a temperature profile for an occultation over the Antarctic continent on 1 February 2004, 16:03 UTC, at 80°S and 54°E is depicted in Figure 6.1a. Also shown are the temperature perturbations T' (Figure 6.1b) obtained by high-pass filtering the temperature profile, the Brunt-Väisälä frequency squared N^2 (Figure 6.1c), and the resulting potential energy profile E_p (Figure 6.1d). In this particular profile, enhancement of potential energy is found between 20 and 25 km as well as above 28 km.

As mentioned above, the true vertical resolution of the temperature profiles is approximately 1.4 km, therefore only waves with vertical wavelengths greater than 2.8 km can be detected. The processing technique used here employs a filter with a length of 10 km which leads to little sensitivity for waves with vertical wavelengths greater than 10 km. As mentioned in the introduction, this observational filter implies that wave activity variations with height, time, or location have to be treated cautiously. Because of the resolved wavelength range, the current study complements work using radiosondes (which have good sensitivity to gravity waves with vertical wavelengths below approximately 4 km) and microwave limb sounders (sensitivity to waves with vertical wavelengths greater than 10 km) very well. The detection of gravity waves with small horizontal wavelengths depends on the viewing angle. E_p values estimated with radiosonde observations

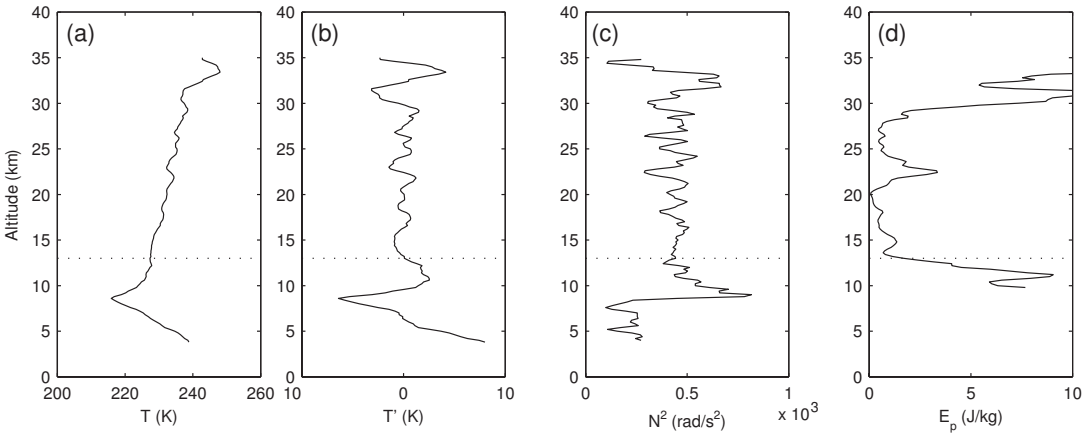

Figure 6.1: Temperature profile (a), temperature perturbations (b), Brunt-Väisälä frequency squared (c), and potential energy (d) for the profile obtained by CHAMP on 01 February 2004 16:03 UTC at 80°S, 54°E.

are slightly larger than those observed using the RO technique (Ratnam et al., 2004a), which may be due to the resolved vertical wavelengths, the horizontal resolution, and spherical symmetry assumptions implemented in the retrieval of the RO temperature profiles. We conclude that in general E_p is underestimated but will investigate this further in the discussion section. The RO technique yields profiles of dry temperature, which are a good approximation to temperature profiles above the tropopause. However, below the tropopause there can be significant differences between temperature and dry temperature. Therefore we do not examine tropospheric data in this study. A particular problem associated with the high-pass filter arises near the tropopause (Ratnam et al., 2004b). In summer and autumn a sharp tropopause, as seen in Figure 6.1a, leaves a clear signature in the temperature perturbation profile (Figure 6.1b) and therefore leads to an enhancement in E_p in Figure 6.1d. Therefore during summer and autumn E_p cannot be used as an estimator for gravity wave activity between the tropopause and 3–4 km above it. The minimum altitude at which E_p becomes a useful variable for measuring wave activity is indicated by the dotted lines in Figure 6.1.

For the present study RO data from 1 January 2002 to 30 June 2006 are employed. Although CHAMP RO data are available from 14 May 2001, the number of profiles over Antarctica during 2001 is low and is thus not presented here. In 2002 a stratospheric warming occurred in the southern hemisphere, creating unusual dynamics in the stratosphere (Newman and Nash, 2005; Ratnam et al., 2004b), therefore data from winter and spring 2002 will not be representative of the climatological mean and have to be treated with caution. Only the first six months of 2006 of CHAMP RO are available, thus data from 2006 will no be discussed in detail.

Wind velocities presented in this chapter were taken from the daily NCEP/NCAR reanalysis which is described in chapter 2.

6.3 Statistical Properties of E_p

The distribution of E_p values at a specific altitude over Antarctica is very similar to the lognormal distribution. Figure 6.2 displays the normalised histogram of E_p values over Antarctica in the height region 20 to 22 km south of 60°S. At other altitudes the histogram looks very similar to the one presented in Figure 6.2, however, the mean and standard deviation vary slightly with height. The time period covered is January 2002 to June 2006 and all available 40,092 profiles were used. Depicted on top of the measured distribution is the probability density function for the lognormal distribution

$$y = \frac{1}{x\sigma\sqrt{2\pi}} e^{-(\ln x - \mu)^2/2\sigma^2} \tag{6.2}$$

where the expected value $\mu = -0.70$ and the standard deviation $\sigma = 1.1$ were calculated from the actual distribution of E_p using maximum likelihood estimation of parameters:

$$\hat{\mu} = \frac{\Sigma_k \ln x_k}{n} \tag{6.3}$$

$$\hat{\sigma}^2 = \frac{\Sigma_k (\ln x_k - \hat{\mu})^2}{n} \tag{6.4}$$

The fact that E_p has a lognormal rather than a normal distribution has implications for the way the mean of E_p should be formed with regards to time and geographic position at any given height. Thus, the geometric mean (or median of the lognormal distribution) $m' = \exp(\mu)$ and the geometric standard deviation $s' = \exp(\sigma)$ are more appropriate parameters to describe E_p than the arithmetic (or sample) mean and standard deviation. Although commonly distributions are characterised by their expected value μ and the standard deviation σ, the geometric mean and geometric standard deviation are easier to interpret in the case of the lognormal distribution.

6.4 Results

6.4.1 Seasonal Variation of Potential Energy

In order to examine the seasonal variation of gravity wave activity, monthly means of all E_p profiles over Antarctica were formed. The results at each altitude were normalised by dividing the value for each month by the mean value over the

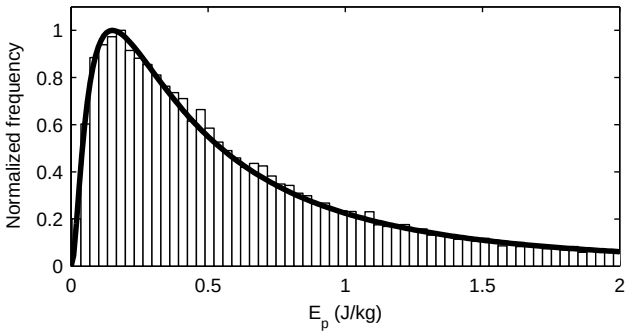

Figure 6.2: Bars: Normalised histogram of E_p at 20 to 22 km for January 2002 to June 2006 and for 60°S to 90°S. Line: Lognormal probability density function.

entire period from this altitude. The resultant ratio of potential energy to mean potential energy as a function of height and time is presented in Figure 6.3 for the years 2002 to 2006. The bold line indicates the height of the thermal tropopause. Note that in winter and spring there is no sharp tropopause, so the altitude shown here has a very large standard deviation (not shown) during those months. Zängl and Hoinka (2001) discussed this feature and suggested the dynamical criterion for the tropopause would be better suited to the identification of the tropopause altitude during polar winter, but since CHAMP only provides temperature data, the thermal criterion was adopted. As mentioned above, enhancements between the tropopause and 3–4 km above are associated with the filter and the tropopause. A strong annual variation is evident above 15 km. The maximum appears between August and September at 30 km and appears to propagate downward, reaching 18 km with a peak near 20 km altitude between September and November.

From Figure 6.3 interannual variation is also evident. The winter maximum as well as the spring maximum are strongest in 2004. In October 2004 potential energy exceeds the mean value at 20 km by a factor of 2.5, while in 2003 and 2005 the maxima occur in November and exceed mean wave activity by a factor of 2 and 1.6, respectively. The pattern of wave activity observed in 2002 is different to all other years in several aspects. The seasonal cycle appears to be shifted towards earlier times by approximately two months. In addition, the maximum wave activity, which occurs in August and September, is much weaker than in other years. At 20 km during times of maximum wave activity values exceed the mean by a factor of 1.4 only. This shift in 2002 however also means that during autumn and winter activity is stronger than usual. Larger than normal wave activity during the Antarctic winter of 2002 has previously been reported by Ratnam et al. (2004b). The minimum activity in summer occurs in January in all years and does not appear to be subject to strong year to year variations. The interannual variations require further analysis and will be the subject of future work.

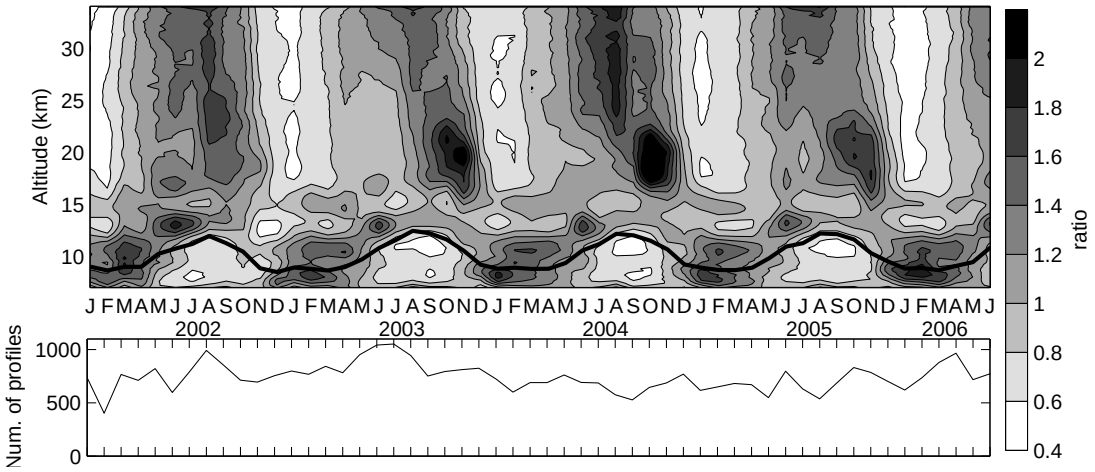

Figure 6.3: Top panel: Time and height dependence of E_p for 2002 to 2006 for 60°S to 90°S. The bold line indicates the height of the tropopause. Bottom panel: Number of available profiles per month.

Also shown in Figure 6.3 is the variation of the number of profiles available for each month. There is no dominant seasonal cycle evident, so an influence of the temporal measurement distribution on the seasonal cycle of gravity wave potential energy can be ruled out.

6.4.2 Altitudinal Variation

Amplitudes of gravity waves grow exponentially with altitude because of conservation of energy and the exponential decrease of atmospheric density with altitude. However, wave sources in the stratosphere and wave dissipation have the potential to modify the behaviour of potential energy as a function of altitude. The present study examines wavegrowth using CHAMP RO profiles from the Antarctic. Figure 6.4 depicts mean potential energy profiles for summer 2003/4 (solid line), autumn (dotted line), winter (dashed line), and spring (dash-dotted line) in 2004. E_p is not a valid estimator for gravity wave potential energy up to 3–4 km above the tropopause in summer and autumn as discussed in section 6.2. Using the height of the tropopause from Figure 6.3 (bold line), E_p is then likely to be a good approximation for potential energy above 12–13 km during summer and autumn. In winter and spring no sharp tropopause exists, thus no strict restrictions apply to the altitude range used (Zängl and Hoinka, 2001). Therefore we will assume 13 km to be the lower limit for studying potential energy with the described technique. Figure 6.4 shows an exponential increase of gravity wave activity above approximately 18 km altitude for all seasons. The scale height of E_p is approximately 10 km. However, between 13 and 18 km there is an exponential decrease in potential energy during all seasons except spring. It is possible that

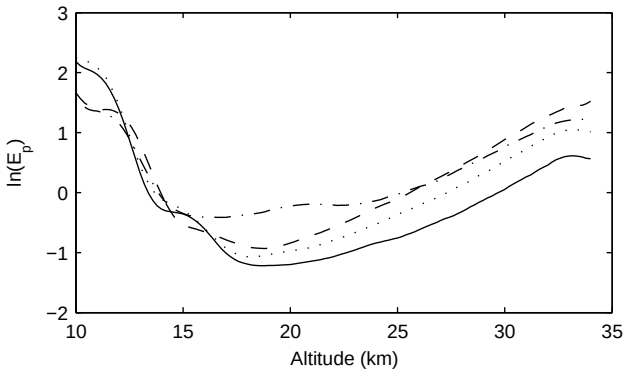

Figure 6.4: Logarithm of potential energy over Antarctica as a function of altitude for summer (solid line, DJF 2003–2004), autumn (dotted line, MAM 2004), winter (dashed line, JJA 2004), and spring (dash-dotted line, SON 2004).

dissipation or critical level filtering of wave activity create this feature. In the discussion section critical level filtering will be examined in more detail. Because of the difficulties in interpreting the results for E_p in the lower stratosphere the remainder of this section focusses on the altitude region above 18 km. There is the possibility that the increase of potential energy at higher altitudes is partly due to ionospheric residuals. This has not been investigated further.

6.4.3 Geographic Variation

The geographic variation of potential energy is examined by studying the variation of E_p with respect to latitude and longitude. Unfortunately the resolution of the CHAMP data is too coarse to allow conclusions to be drawn from latitude/longitude maps of wave activity. However, averaging over latitude or longitude yields consistent results. Figure 6.5 depicts E_p as a function of longitude for the year 2003 in two altitude regions, 18–22 km (solid line) and 23–27 km (dashed line). Profiles were averaged over 60°S to 90°S and 1° longitude bins, then smoothed with a 20 point running mean and normalised. The crosses depict the unsmoothed data. Strong wave activity is observed in the lower stratosphere (18–22 km) over the Transantarctic mountains (approx. 160°E) and over the Antarctic Peninsula (approx. 60°W). It is unlikely that this distribution of wave energy is generated by sources such as geostrophic adjustment or shear. These sources are more likely to account for the wave energy that does not depend on longitude. Instead it suggests that topography is an important factor over both these regions which have mountain ranges with altitudes reaching 4000 m. The enhancement over the Peninsula exceeds 20% of the mean potential energy. At higher altitudes (23–27 km) this relationship is less pronounced, suggesting that the topographically generated signal may have been partially filtered from the wave field at this altitude. The longitudinal variation of E_p is similar in other

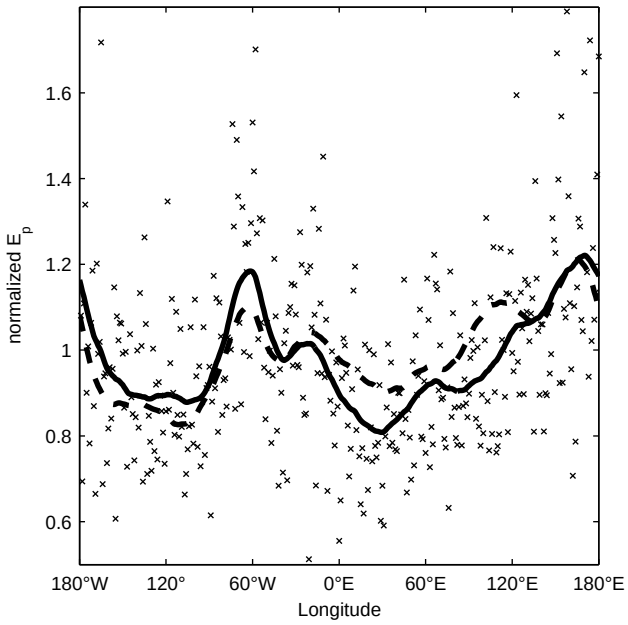

Figure 6.5: Longitudinal dependence of E_p at 18–22 km (solid line) and 23–27 km (dotted line) for 2003. Crosses show the unsmoothed values (1° longitudinal resolution) at 18–22 km.

years (not shown).

Enhancements around the Antarctic Peninsula have also been observed by other instruments (Wu and Jiang, 2002) and are now examined in more detail. Figure 6.6 and Figure 6.7 show all individual occultations in 2004 where E_p was smaller than 0.5 J/kg and larger than 3 J/kg, respectively, in the lower stratosphere (18–26 km) over the Peninsula. The arrows attached to each occultation represent the strength and direction of the wind at 1000 hPa taken from the NCEP/NCAR reanalysis for the respective latitude, longitude and day of the occultation. While in the case of low E_p values (Figure 6.6) the wind shows no preferred pattern, strong eastward winds are evident when large gravity wave activity is observed (Figure 6.7). Statistically, the correlation between E_p at 18–22 km and the strength of the zonal wind in the troposphere over the Peninsula is significant and maximises between 1 and 10 km altitude (not shown). The correlation coefficient varies from year to year and reaches between 0.15 and 0.25. The significance level exceeds 99% in all cases. For E_p at 23–27 km this height dependence is weaker but the correlation coefficient still maximises in the troposphere. The fact that correlation between wave activity in the lower stratosphere and wind in the troposphere is observed, again indicates that flow over the topography of the Peninsula contributes significantly to wave activity in the stratosphere. The reduction of the correlation coefficient for E_p at higher altitudes could be interpreted as filtering of mountain waves. Over areas without

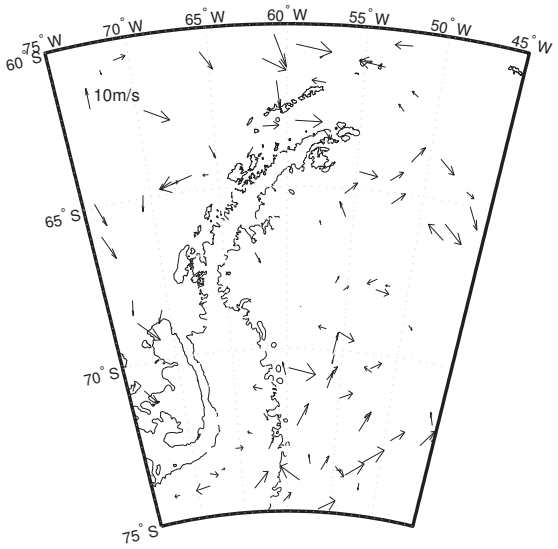

Figure 6.6: NCEP/NCAR 1000 hPa wind vectors of occultations with $E_p < 0.5\ J/kg$ in the 18–26 km region over the Antarctica Peninsula in 2004.

significant topography this correlation is not found. For example in an area centred over Syowa, the correlation coefficient does not exceed 0.05, similar to the results presented in Yoshiki and Sato (2000). In their work, a correlation between gravity wave activity at 15–20 km over Syowa and the wind in the lower stratosphere was reported, but the correlation with tropospheric wind velocities was negligible, therefore the wave activity was attributed to stratospheric sources.

Figure 6.8 shows the variation of E_p with latitude between 45°S and 90°S for 2002–2006 in two altitude regions, 18–22 km (solid lines) and 23–27 km (dotted lines, offset by 1 for clarity). The depicted data represent an average for all longitudes. Grey lines represent individual years, black lines the average for the entire period. Small E_p values are observed around the pole in both altitude regions (60% of the mean). An increase in E_p towards 75°S is found in both regions of the lower stratosphere, although the relative increase is higher in the low-altitude region. At 18–22 km potential energy further increases between 65°S and 45°S to 140% of the mean, but at 23–27 km there is no further increase towards midlatitudes. Individual years (grey lines) show very similar behaviour to the average of 2002–2006 (bold lines). The large value at about 47°S in the 18–22 km altitude band is for the year 2006 and is probably related to the fact that there is only six months of data available. Numerous studies have suggested enhanced gravity wave activity at the edge of the polar vortices (Yoshiki et al., 2004). In order to examine this in more detail, gravity wave energy is studied as a function of distance to the vortex edge. The concept of equivalent latitude, defined by

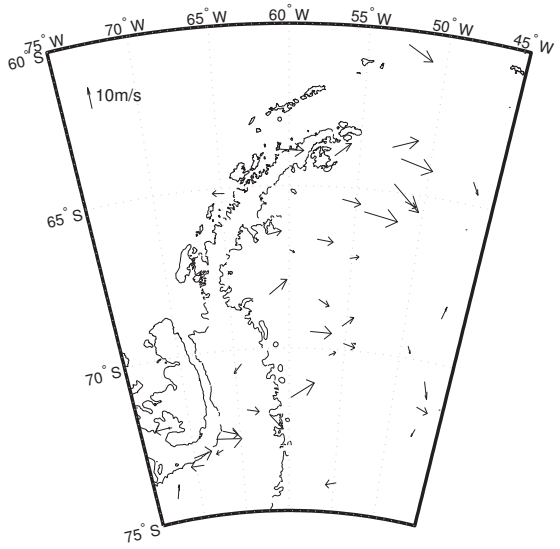

Figure 6.7: Same as Figure 6.6 but for occultations with $E_p > 3\ J/kg$.

Nash et al. (1996), is helpful in this context and has also been used by Yoshiki et al. (2004) for studying the relationship between wave energy and distance to the vortex. Equivalent latitude is defined as the latitude whose latitude circle covers the same area as a potential vorticity (PV) contour encloses. Distance to the vortex edge is measured by subtracting the equivalent latitude of each individual RO measurement from the equivalent latitude of the vortex edge on the day of the measurement. The equivalent latitude of the vortex edge at 550 K was calculated using NCEP/NCAR PV data. By using the geographic grid point in the PV data closest to each RO event, a PV value was assigned to every RO measurement. Equivalent latitude was calculated as a function of PV, so that an equivalent latitude could be assigned to each measurement. Figure 6.9 displays the mean potential energy at 23 to 27 km altitude for 1 May to 20 November in the years 2002 (solid line), 2003 (dashed line), 2004 (dotted line), and 2005 (dash-dotted line) as a function of distance to the vortex edge. The dates were chosen so that the vortex edge was clearly defined in all years. The result has been smoothed with a 5 point running mean. It is clear that the CHAMP RO data confirm the findings of other measurements in that potential energy is enhanced near the vortex edge. In the presented cases the enhancement exceeds 1.4 J/kg (apart from 2005 where it only reaches 1.3 J/kg) and spans about 10° to 20° of equivalent latitude. Further away from the vortex, potential energy varies between 0.8 and 1.2 J/kg. Note this is particularly clear in 2003. At altitudes below 20 km and above 30 km little enhancement is found around the vortex edge (not shown). This is highly indicative that the region where critical level filtering

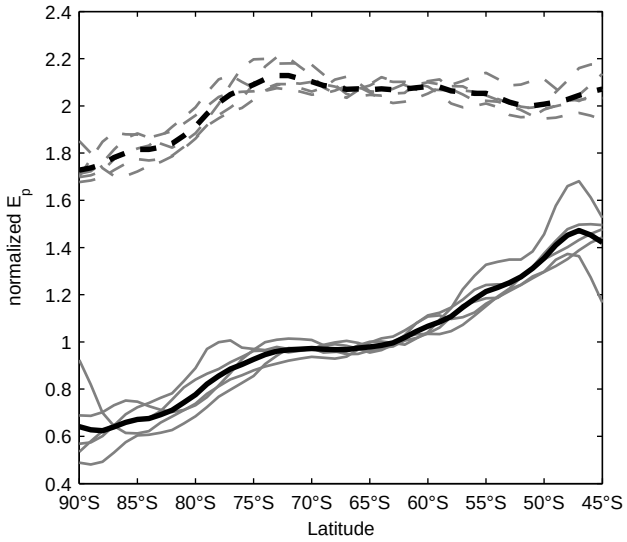

Figure 6.8: Latitudinal dependence of E_p at 18–22 km (solid lines) and 23–27 km (dotted lines, offset by 1) for 2002–2006. Grey lines represent individual years, black lines the average for the entire period.

occurs is between 20 and 30 km.

6.4.4 Vertical Wavenumber Spectra

In order to identify characteristics of the gravity wave spectrum, power spectral density (PSD) is examined as a function of vertical wavenumber. The PSD was estimated by computing the Fast Fourier Transform (FFT) for each temperature profile after detrending and applying a Hann window to the selected altitude region (18 to 35 km). The spectra were then averaged by forming the arithmetic mean. In Figure 6.10 the PSD for all profiles (solid lines), for profiles with E_p at 20–25 km of less than 0.5 J/kg (dotted lines), and more than 0.5 J/kg (dashed lines) are displayed. The top panel depicts spectra from 2003, the middle and bottom panel show the respective data from 2004 and 2005. Note the kink at around 1 km vertical wavelength in the spectrum for small wave energy, which occurs in all years. This feature occurs at the limit of the vertical resolution of the RO data and will be examined in more detail in the discussion section. There is little interannual variation in the vertical wavenumber spectrum evident in Figure 6.10.

To determine the vertical wavelengths at which the seasonal variation has the largest impact, the spectra for each month were averaged separately. Figure 6.11 depicts the normalised PSD for 2003 at the wavelengths 12.8 km (solid line), 5.1 km (dotted line), 3.7 km (dashed line), and 2.6 km (dash-dotted line). It is

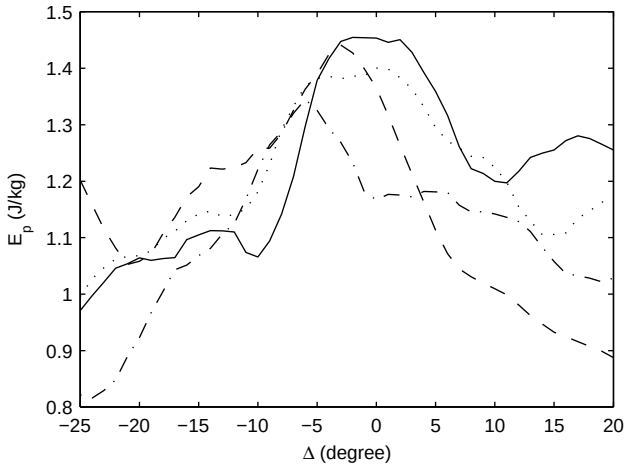

Figure 6.9: E_p at 23–27 km as a function of distance to the vortex edge for 2002 (solid line), 2003 (dashed line), 2004 (dotted line) and 2005 (dash-dotted line). Positive Δ is towards the pole.

evident that the seasonal pattern is more pronounced at long vertical wavelengths. A similar behaviour is observed in other years (not shown). This is likely to be a result of Doppler shifting of the spectrum as discussed in Whiteway et al. (1997). Following Whiteway et al. (1997), the gravity wave dispersion relation for medium frequency waves (which have frequencies much greater than the Coriolis parameter and much smaller than the Brunt-Väisälä frequency) can be written as

$$\lambda_z = |c - U\cos\Theta|/N \tag{6.5}$$

where λ_z is the wave's vertical wavelength, c is its horizontal phase speed, U is the background wind speed, Θ is the angle between the wind and the direction of wave propagation, and N is the Brunt-Väisälä frequency. According to equation 6.5, for gravity waves with small phase speeds, large background winds will lead to long vertical wavelengths. Consequently the wave will saturate or reach instability at greater altitudes and therefore grow to larger amplitudes. When discussing the geographical dependence of wave activity (section 6.4.3) it was shown that mountain waves with small phase velocities strongly contribute to gravity wave activity over Antarctica. These waves will be shifted towards longer vertical wavelengths in the strong eastward wind during winter and early spring, explaining the enhancement at long vertical wavelengths in Figure 6.11.

6.5 Discussion

In the spectrum for small wave energy in Figure 6.10 there is a deviation from a straight line spectrum at around 1 km vertical wavelength as mentioned in

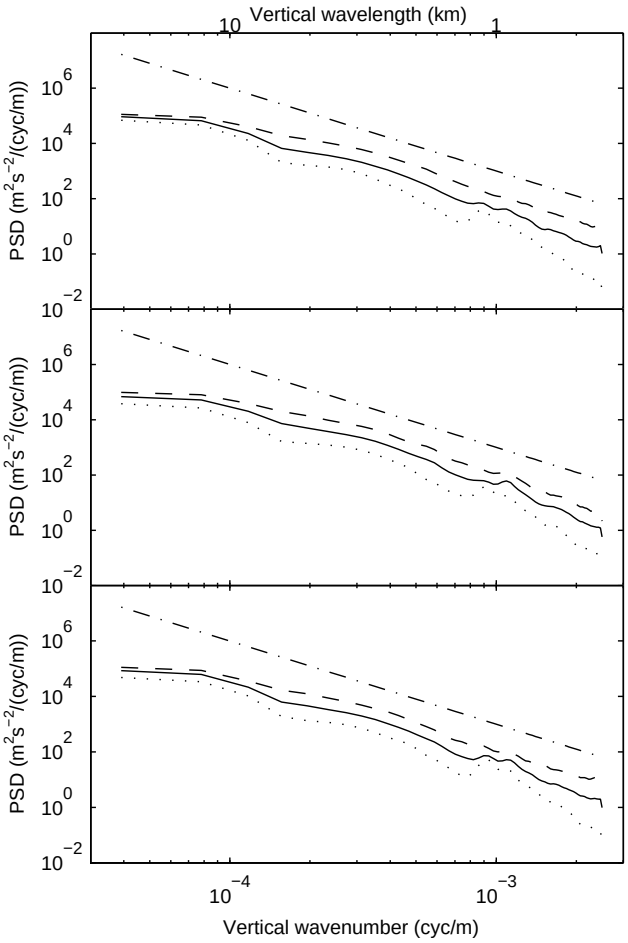

Figure 6.10: Power Spectral density for all profiles in 2003 (top panel), 2004 (middle panel), and 2005 (bottom panel). The solid lines were composed using all profiles from the respective year, the dotted lines are the spectra for profiles where $\bar{E}_p$ between 20 and 25 km altitude was less than 0.5 J/kg, the dashed lines for profiles with more than 2 J/kg. The dash-dotted lines have the gradient -3 for comparison.

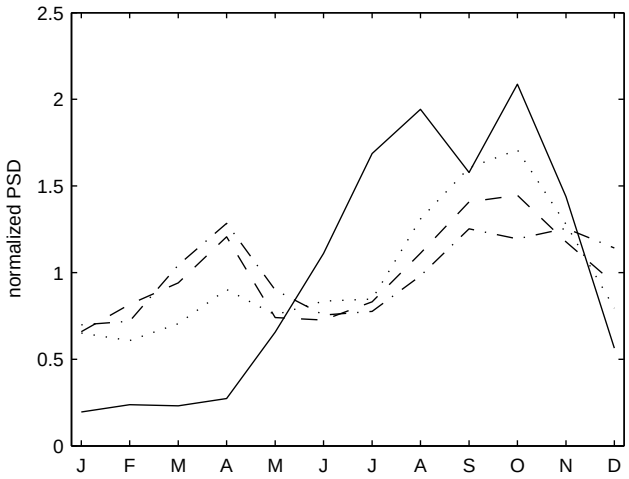

Figure 6.11: Normalised PSD at wavelengths 12.8 km (solid line), 5.1 km (dotted line), 3.7 km (dashed line), and 2.6 km (dash-dotted line) for 2003.

section 6.4.4. A Monte Carlo simulation was performed in order to eliminate the possibility that this is a geophysical feature. The simulation examines if this feature is likely to be a result of the difference between the true vertical resolution of 1.4 km, imposed by diffraction theory, and the resolution of the data set as supplied by the GFZ, which is 200 m. Two hundred temperature profiles containing fractional Gaussian noise (Mandelbrot and Vanness, 1968) were generated at a resolution of 200 m. The profiles were tapered and detrended and then the PSD was calculated. The spectra were averaged and a smooth spectrum with a negative gradient depending on the Hurst parameter was found as expected (not shown). In a second run the profiles were sampled at 1.4 km resolution and interpolated to 200 m. The resulting spectrum showed similar characteristics to the spectrum for small wave energy in Figure 6.10 at around 1 km and it is therefore assumed that the feature in the RO spectra arises from the fact that the RO data are oversampled. However, it is surprising that this feature only appears in the spectra that contain little potential energy. This result will be examined in future work.

The vertical wavenumber spectrum (Figure 6.10) shows a falloff in PSD at a vertical wavelength of approximately 10 km which is probably due to the filter length of 10 km. One of the reviewers of the paper published from this work pointed out that all of the spectra show a local maximum at 3 km vertical wavelength, which is similar to the finding by Allen and Vincent (1995), who reported a peak at 3 km wavelength using radiosonde flight data from Davis. As both techniques identify this maximum, this indicates that this is probably an accurate characteristic wavelength. Note that this wavelength range is located in different parts of the resolvable wavelength spectrum of the radio occultation and balloon flight techniques. However, it is possible that the filtering conceals the true

characteristic wavenumber. Other measurement techniques, for example lidar, allow the background profile to be subtracted before wave energy is calculated because the measurements are always made at the same geographic location. RO profiles are scattered randomly over the globe, and because geographic variability of the background atmosphere is large a background profile cannot be computed. In principle it is possible to fit a cubic spline or similar functions to the profile which could improve the accuracy of the spectrum, however this is subject to its own problems and has not been investigated further.

Recently, the circumstances under which the radio occultation technique is able to resolve gravity waves with short horizontal wavelengths were discussed (de la Torre and Alexander, 2005). The horizontal resolution of each measurement is of the order of several hundred kilometres along the line of sight of the satellite, and of the order of a kilometre across the LOS (Kursinski et al., 1997). Mountain waves have horizontal wavelengths of tens to hundreds of kilometres (Fritts and Alexander, 2003) and therefore detection depends on the angle between the LOS and the wavefront of the mountain wave. Thus it is important to examine the likely impact that these observational constraints would have. Statistically, 52% of the occultations from 2002 to 2006 had a LOS within 30° of the north/south axis in this region. The Antarctic Peninsula and the Transantarctic Mountains are also approximately aligned on this axis and together with the prevailing westerly winds are likely to generate mountain waves with wavefronts parallel to the north/south axis. This creates a viewing geometry that theoretically favours the detection of the mountain waves by CHAMP in these regions. It was examined if a relationship between the viewing angle and the direction of wave propagation existed. The only available information that can serve as an approximation for the direction of wave propagation is the direction of the background wind. For every RO measurement over the Antarctic, the direction of the background wind at 100, 500, and 1000 hPa was determined from the NCEP/NCAR reanalysis. Potential energy at 18–22 km was then examined as a function of the angle between the wind and the LOS direction for the RO measurement. This is depicted in Figure 6.12 for all RO measurements in 2003. E_p is not enhanced for any particular range of angles between the LOS and the wind at any altitude. Although using NCEP/NCAR winds as a proxy for the orientation of wave fronts is a crude approximation, this suggests that the observational filtering created by the variation of horizontal resolution along and across the LOS is not as important as expected from theory. This result was very similar if just the region of the Antarctic Peninsula was examined (not shown).

The seasonal variation over Antarctica observed by the CHAMP RO experiment is very similar to that described in other studies, see for example Yoshiki and Sato (2000). Observational filtering, source variability and critical level filtering are the most important factors that have the potential to determine the observed seasonal variation.

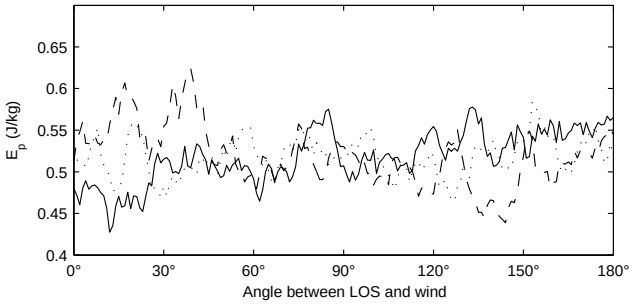

Figure 6.12: Potential energy at 18–22 km over Antarctica for 2003 as a function of the angle between the LOS and the background wind at 1000 hPa (solid line), 500 hPa (dotted line) and 100 hPa (dashed line). Wind data were taken from NCEP/NCAR.

The fact that only gravity waves with vertical wavelengths between approximately 2.8 and 10 km can be observed creates an observational filter. The observed seasonal variation and the enhancement around the vortex edge could be results of a combination of refraction with this filter as described in the following. Gravity waves with vertical wavelengths that are not observable by RO could get refracted to wavelengths that lie within the resolved portion of the spectrum, similarly waves with wavelengths that lie in the observed range could be refracted to wavelengths that are not observable. Depending on the phase velocities of the waves and the properties of the background wind, this can be an effective mechanism (Alexander, 1998). However, given the fact that other instruments have observed the same seasonal variations over different vertical wavelength ranges (Yoshiki and Sato, 2000; Wu and Jiang, 2002), we conclude that observational filtering is unlikely to determine the observed variations in this case.

For waves generated by flow over topography, the strength and direction of the surface winds will determine the amount of wave activity. If the direction or strength of the surface wind vary with time of year, this source will have a seasonal variation. However, on the Antarctic Peninsula, where orography is likely to be an important source, surface wind direction and speed, taken from the NCEP/NCAR data set, were not found to have significant seasonal variations (not shown). The spring maximum of potential energy has previously at least partly been attributed to waves generated by the polar night jet (Yoshiki et al., 2004) and could be an important factor in terms of source variability. However, the enhancements found during winter and at the edge of the vortex have also been explained by Doppler shifting and reduced critical level filtering, which is a consequence of the strong westerly winds (Whiteway et al., 1997).

Critical level filtering is an important mechanism that can have severe in-

fluences on the gravity wave spectrum. The impact of filtering on mountain waves, which have horizontal phase velocities of zero, is especially drastic, as a rotation of the wind vector by 180° between two altitude levels filters all mountain waves from the gravity wave spectrum. The impact of rotation can be studied by calculating the amount the wind vector turned between the ground and a level at which CHAMP can observe wave activity. For every occultation we calculated the amount of rotation at the grid point in the NCEP/NCAR reanalysis closest to the occultation. The ground level was determined using Antarctic surface data, and 100 hPa (approximately 18 km) was chosen as the upper level to coincide with the lower boundary for the calculation of wave activity. The rotation between the two levels was then compared to potential energy. The results for three different areas are shown in Figure 6.13. Over the Peninsula (75°S–60°S and 75°W–45°W, solid line) there is a strong and almost linear relationship between wind rotation and potential energy, indicating that critical level filtering of mountain waves is a very important mechanism in this region. Over the entire continent (area south of 60°S, dashed line) this linear relationship is much weaker but still significant. This result still holds if the Peninsula is excluded (not shown). Syowa is located at 69°S, 40°E and for the present study measurements from the region 75°S to 60°S and 30°E to 75°E were used. The dotted line shows the results for this area and there is no relationship apparent, suggesting that mountain waves and critical level filtering are not important at that site. This confirms the results of Yoshiki and Sato (2000), but suggests that their results are restricted to east Antarctica away from mountainous areas. The seasonal variation of E_p has been analysed separately for the Antarctic Peninsula. During the summers, E_p was as low as 20% of its three year mean value (not shown). Over the entire continent however, E_p only falls to 45% of the mean during summer (Figure 6.3). This suggests that mountain waves over the Antarctic Peninsula experience drastic critical level filtering in summer.

In order to show that critical level filtering and Doppler shifting have the potential to explain a large fraction of the seasonal variation of potential energy over Antarctica, the background wind is examined in more detail. Figure 6.14 depicts the NCEP/NCAR zonal mean wind for the year 2003 at 70°S. The zonal wind in the troposphere is mainly eastward throughout the year, except below 5 km altitude during December and January. In the lowermost stratosphere the wind is eastward even during summer. Above approximately 70 hPa there is again a seasonal pattern with strong eastward winds during autumn, winter and spring and westward winds during summer. In December and January waves with small horizontal phase velocities are likely to be filtered at both zero wind lines. During all other times of the year, the strength of the eastward wind in the lower atmosphere determines the amount of Doppler shifting according to the gravity wave dispersion relation. Waves shifted to larger vertical wavelengths are able to grow to larger amplitudes before saturating. This is consistent with the finding that potential energy is largest during winter and spring when the

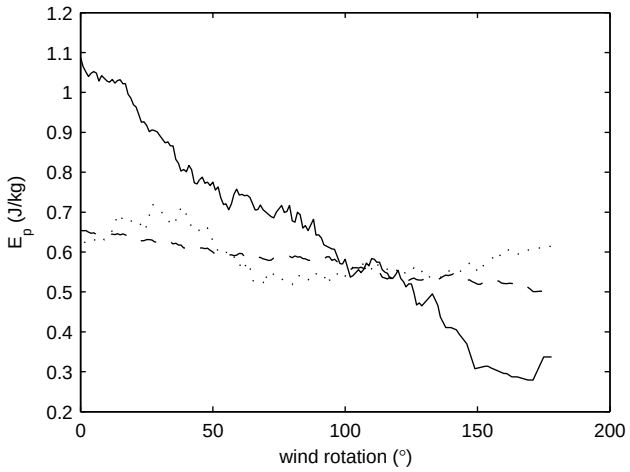

Figure 6.13: Potential energy at 18 to 23 km as a function of wind rotation over the Antarctic Peninsula (solid line), Syowa (dotted line) and the entire continent (dashed line) for 2005.

eastward winds maximise (Figure 6.14). As described in Whiteway et al. (1997), this explanation is also valid for the enhancement of wave activity near the edge of the vortex where wind velocities maximise.

6.6 Conclusions and Future Work

Temperature profiles obtained by the radio occultation experiment on the CHAMP satellite were used to infer gravity wave activity over the Antarctic. Significant seasonal variation was found and attributed to the seasonal variation of critical level filtering and Doppler shifting by the mean winds. Due to the possible effects

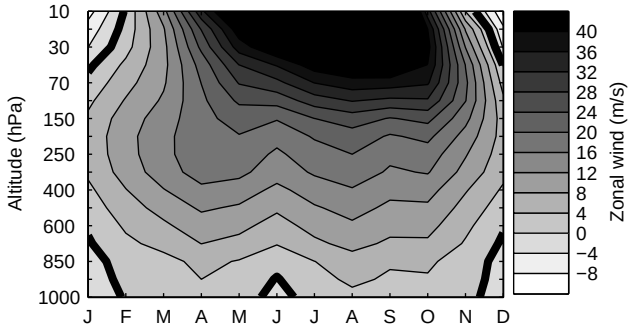

Figure 6.14: NCEP/NCAR reanalysis zonal mean zonal wind at 70°S during 2003. The bold line marks the zero wind line.

of observational filtering in combination with wave Doppler shifting and refraction, any variation of wave activity has to be interpreted with caution. However, instruments observing wave activity over other vertical wavelength ranges have found similar seasonal patterns, therefore the CHAMP RO data are assumed to be a good approximation to the real wave activity. Large enhancements of potential energy were noted over mountainous areas, in particular the Antarctic Peninsula. Wave forcing by means of flow over topography appeared to be the most likely cause for this finding. This was confirmed by the fact that strong surface wind velocities perpendicular to the Peninsula were observed when large wave activity was measured by the RO experiment. In addition, there is an almost linear relationship between the amount of rotation of the background wind and wave activity, indicating that the observed waves are likely to have a near zero phase speed and are therefore likely to be mountain waves. At the same time this supports the interpretation that the seasonal variation is partially associated with critical level filtering. Wave activity enhancements were also found around the edge of the polar vortex, which was attributed to reduced critical level filtering and Doppler shifting. Additional wave sources, such as geostrophic adjustment or shear associated with the jet, were not necessary to explain this enhancement.

Future work includes the analysis of other wave sources, for example fronts, with respect to wave activity. Also, RO amplitude data (Liou et al., 2005, 2006) could provide valuable additional information about gravity wave activity, especially at smaller vertical wavelengths, and should be used for similar studies. Combining the current results with an examination of the gravity wave field in the mesosphere and lower thermosphere is likely to be of interest. The Scott Base MFSA radar now has the capability to resolve high-frequency motions (see chapter 3), but due to time constraints for this thesis an analysis of gravity waves from the radar data, and combination with the stratospheric wave activity measurements presented here, could not be included in this thesis. However, work by R. E. Hibbins (personal communication, 2006) shows that gravity wave activity in the mesosphere and lower thermosphere over Rothera has a similar seasonal pattern to that observed in the lower stratosphere in the present study. This could mean that the lower stratosphere is the dominant region for gravity wave filtering, and therefore wave breaking, in the atmosphere over Antarctica. This could have consequences for the polar stratosphere mean circulation, which is strongly influenced by wave breaking according to the downward control principle (Haynes et al., 1991; Garcia and Boville, 1994).

Chapter 7

Short-Period Planetary Waves in the Antarctic Middle Atmosphere

Thus far, the analysis of Antarctic middle atmosphere dynamics in this thesis has concentrated on background winds, tides (chapters 4 and 5) and gravity waves (chapter 6). In this chapter, attention is directed to Antarctic planetary waves with periods between two and four days. The waves are characterised using data from the MFSA radars at Scott Base, Rothera and Davis. In order to investigate the origin of the observed waves, the ground-based data are complemented by temperature measurements from the EOS MLS instrument on the Aura satellite as well as wind velocity data from the UKMO stratospheric assimilation.

7.1 Introduction

Planetary waves play an important role in the global circulation (chapter 1) and are routinely observed from the troposphere to the mesosphere using a variety of different instruments. Extensive observational and theoretical studies have led to a good understanding of many properties of planetary waves (Andrews et al., 1987). Planetary waves with periods between two and four days have received a great deal of attention over the last 35 years. The quasi-two-day wave (QTDW) often dominates the wind field at low- and mid-latitudes during summer, and waves with periods of two to four days are prominent in the stratosphere and mesosphere at high latitudes during winter. These waves can be observed in many atmospheric parameters.

A wind oscillation with a period of approximately 51 hours was described for the first time by Muller (1972) during July and August in the upper mesosphere at 53°N. This study was followed by many other studies (e.g. Kalchenko and Bulgakov, 1973; Craig and Elford, 1981) that reported observations of a similar phenomenon during the summer solstice in the northern and southern hemispheres. A main characteristic of all reports is the burst-like occurrence shortly after the solstice. Southern hemisphere data usually showed a period closer to 48 hours, but in the northern hemisphere the oscillation was reported

to be longer than two days, with periods of up to 53 hours being observed. The wave was termed the quasi-two-day wave (QTDW) because its period varied with season and location. The wave has since been studied extensively using radar data, satellite data, and models. While at mid-latitudes the zonal and meridional component have similar amplitudes, the meridional wind component was found to dominate over the zonal component towards the equator. In general, the southern hemisphere wind amplitudes were observed to reach 50 m/s and are larger by a factor of about 2 compared with northern hemisphere observations where meridional amplitudes of 20 m/s were reported. Satellite studies using temperature data from Nimbus 7 (Rodgers and Prata, 1981), UARS (Wu et al., 1993; Limpasuvan and Wu, 2003), TIMED (Garcia et al., 2005), and EOS Aura (Limpasuvan et al., 2005) show temperature amplitudes of up to 11 K in southern summers and weaker amplitudes in northern summers. The QTDW was also detected in satellite measurements of water vapour (Limpasuvan and Wu, 2003) and wind (Wu et al., 1993; Limpasuvan et al., 2005). Soon after the discovery of the oscillation, studies of the zonal structure of the wave followed. Radar as well as satellite measurements have now established that the wave has a zonal wavenumber of 3 in both hemispheres (e.g. Glass et al., 1975; Wu et al., 1993), sometimes mixed with other modes of wavenumber 4 (Meek et al., 1996), and it propagates westward. Many researchers have attempted to determine the phase tilt and the vertical wavelength of the QTDW, but the results vary greatly. Vertical wavelengths as short as 35 km and as long as 400 km have been reported by Gurubaran et al. (2001) and Craig and Elford (1981), respectively. The phase of the QTDW was often found to vary little in local time and thus it has been suggested that it is locked to atmospheric tides (Walterscheid and Vincent, 1996; Craig and Elford, 1981; Thayaparan et al., 1997; Jacobi et al., 1997a).

The origin of the QTDW has been discussed widely. Salby (1981a) reviewed the middle atmosphere QTDW observations and showed that a wave with a period near 2.1 days and zonal wavenumber 3 structure is a resonant Eigenmode, called a Rossby-gravity normal mode, in a windless isothermal atmosphere. In more realistic wind fields, the mode's period was approximately 2.22 days during the solstice and showed features very similar to those observed. Although characteristics of the Rossby-gravity wave mode depend on the background wind, this was not seen as a sufficient explanation of the burst-like behaviour of the QTDW and hence an alternative explanation was proposed by Plumb (1983). Plumb (1983) investigated whether the strong wind velocity gradients at the edge of the mesospheric summer jet could generate instabilities that could generate the QTDW. A one-dimensional instability analysis showed that if the vertical shear in the jet is large enough, the jet becomes baroclinically unstable and creates a wave with properties similar to those observed. Pfister (1985) obtained similar results for wind amplitudes with a two-dimensional quasi-geostrophic model, but temperature and geopotential maxima occurred at middle to high latitudes which does not agree with observations. The instability theory was supported by studies

of the meridional gradient of quasi-geostrophic potential vorticity in the NMC reanalysis data set (Randel, 1994), in general circulation models (Norton and Thuburn, 1996), and in radar and UARS HRDI data (Fritts et al., 1999).

Salby and Callaghan (2001) investigated whether a coupling between the Rossby-normal mode and instabilities could occur. For their work, Salby and Callaghan (2001) used complex frequencies which allow for amplification and decay of the wave. The primitive equations are then solved in the presence of a background wind, and the imaginary part of the solutions yields information about the amplification or decay of the different modes through interaction with the background wind. Many of the observed features of the QTDW were successfully reproduced, but the amplitudes are too large. In a three-dimensional spectral model that solves the non-linear primitive equations, Salby and Callaghan (2003) were able to excite a QTDW with wavenumber 3 by introducing fluctuations in tropospheric wave structure. Tropospheric planetary waves were forced with a given latitudinal structure and a time-dependent complex amplitude represented stochastically. Observed features of the QTDW, like the constant presence of the QTDW at low-latitudes and the enhancement during solstice, were reproduced by the model. Reversals of the meridional potential vorticity gradient, and thus instabilities, played a major role in the results. Schröder and Schmitz (2004) described QTDW generation through mixed barotropic-inertial instabilities which generated waves with wavenumbers 3 and 4 in their model.

During winter, a QTDW has also been identified in the stratosphere and mesosphere. However, it appears to be connected to waves with periods between 1.7 and 4 days which are now reviewed briefly. Waves in this period range were discovered in satellite measurements by Venne and Stanford (1979) and were found to have eastward phase velocities. Because of rapid growth with height and small phase variations, the waves were concluded to be forced in situ. Instability analysis using observational data and models showed that barotropic and/or baroclinic instabilities of the polar night jet can generate the observed waves (Charney and Stern, 1962; Hartmann, 1983; Manney et al., 1988; Randel and Lait, 1991; Manney, 1991), similar to QTDW generation by the summer mesosphere jet proposed by Plumb (1983). Waves with periods between two and four days in the Antarctic mesosphere were described by Fraser et al. (1993) and found to be consistent with barotropic instability studies. In the polar winter mesosphere a QTDW was reported by Nozawa et al. (2003a). Nozawa et al. (2003a) used wind measurements from an MFSA radar at Tromso (70°N) and found that the amplitude maximises between 70 and 82 km near winter solstice. Later Nozawa et al. (2003b) confirmed these findings using data from MFSA radars at Tromso (70°N) and Poker Flat (65°N). Seasonal variations of the QTDW corresponded closely between the two sites, but variations on shorter time-scales were not synchronised well. Nozawa et al. (2003b) reported that the zonal wavenumber appeared to be 2 or 4 more often than 3; moreover, the possibility that the wave moves eastward was considered. A winter QTDW has

also been observed at Saskatoon (52°N) using MFSA radar data (Chshyolkova et al., 2005). Similar to the studies by Nozawa et al., the wave's amplitude was reported to maximise at lower altitudes (approximately 70 km) than the summer QTDW (85–88 km). Lawrence et al. (1995) used radar observations together with stratospheric analyses to show that a 4-day wave can reach to the Antarctic upper mesosphere. The study confirmed that the wave is associated with quasi-nondispersive warm pools that rotate in the polar vortex.

In the present work, waves with periods between two and four days observed over the southern polar regions during summer and winter are characterised using MFSA radars at Scott Base, Rothera and Davis. The ground-based data are complemented by EOS MLS satellite data and the UKMO stratospheric assimilation to investigate the origins of the planetary waves. The possible connections of an unusually large 2 day wave event in May 2005 to a simultaneous solar proton event are explored.

7.2 Data and Analysis Techniques

Wind velocity data from the MFSA radars data at Scott Base (78°S, 167°E), Davis (69°S, 78°E), and Rothera (68°S, 68°W) is employed. The technique and the instruments have been described in chapter 2.

In addition to these ground-based instruments, temperature measurements from the Earth Observing System Microwave Limb Sounder (EOS MLS) on the Aura satellite are used. Details about the instrument including measurement precision and vertical resolution can be found in chapter 2 and in Waters et al. (2006). Version 1.51 of the EOS MLS data is employed in the present study.

For spectral analysis of the MLS temperature data a least squares method is employed (Wu et al., 1995). Frequency, σ, and wavenumber, s, are found by fitting a model of the form

$$y_i = A\cos(2\pi(\sigma t_i + s\lambda_i)) + B\sin(2\pi(\sigma t_i + s\lambda_i)) \tag{7.1}$$

to the set of zero mean observations y_i. y_i are measured at t_i (days, in universal time (UT)) and normalized longitude λ_i. For the present work we used a length of 10 days for the fits, and incremented the window in steps of one day.

The year 2005 is the only year for which data from all three radars and the MLS instrument is available, therefore the present study discusses only a single year. In order to discuss climatological features, longer data sets would be necessary. However, this is beyond the scope of the present study.

Data is available from the MLS instrument for every day in 2005 except for 10 days which are randomly distributed throughout the year. A strong solar

proton event (SPE) in January caused total reflection of the medium frequency signal and thus no data is available from Davis and Scott Base during this period. The Rothera radar was not in operation for one week in February. The radar at Scott Base was not operational for several periods during the 2005 winter due to technical problems. Other gaps in the radar data sets are confined to limited altitude regions and are due to low signal-to-noise ratios.

7.3 Results

A spectral analysis of the Scott Base, Davis, and Rothera MFSA radars observations is performed in order to determine the amount of wave activity in the range of periods between two and four days. Figure 7.1 depicts a running Lomb-Scargle periodogram (Press et al., 1992) analysis of zonal wind velocities at 90 km for the year 2005 for each of the three radars. In order to detect waves with rapidly changing amplitudes and phases, intervals of 10 days were chosen and the rectangular window was shifted by 1 day increments through the entire year. Only frequencies with significance values greater than 95% are displayed. Grey areas do not contain any significant frequencies, white areas denote times when no data is available. The period axes has a logarithmic scale. A distinct feature at all three sites are the diurnal and semi-diurnal tides. Features of atmospheric tides at southern high latitudes have already been discussed in chapters 4 and 5. Generally, there is a reasonable agreement of tidal power at the three stations, considering the latitudinal and longitudinal separation. At Rothera, tidal amplitudes appear smaller than at Scott Base and Davis, possibly due to interactions with gravity waves (Fritts and Vincent, 1987) since mountain waves have been found to enhance the gravity wave field significantly in this area (Wu and Jiang, 2002, see also chapter 6). In early February lower frequency motions in summer can be observed at 90 km at the three sites, although at Davis the event is largest. The period lies between 50 and 53 hours at all stations. Both the time of occurrence and the period indicate that this might be related to the QTDW observed at mid and low southern latitudes after summer solstice every year. Note that the amplitude of this QTDW event in February is smaller at other altitudes (not shown) and the wave has maximum amplitude between 85 and 90 km. This is consistent with other observations of the low- and mid-latitude QTDW (Chshyolkova et al., 2005).

The relationship between the observed oscillation and the low- and mid-latitude QTDW can be further investigated by analysing the zonal structure of the wave, as the QTDW is most often found to be of wavenumber 3 or 4. The zonal wavenumber can be inferred using the phase differences of the wave between the three stations. Wavelet analysis is used to estimate the phases of the QTDW at the three stations. The commonly used Morlet function was employed here as a basis function. More details on the analysis method can be found in Torrence and

(a)

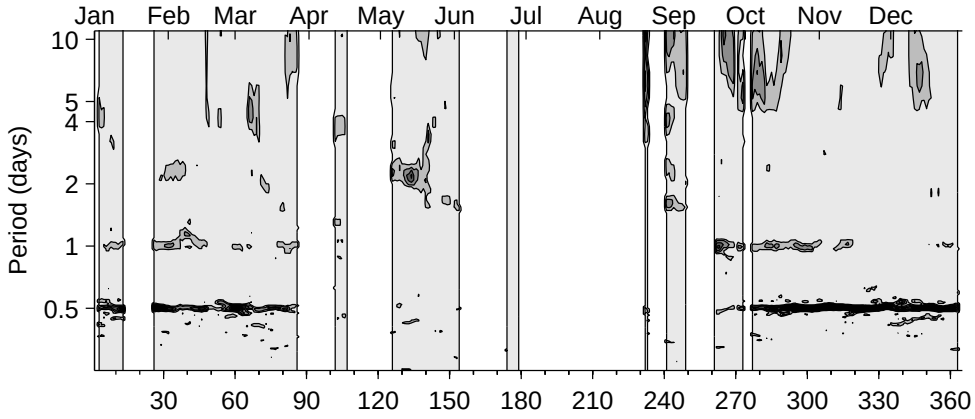

(b)

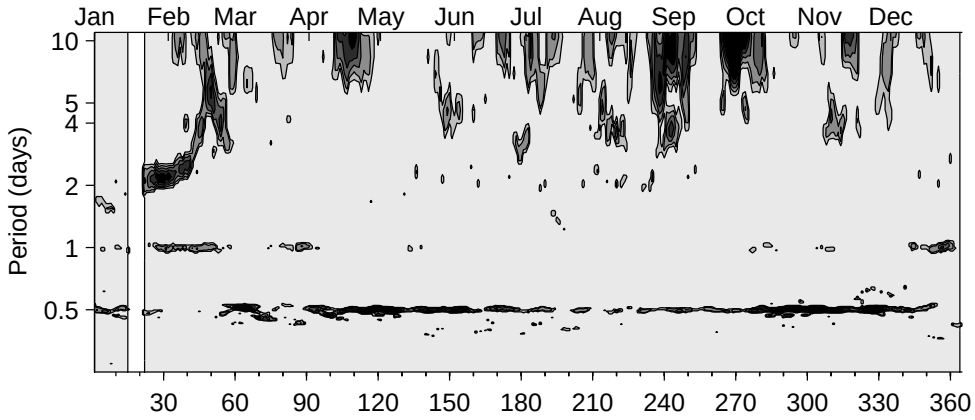

(c)

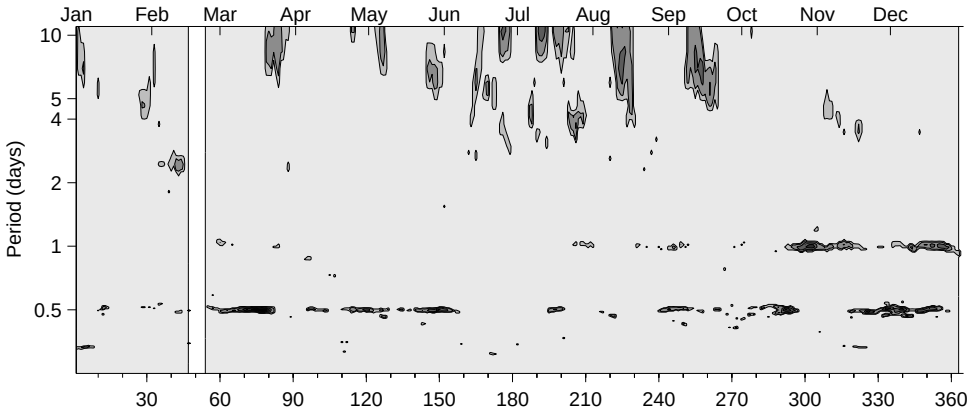

Figure 7.1: Running Lomb-Scargle periodograms (power spectral density) of zonal wind velocities at Scott Base (a), Davis (b), and Rothera (c) at 90 km for the year 2005.

Compo (1998). The wavelet analysis of the zonal wind at 90 km for Scott Base, Rothera and Davis is shown in Figure 7.2. Note that the wavelet analysis was performed for a longer time series than shown so that the *cone of influence* falls outside the depicted interval. All three sites show strong oscillations at approximately 51 hours. They are weakest at Rothera, where the wave is only clearly discernible from 28 January to 2 February, and strongest at Davis. At Scott Base the QTDW is evident throughout the depicted period, although it shows greater variability than at Davis. A 51 hour oscillation was fitted to rectangular 2-day windows of the time-series with a period of 51 hours extracted from the wavelet analysis. This yields the phase of the oscillation for each day and the phase differences between all sites can then be calculated. The phase differences as a function of time are depicted in Figure 7.3a for Rothera/Scott Base, in Figure 7.3b for Scott Base/Davis, and in Figure 7.3c for Davis/Rothera. All phase differences are shown assuming westward propagation of the wave as expected during summer. The lines show the theoretical phase difference for pure wavenumber 1, 2, 3, and 4 waves calculated based on the longitudinal differences between the sites. All three pairs of stations indicate a reasonably good agreement with a wavenumber 3 wave in both the zonal (crosses) and meridional (diamonds) wind measurements. The discrepancies between the theoretical value and the measured phase differences are less than 5 hours in the zonal wind and less than 10 hours in the meridional wind on most days. Note that the differing phase differences on the last two days in Figure 7.3a are probably due to the low amplitude of the QTDW in the Rothera data (see Figure 7.2c), which leads to an inaccurate phase determination. Overall this result suggests that the zonal structure of the wave observed at the three sites is a wavenumber 3 structure which further supports the hypothesis that the wave observed at these high latitude sites is associated with the low- and mid-latitude QTDW.

The wavenumber of waves observed in satellite temperature measurements can be easily obtained using wavenumber/frequency spectral analysis (Wu et al., 1995). This gives a more reliable estimate of the wavenumber and propagation direction than the limited ground-based measurements. The analysis for 25 January to 9 February 2005 of MLS temperature at 0.005 hPa (approximately 86 km) using data at 70°S is depicted in Figure 7.4. Only frequency/wavenumber pairs significant above the 95% level are displayed. The strongest peak appears at frequency 0.5 cyc/d with wavenumber 3 (westward propagating) agreeing well with the radar observations. Peaks at other frequencies have much less power and are likely to be associated with noise. An oscillation with a period of 2 days and eastward propagating wavenumber 2 is also found. However, it is possible that this is an alias to the wavenumber 3 mode. The spectral resolution of this analysis technique is given by (Wu et al., 1995):

$$(\Delta\sigma T)^2 + (\Delta s)^2 = a^2, \tag{7.2}$$

where $\Delta\sigma$ is the resolution in frequency, Δs is the resolution in wavenumber, T is the total sample length and a is a constant for which values between 1 and 1.45

(a)

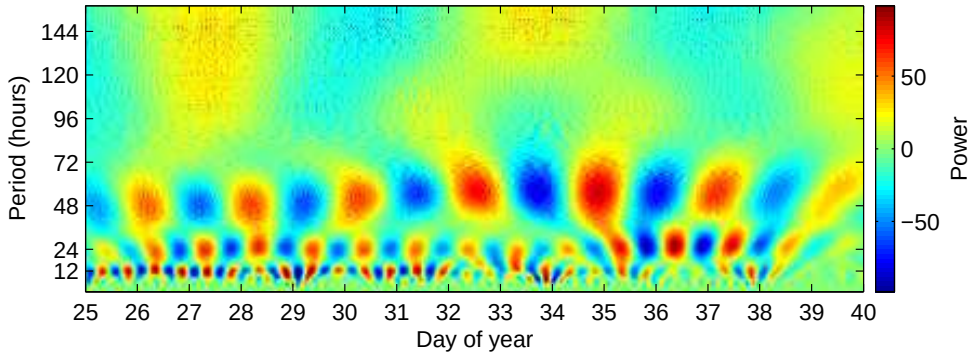

(b)

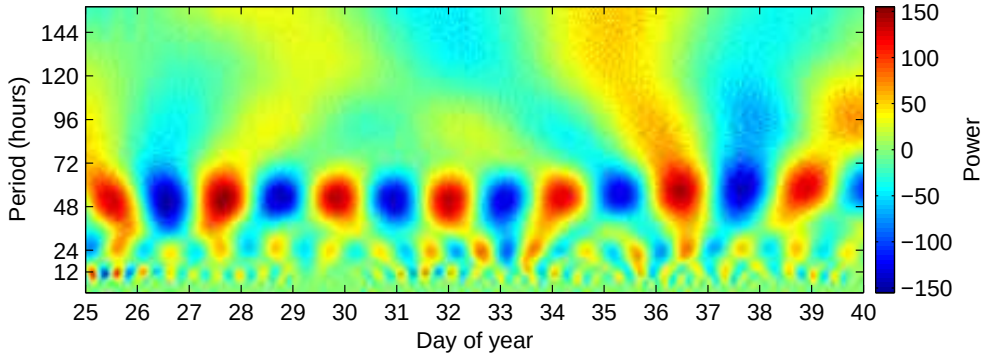

(c)

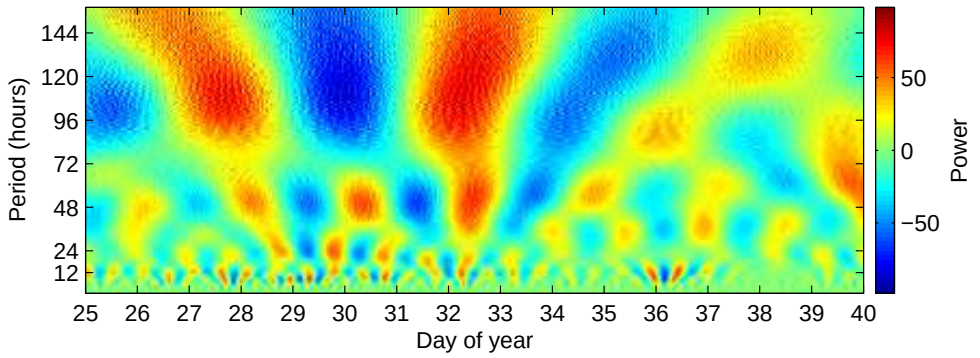

Figure 7.2: Wavelet analysis of the zonal wind measured at Scott Base (a), Davis (b), and Rothera (c) for 25 January to 9 February 2005 at 90 km. Positive power indicates eastward velocities, negative power indicates westward velocities

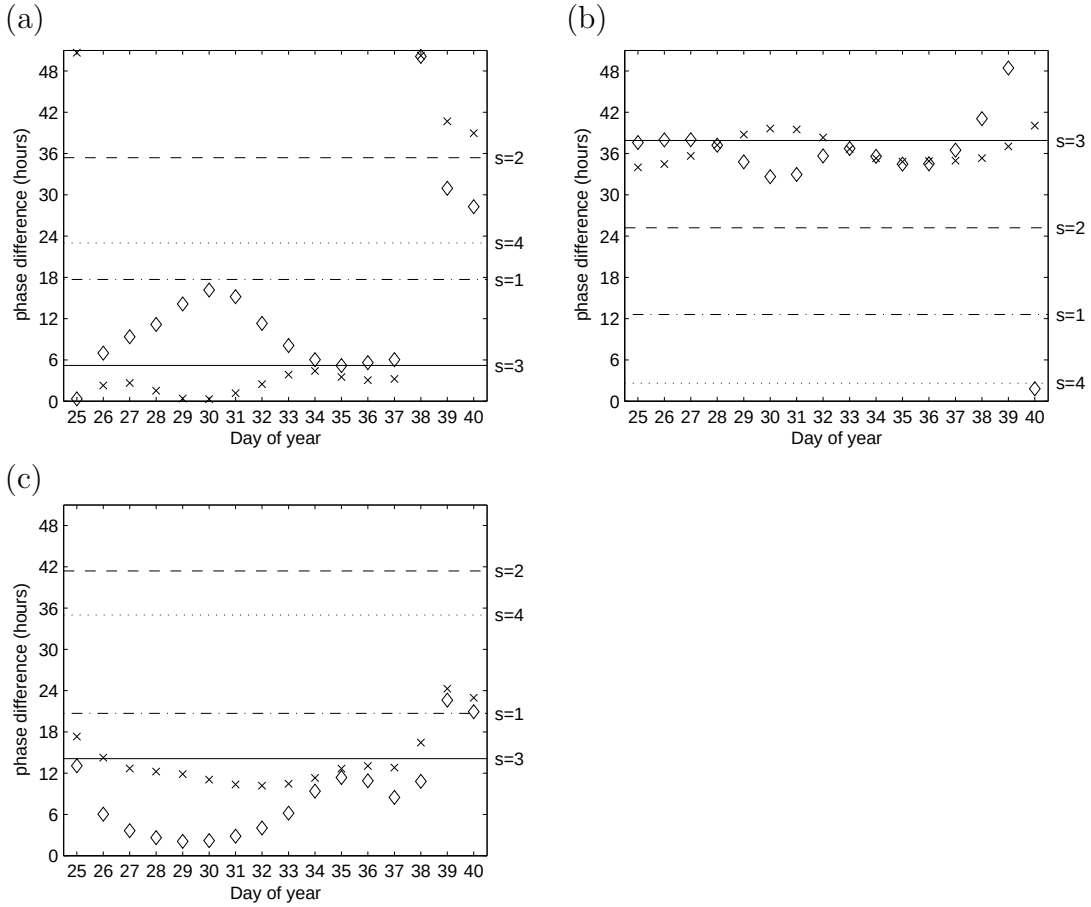

Figure 7.3: Phase differences of the 51 hour wave between Rothera/Scott Base (a), Scott Base/Davis (b), and Davis/Rothera (c) for 25 January to 9 February 2005 at 90 km. Crosses: zonal wind, diamonds: meridional wind. Dash-dotted, dashed, Solid and dotted lines denote the expected phase differences for wavenumber 1, 2, 3, and 4, respectively, for the given longitudinal separations.

have been recommended (Wu et al., 1995). For example, in order to distinguish between waves with periods of 2 and 3 days, a total length of at least 7 days is required. Therefore the employed length of 16 days is suited to localise the period sufficiently in this case.

In order to further investigate the association of the observed wave with the mid- and low-latitude QTDW, the latitudinal extent of the wave is examined. The amplitude of waves with a period of 48 hours and wavenumber 3 (westward) is depicted in Figure 7.5 as a function of latitude and time using the MLS temperature data at 0.005 hPa (86 km). The time-series for each latitude were smoothed with a five-day running average. A large QTDW wave event can be observed in January and early February in the southern hemisphere which also reaches

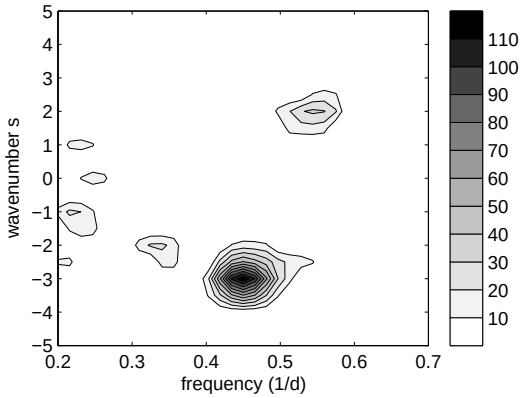

Figure 7.4: Wavenumber/frequency spectrum of MLS temperature data at 0.005 hPa (86 km) and 70°S for 10 January to 31 January 2005. Positive (negative) wavenumbers denote eastward (westward) propagation.

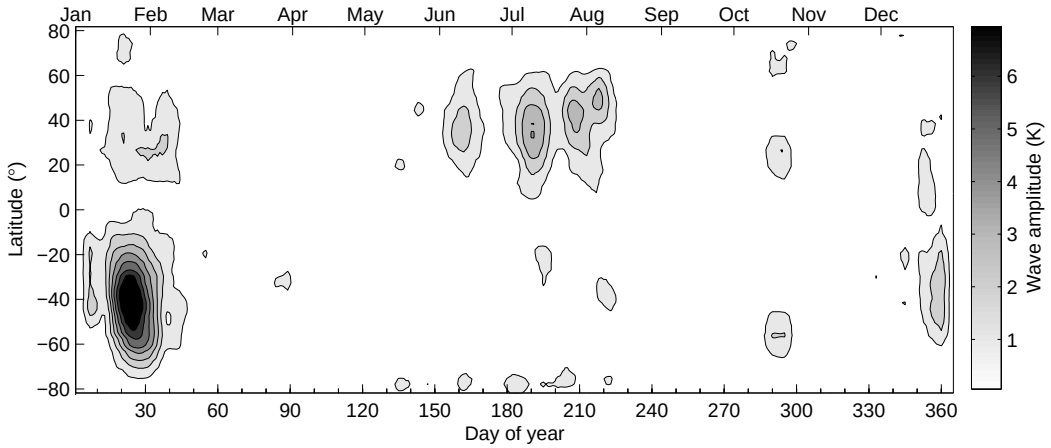

Figure 7.5: Amplitude of waves with zonal wavenumber 3 (westward) and a period of 2 days as a function of latitude and day of year using MLS temperature data at 0.005 hPa (86 km).

to northern hemisphere mid-latitudes. This large latitudinal extent has been observed previously by Limpasuvan et al. (2005). In the northern hemisphere summer a weaker period of 2-day wave activity is found between June and the beginning of August as expected. In December the southern hemisphere QTDW appears again. The January and February event at low- and mid-latitudes has been described by Limpasuvan et al. (2005) using MLS data. It extends to 78°S, confirming that the two day oscillations in the wind measurements over Antarctica at 68°S, 69°S, and 78°S are likely to be associated with the well known QTDW.

In order to examine wave activity during winter, Lomb-Scargle periodograms of the radar wind data at 90 km (Figure 7.1) are compared with periodograms at

80 km which are depicted in Figure 7.6. Both Figures show the power spectral density of significant (above 95%) frequencies in the zonal winds. At 90 km (Figure 7.1), in winter some wave activity is evident at periods between two and four days from. However, wave activity is stronger at lower altitudes as seen in Figure 7.6. This difference in altitude between the summer and winter 2-day oscillations has also been observed by Chshyolkova et al. (2005). In the spectral region below 1 cyc/d episodes of strong wave activity at various frequencies are found between March and October. Due to differences in latitude, local influences by gravity waves, instrumental differences, and data gaps, the similarities in wave activity at the three sites are not strong. However, common features can be detected. The first particularly strong event in the two to four day period range is found in May. It is centered around 52.5 hours and is discernable in all three data sets, although it is especially clear at Davis and Scott Base. Further events with a similar period are found in June and at the beginning of August. Waves with periods of approximately 4 days are found in July and September.

Similar to the study of the summer QTDW above, the winter waves are examined using MLS temperature data. Wavenumber/frequency analysis for periods of strong wave activity as seen in the radar data sets are shown in Figure 7.7. An altitude of 0.1 hPa (64 km) and a latitude of 70°S, close to the latitudes of the radars, were chosen for the generation of the spectra. The altitude is below the altitudes that can be examined by the radars, but the power in the desired frequency range was even stronger than at 80 km.

Figure 7.7a covers the period 12 May to 23 May 2005. A strong eastward propagating wavenumber 2 mode with a frequency of 50.7 hours is evident. The observed 2-day wind oscillations at Scott Base, Davis, and Rothera in May (Figure 7.6) are likely to be associated with this wave. In addition, the temperature spectrum shows some power in the eastward propagating 4-day wave area. There is some evidence for an oscillation with a similar period in the radar data also. Figure 7.7b depicts the spectrum for the same altitude/latitude region but for 25 June to 9 July 2005. In this case, power is distributed over a range of frequencies and wavenumbers. Again, a QTDW wave with wavenumber 2 is evident, but there are also strong 3-day and 4-day oscillations with zonal wavenumber 1.

The combined appearance of several waves with similar phase speeds as seen for example in Figure 7.7b has in the past led to the suggestion that the waves are quasi-non-dispersive. When several non-dispersive waves with small wavenumbers circle the pole at the same velocity strong temperature maxima occur which have been termed “warm pools” (Prata, 1984). They can be directly observed in MLS temperature maps during several periods. As an example, Figure 7.8 depicts interpolated (2° latitude and 10° longitude grid) temperature maps at 0.3 hPa (57 km) for 5–7 August 2005 in intervals of 12 hours. The blue crosses approximately mark the temperature maxima. The warmest region in Figure 7.8a is located at approximately 0° longitude and moves eastward until it reaches

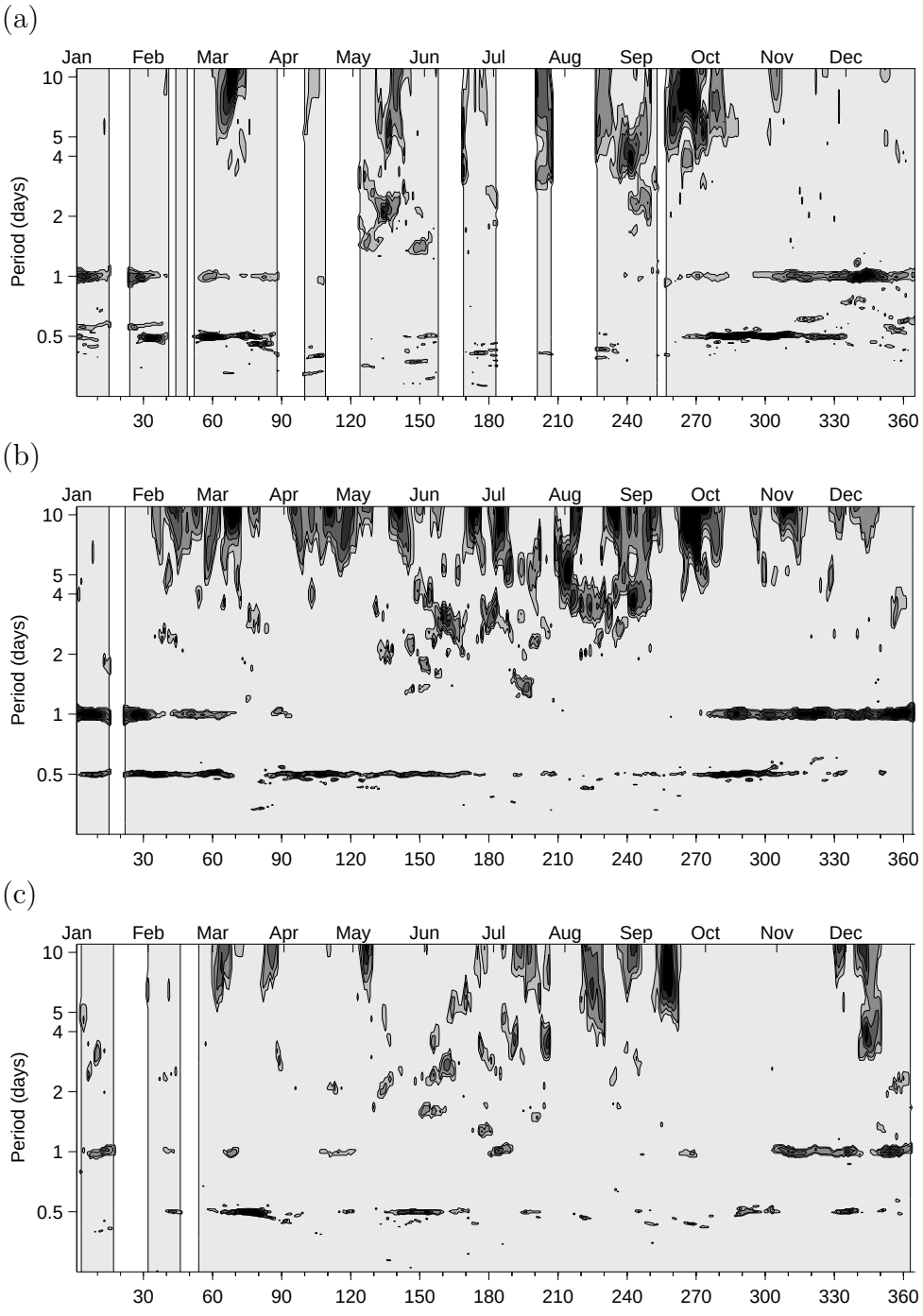

Figure 7.6: Running Lomb-Scargle periodograms (power spectral density) of zonal wind velocities at Scott Base (a), Davis (b), and Rothera (c) at 80 km for the year 2005.

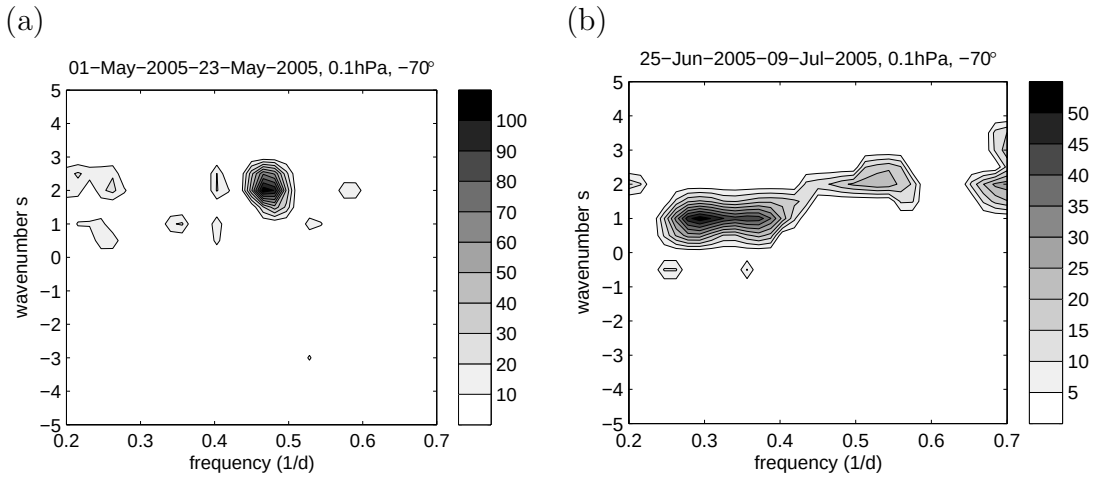

Figure 7.7: Wavenumber/frequency spectrum of MLS temperature data at 0.1 hPa (64 km) and 70°S for two different periods in winter 2005. Positive (negative) wavenumbers denote eastward (westward) propagation.

90°W in the last map of the sequence, Figure 7.8f. The average velocity of the warm pool is therefore about 90° longitude per day, which can be described as a wavenumber 1 wave with a period of four days. Note the presence of a secondary temperature maximum located opposite of the pole. In combination with the primary maximum, this leads to a wavenumber 2 wave with a period of 2 days.

The behaviour of the primary maximum is further studied by analysing its position as a function of time for the entire winter of 2005. This is depicted in Figure 7.9 where the unwrapped longitude of the temperature maximum at 0.3 hPa was determined on interpolated 12 hourly temperature maps of the area south of 40°S (similar to the blue crosses in Figure 7.8). There is little consistent zonal movement before day 200 (19 July), but after that the temperature maximum rotates around the pole at a constant angular velocity of approximately 4 to 4.5 days per rotation. This feature exists for about 1 month. These findings agree well with previous observations related to warm pools and their phase velocities (e.g. Lawrence et al., 1995).

The 2- and 4-day temperature oscillations are further discussed by analysing their behaviour as a function of altitude and time of year at 60°S (Figure 7.10) and 70°S (Figure 7.11). Wave amplitudes of the eastward propagating 2-day wave with zonal wavenumber 2 (Figures 7.10a and 7.11a) and the 4-day wave with wavenumber 1 (Figures 7.10b and 7.11b) as well as the mean amplitude of both (Figures 7.10c and 7.11c) are shown. Periods of strong 2-day wave activity are noted in May and June in the upper stratosphere and mesosphere at both latitudes with maximum amplitudes of about 5 K. Smaller amplitude waves occur until September. The 4-day wave reaches amplitudes of 8 K and strong episodes persist until September. In the stratosphere the wave moves

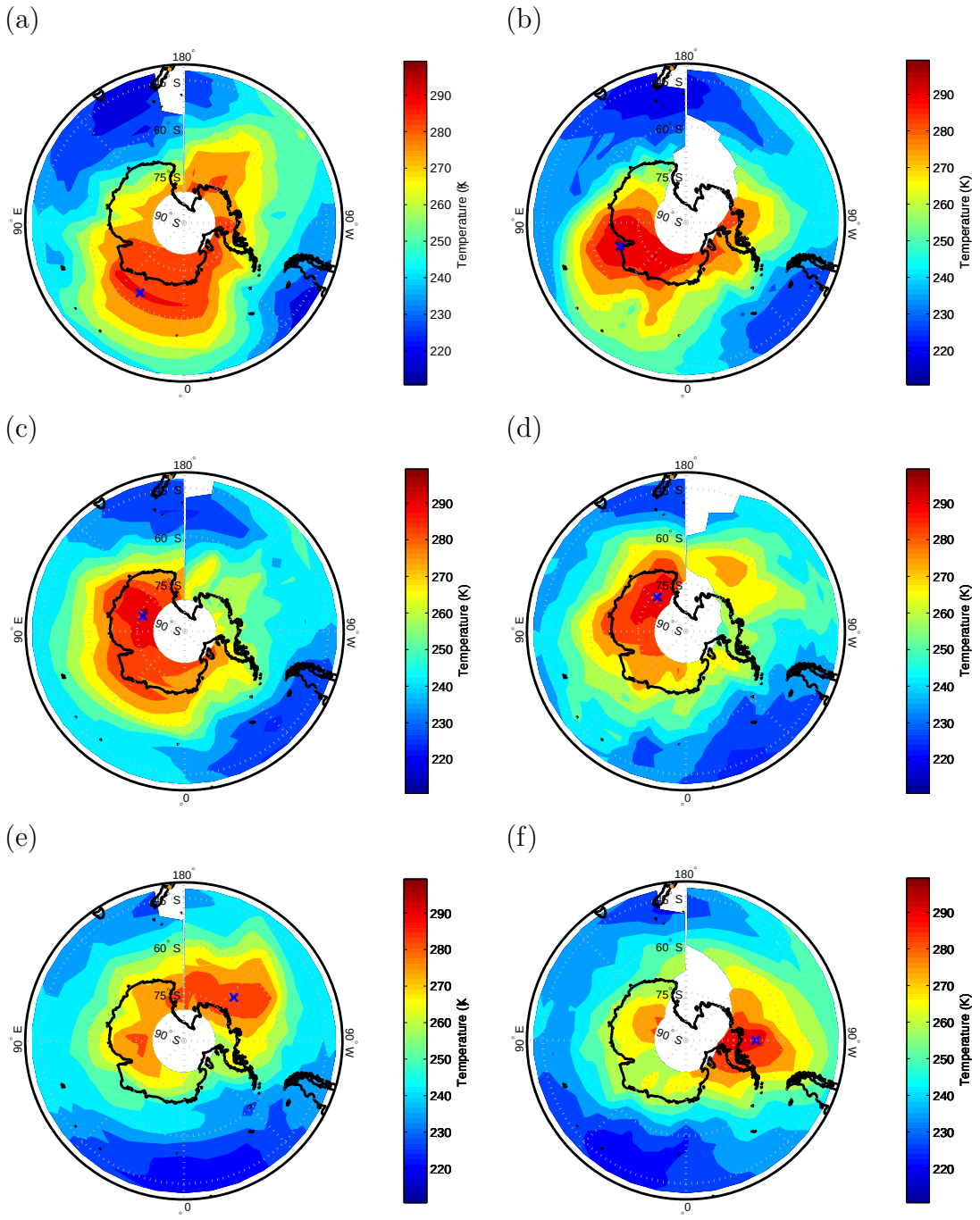

Figure 7.8: 12-hourly temperature maps for 0.3 hPa (57 km) obtained by MLS for 5–7 August 2005.

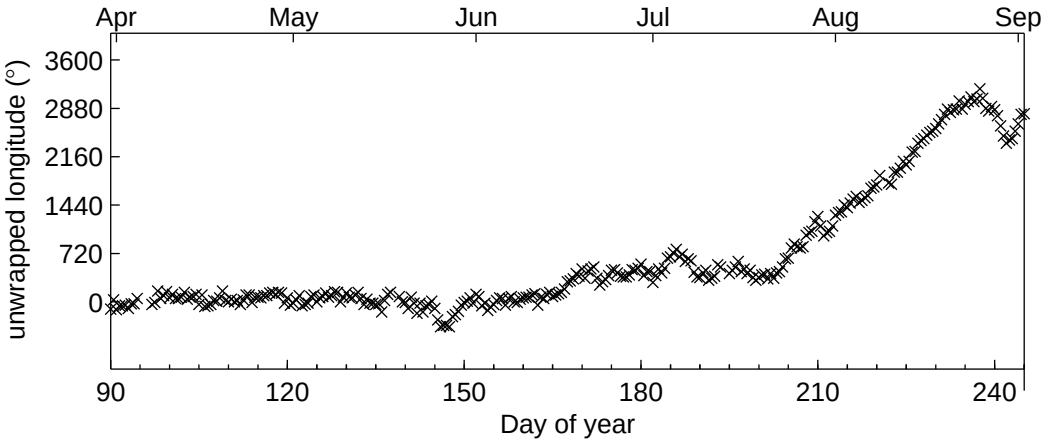

Figure 7.9: Unwrapped longitude of the maximum on 12-hourly interpolated temperature maps at 0.3 hPa during winter 2005.

towards lower altitudes in time until late October. The mean amplitude of the two waves shows a relatively constant amplitude throughout the southern hemisphere winter. At 70°S and 50 km altitude for example, the coefficient of variation is 36%, compared with 63% for the two-day wave and 48% for the four-day wave. This could be interpreted as the presence of a relatively constant source of wave forcing which leads to the 4-day and 2-day wave depending on other unknown factors. A potential candidate for such a constant source is the polar night jet which can create shear instabilities. This has previously been pointed out by (e.g. Plumb, 1983).

7.4 Discussion

Planetary waves in the stratosphere and mesosphere with periods between two and four days have been successfully reproduced in mechanistic and general circulation models. These studies indicate that baroclinic and barotropic instabilities are important for the generation of this type of wave. In order to examine the importance of the two types of instabilities, the relationships between instabilities and wave activity are explored in the following.

Baroclinic instabilities are associated with the vertical shear of the horizontal wind, whereas barotropic instabilities arise from the horizontal shear of the zonal wind. The vertical shear can be approximated through the thermal wind shear balance equation (Andrews, 2000):

$$-\frac{g}{T}\frac{\partial T}{\partial y} = f\frac{\partial u}{\partial z} \tag{7.3}$$

where $\partial T/\partial y$ is temperature gradient in the meridional direction, u is the zonal

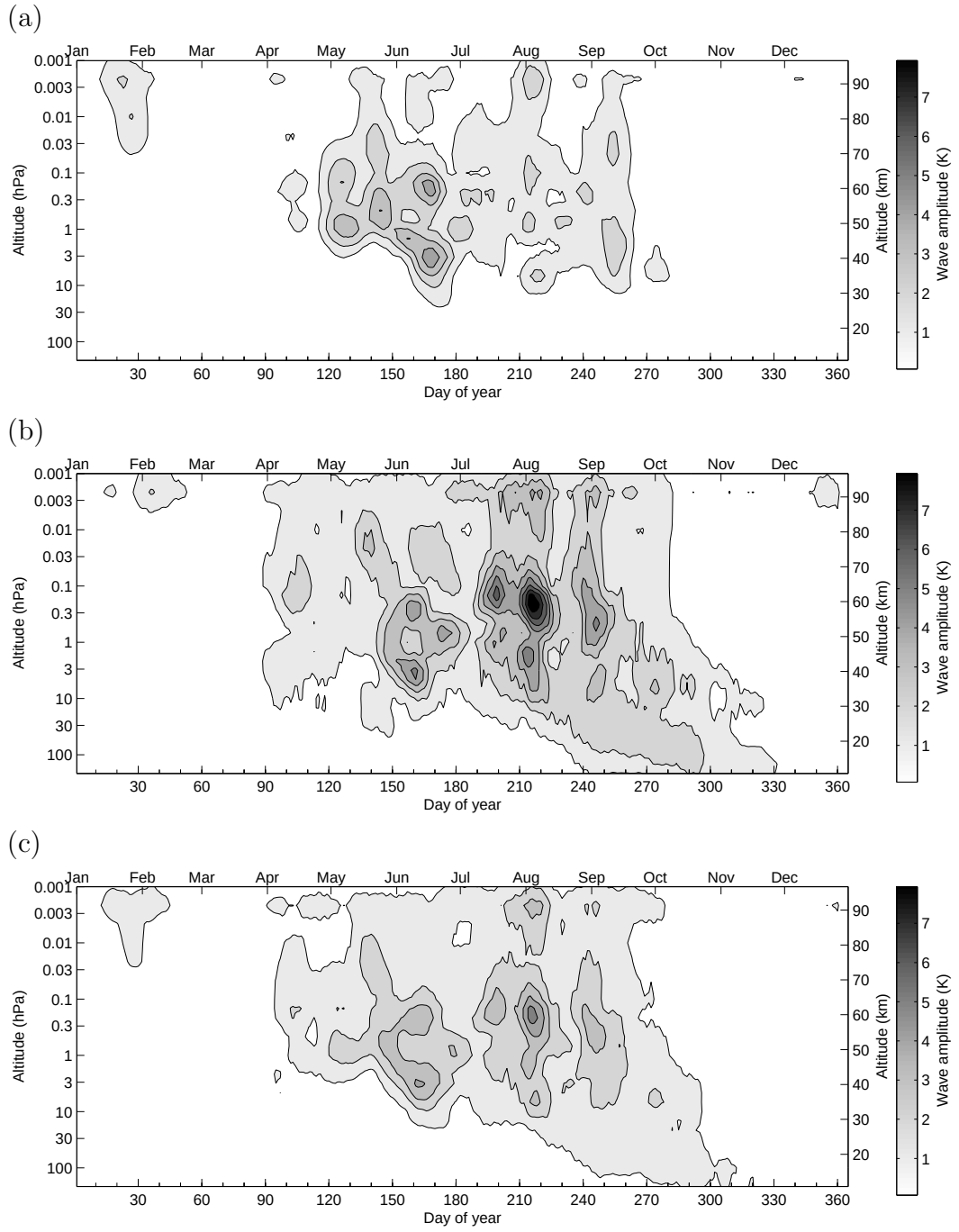

Figure 7.10: MLS temperature amplitudes of the 2-day wave with wavenumber 2 (a), the 4-day wave with wavenumber 1 (b), and the average of both (c) at 60°S for the year 2005.

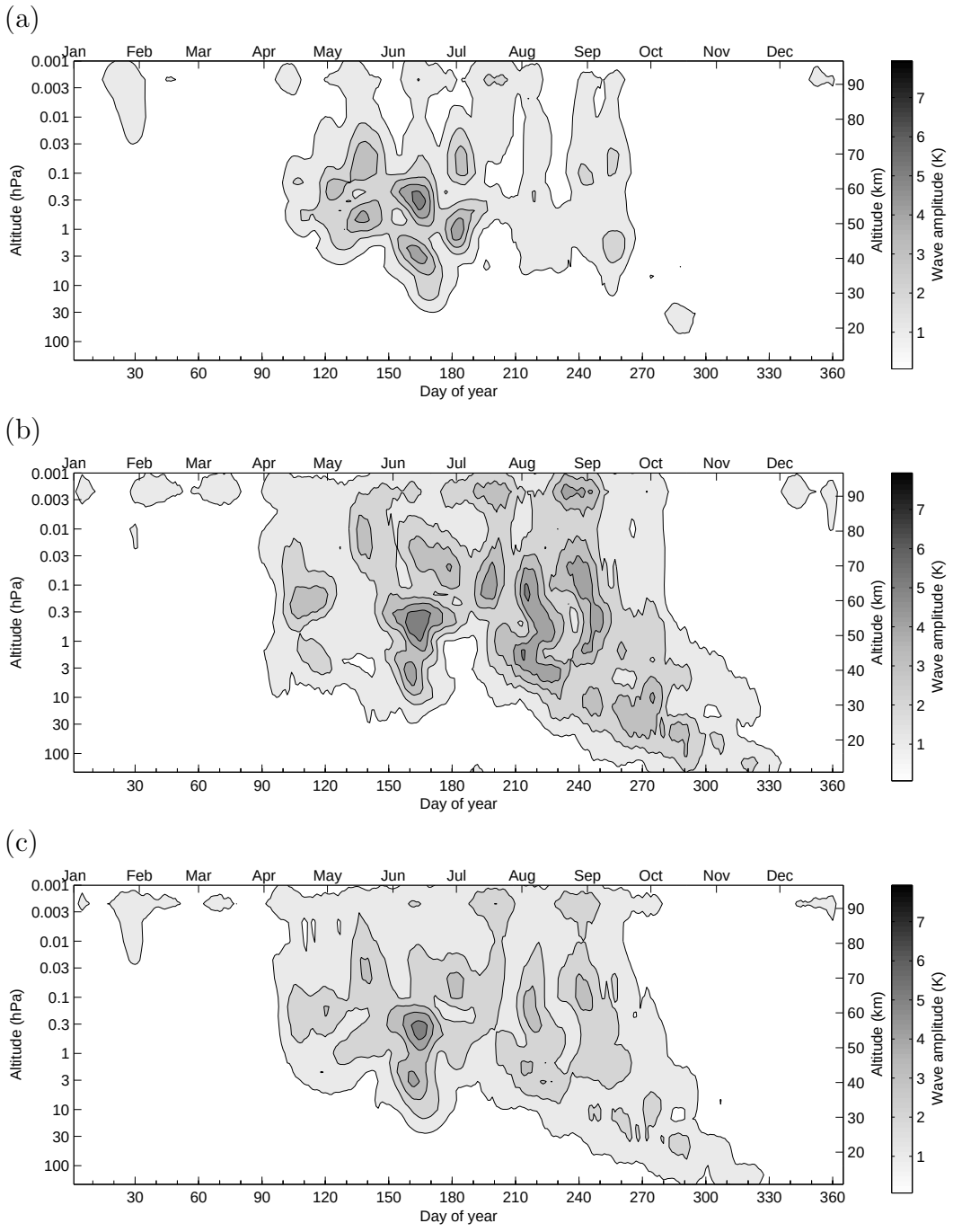

Figure 7.11: Same as Figure 7.10 but at 70°S.

wind, z is altitude, f is the Coriolis parameter, and g is the acceleration due to gravity.

Due to the high inclination of the Aura satellite, the temperature measurements of the MLS instrument are performed along circles of constant longitude to a reasonably good approximation, although this does not hold true in the vicinity of the pole. Therefore the latitudinal temperature gradient can be computed from consecutive measurements up to approximately 70° latitude. The vertical wind shear is easily computed using equation 7.3. The derived wind shear for 60°S and 70°S is depicted in Figure 7.12a and Figure 7.12b, respectively. Strong shear is observed during summer above 75 km, and in winter shear is found throughout the stratosphere and mesosphere below 70 km with a gap at about 40 km which is the altitude where the jet maximises (Hibbins et al., 2005). At 70°S the shear is generally weaker than at 60°S during winter. Hibbins et al. (2005) studied the mean wind field at Rothera (68°S) and found that the summer mesospheric jet maximised at 65 km, the winter jet had maximum velocities at 40 km. Strong vertical shear was observed in the altitude regions up to 20 km above the jets. This is confirmed by the findings here. The shear is generated by breaking gravity waves which reverse the flow above the winter and summer jets.

The observed shear has the potential to cause baroclinic instabilities which can create planetary scale waves by releasing potential energy. The vertical shear is related to baroclinity b, which is defined as:

$$b = \frac{1}{P}\frac{\partial P}{\partial \phi} - \frac{1}{\rho}\frac{\partial \rho}{\partial \phi} \tag{7.4}$$

Using the ideal gas law it can be shown that:

$$b = \frac{1}{T}\frac{\partial T}{\partial \phi} \tag{7.5}$$

With equation 7.3 it follows that $\partial u/\partial z \propto N$. It can be shown that a baroclinic atmosphere can release potential energy (Andrews, 2000). Eady's model of baroclinic instability, based on linearised quasi-geostrophic equations, indicates that some disturbances can experience exponential growth in time, which is a sign of instability. If this mechanism is effective in the middle atmosphere, a relationship between wave activity and shear would be expected.

During summer, the strong shear between 80 and 90 km corresponds well with the time and altitude where wave activity was observed in the radar and temperature data (e.g. Figure 7.2). Comparison of the time and altitude behaviour of the winter planetary waves (Figures 7.10 and 7.11) with the observed shear (Figure 7.12) shows that a similar pattern is also observed. For example, the burst of wave activity in late July and early August at 0.3 hPa (57 km) in Figure 7.10c corresponds well to an enhancement in vertical shear (Figure 7.12). It should be noted that the similarities are greater at 60°S, where the shear is also larger

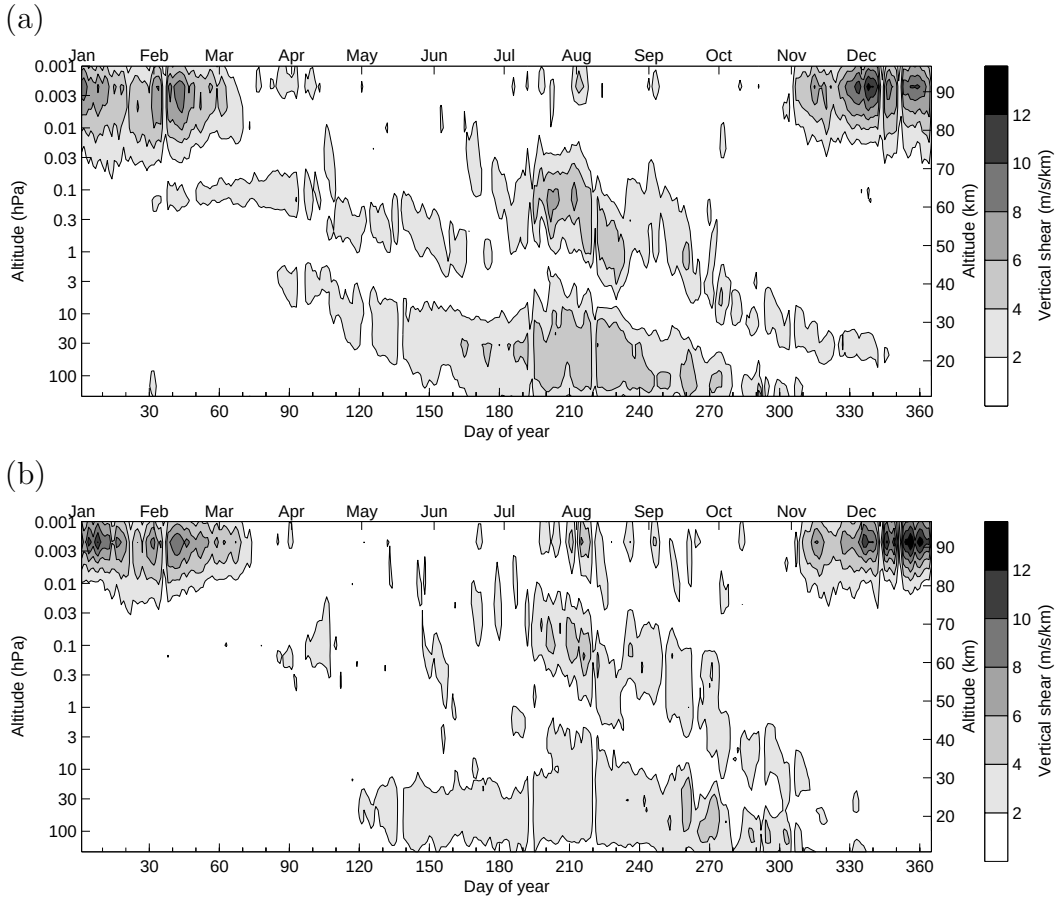

Figure 7.12: Vertical wind shear at 60°S (a) and 70°S (b) during 2005, derived from MLS temperature measurements.

in general, than at 70°S. The relationship can be further examined by studying the correlation between the two quantities. The mean amplitude of waves with periods of two and four days and zonal wavenumbers 2 and 1, respectively, was chosen as a measure of wave activity. The correlation coefficient was only computed for the period from June to September in order to avoid contamination by the seasonal variation. The Pearson correlation coefficient is only valid if the probability distribution is normal, but if the seasonal variation was included, the distribution of values would not be normal. At 60°S the correlation is significant between 60 and 70 km altitude, the correlation coefficient exceeds 0.6. At 70°S the correlation is not significant but the coefficient also maximises between 60 and 70 km.

It has also been shown that barotropic instabilities have the ability to create short-period planetary waves (e.g. Hartmann, 1983). It is not possible to infer the latitudinal shear of the zonal wind from MLS measurements, therefore the UKMO (United Kingdom Met Office) assimilated data are used to approximate this

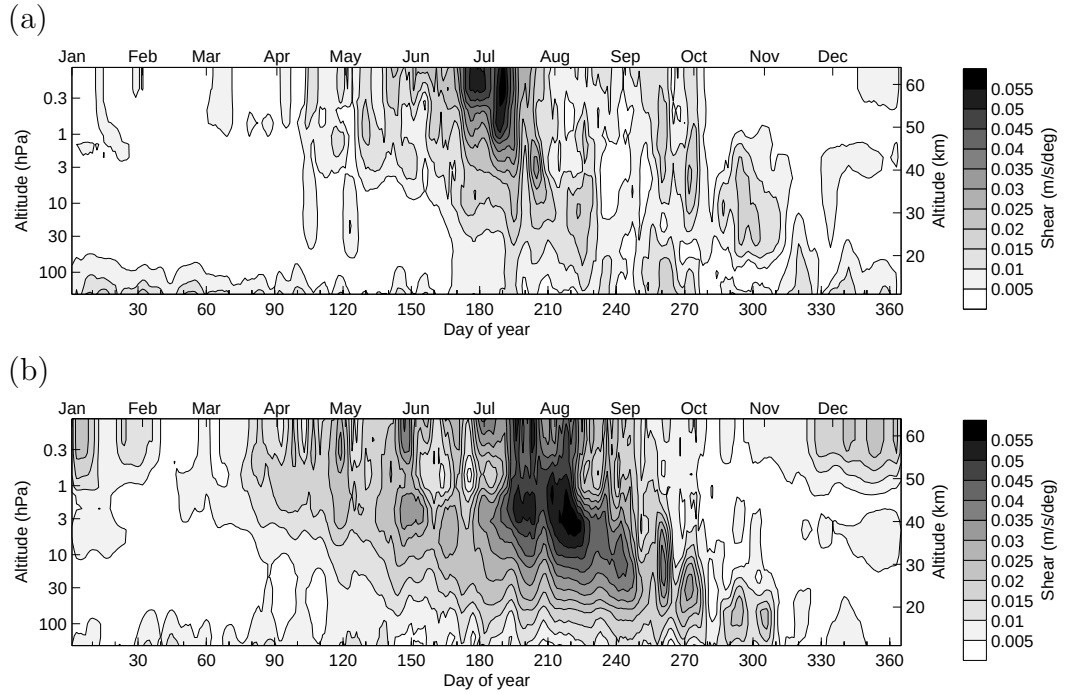

Figure 7.13: Horizontal wind shear at 60°S (a) and 70°S (b) during 2005, derived from UKMO zonal wind data.

parameter. However, the upper boundary of the UKMO data is at 0.1 hPa and therefore the wave activity period in summer, which occurs above that altitude, cannot be examined with this data set. The horizontal shear as a function of altitude and time in 2005, derived as the latitudinal gradient of the zonal wind, is shown for 60°S and 70°S in Figure 7.13. The correspondence between horizontal shear (Figure 7.13) and wave activity (Figure 7.10 and 7.11) is especially good at 70°S.

Similar to the analysis of the relationship between baroclinity and wave activity, the correlation coefficients were calculated for wave activity and the horizontal wind shear. The correlation is found to be significant only at 70°S, above 60 km. Note that the horizontal shear is larger at 70°S than at 60°S (Figure 7.13).

Summarising the results from the shear analysis, both horizontal and vertical shear appear to be related to wave activity. However, wave activity relates most strongly to the dominant type of shear in the latitudinal region examined. This is physically sensible and indicates that the above described mechanisms of instability generation through shear contribute significantly to wave activity in the stratosphere and mesosphere.

As mentioned before, an unusually large amplitude wave with a period of 2 days is evident in mid-May 2005 (Figure 7.6). The amplitude of the 2 day

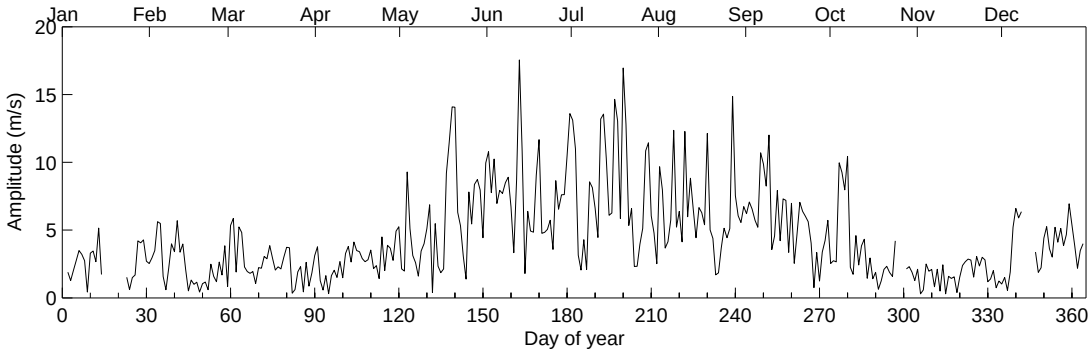

Figure 7.14: Amplitude of the two-day wave at 75 km at Davis during 2005.

oscillation at Davis for 2005 is shown in Figure 7.14 and displays a very rapid amplitude increase around 15 May (day number 135). This event is also the first period of significant two-day wave activity during the winter of 2005. At Scott Base, the amplitude of the oscillation reached 60 m/s (not shown). However, neither a large vertical (Figure 7.12) or horizontal (Figure 7.13) shear of the zonal wind is evident for this period. The magnitude of this event very early in the winter is unexpected and requires study. Although highly speculative, we briefly investigate if this event could be related to a solar proton event (SPE) which occurred just before the wave reached large amplitudes. Figure 7.15 depicts the solar proton flux for this period. An SPE is evident from 14–16 May, the 10 MeV proton flux exceeds 1000 particles/(cm s sr). The magnetic K_p index reached a value of 9 on 15 May (not shown). The radar data displays a gap of several hours because no backscattered signal is received at the time when the energetic particles reach the planet (not shown), which is likely to be due to absorption of the radar signal. From this it can be inferred that the SPE was large enough to cause a significant rise of ionisation in the mesosphere which led to radio absorption conditions. Possible connections between the quasi 2-day wave and solar or magnetic activity have been noted in the literature. Clark (1989) used meteor winds to show that the wave's amplitude is correlated with the magnetic index A_p, and Limpasuvan et al. (2005) noted a large 2-day wave event in early 2005 only a few days after a major solar proton event. However, to the author's knowledge, no explanation for these relationships has been offered in the literature. In the following, this relationship will be investigated further using observations from the MLS instrument.

Energetic particles created by SPEs are guided by the Earth's magnetic field and therefore reach the geographic area of the magnetic poles. The magnetic south pole is currently located at 64°S and 138°E. Depending on the energy distribution of the particles they can penetrate into the mesosphere and stratosphere where they interact with various chemical species. In particular, these interactions lead to ionisation, excitation, dissociation and dissociative ionisation

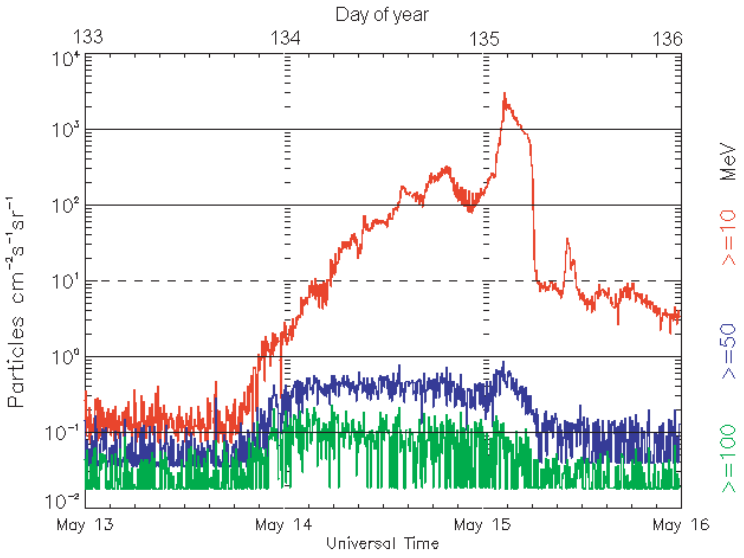

Figure 7.15: GOES11 Proton Flux (5 minute data) for 14 May to 16 May 2005.

of the background constituents, which lead to the production of odd hydrogen HO_x (H, OH, HO_2) and odd nitrogen NO_y (N, NO, NO_2, NO_3, ...) (Solomon et al., 1981) which are known to have the ability to destroy ozone. For example, the January 2005 SPEs led to a short-term ozone loss of over 40% at 60 km altitude (Damiani, 2006). MLS provides observations of OH and O_3 volume mixing ratios which can be used to study the effects of the May 2005 SPE in more detail.

Figure 7.16a shows the time series of the zonal mean volume mixing ratio for the area south of 55°S at 0.022 hPa. Enhancements of up to 240% in OH concentration are found on 14 and 15 May, the days on which the solar proton event occurred. The concentration drops to amounts similar to the original value after two days. Increases of OH after SPEs are for example described by Solomon et al. (1981).

The ozone concentration during the same time and in the same region is depicted in Figure 7.16b. The mean volume mixing ratio decreases from 1.4 ppbv at 12 UT on 14 May to 0.8 ppbv at 12 UT on 15 May, a loss of more than 40%. The concentration fully recovers by about 20 May. The reduced amount of ozone leads to a decrease in absorption of UV which could potentially lead to a cooling in this area. This can be directly investigated using MLS temperature measurements. The zonal mean temperature time series of the same area and the same altitude is depicted in Figure 7.16c. A temperature decrease of approximately 3°K can be observed from approximately 16 to 20 May, indicating that the ozone loss led to a significant cooling. This effect has been verified using chemistry-climate models that can simulate the effects of solar proton events and the associated ion

production, see e.g. Baumgaertner et al. (2007).

The geographical extent of the ozone depletion is depicted as a series of volume mixing ratio maps at 0.05 hPa (70 km) in Figure 7.17. Although the data quality at this altitude is not reliable enough for detailed analysis of the maps, it appears that ozone depletion on 15 May (Figure 7.17c) occurs predominantly in the region 180°E±60° and most severely at 150°E. However, on the following day, (16 May, Figure 7.17d), depletion is almost zonally symmetric which is possibly due to transport and mixing.

The observed ozone loss on 15 May in the area of the magnetic pole and the associated reduction of UV absorption are likely to lead to a temperature decrease predominantly in the same area. Figure 7.18 depicts the individual temperature measurements on a map for 15 May. It is evident that the temperature structure is dominated by a zonal wavenumber 1 structure with an amplitude of more than 10°K. Therefore, the impact of the ozone loss is difficult to identify in this way. However, interaction between the cooling due to ozone loss and the dynamically created zonal temperature structure present before the SPE has the potential to serve as an explanation for the observed amplitude increase of the two-day wave. Zonally asymmetric cooling is proposed to affect properties of planetary waves through nonlinear effects. If the cold phase of a planetary wave was located in the area where the cooling occurs, an increase in the wave amplitude might be possible. The local oscillation between two temperature extremes would get a boost during the cold phase, analogous to a swing that is briefly accelerated at the point of extreme deflection. Examination of Figure 7.18 suggests that a zonal wavenumber 1 structure at around 70°S has it's cold phase between approximately 90°E and 180°E, confirming the possibility of such a scenario for the May 2005 SPE. However, without 3-dimensional modelling the effectiveness of this mechanism cannot be explored further. Unfortunately this phenomenon would be difficult to study statistically with a time series of planetary wave parameters due to the rarity of such events.

7.5 Conclusions

MFSA radar wind measurements at Scott Base, Rothera, and Davis showed an oscillation with a period of approximately two days during late January and early February 2005. The amplitude of the oscillation maximises at about 90 km altitude and was found to have a westward propagating zonal wavenumber 3 structure which indicates a relationship to the QTDW commonly observed at low- and mid-latitudes. Satellite measurements of the latitudinal extent confirm this conclusion.

In winter, oscillations with periods between two and four days are prominent with maximum amplitudes below 80 km. These waves were found to be eastward

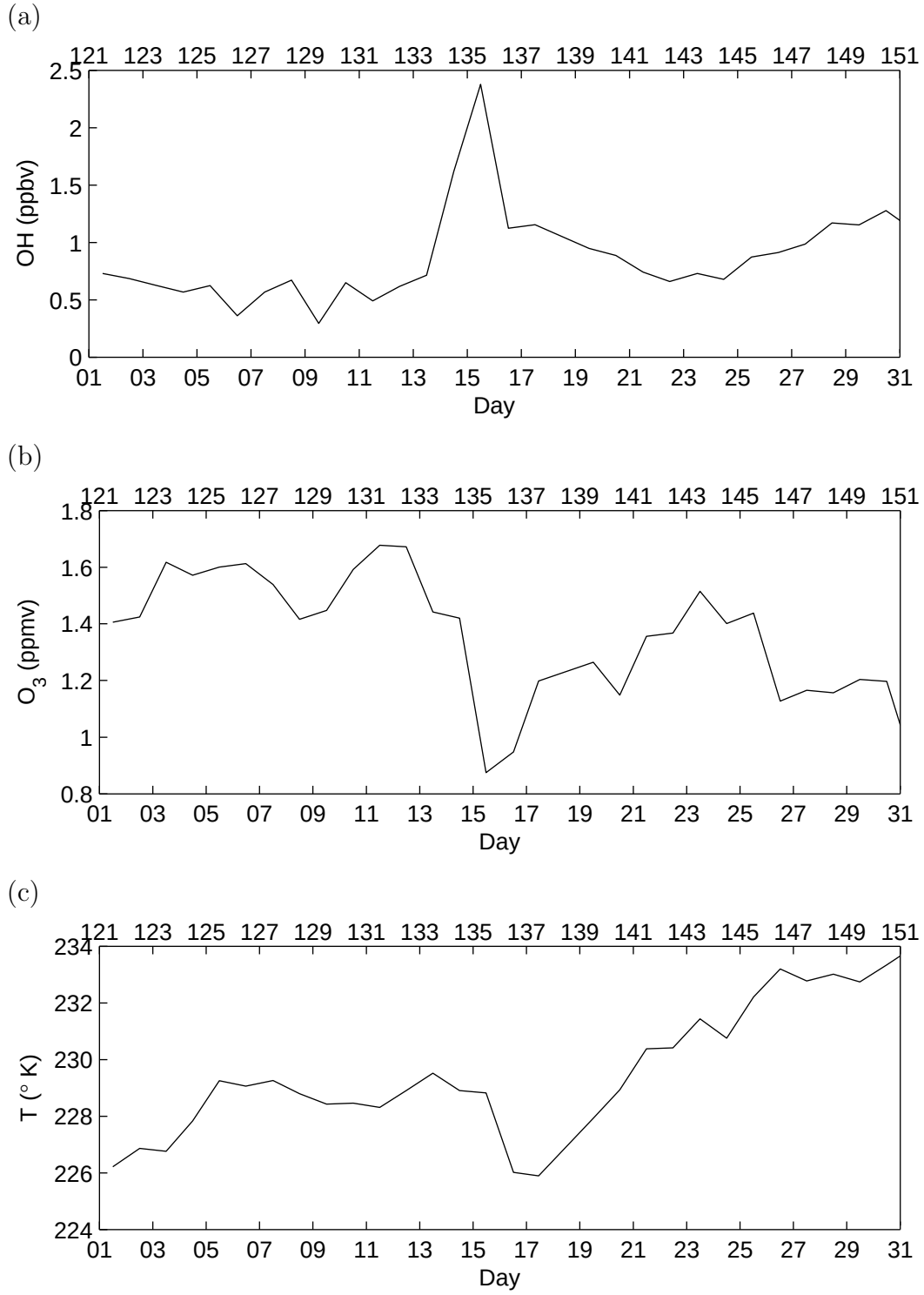

Figure 7.16: MLS time series of zonal mean OH (a), O_3 (b), and temperature (c) for 55°S to 82°S at 0.021 hPa for May 2005.

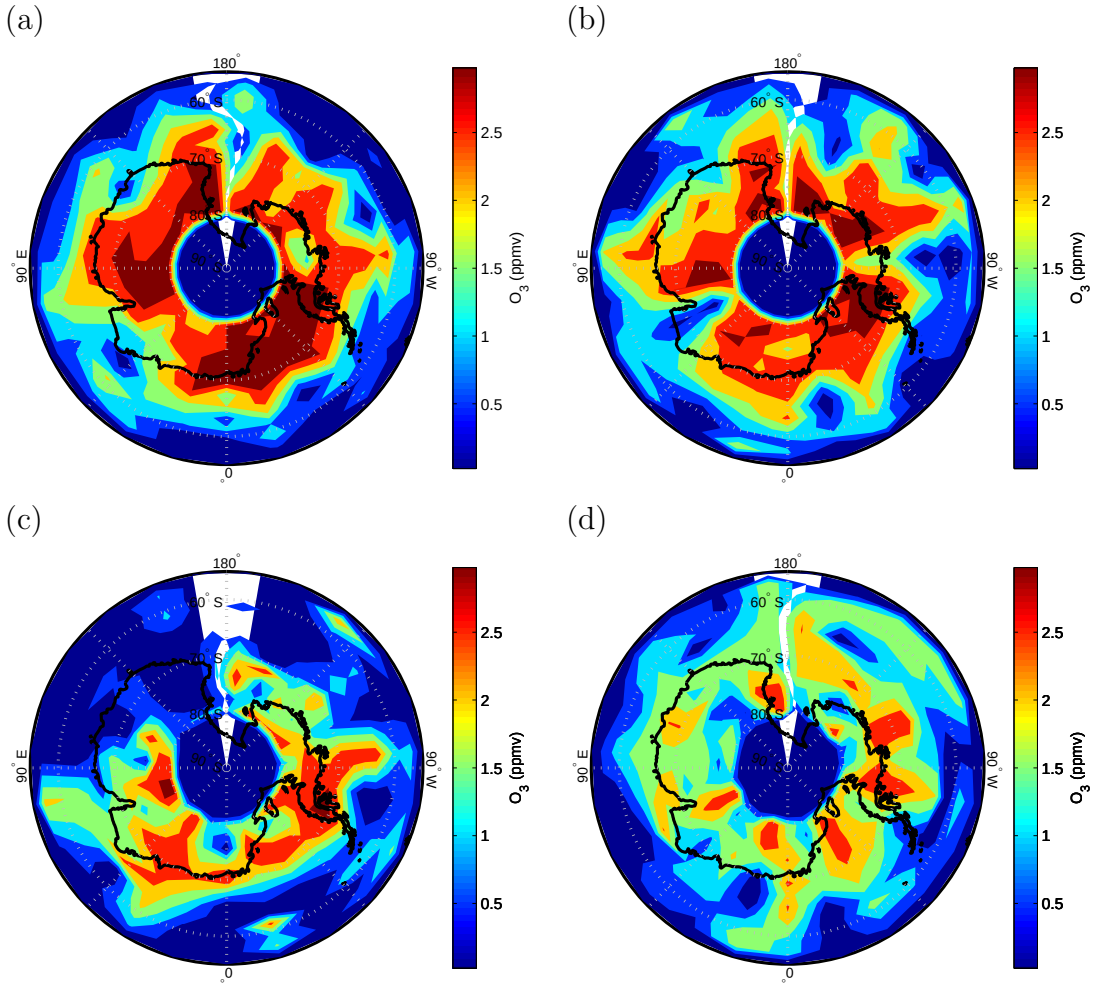

Figure 7.17: Daily maps of MLS ozone volume mixing ratio at 0.05 hPa (70 km) for 13 May (a), 14 May (b), 15 May (c), and 16 May 2005 (d).

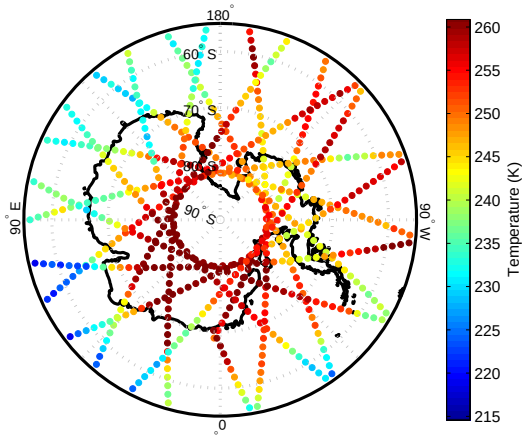

Figure 7.18: Map of temperature measurements by MLS on 15 May 2005 at 0.05 hPa (70 km).

propagating and to have zonal wavenumbers of 1 and 2. The observations showed that the average wave activity, computed as the mean of the two- and four-day oscillations, is more constant than the activity of the individual waves. This can be interpreted as the existence of a relatively constant wave-forcing mechanism such as shear instabilities. Vertical and horizontal shear of the zonal wind, which can create baroclinic and barotropic instabilities, respectively, were studied using satellite and assimilated data in order to determine if a relationship to wave activity exists. The results indicated that vertical shear, which is larger at 60°S than at 70°S, contributes more to wave activity at 60°S. The opposite is true for the horizontal shear, which is largest at 70°S and appears to contribute more to wave activity there than vertical shear.

The baroclinic and barotropic instabilities are related to the stratospheric / mesospheric jet. For both types of instabilities the part of the time-dependence that depends on the strength of the jet are similar. However, the variation of the horizontal and vertical location of the jet will influence the baroclinic and barotropic instabilities in a different way. Therefore, distinguishing between the two types of instabilities in the data will be possible.

A two-day wave with unusually large amplitudes was found in mid-May 2005 in the radar and satellite measurements. A link to an SPE, which occurred just before the amplitude boost, was suggested and investigated. Energetic particles created by the SPE are guided by the Earth's magnetic field and reach the middle atmosphere above the magnetic poles. This leads to the production of species such as OH which destroy ozone in this area. The reduction of ozone leads to a reduction of absorption of UV and could therefore lead to a cooling. The OH enhancements, ozone loss, and temperature decrease were all observed in the case of the SPE in May 2005. It is likely that the temperature decrease mainly

occurred in the same geographic area as the ozone loss. It is hypothesised that an already present planetary wave, which had a small amplitude because the weak early winter jet did not produce strong instabilities yet, was amplified by the SPE through additional cooling in the cold phase of the wave. This mechanism requires further study using 3-dimensional chemistry-climate modelling.

Chapter 8

Conclusions and Future Work

The dynamics of the middle atmosphere are governed by different types of atmospheric waves. This thesis focussed on the examination of waves with periods up to four days which include gravity waves, tides, and short-period planetary waves. Emphasis was placed on the local generation mechanisms of waves and interactions which lead to modulations of wave amplitude on a large variety of scales. The geographical area for this work was constrained to Antarctica. Only data from stations on the Antarctic continent were employed, and the analysis of satellite data was generally limited to the area south of 60°S, which encompasses Antarctica and parts of the Southern Ocean. Ground-based measurements discussed originate from MFSA radars at Scott Base, Rothera, and Davis and from an IDI at Halley. All these instruments measure wind velocity and direction in the upper mesosphere and lower thermosphere. Satellite measurements of temperature from the CHAMP satellite, which employs the radio occultation principle, and temperature, hydroxyl, and ozone measurements obtained from the EOS MLS instrument, a microwave limb-viewing experiment on the Aura satellite, are also used. The measurements are complemented by the NCEP/NCAR reanalysis as well as the UKMO stratospheric assimilated data for further analysis.

The first part of this thesis was concerned with the upgrade of the MFSA radar at Scott Base with the aim of ensuring continued operation and increasing system capabilities for the measurement of gravity waves. The upgrade was carried out in December 2004, followed by some further improvements. The main features of the new system are its high precision (12 bit), its increased sampling frequency (20 Hz), continuous data acquisition, and raw data storage. This was made possible by the installation of a new data acquisition card, a DATEL PCI416L, a new PC, and multi-threading software. When comparing the old wind velocity data with the new data it becomes evident that the quality and quantity have improved drastically; the number of velocity measurements has increased by a factor of 15. Faults can now be detected more easily because the measurements can be accessed easily from New Zealand using FTP. Using the same connection, operational parameters or the entire software package can be upgraded remotely if necessary. The new possibility of saving raw I and Q data has been exploited and parameters of the FCA algorithm have been significantly improved. The data is

now very well suited for the detection of gravity waves and therefore enables us to study wave properties, wave propagation, and interactions. Unfortunately, time constraints for this thesis prohibited the analysis of the new data with respect to gravity waves, but possibilities and aims for such studies are outlined below.

Because the Scott Base MFSA radar has been in operation since 1982, the data set allowed us to create accurate climatologies of the background winds and tidal oscillations, and to study their seasonal and interannual variations in detail. The study motivated many of the questions addressed in following chapters, such as the analysis of the zonal structure of the semi-diurnal tide and its interaction with wavenumber 1 planetary wave structures. In order to study the climatologies and variabilities, a database of the wind velocities from 1982 to 2005 has been compiled from the entire set of measurements which were previously only available in different formats spanning only a few years each. Statistical analysis of the mean winds and tidal amplitudes was then performed. Gaps in the data set with lengths of up to a year, and several hardware changes meant that care had to be taken when analysing and interpreting the data. For example, clock problems during 1992–1995 meant that tidal parameters are not reliable during that period. It was shown that the seasonal behaviour of the semi-diurnal tide bears a striking resemblance to the behaviour of planetary wave activity at high latitudes in the northern and southern hemispheres. A large wavenumber 1 tide generated through nonlinear interaction between a wavenumber 2 tide and wavenumber 1 planetary wave, as suggested for example by Angelats i Coll and Forbes (2002), could be responsible for this finding. Large peaks in the semi-diurnal amplitude could also be related to the timing of zero winds in the stratosphere (McLandress, 2002b). Amplitude damping by enhanced gravity wave activity in winter is also a possible explanation for the observed correlations (Fritts, 1995b). No relationship between the QBO and wind parameters was evident in the interannual variations, although such effects have been reported using models (Hagan et al., 1999). Additionally accounting for solar activity, as suggested by Labitzke (2005), did not change this finding. However, the measurements showed a positive amplitude trend for the diurnal and the semi-diurnal tide and a modulation with a period of 11 years. The latter amplitude modulation shows a clear relationship to the 11-year solar cycle, similar to observations at other sites (Bremer et al., 1997). The tidal amplitudes are observed to increase when the data from 1987 to 2004 is utilised. Tidal amplitude data before 1987 cannot be used for this analysis because of differing measuring/processing schemes. The positive trend in the tidal amplitudes was found in the zonal and meridional diurnal and semi-diurnal tides at all heights.

Several phenomena that could contribute to the observed relationship between tidal amplitudes and solar activity, as well as the positive amplitude trends were discussed. The long-term changes in planetary wave amplitudes are similar to those observed in the tides. Therefore, it is possible that planetary waves contribute not only to the seasonal but also to the interannual variation of the

tide. The apparent long-term behaviour of the tides might also be controlled by the observed short peaks in early and late summer. These peaks appear to correlate with the changeover between the winter and summer circulation in the stratosphere. Long-term changes in polar vortex location, strength and duration, as described for example in Labitzke (2004), could affect the timing and therefore the strength of the amplitude peaks. Further work is needed to clarify the origin of the tidal amplitude peaks; only then can the impact of a shift of the peak in time be assessed. A third possible mechanism explaining the relationship of the tides to the solar cycle and the observed trends is based on vertical displacement of pressure levels induced by solar activity changes and greenhouse cooling. Estimations of the magnitude of amplitude changes through vertical displacement indicated that this effect can only account for a small part of the observed trend. The results with respect to the tidal amplitude trend analysis contradict earlier publications (see for example the multi-site study by Bremer et al., 1997) and support a summary by Lastovicka (2005) who concluded that the wind variability with respect to time and geographic location is not fully understood at present and reliable long-term observations from several stations seem necessary. The large interannual variability suggests the importance of long-term records in identifying precise climatological values.

In the discussion of seasonal and interannual variability of the tides at Scott Base it was noted that the presence of more than one tidal wavenumber component might be partially responsible for the observed behaviour. This is also expected from observational results presented by Hernandez et al. (1993) and Angelats i Coll and Forbes (2002) for example. Therefore, the semi-diurnal tide was studied in more detail by combining the Scott Base data set with wind measurements from the same altitude region performed at Halley, approximately the longitudinal conjugate point, with an imaging Doppler interferometer. It was shown that the zonal structure of the semi-diurnal tide at the latitudes of Scott Base and Halley can be described consistently using a combination of wavenumber 1 and 2 waves. The combination of the data sets allowed the separation of the wave components under certain assumptions. In summer the wavenumber 1 component is often dominant; through most of the winter months both components have similarly small amplitudes. Agreement with a study by Riggin et al. (1999) was reasonable, although they had used a smaller data set and a different analysis technique. Amplitudes of the wavenumber 1 tide in the southern and northern hemispheres were confirmed as having a strong relationship with planetary wavenumber 1 activity. Further, it was observed that when the wavenumber 1 tide was large the longitude where maxima of the s=1 and s=2 tide coincide is related to the maximum of the planetary wave. Therefore, generation of the wavenumber 1 tide through interaction between the wavenumber 2 tide and planetary waves seems likely. The regions where this interaction is most likely to occur were identified as being the upper stratosphere at mid- to high-latitudes. This finding substantiates the speculations in chapter 4 that planetary waves

are at least partially responsible for seasonal and interannual variations of tidal amplitudes at Scott Base.

For the study of middle atmosphere gravity waves, a climatology of wave activity in the stratosphere was deemed necessary before further study of propagation and interactions at higher altitudes. For this purpose, temperature profiles obtained by the radio occultation (RO) experiment on the CHAMP satellite were used to infer gravity wave activity over the Antarctic. Similar studies for example by Ratnam et al. (2004a) have used CHAMP RO data for such studies in the recent past. Significant seasonal variation was found, similar to the results obtained by Yoshiki and Sato (2000) using radiosonde data, and attributed to the seasonal variation of critical level filtering and Doppler shifting by the mean winds. Critical level filtering has previously been reported to be important in the Arctic, for example by Whiteway and Duck (1996). Due to the possible effects of observational filtering in combination with wave Doppler shifting and refraction, any variation of wave activity has to be interpreted with caution. However, instruments observing wave activity over other vertical wavelength ranges have found similar seasonal patterns; therefore, the CHAMP RO data are assumed to be a good approximation to the real wave activity. Large enhancements of potential energy were noted over mountainous areas, in particular the Antarctic Peninsula. This had previously been noticed by Wu and Jiang (2002) using MLS radiance fluctuations. Wave forcing by means of flow over topography, described for example by Bacmeister et al. (1990), appeared to be the most likely cause for this finding. This was confirmed by the fact that strong surface wind velocities perpendicular to the Peninsula were observed when large wave activity was measured by the RO experiment. In addition, there is an almost linear relationship between the amount of rotation of the background wind and wave activity over the Peninsula, indicating that gravity waves are filtered at a critical level when the background wind in the direction perpendicular to the wave fronts is zero. This suggests that a significant part of the wave spectrum has a near zero phase speed; these waves are therefore likely to be mountain waves. At the same time, this supports the interpretation that the seasonal variation is partially associated with critical level filtering. Wave activity enhancements were also found around the edge of the polar vortex; this observation was attributed to reduced critical level filtering and Doppler shifting. Additional wave sources, such as geostrophic adjustment or shear associated with the jet, were not necessary to explain this enhancement.

The detection of large amplitude events at planetary wave periods in the improved Scott Base MFSA radar data motivated an examination of the behaviour and origin of planetary waves with periods of between two and four days. Events with similar periods in Scott Base MFSA radar observations have been reported previously by Fraser et al. (1993). Only limited conclusions can be drawn from data from a single site, so MFSA radar wind measurements at Scott Base, Rothera, and Davis as well as EOS MLS measurements were combined

for this analysis. An oscillation with a period of approximately two days during late January and early February 2005 was reported. Its largest amplitude was observed at about 90 km altitude and it showed a westward propagating zonal wavenumber 3 structure which indicates a relationship to the quasi two-day wave commonly observed at low- and mid-latitudes (e.g. Limpasuvan and Wu, 2003). Satellite measurements of the latitudinal extent confirmed this conclusion. In winter, oscillations with periods between two and four days were prominent. The radars showed that their amplitudes maximised below 80 km. This finding is consistent with northern hemisphere studies by Nozawa et al. (2003a) and Chshyolkova et al. (2005). Further analysis with satellite temperature measurements indicated that amplitudes up to 8°K were reached at the stratopause and in the lower mesosphere. These waves were found to be eastward propagating and to have zonal wavenumbers of 1 and 2. The observations showed that the average wave activity, computed as the mean of the two- and four-day oscillations, is more constant than the activity of the individual waves. This can be interpreted as the existence of a relatively constant wave-forcing mechanism such as shear instabilities created by jets which have previously been pointed out as sources for instabilities (e.g. Plumb, 1983).

Vertical and horizontal shear of the zonal wind, which can create baroclinic and barotropic instabilities respectively, were studied using satellite and assimilated data in order to determine if a relationship to wave activity exists. The results indicated that vertical shear, which is greater at 60°S than at 70°S, contributes more to wave activity at 60°S. The opposite is true for the horizontal shear, which is greatest at 70°S and appears to contribute more to wave activity there than vertical shear.

A two-day wave with unusually large amplitudes was observed in mid-May 2005 in the radar and satellite measurements. A link to an SPE, which occurred just before the amplitude enhancement, was suggested and investigated. Limpasuvan et al. (2005) had reported a similar coincidence during January 2005. Energetic particles created by the SPE are guided by the Earth's magnetic field and reach the middle atmosphere above the magnetic poles. This leads to the production of species such as OH which destroy ozone in this area. The reduction of ozone leads to a reduction of absorption of UV and could therefore lead to a cooling. An enhancement of OH was observed shortly after the SPE in May 2005, followed by a loss of ozone and a subsequent temperature decrease. It is likely that the temperature decrease mainly occurred in the same geographic area as the ozone loss. It is hypothesised that an already present planetary wave, which had a small amplitude because the weak early winter jet did not yet produce strong instabilities, was amplified by the SPE through additional cooling in the cold phase of the wave. This mechanism requires further study using 3-dimensional chemistry-climate modelling.

The work in this thesis lays the basis for further study in many areas of wave

dynamics. In particular, the study of gravity wave propagation and interactions had originally been planned to be part of this thesis, but, as already mentioned, this turned out to be beyond the thesis time frame. Much of the presented work has lead to many new questions and many aspects had to be left out. Therefore, some suggestions for important and hopefully fruitful avenues of further work are outlined below.

The study of long-term changes of wind parameters at Scott Base only included tidal amplitudes and did not discuss multi-year oscillations or trends in the tidal phases. Long-term variations in the phases have so far received little attention in the literature. However, any changes in the propagation conditions for tides, such as changes of stratospheric or mesospheric winds or temperatures, could lead to changes in the phases of the tides and an investigation using the long record from Scott Base could yield interesting results. However, care would need to be taken because relative amplitude changes of different tidal wavenumber components also lead to local phase changes (see chapter 5). A recent study by Jacobi and Kürschner (2006) attributed long-term changes of tidal phases over Europe to mesospheric cooling.

Observations of polar mesospheric clouds (PMC) have shown a negative correlation between PMC parameters (frequency and brightness) with solar activity as well as a positive trend (e.g. DeLand et al., 2006). This finding corresponds well to the observations from the Scott Base MFSA radar with respect to tidal amplitudes. Because temperature is a critical parameter for the formation of PMCs, this relationship might be more than incidental. A rigorous statistical comparison is necessary to confirm this. The relationship can be further investigated by modelling ice particle properties and analysis of their dependence on tidally modulated temperature. Modelling work on these aspects has already begun by Thomas et al. (2006).

The analysis of the zonal structure of the semi-diurnal tide was only able to account for one odd and one even component. However, there have been suggestions that there are at least three different components present over Antarctica (Angelats i Coll and Forbes, 2002, D. J. Murphy, personal communication). Installation of an additional radar at a suitable site would make it possible to resolve three components and could therefore help to clarify this issue. For example, an inexpensive meteor radar could be installed at Sky-Blu (75°S, 72°W), a research station operated during the summer by the British Antarctic Survey. Its latitude (close to the latitudes of Scott Base and Halley) and longitude (approximately half-way between Scott Base and Halley) would make it well suited for such a study. The only major disadvantage would be the fact that meteor and MFSA radars are known to measure different tidal amplitudes. This would make interpretation of the results difficult. The which would make the interpretation more difficult. The proposed work would also benefit from the anticipated installation of a modern MFSA configuration at Halley in the near future. The MFSA radar

is likely to provide much better data quality than the Halley IDI.

There is much scope for further work with respect to gravity waves. The gravity wave analysis with RO data suggested a strong seasonal variation of wave activity. By examining the data from the upgraded Scott Base MFSA radar, a similar study is now possible for the upper mesosphere and lower thermosphere. A comparison between the results would allow conclusions to be drawn about wave propagation conditions as a function of year, additional wave sources, and filtering. Work by R. E. Hibbins (personal communication, 2006) shows that gravity wave activity in the mesosphere over Rothera has a similar seasonal pattern to that observed in the lower stratosphere in the present study. This could mean that the lower stratosphere is the dominant region for gravity wave filtering, and therefore wave breaking, in the atmosphere over Antarctica. This could have consequences for the polar stratosphere mean circulation, which is strongly influenced by wave breaking, according to the downward control principle (Haynes et al., 1991; Garcia and Boville, 1994). Analysis of gravity waves spanning the stratosphere and mesosphere could also help to assess the role of the Antarctic gravity wave field in the departure from thermal equilibrium of the polar summer mesopause.

The analysis of gravity waves using RO measurements could be extended to include other wave sources, for example fronts. Also, RO amplitude data (Liou et al., 2005, 2006) could provide valuable additional information about gravity wave activity, especially at smaller vertical wavelengths, and should be used for similar studies. Since the launch of the FORMOSAT-3/COSMIC constellation and MetOp-A much more data is available for such analysis.

The examination of the zonal structure of the semi-diurnal tide and the planetary wave activity study suggested a possible influence of solar flares on polar middle atmosphere dynamics. Due to the rarity of such events and the limited amount of data available for further investigations, chemistry-climate models (CCM) might be better suited to advance our understanding of such events and their effects. For example, a CCM could be used to study the response of ozone, temperature and dynamics to artificially introduced disturbances in mesospheric OH mixing ratios. Such research is likely to be carried out in the framework of the ProSECCO/CAWSES project (MPI-C, 2006).

Appendix A

Technical Documentation for the Scott Base MFSA Radar Software

This appendix documents the MFSA radar software Version 2.1 Revision 30.

A.1 Introduction

The radar software is in charge of data acquisition and processing of the data obtained by the Medium Frequency Radar at Arrival Heights / Scott Base, Antarctica. It was written for the data acquisition card DATEL PCI416-L and makes use DATEL's the Windows XP drivers that control the low-level functions of the card. For the user, the software consists of only a few easy-to-use interfaces. This documentation is intended for debugging and future reference in case of updates. It describes the basic principles of the program and discusses vital sections of the code. The program is written in Microsoft Visual C++ 6.0. Parts of the software, namely mathematical functions, the graphical ActiveX displays, the basic serial port communication class and the ZIP functions were developed by other people (see section class overview).

A.2 Version history

Version	Operation start date
V1.0 Rev 24	12 December 2004
V2.0 Rev 27	5 December 2005
V2.0 Rev 28	28 January 2006
V2.0 Rev 29	7 March 2006
V2.1 Rev 30	20 November 2006

A.3 Software features

1. Continuous data acquisition
2. Independent threads for data acquisition and wind analysis
3. Raw data can be saved to hard drive in the NetCDF format
4. Logging, automatic reboot and software restart on any major failures
5. Logging of minor errors
6. Update of the system time via a GPS receiver connected to the serial port
7. Raw data is zipped and the original files deleted to conserve space
8. Graphical display of raw and analysed data
9. Internal or external triggering

For on-site installation the data acquisition software can be installed via an automatic installer. For remote updates, the software can be stopped and then updated using FTP. An additional tool "RadarRestarter" can then be used to restart the computer to start the updated software.

The MFSA experiment shares the transmitter and data acquisition system with a Polarimeter. However, the polarimeter data is not analysed in real time.

A.4 Installation instructions

Channels:

0,1	Winds antenna A
2,3	Winds antenna B
4,5	Winds antenna C
6	Polarimeter phase information
7	Polarimeter data

A map of the physical layout of the aerials is depicted in chapter 2, Figure 2.11.

1. Hardware: DATEL PCI416L
2. Operating system: Windows XP Professional SP1/2
3. Change bios setting to autostart on power on
4. Check Card hardware jumpers that they're set to ± 5 V

5. Windows XP will launch its "Found New Hardware" Wizard when the card is put into the computer
   (a) Select "Install from a a list or Specific Location (advanced)"
   (b) Select "Search for best driver in these locations"
   (c) Select "Search Removable Media" (the drivers are in the `Win2000_XP_drivers` directory on the CD)
6. In "Control Panel", "System", Tab "Hardware" click on "Device Manager".
   (a) Doubleclick "Data acquisition devices"
   (b) then doubleclick on the newly appeared "PCI416"
   (c) In the new window select tab "Advanced".
   (d) Enter an appropriate value for "DMABufferSize" (at least: number of channels times the number of sampled range bins times PRF times FCA length in seconds times four (12 bit so 2 bytes per sample, and double buffering))
7. Date and Time properties (doubleclick on clock):
   (a) disable daylight savings
   (b) disable Internet time update (only Windows XP SP2)
8. In "Control Panel", "Display", "Settings" Tab: change screen resolution to 1024x768
9. In "Control Panel", "User Accounts" - "select logon and logoff options" enable "Use the Welcome screen", this will cause automatic logon
10. Install drivers for hardware (network etc)
11. Network setup:
    - IP: 192.133.31.244, dns name radar.scott.aq
    - Gateway: 192.133.31.129
    - Subnet mask: 255.255.255.0
    - Primary DNS: 192.133.31.146
    - Secondary DNS: 131.203.248.1
    - Workgroup: k055
    - Do not join domain, but use scott.aq as DNS
    - Web-proxy: 192.133.31.145:8081
12. Merge the file `mousefix.reg` from the radar CD with the registry. This is a fix for problems with the GPS receiver and the mouse.

13. From the radar CD install all software packages (DATEL drivers, radar data acquisition software, war-FTP server, WinZip, Nero, UPS software
14. War-FTP configuration:
    - Server Name: K055 server, system password: ****
    - WarFTP user manager: add the following directories to the sysadmin File access menu: C:\FCA, C:\MFradar2.1, C:\logs, Q:\WIND, Q:\POL
    - make all directories above recursively readable, writable, etc.

For changes of the radar data acquisition software, Microsoft Visual Studio 6.0 (SP6) should be utilised. The installer package can be complied with Inno Setup Compiler Version 5.1.5.

A.5 Class overview

Main class: radar (extended by files DAQ, FCA, POL, FCAutils, utils) Main dialogs:

- radarDlg: Main menu
- normalrun: Dialogue for normal operation of the radar

Classes for Settings Dialogs:

- DAQSettings
- FCASettings

Helper classes

- GPSclockReader
- ZIPArchive (Dracz, 2005)
- Ntgraph
- NetCDF associated classes

Other:

- picture – used by ntgraph

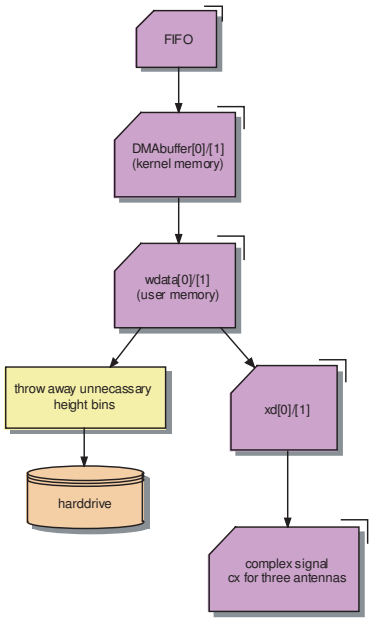

Figure A.1: Flowchart of data within the MFSA radar data acquisition software.

- font – used by ntgraph
- SerialPort – used by GPSclockReader.
- Resource – C++ internal
- StdAfx – C++ internal

A.6 Flowcharts

A flowchart of the data acquisition software is presented in chapter 3, Figure 3.4. Figure A.1 depicts the data flow within the program.

A.7 Function descriptions

1. Data acquisition related functions
   - `UINT DAQthread(LPVOID pParam)` – Main function that controls the card and copies the data into memory.
   - `init_dll()` – Initializes the card drivers.
   - `clean_up_dll(LPVOID pParam)` – Clean up card drivers.
   - `init_variables(LPVOID pParam)` – Creates dynamic arrays.

- `clean_up_variables(LPVOID pParam)` – Deletes dynamic arrays.
- `save_WIND_netcdf(LPVOID pParam)` – Saves I and Q MFSA radar data in NetCDF format.
- `save_POL_netcdf(LPVOID pParam)` – Saves raw Polarimeter radar data in NetCDF format.
- `POLpretrigger(LPVOID pParam)` – Configures Polarimeter receiver to correct starting state.

2. Functions related to the winds analysis

- `FCAcopybuffer(LPVOID pParam)` – Called by DAQthread to copy data to FCA data structure after every block.
- `FCAthread(LPVOID pParam)` – Performs the Full Correlation Analysis analysis.
- `float comcovar(std::complex <float> *x, std::complex <float> *y, int n, int lag)` – Calculates complex covariance.
- `float db2volts(float dbs, float vref)` – Converts noise value in decibels to volts.
- `void despikeg(float cxxz, float *xc, int slag, float a[], int ma, float &noisig, int &ifail)` – Takes the autocovariance function, xc[1..maxlag] and the zero-lag spike (cxxz) as input, does a nonlinear fit to gaussian a(1)*exp(-(x/a(2))2) and returns the fitted coefficients and the noise-to-signal ratio.
- `void fitpol(float x[], float y[],int i1, int i2, float c[], int nc)` – Fit y(i1)..y(i2) to an nc-1 order polynomial, returning the polynomial coefficients in c(1...nc). Used for fitting to mean auto-correlation function.
- `int ibig(float x[], float y[],int i1,int i2)` – returns index of maximum of y between i1 and i2. Called by `delay`.
- `float slope(float x, float c[], int morder)` – Calculates the first derivative of the fitted polynomial at x. Used by `delay`.
- `float rtbis(float (*func)(float,float[],int), float x1, float x2, float xacc, float foffset, float c[], int morder, int &ifail)` – Using the bisection method, find the root of a function func known to lie between x1 and x2. Adapted from Press et al. (1992). Used by `delay` and `xfory`.
- `float xfory(float x[], float y[], int i1, int i2, float ye, float c[], int morder, int maxlag, float ttol, int &ifail)` – root-finding routine except that we want the value of x at y=ye, not at y=0.

- `float yfit(float x,float c[],int morder)` – Evaluate the polynomial at x.
- `float delay(float x[], float y[],int i1, int i2, int &im, float c[], int morder, int maxlag, float ttol, int &ifail)` – Finds maximum of cross-correlation function of transmitter pulse.
- `int round(float x)` Rounds value to nearest integer.
- `void mrqmin(float x[], float y[], float sig[], int ndata, float a[], int ma, int mfit, float **covar, float **alpha, float *chisq, void (*funcs)(float, float [], float *, float [], int, int &), float *alamda, int &ifail)` – Nonlinear fitting routine using the Levenberg-Marquardt method, attempting to reduce the value `chi^2` of a fit between a set of data points x[1..ndata], y[1..ndata] with individual standard deviations sig[1..ndata], and a nonlinear function dependent on coefficients a[1..ma]. The program returns current best-fit values for the parameters a[1..ma] and `chi^2=chisq`. Supply a routine `funcs(x,a,yfit,dyda,ma)` that evaluates the fitting function `yfit` and its derivatives `dyda[1..ma]` with respect to the fitting parameters 'a' at 'x'. Adapted from Press et al. (1992). Used by `despike`.
- `void fgauss(float x, float a[], float *y, float dyda[], int na, int &ifail)` – Gauss function with mean value = 0 used by `despike/mrqmin`. Adapted from Press et al. (1992).
- `void svdfit(float x[], float y[], float sig[], int ndata, float a[], int ma, float **u, float **v, float w[], float *chisq, void (*funcs)(float, float [], int))` – Linear least squares fitting using singular value decomposition. Given a set of data points `x[1..ndata],y[1..ndata]` with individual standard deviations `sig[1..ndata]`, use `chi^2` minimization to determine the coefficients a[1..ma] of the fitting function y=sum(a*afunc(x)). The program returns values for the `ma` fit parameters `a`, and `chisq`. Adapted from Press et al. (1992). Called by `fitpol`.
- `void fcapoly(float x, float p[], int np)` – polynomial of degree np-1, with coefficients in the array p[1..np] for `fitpol/svdfit`. Adapted from Press et al. (1992).

3. General functions (utils.cpp)

- `void logmsg(CString message)` – Log message.
- `void reboot(CString message)` – Log message and reboot, for critical failures like memory allocation etc.
- `UINT checkForRestartRequest(LPVOID pParam)` – checks file `c:\logs\RestartRequest.txt` to see if user requested:

- DAQ restart (end thread and start new DAQ thread) (value 1)
- Exit program (restart via application 'RadarRestart') (value 2)
- Computer restart (value 3)

A.8 Documentation of vital code sections

The main data structure

The structure that holds all the global variables and data to exchange between functions is hosted in a structure called `SradarData`. Only one object of it is created at program launch called `sData` (in radar.cpp). A pointer to this object is passed to all functions that need access to its variables. In those functions, the name of the pointer is always `tData`.

The data acquisition function's (DAQ.cpp) main section

After processing each block, we have to wait until enough data for the next block is collected.

```
do // wait for DMA transfer to complete
{
    WaitForSingleObject(waithandle,300); // 300 ms
    pci416_dma_status(which_device, &dmastat);
}
while (!dmastat  && !tData->DAQstopflag);
```

The block is full, so we tell the driver to use the other DMA buffer for new data:

```
pci416_reload_dma(which_device, bufno, &cb_bufsize, &dmabufhnd);
```

Then the data is copied into the user memory wdata:

```
bufno = !bufno;
pci416_copy_dmabuffer(which_device, bufno, 0, &cb_bufsize, (DWORD *)pwdata);
```

Now copy data into appropriate data structures:

```
for (p=0; p<pulses_pb; p++)
{
    for (r=GPr_start; r<=GPr_end; r++)
        for (ch=GP_1stch; ch<GP_1stch+tData->GP_numch; ch++)
            tData->GPraw[p][r-GPr_start][ch-GP_1stch]=*(pwdata+p*samples_pt+r*DAQ_numch+ch);
    for (r=WINDr_start; r<=WINDr_end; r++)
        for (ch=0; ch<tData->WIND_numch; ch++)
            tData->WINDraw[p][r-WINDr_start][ch]=*(pwdata+p*samples_pt+r*DAQ_numch+ch);
    for (r=POLr_start; r<=POLr_end; r++)
        tData->POLraw[p][r-POLr_start]=*(pwdata+p*samples_pt+r*DAQ_numch+POL_datach);
    tData->POLphase[p]=*(pwdata+p*samples_pt+15*DAQ_numch+POL_phasech); // use range 15
}
```

Save data to harddrive:

```
save_WIND_netcdf(pParam);
save_POL_netcdf(pParam);
```

Now copy data structure to FCA structures and call FCA function:

```
FCAcopybuffer(pParam);
```

Full Correlation Analysis (FCA.cpp)

Note: For clarity, for many variables the `tData->` prefix has been omitted. The same applies to "bufferoffset" used to distinguish between the two buffers in the data structure `xd` (double buffering). Hence `xd[pulse]` reads `xd[bufferoffset+pulse]` in the original code.

A.8.1 Initialization

After initialization of the data structures the offset for the current buffer is calculated and the FCA wind velocity data file is created:

```
bufferoffset = FCAbuffer*ksamples;

// create file for FCA data
theTime = DAQtime;
dir_name = theTime.Format("c:\\FCA\\%Y\\%m\\%d");
if (!WriteDirectory(dir_name))
    reboot("Error -- can't create directory for FCA file");

file_name = theTime.Format("c:\\FCA\\%Y\\%m\\%d\\FCA%Y-%m-%d-%H.dat");
FCAout_file.open(file_name,ios::out|ios::app);
if (!FCAout_file.is_open()) {
    reboot("Error -- can't open FCA file for write.");
}

// write header info to file
...
```

A.8.2 Ground pulse search

The range of the ground pulse is calculated, written to the data file, and checked for validity:

```
findFCAgp(pParam,txzero,txstd);
// write ground pulse data to file
...
if ((txzero[0]<=0.0)||(txzero[0]>MAXGPBIN-1))
{
    // gp missing: message and log it, don't analyse this dataset
    logmsg("FCA: ground pulse missing, omitting data set");
    goto stopdataset;
}
```

A.8.3 Noise calculation

The noise level is calculated as the RMS from channels 1, 3, 5. Firstly, we average over all pulses from each channel and height, which yields the means `av`.

```
// find average from xd[allpulses] for each ch and height
for (pulse=0; pulse<ksamples; pulse++)
{
    // substract 41 so that txzero+40 doesn't exceed xd array size
    for (i=1; i<=maxhts-MAXGPBIN-1; i++)
        for (ch=1; ch<=6; ch++)
            // add xd[allpulses] for each ch and height
            av[ch][i]+=(float)xd[pulse][ch-1][round(txzero[pulse])+i-1];
}

for (ch=1; ch<=6; ch++)
    for (i=1; i<=maxhts-MAXGPBIN-1; i++)
        av[ch][i]/=ksamples;
```

Secondly, we form channel means `avx` from the pulse means `av`. We use ranges 10 – 25 km where there is no overloading.

```
for (i=10; i<25; i++)
    for (ch=1; ch<=6; ch++)
            avx[ch]+=av[ch][i];
for (ch=1; ch<=6; ch++)
        avx[ch]=avx[ch]/15.0;
```

Then the RMS values are calculated as rms = (value-mean)^2.

```
for (pulse=0; pulse<ksamples; pulse++)
    for (ch=1; ch<=6; ch++)
        for (i=1; i<=maxhts-MAXGPBIN-1; i++)
            rms[ch][i]+=pow(((float)xd[pulse][ch-1][round(txzero[pulse])+i-1]-avx[ch]),2);
```

Now we form complex signals from the two channels of an antenna and calculate its amplitude.

```
for (pulse=0; pulse<ksamples; pulse++)
    for (i=1; i<=maxhts-MAXGPBIN-1; i++)
        for (ant=1; ant<=3; ant++)
        {
            buffer=(xd[pulse][ant*2-2][round(txzero[pulse])+i-1]-avx[ant*2-1],
                    xd[pulse][ant*2-1][round(txzero[pulse])+i-1]-avx[ant*2]);
            amp[ant][i]+=std::abs(buffer);
        }

vref=0.001f; // 1 mV, smallest allowed voltage

// calculate between channel rms values
factor=1.0/ksamples;
for (ant=1; ant<=3; ant++)
{
    for (i=1; i<=maxhts-MAXGPBIN-1; i++)
```

```
    {
        xx=sqrt(rms[ant*2-1][i]+rms[ant*2][i]); //xx just buffer
        if (xx<1.0) xx=1.0;
        xx=factor*xx*volts;
        if (xx<vref) xx=vref;
        rmsdb[ant][i]=20.0*log10(xx/vref);

        xx=amp[ant][i];
        if (xx<1.0) xx=1.0;
        xx=factor*xx*volts;
        if (xx<vref) xx=vref;
        ampdb[ant][i]=20.0*log10(xx/vref);
    }
}

// Record noise level at 50 km
noisehind=50;
for (ant=1; ant<=3; ant++)
    noise[ant]=db2volts(rmsdb[ant][noisehind],vref);

// write noise level to file
...
```

A.8.4 Calculation of the auto- and cross-correlation functions

All of the following is done separately for all heights:

```
for (hindex=1; hindex<=maxhts-MAXGPBIN-1; hindex++)   // The MAIN height loop
{
height=float(hindex) - (pathdelay);
// pathdelay is half the distance between the trigger and the transmitter (1.6 km)

if (height<minheight) goto eohloop;
if (height>maxheight) goto eohloop;

Firstly, we form a complex signal for each antenna:

for (k=0; k<ksamples; k++)
{
    cx1[k+1]=std::complex <float> (float(xd[k][0][round(txzero[k])+hindex-1])-avx[1],
                                   float(xd[k][1][round(txzero[k])+hindex-1])-avx[2]);
    cx2[k+1]=std::complex <float> (float(xd[k][2][round(txzero[k])+hindex-1])-avx[3],
                                   float(xd[k][3][round(txzero[k])+hindex-1])-avx[4]);
    cx3[k+1]=std::complex <float> (float(xd[k][4][round(txzero[k])+hindex-1])-avx[5],
                                   float(xd[k][5][round(txzero[k])+hindex-1])-avx[6]);
}
}
```

Then we calculate the scalefactors from the zero lag of the autocorrelation function for each signal:

```
scalefactor1=comcovar(cx1,cx1,ksamples,0);
... (all antennas)

for (lag=1; lag<=maxlag; lag++)
{
    xr1[lag]=comcovar(cx1,cx1,ksamples,lag)/scalefactor1;
    ... (all antennas)
    c11[maxlag+1+lag]=xr1[lag]; // pos lags go at the end
```

```
    ... (all antennas)
    if (lag==2) {
        if (xr1[lag]<0.25) { logmsg("FCA: autocorrelation on ant1 < 0.25"); goto eohloop; }
        ... (all antennas)
    }
    c11[maxlag+1-lag]=xr1[lag]; // and negative lags go at the start
    ... (all antennas)
}
```

The autocorrelation functions from all three antennas are despiked by fitting a Gaussian function to them between +/- slag:

```
despikeg(1,xr1,slag,fitcoeffs,mfit,noise[1],ifail);
if (ifail>0) goto eohloop;
c11z=fitcoeffs[1];
... (all antennas)
```

and use these to calculate the log(rms):

```
rms[1][hindex]=10.0 * log10(c11z*scalefactor1);
c11[maxlag+1]=c11z; //0lag
... (all antennas)
```

Calculate the mean autocorrelation function:

```
for (lag=1; lag<=2*maxlag+1; lag++)
    autoc[lag]=(c11[lag]/c11z+c22[lag]/c22z+c33[lag]/c33z) / 3.0f;
```

Do an initial check on the sensibility of the data by checking the mean autocorrelation function:

```
if (autoc[maxlag+1+1]<0.3) goto eohloop;  // lag 1
if (autoc[maxlag+1+2]<0.0) goto eohloop;  // lag 2
```

Reorganise the data into xii: size=1..2*maxlag (no zero lag):

```
for (i=1; i<=maxlag; i++)
{
    xii[i]=autoc[i];
    xlag[i]=-(maxlag+1-i); // so that we know what lag xii has at [i]
}
for (i=1; i<=maxlag ;i++)
{
    xii[maxlag+i]=autoc[maxlag+1+i];
    xlag[maxlag+i]=i;
}

c12z = sqrt(c11z*c22z);
c23z = sqrt(c22z*c33z);
c31z = sqrt(c33z*c11z);
```

Calculate the cross-correlation functions:

```
{for (lag=-maxlag; lag<=maxlag; lag++)
{
    c12[maxlag+1+lag]=comcovar(cx1,cx2,ksamples,lag)/ sqrt(scalefactor1*scalefactor2);
    c23[maxlag+1+lag]=comcovar(cx2,cx3,ksamples,lag)/ sqrt(scalefactor2*scalefactor3);
    c31[maxlag+1+lag]=comcovar(cx3,cx1,ksamples,lag)/ sqrt(scalefactor3*scalefactor1);
}

// normalize the cross-correlation functions
for (lag=1; lag<=maxlag*2+1; lag++)
{
    rho12[lag]=c12[lag] / c12z;
    rho23[lag]=c23[lag] / c23z;
    rho31[lag]=c31[lag] / c31z;
}

// interpolate linearly through zero lag values
rho12[maxlag+1]=0.5 * (rho12[maxlag]+rho12[maxlag+2]); // maxlag+2 is lag "-1"
rho23[maxlag+1]=0.5 * (rho23[maxlag]+rho23[maxlag+2]);
rho31[maxlag+1]=0.5 * (rho31[maxlag]+rho31[maxlag+2]);
```

A.8.5 Full Correlation Analysis

Note that most of the names of variables within the Full Correlation Analysis originate from their mathematical origins and the mathematical description of the technique. See Briggs article in MAP handbook (1984) "The analysis of spaced sensor records by correlation techniques" for details on the analysis.

The first step is the calculation of the fading time `tfad` from the mean autocorrelation function `autoc`.

```
// find the lag where autoc falls below 0.5
for (i=0; i<=maxlag-4; i++)
{
    lx=i;
    if (autoc[maxlag+1+i]<0.5) break;
}

if (lx<3)
    lx=3;

// set up xlag
for (i=1; i<=2*maxlag+1; i++)
    xlag[i] = i-1-maxlag;

it1=maxlag + 1 - lx;
it2=maxlag + 1 + lx;

// Polynomial fit to the autocorrelation function, returned coefficients: cxx(1..nc)
fitpol(xlag,autoc,it1,it2,cxx,nc);

// find the root of the polynomical with coefficients cxx at y=0.5 -> this is the fading time
tfad=xfory(xlag,autoc,maxlag+2,it2,0.5,cxx,morder,maxlag,ttol,ifail)*delt;
if (ifail>0) goto eohloop;
```

Now we calculate the position of the maximum of the cross-correlation func-

tions. `delay` fits a polynomial to the cross-correlation, calculates its first derivative and looks for the root of it.

```
tm[1]=delay(xlag,rho12,4,2*maxlag-2,imax,polycofs,morder,maxlag,ttol,ifail);
rm[1]=yfit(tm[1],polycofs,morder);
tm[1]=tm[1]*delt;

... (same for rho23 and rho31)
```

Find autocorrelation for value of maximum cross-correlation:

```
for (k=1; k<=3; k++)
{
    for (i=1; i<maxlag-3; i++)
    {
        lx=i-1;
        if (autoc[maxlag+i-1]<rm[k]) break; // we start at the zero lag
    }

    it1=maxlag + 2;
    it2=maxlag + 2 + lx;
    te[k]=xfory(xlag,autoc,it1,it2,rm[k],cxx,morder,maxlag,ttol,ifail)*delt;
    if (ifail>0) goto eohloop;

    if (fabs(tm[k])<ttol)
        tm[k]=ttol;
    if (fabs(te[k])<ttol)
        te[k]=ttol;
    tk[k]=sqrt(pow(tm[k],2)+pow(te[k],2));
}
```

Calculate apparent velocities:

```
terr=tm[1] + tm[2] + tm[3];
ntd=100.0 * fabs(terr) / (fabs(tm[1])+fabs(tm[2])+fabs(tm[3]));

for (i=1; i<=3;i++)
    vdash[i]=side[i]/tm[i];

temp2=vdash[1];
temp1=vdash[3];
ava=0.5*temp2*temp1*sin(theta[1]) / sqrt(temp2*temp2+temp1*temp1+2.0*temp2*temp1*cos(theta[1]));
ava=fabs(ava);
temp2=vdash[1] + vdash[3] * (cos(theta[1]));
temp1=vdash[3] * sin(theta[1]);
phia=atan(-temp2/temp1);
if (vdash[1]<0) phia=phia + pi;
ava=2.0 * ava;

// because we want ground values for the ellipse
vpc1=side[1] / tk[1];
vpc2=side[2] / tk[2];
vpc3=side[3] / tk[3];
ael=1.0 / (vpc1*vpc1);
denom=vpc1 * vpc2  * vpc3;
denom=denom * denom;
denom=denom * sin(theta[1])  * sin(theta[2])  * sin(theta[3]);
b1=vpc1 * vpc2  * sin(theta[2]);
b2=vpc1 * vpc3  * sin(theta[1]);
b3=vpc3 * vpc2  * cos(theta[2])  * sin(theta[1]);
b4=vpc3 * vpc2  * cos(theta[1])  * sin(theta[2]);
```

```
hel=(pow(b1,2)-pow(b2,2)+pow(b3,2)-pow(b4,2)) / (2.0*denom);
b1=vpc1 * vpc2;
b2=vpc1 * vpc3;
b3=vpc3 * vpc2;
b1=b1 * 2  * sin(theta[2])  * cos(theta[2]);
b2=b2 * 2  * sin(theta[1])  * cos(theta[1]);
b3=b3 * 2  * sin(theta[3])  * cos(theta[2])  * cos(theta[1]);
bel=(b1+b2-b3) / denom;
abh2=ael * bel - pow(hel,2);
if (abh2<0) goto label3360;
sqmaj=(ael+bel+sqrt(pow((ael+bel),2)-4.0*abh2)) / (2.0*abh2);
sqmin=(ael+bel-sqrt(pow((ael+bel),2)-4.0*abh2)) / (2.0*abh2);
ptn=-hel * sqmin;
qtn=bel * sqmin - 1.0;

psi=atan2(ptn,qtn); // atan2(y,x) principal value of complex number of (x,y)
if ((phia-psi)>(0.5*pi)) psi=psi + pi;
if ((psi-phia)>(0.5*pi)) psi=psi - pi;

// to get minor axis in same direction as the velocity
axrat=sqmaj / sqmin;
pmp=phia - psi;
if (fabs(0.5*pi-fabs(pmp))<0.001)
pmp=1.57f;
if (fabs(1.5*pi-fabs(pmp))<0.001)
    pmp=1.57f;
pmp=sin(pmp) / cos(pmp);
diff=atan(((axrat-1.0)*pmp)/(1.0+axrat*pow(pmp,2)));
phi=phia + diff;
vpcv=pow(vpc1,2) * (1.0+(axrat-1.0)*pow(cos(psi),2)) / (1.0+(axrat-1.0)*pow(cos(phi-psi),2));

label3350:
v=vpcv * cos(diff) / ava;
vcv=vpcv - pow(v,2);
if (vcv>=0)
    vcv=sqrt(vcv);
else
    vcv=-sqrt(-vcv);

vpcv=sqrt(vpcv);
axrat=sqrt(axrat);

// rotate to eastward reference direction
phi=phi - thont;
psi=psi - thont;
goto label3370;

label3360:
vpcv=pow(((vpc1+vpc2+vpc3)/3.0),2);
axrat=1.0;
diff=0;
psi=0;
phi=phia;
sqmin=0;
sqmaj=0;
goto label3350;

label3370:

// rotate phia to correct for triangle orientation
phia=phia - thont;
if (phia<0)
    phia=phia + 2.0*pi;
ua=0.5*ava*cos(phia);
va=0.5*ava*sin(phia);

if (vcv<0)
```

```
{
    v=0.5*ava;
    phi=phia;
}
else
    v=0.5*v;

ut=v*cos(phi);
vt=v*sin(phi);
dangle=(0.5*pi-phi)*deg;
if (dangle<0) dangle=dangle + 360.0;
minax=sqrt(sqmin)*tfad;
t05=tfad*sqrt(1.0+(pow(ut,2)+pow(vt,2))/pow(vcv,2));
d05=minax*sqrt(axrat);

psi=psi*deg;
if (psi<0.0) psi=psi + 360.0;
}
```

A.8.6 Final steps

- Put data into display structure `FCAdisplaydata` and send message to display it.
- Test data with acceptance criteria. If one of the fails, jump to `eohloop`.
- Write calculated data to the harddrive

A.9 Radar data acquisition installer

The code below is a Inno Setup Compiler script with the filename "MFInstallerV2.0.iss". It takes care of the installation of the data acquisition software.

```
[Setup]
AppName=MF Radar Reanalysis Software
AppVerName=MF Radar Reanalysis  Software 2.0 (Rev 28)
AppPublisher=Dept of Physics and Astronomy, UC, A. Baumgaertner
DefaultDirName=C:\MFRadarReanalysis28
DefaultGroupName=MF Radar Reanalysis Software
OutputBaseFilename=setup
Compression=lzma
SolidCompression=yes

[Languages]
Name: "eng"; MessagesFile: "compiler:Default.isl"


[Files]
Source: "C:\DAS\MF\radarREAD28\Release\radar.exe"; DestDir: "{app}"; Flags: ignoreversion
Source: "C:\DAS\General\netCDF\netcdf.dll"; DestDir: "{sys}";
Source: "C:\DAS\MF\radarREAD28\RadarReanalysisSettings.txt"; DestDir: "{app}";
   Flags: ignoreversion

; NOTE: Don't use "Flags: ignoreversion" on any shared system files

[Icons]
Name: "{group}\MF Radar Reanalysis Software V2.0 Rev28"; Filename: "{app}\radar.exe"
```

```
Name: "{group}\Uninstall Radar Reanalysis Software"; Filename: "{uninstallexe}"

[Run]
Filename: "{app}\radar.exe"; Description: "{cm:LaunchProgram,MF Radar Reanlysis Software}";
   Flags: nowait postinstall skipifsilent
```

A.10 Automated data transfer from Arrival Heights to a UC server

The hourly wind velocity data files generated by the MFSA radar data acquisition software described above can be accessed using an FTP connection to the computer at Arrival Heights. An automated hourly download of these data files to a server at the University of Canterbury has been set up. In addition, the data is automatically converted to matlab files and displayed on a university website.

In the following, this system is described in some detail to facilitate changes. A crontab is running on the computer with the address cluster02.phys.canterbury.ac.nz:

```
SHELL=/bin/bash
PATH=/sbin:/bin:/usr/sbin:/usr/bin:/.amd_mounts/fermi/usr/local/phys/Linux/matlab_r14-3
10 * * * * /home/users/physatmo/processmf.sh
```

The crontab can be edited by choosing a suitable editor environment variable (`setenv EDITOR vi`) and then calling `crontab -e`. Every hour this calls the shell script processmf.sh:

```
#!/bin/sh
cd /home/users/physatmo/MFradarScottBaseAutoFTPtransfer/
/usr/local/phys/Linux/matlab_r14-3/bin/matlab -nodisplay -r FTPcluster02
smbmount //physdesk147/Papers ~/Physdesk147 -o username=Papers,password=physatmo
cp ~/html/scatteru.jpg ~/Physdesk147/MFScottBase
cp ~/html/scatterv.jpg ~/Physdesk147/MFScottBase
chmod 755 -R ~/data_store/MF/AH/Matlab
chmod 755 -R ~/data_store/MF/AH/FCA/2006
```

As evident from the listing, the script starts matlab and runs the matlab script FTPcluster02.m. This matlab program consists of three main functions:

```
function todo=determinetodo
function download(todo)
function process(todo)
```

where "todo" is an array of date vectors. "determinetodo" checks which files have to be downloaded. Ideally this should only be the file of the last hour, but if connections or servers were down this often means that more than one file have to be downloaded. This function checks for missing files in the last 5 days. The

"download" function downloads the files requested by "determinetodo". "process" converts the ascii-text-files to matlab .mat files and saves them to the atmospheric group data storage space for general access. In addition, it creates a website that displays the obtained wind velocities as a function of time and altitude for the last week (http://www2.phys.canterbury.ac.nz/ physatmo/index.html).

A.11 Software update via FTP

The configuration of the radar data acquisition software and the program itself can be updated using an FTP connection. This is useful for remote updates from New Zealand but also from Scott Base. The process for changing the configuration in the file "RadarSettings30.txt" consists of the following steps:

1. Download current configuration file c:\logs\RadarSettings30.txt and c:\logs\RadarRestarter.txt from radar.scott.aq
2. Rename the current configuration file on radar.scott.aq to RadarSettings30_backup<date>.txt
3. Make necessary changes to the configuration file. Table A.1 explains the contents of the configuration file.
4. Create file Restartrequest.txt with value '2' in it, this will close the data acquisition software
5. Upload the configuration file and the Restartrequest.txt file to c:\logs\
6. Wait for approximately two minutes (Restartrequest.txt is read after every block of data for the winds analysis)
7. In RadarRestarter.txt, change line 2 from '0' to '1' (Application restart)
8. Upload RadarRestarter.txt to c:\logs\
9. The data acquisition software will restart within three minutes

Installing a new Software version remotely involves similar steps which are detailed below.

1. Stop the currently running software:
   - Create file Restartrequest.txt with value '2' in it
   - Upload Restartrequest.txt to c:\logs\ directory

   - Wait for approximately two minutes (Restartrequest.txt is read after every block of data for the winds analysis)

2. Rename the running software radar.exe to radar_backup<date>.exe in case you have to go back to the this version

3. Upload your new version

4. Upload new settings file. If you have changed the software revision number, you HAVE TO upload a settings file with the correct revision number, e.g. "RadarSettings30.txt" where 30 is the revision number

5. Initiate software start:

   - Download file c:\logs\RadarRestarter.txt
   - Change line 2 from '0' to '1' (Application restart)
   - Upload RadarRestarter.txt to c:\logs\
   - The data acquisition software will restart within three minutes

Note that if a computer restart is required, in RadarRestarter.txt line 3 has to be changed from '0' to '1'.

A.12 Re-Analysis of raw I and Q data

The raw I and Q data saved by the data acquisition software in form of NetCDF files can be used to calculate wind velocities using FCA. A tool written for this purpose allows adjustment of some parameters, but it can also be used as a template for changing more fundamental aspects of the FCA analysis, or even usage of a different algorithm, for example UCAR-STARS. The software tool has the name "MF Radar Reanalysis Software" with the current revision number 28. The input files have to be zipped NetCDF files, the directory structure and NetCDF file structure have to be identical to the files produced by the data acquisition software. The format of the output files is identical to the wind velocity data files of the data acquisition software.

Line Nr	Description	Factory Setting
1:	DAQ number of channels	8
2:	Sampling Frequency	150000
3:	Pulse Repetition Frequency	20
4:	Samples per trigger per channel (number of height bins)	160
5:	save raw data on(1)/off(0)	1
6:	no longer used	0
7:	number of antennas used for WINDS experiment	3
8:	Height bin for raw data saving: WIND start bin (does not equal altitude in km because of groundpulse)	75
9:	Height bin for raw data saving: WIND last bin	134
10:	Height bin for raw data saving: Polarimeter start bin	75
11:	Height bin for raw data saving: Polarimeter last bin	134
12:	Height bin for raw data saving: Groundpulse start bin	10
13:	Height bin for raw data saving: Groundpulse last bin	39
14:	Length of FCA run in seconds	120
15:	Phase information channel number for Polarimeter	6
16:	Polarimeter data channel	7
17:	extended logging on(1)/off(0)	0
18:	datadrive	q:
19:	Antenna used for ground pulse saving	1
20:	internal triggering (1) / external triggering (0)	1
21:	use FCA rejection criteria on(1)/off(0)	0
22:	use GPS for system clock updates on(1)/off(0)	0
23:	run online FCA on(1)/off(0)	1

Table A.1: Documentation of the MFSA radar configuration file "RadarSettings30.txt".

Appendix B

Separation of Waves with Different Wavenumbers and Equal Frequencies

Chapter 5 in this thesis discussed the separation of two zonal wavenumber components of sinusoidal oscillations with periods of 12 hours from time series at two sites. The chosen approach was relatively specific to the problem and here a more general approach is briefly presented. It can be employed for any periods and any longitudinal separation of the measurements. In addition, it can easily be extended for the case of more than two measurement sites and thus additional zonal wavenumbers. An oscillation at two sites A and B is written in polar coordinates as

$$\overrightarrow{A} = r_A \begin{pmatrix} \cos\theta_A \\ \sin\theta_A \end{pmatrix} \tag{B.1}$$

$$\overrightarrow{B} = r_B \begin{pmatrix} \cos\theta_B \\ \sin\theta_B \end{pmatrix} \tag{B.2}$$

where r_A, r_B, θ_A, and θ_B are the respective amplitudes and times of maximum of the oscillation calculated from Fourier or equivalent analysis. If we can assume that the oscillations at both sites are the result of two waves with zonal wavenumber 1 and 2, we can write A and B as

$$\overrightarrow{A} = r_1 \begin{pmatrix} \cos\theta_1 \\ \sin\theta_1 \end{pmatrix} + r_2 \begin{pmatrix} \cos\theta_2 \\ \sin\theta_2 \end{pmatrix} \tag{B.3}$$

$$\overrightarrow{B} = r_1 \begin{pmatrix} \cos(\theta_1 + \Delta\lambda) \\ \sin(\theta_1 + \Delta\lambda) \end{pmatrix} + r_2 \begin{pmatrix} \cos(\theta_2 + 2\Delta\lambda) \\ \sin(\theta_2 + 2\Delta\lambda) \end{pmatrix} \tag{B.4}$$

where r_1, r_2, θ_1, and θ_2 are the amplitudes and times of maximum of the wavenumber 1 and wavenumber 2 wave, respectively. The times of maximum are with respect to A. $\Delta\lambda$ is the longitudinal difference between two sites, which leads to a phase difference of $\Delta\lambda$ between A and B for any wave with zonal wavenumber 1, and a phase difference of $2\Delta\lambda$ for zonal wavenumber 2 waves. Combining equations B.2–B.4 yields a system of four equations with four unknowns. The

solution for $\Delta\lambda \neq \pi$ is:

$$r_1 = \frac{Z_1}{e} \tag{B.5}$$
$$r_2 = \frac{Z_2}{e} \tag{B.6}$$

where

$$\begin{aligned} Z_1 = & \Big[((1+f)(a_1+b_1)^2 + (1+f)(a_2+b_2)^2 \\ & -2(2f^2a_2b_2 + 2f^2a_1b_1 - 2fea_2b_1 - 2ea_2b_1 + 2fea_1b_2 + 2ea_1b_2) \\ & -4f^3a_2b_2 - 4f^3a_1b_1 + 4e^3a_1b_2 - 4e^3a_2b_1)/2\Big]^{\frac{1}{2}} \end{aligned} \tag{B.7}$$

$$\begin{aligned} Z_2 = & \Big[(a_1^2 + b_1^2 + b_2^2 + a_2^2 + a_1^2f + b_2^2f + b_1^2f \\ & +a_2^2f - 2f^2a_2b_2 - 2f^2a_1b_1 + 2fea_2b_1 + 2ea_2b_1 \\ & -2fea_1b_2 - 2ea_1b_2 - 2a_1b_1f - 2a_2b_2f)/2\Big]^{\frac{1}{2}} \end{aligned} \tag{B.8}$$

$$\begin{aligned} \theta_1 = & \arctan\Big[\frac{ea_2 - fa_1 + fb_1 + 2feb_2 + eb_2 - b_1 + 2b_1f^2 - a_1}{Z_1} \cdot \\ & \frac{Z_1}{ea_1 - fb_2 + fa_2 + 2feb_1 + b_1e + b_2 - 2b_2f^2 + a_2}\Big] \end{aligned} \tag{B.9}$$

$$\begin{aligned} \theta_2 = & \arctan\Big[\frac{a_1 - b_1 - eb_2 - ea_2 + fa_1 - fb_1}{Z_2} \cdot \\ & \frac{Z_2}{-ea_1 + b_2 - a_2 - b_1e - fa_2 + fb_2} - \Delta\lambda\Big] \end{aligned} \tag{B.10}$$

$$e = \sin(\Delta\lambda) \tag{B.11}$$
$$f = \cos(\Delta\lambda) \tag{B.12}$$
$$a_1 = r_A \cos\theta_A \tag{B.13}$$
$$a_2 = r_A \sin\theta_A \tag{B.14}$$
$$b_1 = r_B \cos\theta_B \tag{B.15}$$
$$b_2 = r_B \sin\theta_B \tag{B.16}$$

This solution was obtained by using the mathematical tool Maple. It is clear how the analysis could be extended for additional sites and zonal wavenumbers, but due to the increasing complexity of the solutions, computer software such as Maple is likely to be necessary.

Bibliography

Adams, G. W., Edwards, D. P., Brosnahan, J. W., 1985. The Imaging Doppler Interferometer: Data Analysis. Radio Science 20 (6), 1481–1492.

Akmaev, R. A., 2002. Modeling the cooling due to CO2 increases in the mesosphere and lower thermosphere. Physics and Chemistry of the Earth 27 (6-8), 521–528.

Alexander, M. J., 1998. Interpretations of observed climatological patterns in stratospheric gravity wave variance. Journal of Geophysical Research 103 (D8), 8627–8640.

Allen, S. J., Vincent, R. A., 1995. Gravity-Wave Activity in the Lower Atmosphere - Seasonal and Latitudinal Variations. Journal of Geophysical Research 100 (D1), 1327–1350.

Andrews, D. G., 2000. An Introduction to Atmospheric Physics. Cambridge University Press, Cambridge.

Andrews, D. G., Holton, J. R., Leovy, C. B., 1987. Middle atmosphere dynamics. International geophysics series ; v. 40. Academic Press, Orlando.

Angelats i Coll, M., Forbes, J. M., 2002. Nonlinear interactions in the upper atmosphere: The s=1 and s=3 nonmigrating semidiurnal tides. Journal of Geophysical Research 107 (A8), doi:10.1029/2001JA900179.

Bacmeister, J. T., Schoeberl, M. R., Lait, L. R., Newman, P. A., Gary, B., 1990. ER-2 Mountain Wave Encounter over Antarctica - Evidence for Blocking. Geophysical Research Letters 17 (1), 81–84.

Baldwin, M. P., Dunkerton, T. J., 1998. Quasi-biennial modulation of the southern hemisphere stratospheric polar vortex. Geophysical Research Letters 25 (17), 3343–3346.

Baumgaertner, A. J. G., Brühl, C., Jöckel, P., 2007. Responses of Middle Atmosphere Chemistry and Dynamics to Particle Precipitation simulated with ECHAM5/MESSy. Poster at EGU, Vienna 2007: EGU2007-A-09252; AS1.12/ST15-1TH4P-0068.

Baumgaertner, A. J. G., Jarvis, M. J., McDonald, A. J., Fraser, G. J., 2006. Observations of the wavenumber 1 and 2 components of the semi-diurnal tide over Antarctica. Journal of Atmospheric and Solar-Terrestrial Physics 68 (11), 1195–1214.

Baumgaertner, A. J. G., McDonald, A. J., 2007. A gravity wave climatology for Antarctica compiled from CHAMP/GPS radio occultations. Journal of Geophysical Research 112 (D05103), doi:10.1029/2006JD007504.

Baumgaertner, A. J. G., McDonald, A. J., Fraser, G. J., Plank, G. E., 2005. Long-term observations of mean winds and tides in the upper mesosphere and lower thermosphere above Scott Base, Antarctica. Journal of Atmospheric and Solar-Terrestrial Physics 67 (16), 1480–1496.

Beig, G., Keckhut, P., Lowe, R. P., Roble, R. G., Mlynczak, M. G., Scheer, J., Fomichev, V. I., Offermann, D., French, W. J. R., Shepherd, M. G., Semenov, A. I., Remsberg, E. E., She, C. Y., Lubken, F. J., Bremer, J., Clemesha, B. R., Stegman, J., Sigernes, F., Fadnavis, S., 2003. Review of mesospheric temperature trends. Reviews of Geophysics 41 (4), –.

Born, M., Wolf, E., 1980. Principles of Optics, 6th Edition. Pergamon Press.

Bremer, J., Schminder, R., Greisiger, K. M., Hoffmann, P., Kurschner, D., Singer, W., 1997. Solar cycle dependence and long-term trends in the wind field of the mesosphere lower thermosphere. Journal of Atmospheric and Solar-Terrestrial Physics 59 (5), 497–509.

Briggs, B. H., 1984. The analysis of spaced sensor records by correlation techniques. In: Vincent, R. A. (Ed.), Middle Atmosphere Program, Handbook for MAP. Vol. 13. pp. 166–186.

Briggs, B. H., 1993. Observations of Atmospheric Dynamics Using Radar Techniques. Australian Journal of Physics 46 (1), 127–147.

Briggs, B. H., Phillips, G. J., Shinn, D. H., 1950. The Analysis of Observations on Spaced Receivers of the Fading of Radio Signals. Proceedings of the Physical Society of London Section B 63 (362), 106–121.

Briggs, B. H., Vincent, R. A., 1992. Spaced-Antenna Analysis in the Frequency-Domain. Radio Science 27 (2), 117–129.

Brosnahan, J. W., Adams, G. W., 1993. The Mapstar imaging Doppler interferometer (IDI) radar - description and first results. Journal of Atmospheric and Terrestrial Physics 55 (3), 203–228.

Budden, K. G., 1961. Radio waves in the ionosphere. University Press, Cambridge [Eng.].

Burrage, M. D., Skinner, W. R., Gell, D. A., Hays, P. B., Marshall, A. R., Ortland, D. A., Manson, A. H., Franke, S. J., Fritts, D. C., Hoffman, P., McLandress, C., Niciejewski, R., Schmidlin, F. J., Shepherd, G. G., Singer, W., Tsuda, T., Vincent, R. A., 1996. Validation of mesosphere and lower thermosphere winds from the High Resolution Doppler Imager on UARS. Journal of Geophysical Research 101 (D6), 10365–10392.

Burrage, M. D., Wu, D. L., Skinner, W. R., Ortland, D. A., Hays, P. B., 1995. Latitude and seasonal dependence of the semidiurnal tides observed by the high-resolution Doppler imager. Journal of Geophysical Research 100, 11313–11321.

Cariolle, D., Muller, S., Cayla, F., Mccormick, M. P., 1989. Mountain Waves, Polar Stratospheric Clouds, and the Ozone Depletion over Antarctica. Journal of Geophysical Research 94 (D9), 11233–11240.

Carslaw, K. S., Wirth, M., Tsias, A., Luo, B. P., Dörnbrack, A., Leutbecher, M., Volkert, H., Renger, W., Bacmeister, J. T., Reimer, E., Peter, T., 1998. Increased stratospheric ozone depletion due to mountain-induced atmospheric waves. Nature 391 (6668), 675–678.

Chapman, S., Lindzen, R. S., 1970. Atmospheric tides: Thermal and gravitational. Reidel, Dordrecht.

Charney, J. G., Drazin, P. G., 1961. Propagation of Planetary-Scale Disturbances from the Lower into the Upper Atmosphere. Journal of Geophysical Research 66 (1), 83–109.

Charney, J. G., Stern, M. E., 1962. On the Stability of Internal Baroclinic Jets in a Rotating Atmosphere. Journal of the Atmospheric Sciences 19 (2), 159–172.

Chshyolkova, T., Manson, A. H., Meek, C. E., 2005. Climatology of the quasi two-day wave over Saskatoon (52 degrees N, 107 degrees W): 14 Years of MF radar observations. Advances in Space Research 35 (11), 2011–2016.

Cierpik, K. M., Forbes, J. M., Miyahara, S., Miyoshi, Y., Fahrutdinova, A., Jacobi, C., Manson, A., Meek, C., Mitchell, N. J., Portnyagin, Y., 2003. Longitude variability of the solar semidiurnal tide in the lower thermosphere through assimilation of ground- and space-based wind measurements. Journal of Geophysical Research 108 (A5), doi:10.1029/2002JA009349.

Clark, R. R., 1989. The Quasi 2-Day Wave at Durham (43°N) - Solar and Magnetic Effects. Journal of Atmospheric and Terrestrial Physics 51 (7-8), 617–622.

Craig, R. L., Elford, W. G., 1981. Observations of the Quasi 2-Day Wave near 90 Km Altitude at Adelaide (35°S). Journal of Atmospheric and Terrestrial Physics 43 (10), 1051–1056.

Damiani, A., 2006. Southern ozone variations induced by solar particle events during 15 January-5 February 2005. Journal of Atmospheric and Solar-Terrestrial Physics.

Dartt, D., Nastrom, G., Belmont, A., 1983. Seasonal and Solar-Cycle Wind Variations, 80-100 Km. Journal of Atmospheric and Terrestrial Physics 45 (10), 707–718.

de la Torre, A., Alexander, P., 2005. Gravity waves above Andes detected from GPS radio occultation temperature profiles: Mountain forcing? Geophysical Research Letters 32, L17815, doi:10.1029/2005GL022959.

de la Torre, A., Tsuda, T., Hajj, G. A., Wickert, J., 2004. A global distribution of the stratospheric gravity wave activity from GPS occultation profiles with SAC-C and CHAMP. Journal of the Meteorological Society of Japan 82 (1B), 407–417.

DeLand, M. T., Shettle, E. P., Thomas, G. E., Olivero, J. J., 2006. A quarter-century of satellite polar mesospheric cloud observations. Journal of Atmospheric and Solar-Terrestrial Physics 68 (1), 9–29.

Dickinson, R. E., 1968. Planetary Rossby Waves Propagating Vertically through Weak Westerly Wind Wave Guides. Journal of the Atmospheric Sciences 25 (6), 984–1002.

Dracz, T., 2005. The ZipArchive library , http://www.artpol-software.com/zipdoc/.

Duck, T. J., Whiteway, J. A., 2000. Seasonal transition in gravity wave activity during the springtime stratospheric vortex breakdown. Geophysical Research Letters 27 (21), 3477–3480.

D'Yachenko, V. A., Lysenko, I. A., Portnyagin, Y. I., 1986. Long-Term Periodicities in Lower Thermospheric Wind Variations. Journal of Atmospheric and Terrestrial Physics 48 (11-12), 1117–1119.

Emmert, J. T., Picone, J. M., Lean, J. L., Knowles, S. H., 2004. Global change in the thermosphere: Compelling evidence of a secular decrease in density. Journal of Geophysical Research 109, A02301, doi:10.1029/2003JA010176.

Fahrutdinova, A. N., Ganin, V. A., Berdunov, N. V., Ishmuratov, R. A., Hutorova, O. G., 1997. Long-term variations of circulation in the mid-latitude upper Mesosphere lower Thermosphere. Advances in Space Research 20 (6), 1161–1164.

Farley, D. T., Ierkic, H. M., Fejer, B. G., 1981. Radar Interferometry: a New Technique for Studying Plasma Turbulence in the Ionosphere. Journal of Geophysical Research 86, 1467–1472.

Fishbach, F. F., 1965. A satellite method for temperature and pressure below 24 km. Bulletin of the American Meteorological Society 9, 528–532.

Forbes, J. M., 1982a. Atmospheric Tides, I, Model Description and Results for the Solar Diurnal Component. Journal of Geophysical Research 87, 5222–5240.

Forbes, J. M., 1982b. Atmospheric Tides, II, The Solar and Lunar Semi-Diurnal Components. Journal of Geophysical Research 87, 5241–5252.

Forbes, J. M., 1984. Middle Atmosphere Tides. Journal of Atmospheric and Terrestrial Physics 46 (11), 1049–1067.

Forbes, J. M., 1991. Middle Atmosphere Tides and Coupling between Atmospheric Regions. Journal of Geomagnetism and Geoelectricity 43, 597–609.

Forbes, J. M., 1995. Tidal and Planetary Waves. In: Johnson, R. M., Killeen, T. L. (Eds.), The Upper Mesosphere and Lower Thermosphere: A Review of Experiment and Theory. Vol. 87 of Geophysical Monograph. AGU, pp. 67–87.

Forbes, J. M., Garrett, H. B., 1978. Thermal Excitation of Atmospheric Tides Due to Insolation Absorption by O_3 and H_2O. Geophysical Research Letters 5 (12), 1013–1016.

Forbes, J. M., Garrett, H. B., 1979. Theoretical Studies of Atmospheric Tides. Reviews of Geophysics 17 (8), 1951–1981.

Forbes, J. M., Makarov, N. A., Portnyagin, Y. I., 1995. First Results from the Meteor Radar at South-Pole - a Large 12-Hour Oscillation with Zonal Wave-Number One. Geophysical Research Letters 22 (23), 3247–3250.

Forbes, J. M., Palo, S. E., Zhang, X., Portnyagin, Y. I., Makarov, N. A., Merzlyakov, E. G., 1999. Lamb waves in the lower thermosphere: Observational evidence and global consequences. Journal of Geophysical Research 104 (A8), 17107–17115.

Fraser, G., 1994. Observations of the middle atmosphere by medium frequency radars. Tech. rep., University of Canterbury.

Fraser, G. J., 1965. Measurement of Atmospheric Winds at Altitudes of 64-120 km using Ground-Based Radio Equipment. Journal of the Atmospheric Sciences 22 (2), 217–218.

Fraser, G. J., 1984. Summer Circulation in the Antarctic Middle Atmosphere. Journal of Atmospheric and Terrestrial Physics 46 (2), 143–146.

Fraser, G. J., 1989. Monthly Mean Winds in the Mesosphere at 44S and 78S. Pure and Applied Geophysics 130 (2-3), 291–301.

Fraser, G. J., 1990. Long-term variations in mid-latitude Southern Hemisphere mesospheric winds. Advances in Space Research 10 (10), 247–250.

Fraser, G. J., Hernandez, G., Smith, R. W., 1993. Eastward-Moving 2-4 Day Waves in the Winter Antarctic Mesosphere. Geophysical Research Letters 20 (15), 1547–1550.

Fraser, G. J., Vincent, R. A., Manson, A. H., Meek, C. E., Clark, R. R., 1989. Inter-Annual Variability of Tides in the Mesosphere and Lower Thermosphere. Journal of Atmospheric and Terrestrial Physics 51 (7-8), 555–567.

Fritts, D. C., 1984. Gravity-Wave Saturation in the Middle Atmosphere: A Review of Theory and Observations. Reviews of Geophysics 22 (3), 275–308.

Fritts, D. C., 1995a. Gravity Wave Forcing and Effects in the Mesosphere and Lower Thermosphere. In: Johnson, R. M., Killeen, T. L. (Eds.), The Upper Mesosphere and Lower Thermosphere: A Review of Experiment and Theory. Vol. 87 of Geophysical Monograph. AGU, pp. 89–100.

Fritts, D. C., 1995b. Gravity Wave-Tidal Interactions in the Middle Atmoshpere: Observations and Theory. In: Johnson, R. M., Killeen, T. L. (Eds.), The Upper Mesosphere and Lower Thermosphere: A Review of Experiment and Theory. Vol. 87 of Geophysical Monograph. AGU, pp. 121–131.

Fritts, D. C., Alexander, M. J., 2003. Gravity wave dynamics and effects in the middle atmosphere. Reviews of Geophysics 41 (1), 1003, doi:10.1029/2001RG000106.

Fritts, D. C., Isler, J. R., Lieberman, R. S., Burrage, M. D., Marsh, D. R., Nakamura, T. K., Tsuda, T., Vincent, R. A., 1999. Two-day wave structure and mean flow interactions observed by radar and High Resolution Doppler Imager. Journal of Geophysical Research 104 (D4), 3953–3969.

Fritts, D. C., Vincent, R. A., 1987. Mesospheric Momentum Flux Studies at Adelaide, Australia - Observations and a Gravity Wave-Tidal Interaction-Model. Journal of the Atmospheric Sciences 44 (3), 605–619.

Froidevaux, L., Livesey, N. J., Read, W. G., Jiang, Y. B. B., Jimenez, C., Filipiak, M. J., Schwartz, M. J., Santee, M. L., Pumphrey, H. C., Jiang, J. H., Wu, D. L., Manney, G. L., Drouin, B. J., Waters, J. W., Fetzer, E. J., Bernath, P. F., Boone, C. D., Walker, K. A., Jucks, K. W., Toon, G. C., Margitan, J. J., Sen, B., Webster, C. R., Christensen, L. E., Elkins, J. W., Atlas, E., Lueb, R. A., Hendershot, R., 2006. Early validation analyses of atmospheric profiles from EOS MLS on the Aura satellite. Ieee Transactions on Geoscience and Remote Sensing 44 (5), 1106–1121.

Garcia, R. R., Boville, B. A., 1994. Downward Control of the Mean Meridional Circulation and Temperature Distribution of the Polar Winter Stratosphere. Journal of the Atmospheric Sciences 51 (15), 2238–2245.

Garcia, R. R., Lieberman, R., Russell, J. M., Mlynczak, M. G., 2005. Large-scale waves in the mesosphere and lower thermosphere observed by SABER. Journal of the Atmospheric Sciences 62 (12), 4384–4399.

Gavrilov, N. M., Fukao, S., Nakamura, T., Jacobi, C., Kurschner, D., Manson, A. H., Meek, C. E., 2002. Comparative study of interannual changes of the mean winds and gravity wave activity in the middle atmosphere over Japan, Central Europe and Canada. Journal of Atmospheric and Solar-Terrestrial Physics 64 (8-11), 1003–1010.

Glass, M., Fellous, J. L., Massebeuf, M., Spizzichino, A., Lysenko, I. A., Portniaghin, Y. I., 1975. Comparison and Interpretation of Results of Simultaneous Wind Measurements in Lower Thermosphere at Garchy (France) and Obninsk (USSR) by Meteor Radar Technique. Journal of Atmospheric and Terrestrial Physics 37 (8), 1077–1087.

Greet, P. A., Murphy, D. J., Vincent, R., Dyson, P. L., 2000. A comparison of optical and radar measurements of mesospheric winds and tides. Geophysical Research Letters 27 (16), 2477–2480.

Greisiger, K. M., Schminder, R., Kurschner, D., 1987. Long-period variations of wind parameters in the mesopause region and the solar cycle dependence. Journal of Atmospheric and Terrestrial Physics 49 (3), 281–285.

Gruzdev, A. N., Brasseur, G. P., 2005. Long-term changes in the mesosphere calculated by a two-dimensional model. Journal of Geophysical Research 110, D03304, doi:10.1029/2003JD004410.

Gurubaran, S., Rajaram, R., 1999. Long-term variability in the mesospheric tidal winds observed by MF radar over Tirunelveli (8.7°N, 77.8°E). Geophysical Research Letters 26 (8), 1113–1116.

Gurubaran, S., Sridharan, S., Ramkumar, T. K., Rajaram, R., 2001. The mesospheric quasi-2-day wave over Tirunelveli (8.7°N). Journal of Atmospheric and Solar-Terrestrial Physics 63 (10), 975–985.

Hagan, M. E., Burrage, M. D., Forbes, J. M., Hackney, J., Randel, W. J., Zhang, X., 1999. QBO effects on the diurnal tide in the upper atmosphere. Earth Planets and Space 51 (7-8), 571–578.

Hagan, M. E., Forbes, J. M., Vial, F., 1995. On Modeling Migrating Solar Tides. Geophysical Research Letters 22 (8), 893–896.

Hagan, M. E., Vial, F., Forbes, J. M., 1992. Variability in the Upward Propagating Semidiurnal Tide Due to Effects of QBO in the Lower Atmosphere. Journal of Atmospheric and Terrestrial Physics 54 (11-12), 1465–1474.

Hajj, G. A., Kursinski, E. R., Romans, L. J., Bertiger, W. I., Leroy, S. S., 2002. A technical description of atmospheric sounding by GPS occultation. Journal of Atmospheric and Solar-Terrestrial Physics 64 (4), 451–469.

Hartmann, D. L., 1983. Barotropic Instability of the Polar Night Jet-Stream. Journal of the Atmospheric Sciences 40 (4), 817–835.

Haurwitz, B., 1940. The motion of atmospheric disturbances on the spherical earth. Journal of Marine Research 3 (3), 254–267.

Haurwitz, B., Cowley, A. D., 1973. Diurnal and Semidiurnal Barometric Oscillations, Global Distribution and Annual Variation. Pure and Applied Geophysics 102 (1), 193–222.

Haynes, P. H., Marks, C. J., McIntyre, M. E., Shepherd, T. G., Shine, K. P., 1991. On the Downward Control of Extratropical Diabatic Circulations by Eddy-Induced Mean Zonal Forces. Journal of the Atmospheric Sciences 48 (4), 651–679.

Hernandez, G., Fraser, G. J., Smith, R. W., 1993. Mesospheric 12-Hour Oscillation near South-Pole, Antarctica. Geophysical Research Letters 20 (17), 1787–1790.

Hibbins, R. E., Shanklin, J. D., Espy, P. J., Jarvis, M. J., Riggin, D. M., Fritts, D. C., Lübken, F.-J., 2005. Seasonal variations in the horizontal wind structure from 0-100 km above Rothera station, Antarctica (67°S, 68°W). Atmospheric Chemistry and Physics 5, 2973–2980.

Hines, C. O., 1960. Internal Atmospheric Gravity-Waves at Ionospheric Heights. Canadian Journal of Physics 38, 1441–1481.

Hines, C. O., Adams, G. W., Brosnahan, J. W., Djuth, F. T., Sulzer, M. P., Tepley, C. A., Vanbaelen, J. S., 1993. Multi-Instrument Observations of Mesospheric Motions over Arecibo - Comparisons and Interpretations. Journal of Atmospheric and Terrestrial Physics 55 (3), 241–287.

Hines, C. O., Rao, R. R., 1968. Validity of 3-Station Methods of Determining Ionospheric Motions. Journal of Atmospheric and Terrestrial Physics 30 (5), 979–993.

Hocking, W. K., 1997. Recent advances in radar instrumentation and techniques for studies of the mesosphere, stratosphere, and troposphere. Radio Science 32 (6), 2241–2270.

Hocking, W. K., May, P., Rottger, J., 1989. Interpretation, Reliability and Accuracies of Parameters Deduced by the Spaced Antenna Method in Middle Atmosphere Applications. Pure and Applied Geophysics 130 (2-3), 571–604.

Hocking, W. K., Thayaparan, T., 1997. Simultaneous and colocated observation of winds and tides by MF and meteor radars over London, Canada (43 degrees N, 81 degrees W), during 1994-1996. Radio Science 32 (2), 833–865.

Holdsworth, D. A., 1999a. Influence of instrumental effects upon the full correlation analysis. Radio Science 34 (3), 643–655.

Holdsworth, D. A., 1999b. Spatial correlation analysis revisited: Theory, and application to "radar backscatter model" data. Radio Science 34 (3), 629–641.

Holloway, C. L., Doviak, R. J., Cohn, S. A., Lataitis, R. J., VanBaelen, J. S., 1997. Cross correlations and cross spectra for spaced antenna wind profilers, 2. Algorithms to estimate wind and turbulence. Radio Science 32 (3), 967–982.

Holton, J. R., 1975. The Dynamic Meteorology of the Stratosphere and Mesosphere. Vol. 15 of Meteorological Monographs. American Meteorological Socity.

Höpfner, M., Larsen, N., Spang, R., Luo, B. P., Ma, J., Svendsen, S. H., Eckermann, S. D., Knudsen, B., Massoli, P., Cairo, F., Stiller, G., Von Clarmann, T., Fischer, H., 2006. MIPAS detects Antarctic stratospheric belt of NAT PSCs caused by mountain waves. Atmospheric Chemistry and Physics 6, 1221–1230.

Hough, S. S., 1897. On the application of harmonic analysis to the dynamical theory of tides, Part I, On Laplace's 'Oscillations of the First Species,' and on the dynamics of ocean currents. Philosophical Transactions of the Royal Society of London A189, 201–257.

Hough, S. S., 1898. On the application of harmonic analysis to the dynamical theory of tides, Part II, On the general integration of Laplace's dynamical equations. Philosophical Transactions of the Royal Society of London A191, 139–185.

Jacobi, C., Kürschner, D., 2006. Long-term trends of MLT region winds over Central Europe. Physics and Chemistry of the Earth 31, 16–21.

Jacobi, C., Portnyagin, Y. I., Solovjova, T. V., Hoffmann, P., Singer, W., Fahrutdinova, A. N., Ishmuratov, R. A., Beard, A. G., Mitchell, N. J., Muller, H. G., Schminder, R., Kürschner, D., Manson, A. H., Meek, C. E., 1999. Climatology of the semidiurnal tide at 52-56° N from ground-based radar wind measurements 1985-1995. Journal of Atmospheric and Solar-Terrestrial Physics 61 (13), 975–991.

Jacobi, C., Schminder, R., Kürschner, D., 1997a. The quasi 2-day wave as seen from D1 LF wind measurements over Central Europe (52°N, 15°E) at Collm. Journal of Atmospheric and Solar-Terrestrial Physics 59 (11), 1277–1286.

Jacobi, C., Schminder, R., Kürschner, D., Bremer, J., Greisiger, K. M., Hoffmann, P., Singer, W., 1997b. Long-term trends in the mesopause wind field obtained from LF D1 wind measurements at Collm, Germany. Advances in Space Research 20 (11), 2085–2088.

Jarvis, M. J., 1996. Quasi-biennial oscillation effects in the semidiurnal tide of the Antarctic lower thermosphere. Geophysical Research Letters 23 (19), 2661–2664.

Johnston, R. J., 1978. Multivariate statistical analysis in geography: a primer on the general linear model. Longman, London; New York.

Jones, G. O. L., Berkey, F. T., Fish, C. S., Hocking, W. K., Taylor, M. J., 2003. Validation of imaging Doppler interferometer winds using meteor radar. Geophysical Research Letters 30 (14).

Jones, G. O. L., Charles, K., Jarvis, M. J., 1997. First mesospheric observations using an imaging Doppler interferometer adaptation of the Dynasonde at Halley, Antarctica. Radio Science 32 (6), 2109–2122.

Kalchenko, B. V., Bulgakov, S. V., 1973. Study of periodic components of wind velocity in the lower thermosphere above the equator. Geomagnetism and Aeronomy (Translation) 13 (955-956).

Kalnay, E., Kanamitsu, M., Kistler, R., Collins, W., Deaven, D., Gandin, L., Iredell, M., Saha, S., White, G., Woollen, J., Zhu, Y., Chelliah, M., Ebisuzaki, W., Higgins, W., Janowiak, J., Mo, K. C., Ropelewski, C., Wang, J., Leetmaa, A., Reynolds, R., Jenne, R., Joseph, D., 1996. The NCEP/NCAR 40-year reanalysis project. Bulletin of the American Meteorological Society 77 (3), 437–471.

Kato, S., Tsuda, T., Watanabe, F., 1982. Thermal Excitation of Non-Migrating Tides. Journal of Atmospheric and Terrestrial Physics 44 (2), 131–146.

Khosravi, R., Brasseur, G., Smith, A., Rusch, D., Walters, S., Chabrillat, S., Kockarts, G., 2002. Response of the mesosphere to human-induced perturbations and solar variability calculated by a 2-D model. Journal of Geophysical Research 107 (D18), 4358, doi:10.1029/2001JD001235.

Kingsley, S. P., Quegan, S., 1999. Understanding RADAR Systems. SciTech (1999), McGraw-Hill Book Company (1992), Mendham, NJ.

Kudeki, E., Rastogi, P. K., Surucu, F., 1993. Systematic-Errors in Radar Wind Estimation - Implications for Comparative Measurements. Radio Science 28 (2), 169–179.

Kursinski, E. R., Hajj, G. A., Schofield, J. T., Linfield, R. P., Hardy, K. R., 1997. Observing Earth's atmosphere with radio occultation measurements using the Global Positioning System. Journal of Geophysical Research 102 (D19), 23429–23465.

Labitzke, K., 2004. On the signal of the 11-year sunpot cycle in the stratosphere over the Antarctic and its modulation by the Quasi-Biennial Oscillation (QBO). Meteorologische Zeitschrift 13 (4), 263–270.

Labitzke, K., 2005. On the solar cycle-QBO relationship: a summary. Journal of Atmospheric and Solar-Terrestrial Physics 67 (1-2), 45–54.

Laplace, P. S., 1799. Mechanique Celeste. Vol. 2. Paris, France, pp. 294–298.

Laplace, P. S., 1825. Mechanique Celeste. Vol. 5. Paris, France, pp. 145–169.

Lastovicka, J., 2005. On the role of solar and geomagnetic activity in long-term trends in the atmosphere-ionosphere system. Journal of Atmospheric and Solar-Terrestrial Physics 67 (1-2), 83–92.

Lawrence, B. N., Fraser, G. J., Vincent, R. A., Phillips, A., 1995. The 4-Day Wave in the Antarctic Mesosphere. Journal of Geophysical Research 100 (D9), 18899–18908.

Lieberman, R. S., Robinson, W. A., Franke, S. J., Vincent, R. A., Isler, J. R., Fritts, D. C., Manson, A. H., Meek, C. E., Fraser, G. J., Fahrutdinova, A., Hocking, W., Thayaparan, T., MacDougall, J., Igarashi, K., Nakamura, T., Tsuda, T., 1998. HRDI observations of mean meridional winds at solstice. Journal of the Atmospheric Sciences 55 (10), 1887–1896.

Limpasuvan, V., Wu, D. L., 2003. Two-day wave observations of UARS Microwave Limb Sounder mesospheric water vapor and temperature. Journal of Geophysical Research 108 (D10), doi:10.1029/2002JD002903.

Limpasuvan, V., Wu, D. L., Schwartz, M. J., Waters, J. W., Wu, Q., Killeen, T. L., 2005. The two-day wave in EOS MLS temperature and wind measurements during 2004-2005 winter. Geophysical Research Letters 32 (17), doi:10.1029/2005GL023396.

Lindzen, R. S., 1979. Atmospheric Tides. Annual Review of Earth and Planetary Sciences 7, 199–225.

Liou, Y. A., Pavelyev, A. G., Wickert, J., 2005. Observation of the gravity waves from GPS/MET radio occultation data. Journal of Atmospheric and Solar-Terrestrial Physics 67 (3), 219–228.

Liou, Y. A., Pavelyev, A. G., Wickert, J., Liu, S. F., Pavelyev, A. A., Schmidt, T., Igarashi, K., 2006. Application of GPS radio occultation method for observation of the internal waves in the atmosphere. Journal of Geophysical Research 111, D06104, doi:10.1029/2005JD005823.

Livesey, N. J., Read, W. G., Filipiak, M. J., Froidevaux, L., Harwood, R. S., Jiang, J. H., Jimenez, C., Pickett, H. M., Pumphrey, H. C., Santee, M. L., Schwartz, M. J., Waters, J. W., Wu, D. L., 2005. Version 1.5 Level 2 data quality and description document. Tech. Rep. JPL D-32381, Jet Propulsion Laboratory.

Livesey, N. J., van Snyder, W., Read, W. G., Wagner, P. A., 2006. Retrieval algorithms for the EOS Microwave Limb Sounder (MLS). Ieee Transactions on Geoscience and Remote Sensing 44 (5), 1144–1155.

Longuet-Higgins, M. S., 1968. The eigenfunctions of Laplace's tidal equations over a sphere. Philosophical Transactions of the Royal Society of London, Series A 262, 511–607.

Lorenc, A. C., Ballard, S. P., Bell, R. S., Ingleby, N. B., Andrews, P. L. F., Barker, D. M., Bray, J. R., Clayton, A. M., Dalby, T., Li, D., Payne, T. J., Saunders, F. W., 2000. The Met. Office global three-dimensional variational data assimilation scheme. Quarterly Journal of the Royal Meteorological Society 126 (570), 2991–3012.

Lübken, F. J., 2000. Nearly zero temperature trend in the polar summer mesosphere. Geophysical Research Letters 27 (21), 3603–3606.

Madden, R. A., 1979. Observations of Large-Scale Traveling Rossby Waves. Reviews of Geophysics 17 (8), 1935–1949.

Mandelbrot, B. B., Vanness, J. W., 1968. Fractional Brownian Motions Fractional Noises and Applications. Siam Review 10 (4), 422–437.

Manney, G. L., 1991. The Stratospheric 4-Day Wave in NMC Data. Journal of the Atmospheric Sciences 48 (15), 1798–1811.

Manney, G. L., Nathan, T. R., Stanford, J. L., 1988. Barotropic Stability of Realistic Stratospheric Jets. Journal of the Atmospheric Sciences 45 (18), 2545–2555.

Manson, A., Meek, C., Hagan, M., Hall, C., Hocking, W., MacDougall, J., Franke, S., Riggin, D., Fritts, D., Vincent, R., Burrage, M., 1999. Seasonal variations of the semi-diurnal and diurnal tides in the MLT: multi-year MF radar observations from 2 to 70 degrees N, and the GSWM tidal model. Journal of Atmospheric and Solar-Terrestrial Physics 61 (11), 809–828.

Manson, A. H., Meek, C., Hagan, M., Koshyk, J., Franke, S., Fritts, D., Hall, C., Hocking, W., Igarashi, K., MacDougall, J., Riggin, D., Vincent, R., 2002. Seasonal variations of the semi-diurnal and diurnal tides in the MLT: multi-year MF radar observations from 2-70 degrees N, modelled tides (GSWM, CMAM). Annales Geophysicae 20 (5), 661–677.

Manson, A. H., Meek, C. E., Avery, S. K., Fraser, G. J., Vincent, R. A., Phillips, A., Clark, R. R., Schminder, R., Kurschner, D., Kazimirovsky, E. S., 1991. Tidal Winds from the Mesosphere, Lower Thermosphere Global Radar Network During the 2nd LTCS Campaign - December 1988. Journal of Geophysical Research-Space Physics 96 (A2), 1117–1127.

Manson, A. H., Meek, C. E., Schminder, R., Kurschner, D., Clark, R. R., Muller, H. G., Vincent, R. A., Phillips, A., Fraser, G. J., Singer, W., Kazimirovsky, E. S., 1990. Tidal Winds from the MLT Global Radar Network During the 1st LTCS Campaign - September 1987. Journal of Atmospheric and Terrestrial Physics 52 (3), 175–183.

Manson, A. H., Meek, C. E., Teitelbaum, H., Vial, F., Schminder, R., Kurschner, D., Smith, M. J., Fraser, G. J., Clark, R. R., 1989. Climatologies of Semi-Diurnal and Diurnal Tides in the Middle Atmosphere (70-110 Km) at Middle Latitudes (40-55-Degrees). Journal of Atmospheric and Terrestrial Physics 51 (7-8), 579–593.

May, P. T., 1988. Statistical Errors in the Determination of Wind Velocities by the Spaced Antenna Technique. Journal of Atmospheric and Terrestrial Physics 50 (1), 21–32.

Mayr, H. G., Mengel, J. G., Talaat, E. R., Porter, H. S., Chan, K. L., 2005a. Mesospheric non-migrating tides generated with planetary waves: I. Characteristics. Journal of Atmospheric and Solar-Terrestrial Physics 67 (11), 959–980.

Mayr, H. G., Mengel, J. G., Talaat, E. R., Porter, H. S., Chan, K. L., 2005b. Mesospheric non-migrating tides generated with planetary waves: II. Influence of gravity waves. Journal of Atmospheric and Solar-Terrestrial Physics 67 (11), 981–991.

McDonald, A. J., Baumgaertner, A. J. G., Fraser, G. J., George, S. E., Marsh, S., 2007. Empirical Mode Decomposition of the Atmospheric Wave Field. Annales Geophysicae 25 (2), 375–384.

McLandress, C., 1998. On the importance of gravity waves in the middle atmosphere and their parameterization in general circulation models. Journal of Atmospheric and Solar-Terrestrial Physics 60 (14), 1357–1383.

McLandress, C., 2002a. The seasonal variation of the propagating diurnal tide in the mesosphere and lower thermosphere. Part I: The role of gravity waves and planetary waves. Journal of the Atmospheric Sciences 59 (5), 893–906.

McLandress, C., 2002b. The seasonal variation of the propagating diurnal tide in the mesosphere and lower thermosphere. Part II: The role of tidal heating and zonal mean winds. Journal of the Atmospheric Sciences 59 (5), 907–922.

McLandress, C., Alexander, M. J., Wu, D. L., 2000. Microwave Limb Sounder observations of gravity waves in the stratosphere: A climatology and interpretation. Journal of Geophysical Research 105 (D9), 11947–11967.

Meek, C. E., Manson, A. H., Franke, S. J., Singer, W., Hoffmann, P., Clark, R. R., Tsuda, T., Nakamura, T., Tsutsumi, M., Hagan, M., Fritts, D. C., Isler, J., Portnyagin, Y. I., 1996. Global study of northern hemisphere quasi-2-day wave events in recent summers near 90 km altitude. Journal of Atmospheric and Terrestrial Physics 58 (13), 1401–1411.

Middleton, H. R., Mitchell, N. J., Muller, H. G., 2002. Mean winds of the mesosphere and lower thermosphere at 52 degrees N in the period 1988-2000. Annales Geophysicae 20 (1), 81–91.

Morel, B., Keckhut, P., Bencherif, H., Hauchecorne, A., Megie, G., Baldy, S., 2004. Investigation of the tidal variations in a 3-D dynamics-chemistry-transport model of the middle atmosphere. Journal of Atmospheric and Solar-Terrestrial Physics 66 (3-4), 251–265.

MPI-C, 2006. Current Projects, ProSECCO/CAWSES.

Muller, H. G., 1972. Long-Period Meteor Wind Oscillations. Philosophical Transactions of the Royal Society of London Series a-Mathematical and Physical Sciences 271 (1217), 585–599.

Murphy, D. J., 2002. Variations in the phase of the semidiurnal tide over Davis, Antarctica. Journal of Atmospheric and Solar-Terrestrial Physics 64 (8-11), 1069–1081.

Murphy, D. J., Tsutsumi, M., Riggin, D. M., Jones, G. O. L., Vincent, R. A., Hagan, M. E., Avery, S. K., 2003. Observations of a nonmigrating component of the semidiurnal tide over Antarctica. Journal of Geophysical Research 108 (D8), 4241, doi10.1029/2002JD003077.

Namboothiri, S. P., Manson, A. H., Meek, C. E., 1993. Variations of mean winds and tides in the upper middle atmosphere over a solar cycle, Saskatoon, Canada, 52 deg N, 107 deg W. Journal of Atmospheric and Terrestrial Physics 55 (10), 1325–1334.

Namboothiri, S. P., Meek, C. E., Manson, A. H., 1994. Variations of mean winds and solar tides in the mesosphere and lower thermosphere over time scales ranging from 6 months to 11 yr: Saskatoon, 52 deg N, 107 deg W. Journal of Atmospheric and Terrestrial Physics 56 (10), 1313–1325.

Nappo, C. J., 2002. An introduction to atmospheric gravity waves. Vol. 85 of International geophysics series. Academic Press, San Diego.

Nash, E. R., Newman, P. A., Rosenfield, J. E., Schoeberl, M. R., 1996. An objective determination of the polar vortex using Ertel's potential vorticity. Journal of Geophysical Research 101 (D5), 9471–9478.

Nastrom, G. D., Fritts, D. C., 1992. Sources of Mesoscale Variability of Gravity-Waves. Part I: Topographic Excitation. Journal of the Atmospheric Sciences 49 (2), 101–110.

Nastrom, G. D., Hansen, A. R., Tsuda, T., Nishida, M., Ware, R., 2000. A comparison of gravity wave energy observed by VHF radar and GPS/MET over central North America. Journal of Geophysical Research 105 (D4), 4685–4687.

Newman, P. A., Nash, E. R., 2005. The unusual Southern Hemisphere stratosphere winter of 2002. Journal of the Atmospheric Sciences 62 (3), 614–628.

NOAA, 2005. Space Environment Center, http://www.sec.noaa.gov.

Norton, W. A., Thuburn, J., 1996. The two-day wave in a middle atmosphere GCM. Geophysical Research Letters 23 (16), 2113–2116.

Nozawa, S., Imaida, S., Brekke, A., Hall, C. M., Manson, A., Meek, C., Oyama, S., Dobashi, K., Fujii, R., 2003a. The quasi 2-day wave observed in the polar mesosphere. Journal of Geophysical Research 108 (D2), 4039, doi:10.1029/2002JD002440.

Nozawa, S., Iwahashi, H., Brekke, A., Hall, C. M., Meek, C., Manson, A., Oyama, S., Murayama, Y., Fujii, R., 2003b. The quasi 2-day wave observed in the polar mesosphere: Comparison of the characteristics observed at Tromso and Poker Flat. Journal of Geophysical Research 108 (D24), 4748, doi:10.1029/2002JD003221.

Palm, S. P., Fromm, M., Spinhirne, J., 2005. Observations of antarctic polar stratospheric clouds by the Geoscience Laser Altimeter System (GLAS). Geophysical Research Letters 32, L22S04, doi:10.1029/2005GL023524.

Pancheva, D., Mitchell, N. J., Hagan, M. E., Manson, A. H., Meek, C. E., Luo, Y., Jacobi, C., Kurschner, D., Clark, R. R., Hocking, W. K., MacDougall, J., Jones, G. O. L., Vincent, R. A., Reid, I. M., Singer, W., Igarashi, K., Fraser, G. I., Nakamura, T., Tsuda, T., Portnyagin, Y., Merzlyakov, E., Fahrutdinova, A. N., Stepanov, A. M., Poole, L. M. G., Malinga, S. B., Kashcheyev, B. L., Oleynikov, A. N., Riggin, D. M., 2002. Global-scale tidal structure in the mesosphere and lower thermosphere during the PSMOS campaign of June-August 1999 and comparisons with the global-scale wave model. Journal of Atmospheric and Solar-Terrestrial Physics 64 (8-11), 1011–1035.

Pawsey, J. L., 1935. Further investigations of the amplitude variations of downcoming wireless waves. Proceedings of the Cambridge Philosophical Society 31, 125.

Pfister, L., 1985. Baroclinic Instability of Easterly Jets with Applications to the Summer Mesosphere. Journal of the Atmospheric Sciences 42 (4), 313–330.

Pfister, W., 1971. Wave-Like Nature of Inhomogeneities in E-Region. Journal of Atmospheric and Terrestrial Physics 33 (7), 999–1025.

Phillips, G. J., Spencer, M., 1955. The effects of anisometric amplitude patterns on the measurement of ionosperic drifts. Proceedings of the Physical Society of London, Section B 68, 481–492.

Pickett, H. M., Drouin, B. J., Canty, T., Kovalenko, L. J., Salawitch, R. J., Livesey, N. J., Read, W. G., Waters, J. W., Jucks, K. W., Traub, W. A., 2006. Validation of Aura MLS HO_x measurements with remote-sensing balloon instruments. Geophysical Research Letters 33 (1), –.

Plumb, R. A., 1983. Baroclinic Instability of the Summer Mesosphere: a Mechanism for the Quasi-Two-Day Wave? Journal of the Atmospheric Sciences 40 (1), 262–270.

Portnyagin, Y. I., Forbes, J. M., Fraser, G. J., Vincent, R. A., Avery, S. K., Lysenko, I. A., Makarov, N. A., 1993a. Dynamics of the Antarctic and Arctic Mesosphere and Lower Thermosphere Regions –II. The Semidiurnal Tide. Journal of Atmospheric and Terrestrial Physics 55 (6), 843–855.

Portnyagin, Y. I., Forbes, J. M., Fraser, G. J., Vincent, R. A., Avery, S. K., Lysenko, I. A., Makarov, N. A., 1993b. Dynamics of the Antarctic and Arctic Mesosphere and Lower Thermosphere Regions –I. The Prevailing Wind. Journal of Atmospheric and Terrestrial Physics 55 (6), 827–841.

Portnyagin, Y. I., Forbes, J. M., Makarov, N. A., Merzlyakov, E. G., Palo, S., 1998. The summertime 12-h wind oscillation with zonal wavenumber s=1 in the lower thermosphere over the South Pole. Annales Geophysicae-Atmospheres Hydrospheres and Space Sciences 16 (7), 828–837.

Portnyagin, Y. I., Merzlyakov, E. G., Solovjova, T. V., Jacobi, C., Krschner, D., Manson, A., Meek, C., 2006. Long-term trends and year-to-year variability of mid-latitude mesosphere/lower thermosphere winds. Journal of Atmospheric and Solar-Terrestrial Physics 68 (17), 1890–1901.

Portnyagin, Y. I., Solovjova, T. V., 2000. Global empirical wind model for the upper mesosphere/lower thermosphere. I. Prevailing wind. Annales Geophysicae-Atmospheres Hydrospheres and Space Sciences 18 (3), 300–315.

Praskovsky, A. A., Praskovskaya, E. A., Hassenpflug, G., Yamamoto, M., Fukao, S., 2004. Wind and turbulence measurements by the Middle and Upper Atmosphere Radar (MUR): comparison of techniques. Annales Geophysicae 22 (11), 3843–3862.

Prata, A. J., 1984. The 4-Day Wave. Journal of the Atmospheric Sciences 41 (1), 150–155.

Press, W. H., Flannery, B. P., Teukolsky, S. A., Vetterling, W. T., 1992. Numerical Recipes in C: The Art of Scientific Computing, 2nd Edition. Cambridge University Press.

Randel, W. J., 1994. Observations of the 2-Day Wave in NMC Stratospheric Analyses. Journal of the Atmospheric Sciences 51 (2), 306–313.

Randel, W. J., Lait, L. R., 1991. Dynamics of the 4-Day Wave in the Southern-Hemisphere Polar Stratosphere. Journal of the Atmospheric Sciences 48 (23), 2496–2508.

Ratcliffe, J. A., Pawsey, J. L., 1933. A study of the intensity variations of downcoming wireless waves. Proceedings of the Cambridge Philosophical Society 29, 301–318.

Ratnam, M. V., Tetzlaff, G., Jacobi, C., 2004a. Global and seasonal variations of stratospheric gravity wave activity deduced from the CHAMP/GPS satellite. Journal of the Atmospheric Sciences 61 (13), 1610–1620.

Ratnam, M. V., Tsuda, T., Jacobi, C., Aoyama, Y., 2004b. Enhancement of gravity wave activity observed during a major Southern Hemisphere stratospheric warming by CHAMP/GPS measurements. Geophysical Research Letters 31 (16), L16101, doi:10.1029/2004GL019789.

Read, W. G., Shippony, Z., Schwartz, M. J., Livesey, N. J., Van Snyder, W., 2006. The clear-sky unpolarized forward model for the EOS Microwave Limb Sounder (MLS). Ieee Transactions on Geoscience and Remote Sensing 44 (5), 1367–1379.

Rees, D., Barnett, J. J., Labitzke, K., 1990. CIRA 1986, Part II Middle Atmopshere Models. Advances in Space Research 10 (2), 187–206.

Rew, R., Davis, G., 1990. NetCDF - an Interface for Scientific Data Access. Ieee Computer Graphics and Applications 10 (4), 76–82.

Riggin, D. M., Fritts, D. C., Jarvis, M. J., Jones, G. O. L., 1999. Spatial structure of the 12-hour wave in the Antarctic as observed by radar. Earth Planets and Space 51 (7-8), 621–628.

Rodgers, C. D., 2000. Inverse methods for atmospheric sounding: theory and practice. Series on atmospheric, oceanic and planetary physics ; v.2. World Scientific, Singapore; River Edge, N.J.

Rodgers, C. D., Prata, A. J., 1981. Evidence for a Traveling 2-Day Wave in the Middle Atmosphere. Journal of Geophysical Research 86 (NC10), 9661–9664.

Rossby, C. G., 1939. Relation between variations in the intensity of the zonal circulation of the atmosphere and the displacements of the semipermanent centers of action. Journal of Marine Research 2 (1), 38–55.

Salby, M. L., 1981a. The 2-Day Wave in the Middle Atmosphere: Observations and Theory. Journal of Geophysical Research 86 (NC10), 9654–9660.

Salby, M. L., 1981b. Rossby Normal-Modes in Nonuniform Background Configurations, Part I, Simple Fields. Journal of the Atmospheric Sciences 38 (9), 1803–1826.

Salby, M. L., 1981c. Rossby Normal-Modes in Nonuniform Background Configurations, Part II, Equinox and Solstice Conditions. Journal of the Atmospheric Sciences 38 (9), 1827–1840.

Salby, M. L., 1984. Survey of Planetary-Scale Traveling Waves - the State of Theory and Observations. Reviews of Geophysics 22 (2), 209–236.

Salby, M. L., Callaghan, P. F., 2001. Seasonal amplification of the 2-day wave: Relationship between normal mode and instability. Journal of the Atmospheric Sciences 58 (14), 1858–1869.

Salby, M. L., Callaghan, P. F., 2003. Dynamics of the 2-day wave in a nonlinear model of the middle and upper atmosphere. Journal of Geophysical Research 108 (D23), 4713, doi:10.1029/2003JD003648.

Salby, M. L., Callaghan, P. F., 2004. Evidence of the solar cycle in the general circulation of the stratosphere. Journal of Climate 17 (1), 34–46.

Schröder, H., Schmitz, G., 2004. A generation mechanism for the 2-day wave near the stratopause: Mixed barotropic-inertial instability. Journal of Geophysical Research 109, D24116, doi:10.1029/2004JD005177.

Schwartz, M. J., Read, W. G., Van Snyder, W., 2006. EOS MLS forward model polarized radiative tranfer for Zeeman-split oxygen lines. Ieee Transactions on Geoscience and Remote Sensing 44 (5), 1182–1191.

Shibata, T., Sato, K., Kobayashi, H., Yabuki, M., Shiobara, M., 2003. Antarctic polar stratospheric clouds under temperature perturbation by nonorographic inertia gravity waves observed by micropulse lidar at Syowa Station. Journal of Geophysical Research 108 (D3), 4105, doi:10.1029/2002JD002713, 2003.

Smith, A. K., Ortland, D. A., 2001. Modeling and analysis of the structure and generation of the terdiurnal tide. Journal of the Atmospheric Sciences 58 (21), 3116–3134.

Solomon, S., Rusch, D. W., Gerard, J. C., Reid, G. C., Crutzen, P. J., 1981. The Effect of Particle-Precipitation Events on the Neutral and Ion Chemistry of the Middle Atmosphere: II. Odd Hydrogen. Planetary and Space Science 29 (8), 885–892.

Sprenger, K., Schminder, R., 1969. Solar cycle dependence of winds in the lower ionosphere. Journal of Atmospheric and Solar-Terrestrial Physics 31, 217 – 221.

Sturman, A., Tapper, N. J., 1996. The weather and climate of Australia and New Zealand. Oxford University Press, Melbourne [Vic.].

Sürücü, F., Franke, S. J., Kudeki, E., 1995. On the Influence of Specular Reflections in MF Radar Wind Measurements. Radio Science 30 (4), 1229–1244.

Swinbank, R., Lahoz, W. A., O'Neill, A., Douglas, C. S., Heaps, A., Podd, D., 1998. Middle atmosphere variability in the UK Meteorological Office Unified Model. Quarterly Journal of the Royal Meteorological Society 124 (549), 1485–1525.

Thayaparan, T., Hocking, W. K., 2002. A long-term comparison of winds and tides measured at London, Canada (43°N, 81°W) by co-located MF and meteor radars during 1994-1999. Journal of Atmospheric and Solar-Terrestrial Physics 64 (8-11), 931–946.

Thayaparan, T., Hocking, W. K., MacDougall, J., 1997. Amplitude, phase, and period variations of the quasi 2-day wave in the mesosphere and lower thermosphere over London, Canada (43°N, 81°W), during 1993 and 1994. Journal of Geophysical Research 102 (D8), 9461–9478.

Thomas, G. E., 1996. Is the polar mesosphere the miner's canary of global change? Advances in Space Research 18 (3), 149–158.

Thomas, G. E., Rapp, M., Palo, S., DeLand, M. T., Baumgaertner, A. J. G., 2006. Long-term Variations of PMC brightness and occurence frequency: Are they caused by changes in atmospheric tides? In: AGU Joint Assembly. Baltimore.

Torrence, C., Compo, G. P., 1998. A practical guide to wavelet analysis. Bulletin of the American Meteorological Society 79 (1), 61–78.

Tsuda, T., Nishida, M., Rocken, C., Ware, R. H., 2000. A global morphology of gravity wave activity in the stratosphere revealed by the GPS occultation data (GPS/MET). Journal of Geophysical Research 105 (D6), 7257–7273.

Venne, D. E., Stanford, J. L., 1979. Observation of a 4-Day Temperature Wave in the Polar Winter Stratosphere. Journal of the Atmospheric Sciences 36 (10), 2016–2019.

Vial, F., 1989. Tides in the Middle Atmosphere. Journal of Atmospheric and Terrestrial Physics 51 (1), 3–17.

Vial, F., Forbes, J. M., 1989. Recent Progress in Tidal Modeling. Journal of Atmospheric and Terrestrial Physics 51 (7-8), 663–671.

Vincent, R. A., Kovalam, S., Fritts, D. C., Isler, J. R., 1998. Long-term MF radar observations of solar tides in the low-latitude mesosphere: Interannual variability and comparisons with the GSWM. Journal of Geophysical Research 103 (D8), 8667–8683.

Vincent, R. A., May, P. T., Hocking, W. K., Elford, W. G., Candy, B. H., Briggs, B. H., 1987. First Results with the Adelaide VHF Radar - Spaced Antenna Studies of Tropospheric Winds. Journal of Atmospheric and Terrestrial Physics 49 (4), 353–366.

Volland, H., 1988. Atmospheric tidal and planetary waves. Atmospheric sciences library. Kluwer Academic Publishers ; Sold and distributed in the U.S.A. and Canada by Kluwer Academic Publishers, Dordrecht ; Boston Norwell, MA, U.S.A.

Walterscheid, R. L., 1980. Traveling Planetary-Waves in the Stratosphere. Pure and Applied Geophysics 118 (1-2), 239–265.

Walterscheid, R. L., Vincent, R. A., 1996. Tidal generation of the phase-locked 2-day wave in the southern hemisphere summer by wave-wave interactions. Journal of Geophysical Research 101 (D21), 26567–26576.

Watanabe, S., Hirooka, T., Miyahara, S., 2002. Interannual Variations of the General Circulation and Polar Stratospheric Ozone Losses in a General Circulation Model. Journal of the Meteorological Society of Japan 80 (4B), 877–895.

Waters, J. W., Froidevaux, L., Harwood, R. S., Jarnot, R. F., Pickett, H. M., Read, W. G., Siegel, P. H., Cofield, R. E., Filipiak, M. J., Flower, D. A., Holden, J. R., Lau, G. K., Livesey, N. J., Manney, G. L., Pumphrey, H. C., Santee, M. L., Wu, D. L., Cuddy, D. T., Lay, R. R., Loo, M. S., Perun, V. S., Schwartz, M. J., Stek, P. C., Thurstans, R. P., Boyles, M. A., Chandra, K. M., Chavez, M. C., Chen, G. S., Chudasama, B. V., Dodge, R., Fuller, R. A., Girard, M. A., Jiang, J. H., Jiang, Y. B., Knosp, B. W., LaBelle, R. C., Lam, J. C., Lee, K. A., Miller, D., Oswald, J. E., Patel, N. C., Pukala, D. M., Quintero, O., Scaff, D. M., Van Snyder, W., Tope, M. C., Wagner, P. A., Walch, M. J., 2006. The Earth Observing System Microwave Limb Sounder (EOS MLS) on the Aura satellite. Ieee Transactions on Geoscience and Remote Sensing 44 (5), 1075–1092.

Whiteway, J. A., Duck, T. J., 1996. Evidence for critical level filtering of atmospheric gravity waves. Geophysical Research Letters 23 (2), 145–148.

Whiteway, J. A., Duck, T. J., Donovan, D. P., Bird, J. C., Pal, S. R., Carswell, A. I., 1997. Measurements of gravity wave activity within and around the Arctic stratospheric vortex. Geophysical Research Letters 24 (11), 1387–1390.

Wu, D. L., Hays, P. B., Skinner, W. R., 1995. A Least-Squares Method for Spectral-Analysis of Space-Time Series. Journal of the Atmospheric Sciences 52 (20), 3501–3511.

Wu, D. L., Hays, P. B., Skinner, W. R., Marshall, A. R., Burrage, M. D., Lieberman, R. S., Ortland, D. A., 1993. Observations of the Quasi 2-Day Wave from the High-Resolution Doppler Imager on UARS. Geophysical Research Letters 20 (24), 2853–2856.

Wu, D. L., Jiang, J. H., 2002. MLS observations of atmospheric gravity waves over Antarctica. Journal of Geophysical Research 107 (D24), 4773, doi:10.1029/2002JD002390.

Wu, D. L., Waters, J. W., 1996. Satellite observations of atmospheric variances: A possible indication of gravity waves. Geophysical Research Letters 23 (24), 3631–3634.

Yamashita, K., Miyahara, S., Miyoshi, Y., Kawano, K., Ninomiya, J., 2002. Seasonal variation of non-migrating semidiurnal tide in the polar MLT region in a general circulation model. Journal of Atmospheric and Solar-Terrestrial Physics 64 (8-11), 1083–1094.

Yoshiki, M., Kizu, N., Sato, K., 2004. Energy enhancements of gravity waves in the Antarctic lower stratosphere associated with variations in the polar vortex and tropospheric disturbances. Journal of Geophysical Research 109 (D23), D23104, doi:10.1029/2004JD004870.

Yoshiki, M., Sato, K., 2000. A statistical study of gravity waves in the polar regions based on operational radiosonde data. Journal of Geophysical Research 105 (D14), 17995–18011.

Zängl, G., Hoinka, K. P., 2001. The Tropopause in the Polar Regions. Journal of Climate 14.